

# Strong field ionization of atoms and molecules: An ultrafast perspective

A thesis submitted in partial fulfillment of  
the requirements for the degree of

**Doctor of Philosophy**

*by*

**Madhusudhan P**

(Roll No. 17330017)

Under the supervision of

**Dr Rajesh Kumar Kushawaha**

Associate Professor

Atomic, Molecular and Optical Physics

Physical Research Laboratory, Ahmedabad, India.



DEPARTMENT OF PHYSICS

INDIAN INSTITUTE OF TECHNOLOGY GANDHINAGAR

2022



©Copyright by  
MADHUSUDHAN P  
2023.



# DECLARATION

I declare that this written submission represents my ideas in my own words and where others' ideas or words have been included, I have adequately cited and referenced the original sources. I also declare that I have adhered to all principles of academic honesty and integrity and have not misrepresented or fabricated or falsified any idea/data/fact/source in my submission. I understand that any violation of the above will be cause for disciplinary action by the Institute and can also evoke penal action from the sources which have thus not been properly cited or from whom proper permission has not been taken when needed.

(Name: Madhusudhan P)

(Roll No: 17330017)

Date: 01<sup>st</sup> August 2023



# CERTIFICATE

It is certified that the work contained in the thesis titled “**Strong field ionization of atoms and molecules: An ultrafast perspective**” by **Madhusudhan P** (Roll no: 17330017), has been carried out under my supervision and that this work has not been submitted elsewhere for degree.

I have read this dissertation and in my opinion, it is fully adequate in scope and quality as a dissertation for the degree of Doctor of Philosophy.

**Dr Rajesh Kumar Kushawaha**  
(Thesis Supervisor)

Associate Professor  
Atomic, Molecular and Optical Physics  
Physical Research Laboratory  
Navarangpura, Ahmedabad, India



---

## Acknowledgements

*I sincerely would like to thank my guide Dr Rajesh Kumar Kushawaha for being the backbone throughout the 5 years of Ph.D tenure. He has taught me to believe in science there is always a solution in the lab with experiments. He has given me the freedom and direction to develop and learn new techniques, programming languages, theories. It wouldn't be wrong to say that I wouldn't be who I am without him. Even though I have troubled him late at nights, early in the mornings, holidays and even when he's busy with official work. I also would like to thank Vinitha Nimma for assisting me almost daily during the course of my experiments. She has been instrumental in all my experiments working in the lab throughout the day to late night. Her dedication towards the lab and the research is unparalleled, and has been seen to work even during the worst cyclones of Ahmedabad that I've witnessed. I would be lying if I said I've learned everything that I know by just studying the research papers, when Mr Pranav Bharadwaj with his quick and intuitive thinking threw a number of questions to deepen the state of understanding. He was the one who recognised the issue with my two-color studies very early on which helped me navigate through the mess and yield reliable, tested and fruitful results. I am immensely grateful to Mrs Pooja Chandravanshi for assisting and teaching me in most, if not all electronic and instrument interface requirements. I would have her on the phone for even the most silliest problems and with all her patience she would help me solve the issues methodically. I am also indebted to Mrs. Rituparna Das for the access of the COLTRIMS setup and also assisting in my research. I owe a great debt of gratitude to my friends at PRL Anshika Bansal, Ashwin Devaraj, and Deepali Agarwal to have engaged me in several scientific discussions which lasted nights. Though the discussions were barely about my research topic, those discussions nurtured the scientific temperament and reshaped my scientific perspective. I am also thankful to many of my lab colleagues Swetapuspa sowmyashree, Dr Prashant Kumar, Kaavil, Dr Nageshwar Rao erupu, Dr Muhammed Shameem for teaching and working with me toward my research objectives. I am also unequivocally delighted to have a strong support system of Doctoral Studies Committee(DSC) comprising of Dr RP Singh, Dr Naveen Chauhan and Prof Dibyendu Choudhary.*

---

*Dr RP Singh who is also the Chairman of AMOPH division has extended his unwavering support of my research or attending conferences and meetings or any other kind of Academic activities. Dr Naveen Chauhan has offered his invaluable advices for my research and also for several other personal qualms. Prof Dibyendu has helped me grow as a researcher and a better presenter with his incisive and clear advices.*

*Academically last but not the least I am unfathomably filled with gratitude to all the labs in PRL who have assisted me to the best of their capacity in my research. This research would not have been possible without the extensive support of our Director, Dr Anil Bharadwaj, the academic committee, all the faculties especially those in AMOPH, administration departments (special mention: Mrs Richa and Mr Pradeep Chauhan) CMG, Canteen, CISF and the housekeeping staff. The workshop of PRL deserves a special mention for constant and round the clock support from the first day of lab installation to the last day of my experiments, their workmanship and tenacity of the jobs by Pramod sir, Kaila sir and mainly Vaghela sir, has many times left me in awe.*

*I am also very thankful to all the students of PRL, my seniors, juniors and specially the batch of 2017 for this journey of Ph.D. Their support and assistance may at times be invisible but their spirit always let me be the researcher that I am today. The volley ball tournaments of PRL has definitely been a very effective stress buster throughout this journey. Dr Aravind Singh deserves a special mention for his support in the volleyball tournament and also in several instances that were related to my academic career.*

*Lastly to all my teachers starting from my mother, my father, my brother and my sister-in-law for their constant guidance and unrelenting support towards this endeavour, I am profoundly thankful. Their never ending love towards me make me feel blessed and give me the freedom to wander into unknown worlds for I know that they will always be there with me as my safety net. Their words of advice throughout my life has served as the map to a bright future. This journey towards the bright future would be lonely without my friends-family. Yamina has always been the fun but also a generous and helpful well-wisher. Preksha and Nayana have been the late-night stressbusters with the insane, never ending debates and conversations. My sister Aishwarya has served the role of an artist putting back the pieces (that I have ended up in more than once) and has always been supportive of me, even when I did not believe in me. Last but by*

---

*far not the least Nikhil, his support and conversations has led me to believe in a better version of myself. I do recognise that I have not been able to assimilate all the teachers in my life into this acknowledgement but they are always alive and kicking inside me.*

**(Madhusudhan P)**



To

*All my teachers*

*who taught me to*

*learn, unlearn and relearn*



---

# Abstract

Light-Matter interactions have served as a great tool to uncover the secrets of nature. At an atomic level, the interaction of light with atoms and molecules holds the key to untangling the electronic structure and dynamics involved in the process. The timescale of the electron and nuclear dynamics in molecules extends from the attosecond ( $10^{-18}$  s) regime to the picosecond ( $10^{-12}$  s) time domain. In molecular reactions, these dynamics play a vital role. To chase these dynamics during the molecular reaction and to control the reaction, an ultrashort (femtosecond to attosecond) light probe is needed. The available commercial femtosecond lasers produce about 25 fs light pulses, which are suitable for probing processes that do not require less than 25 fs pulses, such as molecule rotation and alignment study. For probing and controlling the molecular dissociative reactions at sub-femtosecond or attosecond time resolution, we need either an attosecond light pulses or a new experimental scheme. The two-color method emerged as a powerful technique to study the sub-fs ultrafast processes in atoms and molecules. In the current study, an intense ultrafast laser with a pulse duration of 26 fs and pulse energy of up to 0.6 mJ is used in the two-color ( $\omega - 2\omega$ ) method to study the molecular and electron dynamics in the sub-fs regime. The orthogonal or parallel two-color field generation and phase control method has been used in the current study to understand the ultrafast processes. A homemade Velocity Map Imaging spectrometer (VMI) was used to detect the ions and photoelectrons. Atoms, diatomic molecules, and triatomic molecules were studied in the single-color and two-color fields to elucidate the contribution of the relative phase on the ion and electron yields. It was observed that the ion yield by ionization and fragmentation was sensitive to the relative phase of the two-color fields. The theoretical simulation of the tunneling electron revisits trajectories is performed to explain the experimental findings. In summary, we demonstrated the Quantum control of molecular dissociative reactions using a two-color laser field.



# Contents

<b>Abstract</b>	<b>i</b>
<b>List of Figures</b>	<b>vii</b>
<b>List of Tables</b>	<b>xvii</b>
<b>List of Acronyms</b>	<b>xix</b>
<b>List of Publications</b>	<b>xxi</b>
<b>1 Introduction</b>	<b>1</b>
1.1 Background and Motivation . . . . .	1
1.1.1 Strong-field ionization of atoms and molecules . . . . .	3
1.1.2 Ultrafast dynamics in atoms and molecules . . . . .	6
1.1.3 Quantum control of molecular reactions . . . . .	7
1.1.4 Two-color laser field-induced ionization . . . . .	7
1.1.5 Our Focus: Objectives of thesis . . . . .	8
1.2 Thesis Outline . . . . .	9
1.2.1 Summary and Future works . . . . .	11
<b>2 Methodology</b>	<b>13</b>
2.1 Introduction . . . . .	13
2.2 Ultrafast Lasers . . . . .	14
2.2.1 Mode-locked femtosecond oscillator . . . . .	14
2.2.2 Stretcher/Compressor of femtosecond laser . . . . .	15
2.2.3 Amplifier of femtosecond laser . . . . .	15
2.3 Pulse Characterisation . . . . .	16

2.3.1	Field auto-correlation . . . . .	17
2.3.2	Intensity auto-correlation . . . . .	18
2.3.3	Spectral Phase Interferometry for Direct Electric-field Re- construction (SPIDER) . . . . .	18
2.4	Time of Flight Mass Spectrometer . . . . .	19
2.5	Velocity-Map Imaging . . . . .	21
2.5.1	Simulation . . . . .	23
2.5.2	Construction and Assembly of multi-plate Velocity Map Imaging Spectrometer, mounted on CF200 flange . . . . .	24
2.5.3	Calibration of the VMI spectrometer . . . . .	25
2.6	Two-color setup . . . . .	27
2.6.1	Overlap confirmation by detecting the Third Harmonic Generation . . . . .	27
2.6.2	Pump-probe method . . . . .	30
2.6.3	Wedge-plate method . . . . .	31
2.6.4	Compensation plate . . . . .	31
2.7	Classical Electron Trajectories . . . . .	31
2.7.1	Single color Field . . . . .	34
2.7.2	Orthogonal two-colored linearly polarized fields . . . . .	41
2.7.3	Parallel two-colored linearly polarized fields . . . . .	41
2.8	Theoretical ADK modelling . . . . .	43
2.9	Summary and Conclusions . . . . .	47
<b>3</b>	<b>Single-color and two-color induced ionization of atoms: Argon and Xenon</b> . . . . .	<b>49</b>
3.1	Introduction . . . . .	49
3.2	Methodology . . . . .	51
3.2.1	Single color photoionization experiment . . . . .	51
3.2.2	Two-color photoionization experiment . . . . .	51
3.2.3	ADK ionization rate . . . . .	52
3.3	Results and Discussions . . . . .	52

3.3.1	Single and two-color field-induced ionization of Argon: Intensity dependence . . . . .	52
3.3.2	Phase dependent two-color photoionization Argon: PTC & OTC . . . . .	56
3.3.3	Two-color (PTC) induced Photoelectron Momentum Distribution: Argon . . . . .	59
3.3.4	Two-color (OTC) induced Photoelectron Momentum Distribution: Argon . . . . .	64
3.3.5	Phase dependent two-color photoionization Xenon: PTC & OTC . . . . .	69
3.3.6	Two-color (PTC) induced Photoelectron Momentum Distribution: Xenon . . . . .	69
3.3.7	Two-color (OTC) induced Photoelectron Momentum Distribution: Xenon . . . . .	71
3.4	Summary and Conclusions . . . . .	75
<b>4</b>	<b>Single-color and two-color induced strong-field ionization of diatomic molecules: N<sub>2</sub> and CO</b>	<b>79</b>
4.1	Introduction . . . . .	79
4.2	Two-color Experimental scheme . . . . .	81
4.2.1	Two-color femtosecond laser fields . . . . .	81
4.2.2	Data acquisition scheme . . . . .	85
4.2.3	Data analysis scheme . . . . .	85
4.2.4	Semi-classical tunnel electrons trajectory simulations: In two-color fields . . . . .	86
4.3	Results and Discussions . . . . .	88
4.3.1	Two-color (PTC) fields induced ionization: intensity dependence on ion yield . . . . .	88
4.3.2	Two-color (OTC) fields induced ionization: phase dependence on ion yield . . . . .	94
4.3.3	Two-color induced ionization: Photoelectron momentum distributions . . . . .	100

---

4.4	Conclusions . . . . .	108
<b>5</b>	<b>Strong-field ionization of CO<sub>2</sub></b>	<b>111</b>
5.1	Introduction . . . . .	111
5.2	Experimental scheme . . . . .	113
5.2.1	Single-color photoionization experiment . . . . .	113
5.2.2	Two-color photoionization experiment . . . . .	114
5.3	Results . . . . .	115
5.3.1	Intensity dependent single-color photoionization of CO <sub>2</sub> . .	115
5.3.2	Wavelength dependent photoionization of CO <sub>2</sub> . . . . .	122
5.3.3	Pulse duration dependence photoionization of CO <sub>2</sub> . . . .	123
5.3.4	Intensity dependent two-color photoionization CO <sub>2</sub> : PTC .	127
5.3.5	Intensity dependent two-color photoionization CO <sub>2</sub> : OTC .	130
5.3.6	Phase dependent two-color photoionization CO <sub>2</sub> : PTC . .	133
5.3.7	Phase dependent two-color photoionization CO <sub>2</sub> : OTC . .	138
5.4	Photoelectron momentum distribution of CO <sub>2</sub> induced by two- color (PTC) field . . . . .	139
5.5	Photoelectron momentum distribution of CO <sub>2</sub> induced by two- color (OTC) field . . . . .	142
5.6	Summary and Conclusions . . . . .	148
<b>6</b>	<b>Summary and Future Scope</b>	<b>151</b>

# List of Figures

1.1	Fundamental atomic, molecular and electronic phenomena probed on ultrafast timescales. . . . .	2
1.2	The atomic Coulomb potentials under the influence of intense laser fields are shown for different modes of ionization. . . . .	4
1.3	Schematic of single and two-color fields interacting with atoms, di- and tri-atomic molecules. . . . .	8
2.1	Schematic femtolaser . . . . .	14
2.2	Graphical representation of gaussian ultrashort pulse. . . . .	16
2.3	Schematic representation of SPIDER. M corresponds to mirrors, BS corresponds to Beams plitters, and DS corresponds to delay stage . . . . .	18
2.4	Femtosecond pulse characterization using PRL's SPIDER. . . . .	19
2.5	Schematic of Time-of-flight mass spectrometer . . . . .	21
2.6	[left] Uncalibrated TOF spectrum of Argon, [right] the calibration curve based on the TOF of Argon. . . . .	22
2.7	Calibrated TOF spectrum of Argon obtained at laser intensity $0.69 \text{ PW/cm}^2$ . . . . .	22
2.8	Charged particle trajectories simulation for construction of Multi-plate Velocity Map Imaging Spectrometer. The electrons with KE of 5eV, 10eV, 20eV, and 50eV are projected (focused) at the detector for the given electrodes' potential. The simulation was performed in SIMION software. . . . .	24
2.9	VMI electrode assembly . . . . .	26

2.10	Third Harmonic detection using a spectrometer. FW, SH, and TH peaks are observed at the overlap of FW and SH. . . . .	28
2.11	Yield of Third Harmonic Generation as a function of the delay between FW and SH. . . . .	29
2.12	Schematic of two-color setup, [A] Calcite-based two-color setup, [B] Wedge mirrors based two-color setup, [C] Pump-probe type two-color setup . . . . .	30
2.13	Photoelectron yield as a function of delay in all three setups in PTC	32
2.14	Photoelectron yield as a function of delay in all three setups in OTC. . . . .	33
2.15	[top] 20 Electron trajectories at different birth times in the presence of 400 nm electric field, with peak power $0.46 \text{ PW/cm}^2$ . [bottom] The kinetic energy of the electron at every instant (5 as). The color codes of the kinetic energy of the electrons correspond to their electron trajectories. . . . .	35
2.16	[top]The shaded region in the left panel represents the range of birth times over the electric field of the 400 nm pulse, with peak power $0.46 \text{ PW/cm}^2$ . [bottom] The recollision kinetic energy of the electrons with different birth times. . . . .	36
2.17	[top]20 Electron trajectories at different birth times [left] in the presence of 800 nm electric field, with peak power $0.46 \text{ PW/cm}^2$ . [bottom] The kinetic energy of the electron at every instant (5 as). The color codes of the kinetic energy of the electrons correspond to their electron trajectories. . . . .	37
2.18	[top]The shaded region in the left panel represents the range of birth times over the electric field of the 800 nm pulse, with peak power $0.46 \text{ PW/cm}^2$ . [bottom] The recollision kinetic energy of the electrons with different birth times. . . . .	38
2.19	Top panel represents the 800 nm and 400 nm two-color fields. The bottom panel represents the resultant of orthogonal two-color fields.	40
2.20	Maximum kinetic energy of the revisiting electron in the presence of OTC fields as a function of the birth-time. . . . .	42

2.21	Top panel represents the 800 nm and 400 nm two-color fields. The bottom panel represents the resultant of parallel two-color fields. . . . .	44
2.22	Maximum kinetic energy of the revisiting electron in the presence of PTC fields as a function of the birth-time. . . . .	45
2.23	Theoretical ionization probability of Ar <sup>+</sup> using ADK model . . . . .	47
3.1	[Top] Ion yield of Ar <sup>+</sup> (red), Ar <sup>2+</sup> (blue) and the ADK calculated ion yield of Ar <sup>+</sup> (black line) as a function of intensity of single color 800 nm is compared with the ion yield of [bottom] Ar <sup>+</sup> (red) and Ar <sup>2+</sup> (blue) as a function of the intensity of PTC (800 nm and 400 nm) pulses. . . . .	54
3.2	Photo-ionization of Argon using intense femtosecond laser pulses as a function of laser intensity. . . . .	55
3.3	A scheme of two-color processes . . . . .	55
3.4	Ar <sup>2+</sup> and Ar <sup>+</sup> ions yield as a function of relative phase at intensity ratio ( $I_{SP}/I_{FP}=0.65$ ) . . . . .	57
3.5	Two-color (OTC) induced Ar <sup>2+</sup> and Ar <sup>+</sup> ions yield as a function of relative phase at intensity ratio ( $I_{SP}/I_{FP}=0.65$ ). . . . .	58
3.6	Photoelectron momentum distributions of Ar induced by Two-color parallel polarized field at laser intensity ratio of 2 ( $I_{SP}/I_{FP}=2$ ), [top] at relative phase 0, [bottom] at relative phase $\pi/2$ . Polarization of both fields was in the detector plane. . . . .	60
3.7	[top] Photoelectron yield as a function of delay or relative phase between 800 nm and 400 nm. [bottom] The photoelectron yield at three different intensity ratios ( $I_{SP}/I_{FP}$ ). The yield at the relative phase at 0 and $\pi/2$ is also shown in this figure. . . . .	61
3.8	Asymmetry in $p_x$ as a function of laser intensity ratio. . . . .	64
3.9	Photoelectron momentum distributions of Ar induced by Two-color Orthogonal polarized field at laser intensity ratio of 2 ( $I_{SP}/I_{FP}=2$ ), [top] at relative phase 0, [bottom] at relative phase $\pi/2$ . . . . .	65

3.10 Photoelectron yield as a function of delay or relative phase between 800 nm and 400 nm. Red points are experimental data points. The blue line is based on fittings. . . . .	66
3.11 Asymmetry in $p_x$ and $p_y$ as a function of relative phases at 0 and $\pi/2$ . . . . .	67
3.12 $\text{Xe}^+$ ions yield as a function of relative phase, at $I_{800} = 0.09 \text{ PW/cm}^2$ and $I_{400} = 0.03 \text{ PW/cm}^2$ . The polarization of FW and SH are parallel [top panel], and orthogonal [bottom panel]. . . . .	70
3.13 Photoelectron momentum distributions of Xe induced by Two-color parallel polarized field at laser intensity ratio of 3 ( $I_{FW}/I_{SH} = 3$ ), [top] at relative phase 0, [bottom] at relative phase $\pi/2$ . Polarization of both fields was in the detector plane. . . . .	72
3.14 Photoelectron yield as a function of relative phase, at $I_{800} = 0.09 \text{ PW/cm}^2$ and $I_{400} = 0.03 \text{ PW/cm}^2$ . . . . .	73
3.15 Asymmetry along $p_x$ and $p_y$ induced by two-color (PTC) field at 0 and $\pi$ of relative phase. . . . .	74
3.16 Photoelectron momentum distributions of Xe induced by FW (800 nm) [top, left], SH (400 nm) [top, right] and by Two-color orthogonally polarized field at laser intensity ratio of 3 ( $I_{FP}/I_{SP} = 3$ ), [bottom, left] at relative phase 0, [bottom, right] at relative phase $\pi/2$ . . . . .	76
3.17 Photoelectron yield of Xe at intensities of FW and SH at 0.09 and 0.03 $\text{PW/cm}^2$ respectively, as a function of delay or relative phase between 800 nm and 400 nm. The polarizations of FW and SH are orthogonal to each other. . . . .	77
3.18 Asymmetry along $p_x$ and $p_y$ induced by two-color (OTC) field at 0 and $\pi$ of relative phase. . . . .	78

- 4.1 [a] An experimental setup scheme, [b] the photoelectron VMI spectrum of Xenon at 800 nm and 400 nm wavelength, [c] Two-Color (OTC) and Two-Color (PTC) laser pulses generation scheme, [d, e] pictorial sketch of OTC, and PTC laser fields. HWP: Half Wave Plate, M: Mirror, BBO:  $\beta$ -barium borate crystal, HS: Harmonic Separator. . . . . 82
- 4.2 [Top][a] Electric field of 800 nm, (FW) (in red), 400 nm (SH) (in blue) and the intensity of the sum of the two-color fields (in pink) at phase delays between 0 and  $3\pi/2$ , [Bottom] The yield of  $\text{Ar}^{2+}$  as a function of the relative phase at intensity ratio  $I_{2\omega}/I_{\omega} = 1$ , where  $I_{\omega} = I_{2\omega} = 0.45 \text{ PW/cm}^2$ . The error bars are estimated from the observed counts. . . . . 83
- 4.3 The yield of  $\text{N}_2^+$  and  $\text{N}^+$  ions with the ratio of FW to SH peak powers for OTC induced photoionization of  $\text{N}_2$ . At the ratio 1, the peak powers of FW and SH was maintained at  $0.149 \text{ PW/cm}^2$ . 89
- 4.4 [top]The  $\text{C}^+$ ,  $\text{O}^+$  and  $\text{CO}^+$  ion yield and [Bottom]  $\text{C}^{2+}$ ,  $\text{O}^{2+}$  ion yields as a function of the ratio of FW to SH peak powers of OTC induced photoionization of CO. At the ratio 1, the peak powers of FW and SH was maintained at  $0.149 \text{ PW/cm}^2$  . . . . . 90
- 4.5 [The yield of  $\text{N}_2^+$  and  $\text{N}^+$  ions with the ratio of FW to SH peak powers of PTC induced photoionization of  $\text{N}_2$ . . . . . 91
- 4.6 The  $\text{C}^+$ ,  $\text{O}^+$  and  $\text{CO}^+$  ion yield and [Bottom, right]  $\text{C}^{2+}$ ,  $\text{O}^{2+}$  ion yields as a function of the ratio of FW to SH peak powers of PTC induced photoionization of CO. At the ratio 1, the peak powers of FW and SH was maintained at  $0.149 \text{ PW/cm}^2$  . . . . . 93

4.7	[top] The two-color laser field (OTC) induced photoionization of $N_2$ . The yield of $N_2^+$ and $N^+$ ions is plotted as a function of the relative phase between the FW and SH. The intensity ratio in this experiment is $I_{SH}/I_{FW} = 0.5$ . [bottom] The two-color laser field (OTC) induced ionization of CO. The yield of $CO^+$ , $C^+$ , and $O^+$ ions is plotted as a function of the relative phase between the FW and SH. The intensity ratio in this experiment is also $I_{SH}/I_{FW} = 0.5$ . . . . .	95
4.8	Two-color photoionization of $N_2$ and CO with parallel polarization and $I_{SH}/I_{FW}=0.5$ . Both FW and SH polarizations are kept parallel to the detector plane.[left] Normalized $N_2^+$ ion yield as a function of the relative phase between SH and FW, [right] Normalized $CO^+$ ion yield as a function of the relative phase between SH and FW in units of degrees. . . . .	98
4.9	Classical electron trajectories simulation in the OTC and PTC field. [top] Revisiting electron kinetic energy as a function of birth time for PTC, [bottom] Revisiting electron kinetic energy as a function of birth time for OTC. Color/curve and relative phase in OTC or PTC are self-explained. . . . .	101
4.10	Two-color (OTC) induced photoelectron momentum distributions of CO and $N_2$ at $I_{SH}/I_{FW} =0.5$ , [top] PEMD at relative phase 0, [bottom] PEMD at relative phase $\pi/2$ . In PEMD, visible dark spots are due to defects in the detector, should be ignored. The red arrow is parallel to the detector plane, and the blue circle is perpendicular to the detector plane. . . . .	102
4.11	OTC field induced asymmetry in $p_x$ and $p_y$ at $I_{SH}/I_{FW} =0.5$ , at a relative phase of 0 and $\pi/2$ . The statistical error (maximum) in the asymmetry is about 0.6%, estimated from counts/pixel. The counts/pixel are about $10^5$ . . . . .	104

4.12 Photoelectron momentum distributions of CO and N <sub>2</sub> induced by PTC at laser intensity ratio of 0.5 ( $I_{SH}/I_{FW} = 0.5$ ), [top] at relative phase 0 deg, [bottom] at relative phase $\pi/2$ . Visible dark spots in the image are due to defects in the detector and should be ignored. Both blue and red arrows are parallel to the detector plane. . . . .	105
4.13 Asymmetry in $p_x$ and $p_y$ induced by PTC field at $I_{SH}/I_{FW} = 0.5$ , at relative phase of 0 and $\pi/2$ . The maximum statistical error in the asymmetry is about 0.8% estimated from counts/pixel. The counts/pixel are about $10^5$ . . . . .	106
4.14 Classical-electron trajectory simulation in the OTC field. The black curve represents the electron revisit angle at the relative phase of 0, and the blue curve is at the relative phase of $\pi/2$ . . . .	107
5.1 Ion yield ratio ( $\text{CO}_2^{2+}/\text{CO}_2^+$ ) as a function of laser intensities for linearly polarized light. The intensity-dependent experiments were carried out using 800 nm, 29 fs laser pulses. . . . .	116
5.2 Classical electron trajectories simulation in laser field. [top]Revisiting electron kinetic energy as a function of ionization time. This plot is obtained at 0.15 PW/cm <sup>2</sup> of the laser intensity, [bottom] Revisiting electrons having maximum kinetic energy as a function of laser intensity. . . . .	118
5.3 Intensity dependence of ion yield for linearly polarized light pulses having 29 fs pulse duration. LP: Linear Polarization and CP: Circular Polarization . . . . .	121
5.4 Normalized fragment ion yield with 400 nm and 800 nm wavelengths at the same laser intensity. [a] Yield of singly charged ions, [b] Yield of doubly charged fragments. . . . .	124

5.5	(top panel) Singly charged ion yield ratio as a function of femtosecond pulse durations. The peak intensity was maintained at 0.309 PW/cm <sup>2</sup> . This is recorded using linearly polarized light pulses and 800 nm wavelength.(Bottom panel) The ion yield ratio for circularly polarized light pulses. . . . .	125
5.6	(top panel) The CO <sub>2</sub> <sup>2+</sup> /CO <sub>2</sub> <sup>+</sup> ion yield ratio for linearly and circularly polarized light pulses. (bottom panel)Doubly charged fragment ion (C <sup>2+</sup> and O <sup>2+</sup> ) yield ratio as a function of femtosecond pulse durations. The peak intensity was maintained at 0.309 PW/cm <sup>2</sup> , wavelength of 800 nm . . . . .	126
5.7	[top, left] The CO <sub>2</sub> <sup>+</sup> and CO <sub>2</sub> <sup>2+</sup> ion yield as a function of intensity ratio (I <sub>2ω</sub> /I <sub>ω</sub> ). [top, right] The charged fragments C <sup>+</sup> , O <sup>+</sup> , and CO <sup>+</sup> ion yield as a function of intensity ratio. [bottom] Doubly charged fragments trend as a function of intensity ratio. Error bars obtained from measured counts are shown in each plot. . . . .	128
5.8	Schematic of potential energy curves for singly, doubly, and triply ionized CO <sub>2</sub> . The two colors-induced ionization and tunnel electron revisit are schematically presented. . . . .	131
5.9	[top] The CO <sub>2</sub> <sup>+</sup> and CO <sub>2</sub> <sup>2+</sup> ion yield as a function of intensity ratio (I <sub>2ω</sub> /I <sub>ω</sub> ) induced by OTC field. [mid] The charged fragments C <sup>+</sup> , O <sup>+</sup> , and CO <sup>+</sup> ion yield as a function of intensity ratio. [bottom] Doubly and triply charged fragments trend as a function of intensity ratio. Error bars obtained from measured counts are shown in each plot. . . . .	132
5.10	[top] CO <sub>2</sub> <sup>+</sup> and CO <sub>2</sub> <sup>2+</sup> ion yield as a function of relative phase (Δφ) induced by PTC field. [mid] The charged fragments C <sup>+</sup> , O <sup>+</sup> and CO <sup>+</sup> ion yield as a function of relative phase (Δφ). [bottom] Doubly and triply charged fragments C <sup>2+</sup> , O <sup>2+</sup> , C <sup>3+</sup> and O <sup>3+</sup> ion yields are represented as a function of relative phase (Δφ). The ion yields are observed at intensities 0.20PW/cm <sup>2</sup> of FW and 0.48PW/cm <sup>2</sup> of SH. . . . .	136

5.11	The revisiting kinetic energy of the electrons as a function of relative phase ( $\Delta\Phi$ ) at intensities 0.20PW/cm <sup>2</sup> of FW and 0.48PW/cm <sup>2</sup> of SH. . . . .	137
5.12	[top] CO <sub>2</sub> <sup>+</sup> and CO <sub>2</sub> <sup>2+</sup> ion yield as a function of relative phase ( $\Delta\phi$ ) induced by OTC field. [bottom] The charged fragments C <sup>+</sup> , O <sup>+</sup> and CO <sup>+</sup> ion yield as a function of relative phase ( $\Delta\phi$ ). The ion yields are observed at intensities 0.20 PW/cm <sup>2</sup> of FW and 0.168 PW/cm <sup>2</sup> of SH. The counts of CO <sup>+</sup> , C <sup>+</sup> , and O <sup>+</sup> are about 12000 to 4000, and the error bar is not plotted for clarity. . . . .	140
5.13	[top]Doubly charged fragments C <sup>2+</sup> , O <sup>2+</sup> ion yields as a function of relative phase ( $\Delta\phi$ ). The counts of C <sup>2+</sup> and O <sup>2+</sup> are about 5000 to 7000, and the error bar is not plotted for clarity. [Bottom] Triply charged fragments C <sup>3+</sup> and O <sup>3+</sup> ion yields as a function of relative phase ( $\Delta\phi$ ).The ion yields are observed at intensities 0.20 PW/cm <sup>2</sup> of FW and 0.168 PW/cm <sup>2</sup> of SH. The counts of C <sup>3+</sup> and O <sup>3+</sup> are about 1200 to 2500, and the error bar is not plotted for clarity. . . . .	141
5.14	[top]Photoelectron momentum distribution induced by two-color (PTC, 800 nm + 400 nm) field. [bottom]Photoelectron momentum distribution induced by single-color (400 nm) field. The polarization direction is shown in the figure. . . . .	143
5.15	[top] Photoelectron yield as a function of relative phase. [bottom] Asymmetry along p <sub>x</sub> and p <sub>y</sub> induced by two-color (PTC) field at 0 relative phase. . . . .	144
5.16	[top]Photoelectron momentum distribution induced by two-color (OTC, 800 nm + 400 nm) field. [bottom]Photoelectron momentum distribution induced by single-color (400 nm) field. The polarization direction is shown in the figure. . . . .	146
5.17	[top] Photoelectron yield as a function of relative phase. [bottom] Asymmetry along p <sub>x</sub> and p <sub>y</sub> induced by two-color (OTC) field at 0 relative phase. . . . .	147



# List of Tables

2.1	The parameters used in the theoretical model of ADK for Ar from Ref. [1]are given below. . . . .	46
-----	-----------------------------------------------------------------------------------------------------	----



# List of Acronyms

**ADK** Ammosov–Delone–Krainov

**ATI** Above-Threshold Ionization

**BBO**  $\beta$ -Barium Borate

**CCD** Charged Coupled Device

**FW** Fundamental Wavelength

**HHG** High Harmonic Radiation

**IP** Ionization Potential

**MCP** Micro-Channel Plate detector

**MPI** Multi-Photon Ionization

**NSDI** Non-Sequential Double Ionization

**OTC** Orthogonal Two-Color fields

**PEMD** Photoelectron Momentum Distribution

**PTC** Parallel Two-Color fields

**SH** Secondary-Harmonic Wavelength

**SPIDER** Spectral Phase Interferometry for Direct Electric-field

**TH** Third Harmonic Wavelength

**TI** Tunnel Ionization

**TOF** Time-of-Flight

**VMI** Velocity Map Imaging Spectrometer

---

# List of Publications

## Publications included in thesis

1. **Madhusudhan, P.**, Rituparna Das, Pranav Bhardwaj, Muhammed Shameem KM, Vinitha Nimma, Swetapuspa Soumyashree, and Rajesh K. Kushawaha, "Strong-field ionization of N<sub>2</sub> and CO molecules using two-color laser field", [10.1088/1361-6455/ac9873](https://doi.org/10.1088/1361-6455/ac9873) [J. Phys. B: At. Mol. Opt. Phys. 55 234001]
2. Muhammed Shameem K M, **Madhusudhan P**, Rituparna Das, Pranav Bharadwaj, Nimma Vinitha, Swetapuspa Soumyashree and Rajesh K Kushawaha, "Molecular emission dynamics from a femtosecond filament induced plasma plume", [10.1088/2040-8986/ac528a](https://doi.org/10.1088/2040-8986/ac528a) J. Opt. 24 044015

## Submitted/Under preparation

3. **Madhusudhan, P.**, Pranav Bhardwaj, Rituparna Das, Vinitha Nimma, Muhammed Shameem KM, Swetapuspa Soumyashree, Kanaka Raju Pandiri and Rajesh K. Kushawaha," Non-sequential double ionization of CO<sub>2</sub>: Re-visiting electron induced fragmentation dynamics", [submitted: 18/11/2022]
4. **Madhusudhan, P.**, Pranav Bhardwaj, Vinitha Nimma, and Rajesh K. Kushawaha, "Two-color field induced photoionization of CO<sub>2</sub>", [under preparation]
5. **Madhusudhan, P.**, Pranav Bhardwaj, Vinitha Nimma, and Rajesh K. Kushawaha, "Enhanced ionization by the two-color induced interplay of photoelectron trajectories", [under preparation]
6. **Madhusudhan, P.**, Pranav Bhardwaj, Vinitha Nimma, and Rajesh K. Kushawaha, "Comparitive study of various methods for generating orthogonal two-color fields using VMI spectrometer", [under preparation]

## Other publications (not included in the thesis)

1. Rituparna Das, Deepak K Pandey, Vinitha Nimma, **Madhusudhan P**, Pranav Bhardwaj, Pooja Chandravanshi, Muhammed Shameem KM, Dheeraj Singh, and Rajesh K Kushawaha, "Strong-field ionization of polyatomic molecules: Ultrafast H atom migration and bond formation in photodissociation of CH<sub>3</sub>OH", [10.1039/D0FD00129E](https://doi.org/10.1039/D0FD00129E) *Faraday Discuss.*, 2021,228, 432-450
2. Rituparna Das, Deepak K Pandey, Swetapuspa Soumyashree, **Madhusudhan P**, Vinitha Nimma, Muhammed Shameem KM, Pranav Bhardwaj, Dheeraj Singh, and Rajesh K Kushawaha, "Strong-field ionization of CH<sub>3</sub>Cl: proton migration and association", [10.1039/D2CP02494B](https://doi.org/10.1039/D2CP02494B), *Phys. Chem. Chem. Phys.*, 2022,24, 18306-18320

## Book chapters

1. **Madhusudhan P**, Rituparna Das, Pranav Bharadwaj, Pooja Chandravanshi, Swetapuspa Soumyashree, Vinitha Nimma, and Rajesh K Kushawaha, "Modern Experimental Techniques in Ultrafast Atomic and Molecular Physics", [10.1007/978-981-33-6084-6\\_10](https://doi.org/10.1007/978-981-33-6084-6_10), 978-981-33-6084-6
2. Muhammed Shameem K M, Swetapuspa Soumyashree, **Madhusudhan P**, Vinitha Nimma, Rituparna Das, Pranav Bhardwaj, Prashant Kumar, and Rajesh K Kushawaha,"Nanosecond and Femtosecond Laser-Induced Breakdown Spectroscopy (LIBS): Fundamentals and Applications", [978-1-119-75840-2](https://doi.org/10.1007/978-1-119-75840-2)
3. Muhammed Shameem K M, Swetapuspa Soumyashree, **Madhusudhan P**, Vinitha Nimma, Rituparna Das, Pranav Bhardwaj, Prashant Kumar, and Rajesh K Kushawaha, "Molecular species formation in laser produced plasma", [978-1-119-75840-2](https://doi.org/10.1007/978-1-119-75840-2)

*"You only need one ray of light to chase all the shadows away"*

*Fredrik Backman*



# Chapter 1

## Introduction

### 1.1 Background and Motivation

Light-Matter interactions have served as a great tool to uncover the secrets of nature. At an atomic level, the interaction of light with atoms and molecules holds the key to untangling the electronic structure and dynamics involved in the process. Light-matter interactions also play a quintessential role in the life of biological organisms [2, 3]. The control and manipulation of matter using light (electromagnetic radiation) enable us to synthesize revolutionary medicines for incurable ailments, fabricate highly resistant or highly conductive materials, photosynthesis-based processes, and much more [4, 5, 6, 7]. Understanding the interaction between light and atoms or molecules at a fundamental level and their reaction mechanisms helps us to manipulate matter [8, 9, 10].

Curiosity to understand various physical, chemical, and biological phenomena of nature have accelerated a fervent growth of technologies in the last few decades, which made us capable of probing and controlling the processes at the atomic and molecular level, which are extremely fast. The electron or nuclear dynamics in molecules extend from the attosecond ( $10^{-18}$ s) regime to the picosecond ( $10^{-12}$ s) time domain. The science in this time domain is popularly known as ultrafast science [11].

The interaction of radiation has a significant temporal (time period of electromagnetic radiation) dependence. Therefore, the time period varies from

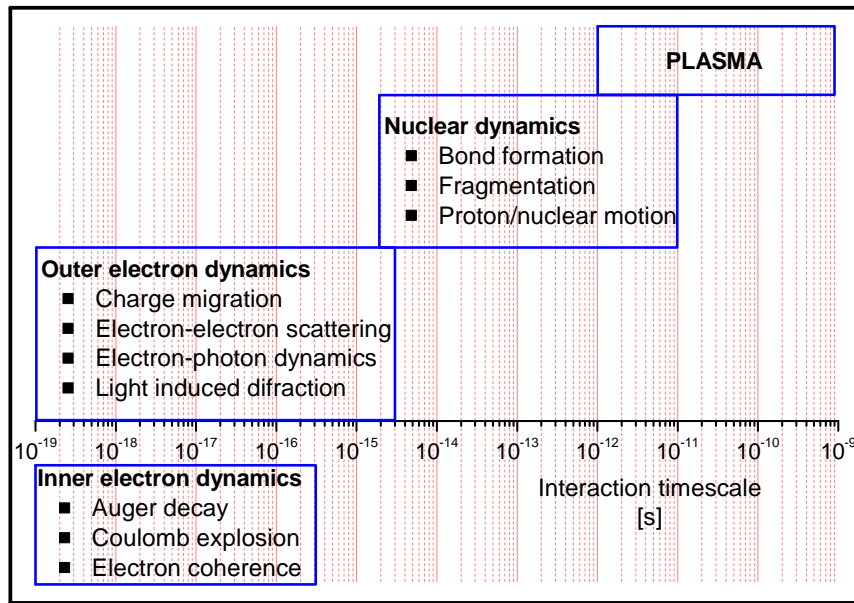


Figure 1.1: Fundamental atomic, molecular and electronic phenomena probed on ultrafast timescales.

several orders of milliseconds to attosecond and lower. Interestingly the attosecond and the femtosecond are the same regimes where chemical and biological interactions play a crucial role. To understand these reactions and therefore control such reactions, probes in the form of the electromagnetic pulse of such a short time scale are necessary.

From photosynthesis in plants [12] to facilitating vision in the human eye [13], there are several reactions involving light-matter interaction in everyday life. We need to understand the mechanism of such reactions. Understanding these reactions is the stepping stone to controlling them. Controlling biological and chemical reactions can either be macroscopic, which is the thermodynamic control by varying temperature, pressure, etc., and also by the quantum coherent control [14].

But as the time period of electromagnetic radiation decreases, the energy required for interaction also goes down. Therefore, excitation/ionization with such radiation is highly unlikely. Therefore it will be particularly useful to have electromagnetic radiation of short time scales but sufficiently intense. Ultrafast intense laser pulses satisfy both the conditions required for the excita-

tion/ionization of atomic and molecular samples.

In 1905, Albert Einstein's theory of the photoelectric effect elucidated the interaction of a single photon with bound electrons. The single photon energy must be more than the electron's binding energy to knock out the electrons. This explanation was the weak limit of a single photon liberating a single electron from the material. While in the year 1965, Keldysh introduced a theory in which low-enough frequencies contributed to the tunnel ionization process dubbing it "Strong-field ionization" [15].

### 1.1.1 Strong-field ionization of atoms and molecules

When the intensity approaches 1 atomic unit ( $50\text{V} / \text{\AA}$ ), the process of ionization has been considered as a Strong-field ionization [16]. The Coulomb field gets distorted in the presence of high laser intensity, which allows the electron to be ionized through quantum tunnelling. At such high intensities, the ionization rate is an exponential function of laser intensity compared to a power function when the field is treated perturbatively.

Keldysh introduced a parameter  $\gamma$  ( $= \sqrt{I_p/2kI\lambda^2}$ ) to classify the ionization into Multiphoton ionization, Tunnel ionization, and Barrier suppression ionization. Here the  $I_p$  is the ionization potential,  $I$  is the intensity of the incident radiation ( $\text{PW}/\text{cm}^2$ ) whose wavelength (nm) is  $\lambda$ , and  $k$  is the constant [15]. Graphical representation of the single ionization, multiphoton ionization, tunnel ionization, and over-the-barrier ionization is summarized in Figure 1.2.

- **Multiphoton Ionization:** The process of simultaneous several photon absorptions leading to photoionization was discovered as an extension of a two-photon transition. It was initially observed in atoms at the same time [17, 18] as the Keldysh theory published. The Keldysh parameter for multiphoton ionization should be more than 1. MPI can also be responsible in the formation of multiply charged ion through a stepwise process [19]. Multiphoton ionization (MPI) has been studied extensively in atoms and small molecules. It has been shown that the MPI process can be observed by the use of high-intensity lasers [20, 21]. In recent years, MPI has also

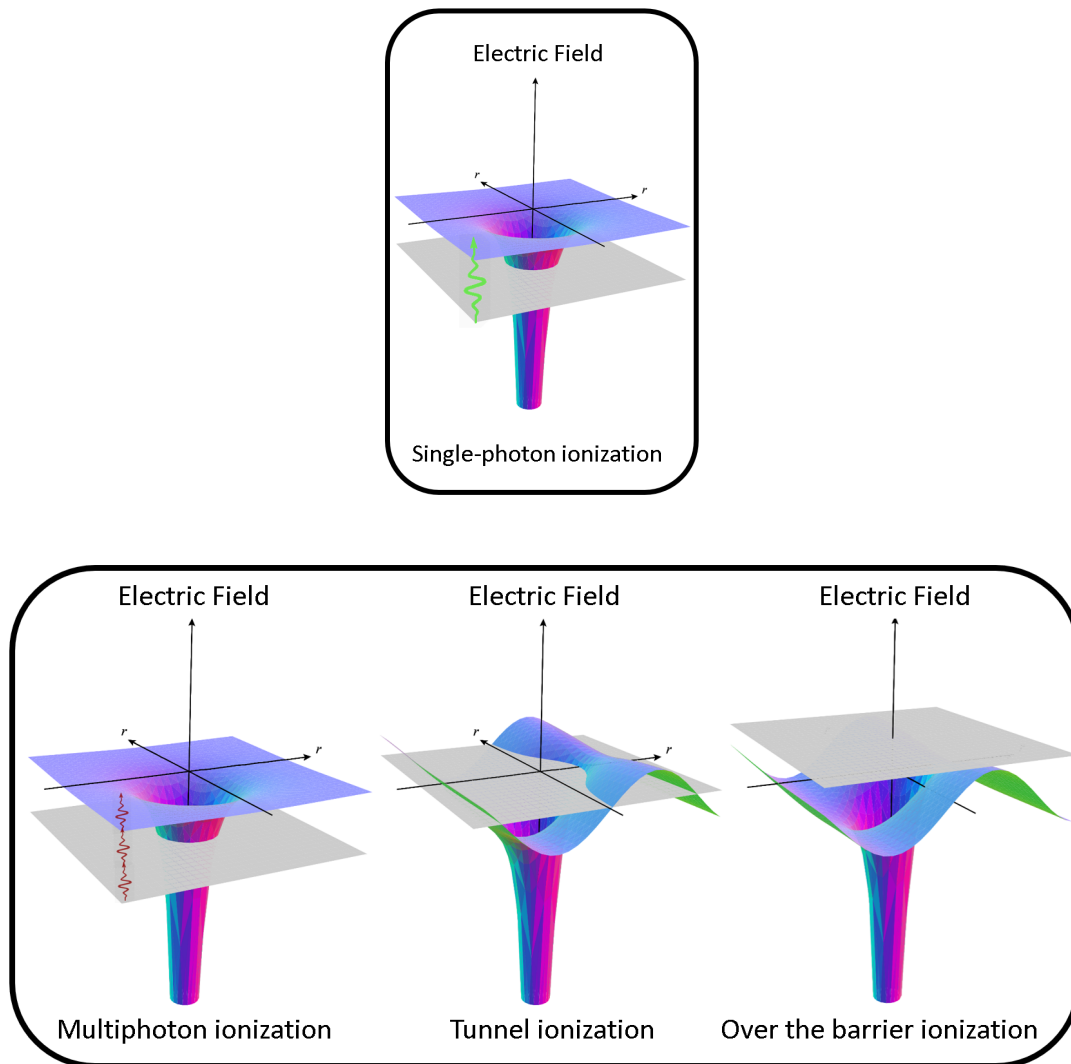


Figure 1.2: The atomic Coulomb potentials under the influence of intense laser fields are shown for different modes of ionization.

been studied in more complex systems such as bio-molecules, clusters, and solids [22, 23, 24]. The use of MPI in these systems has provided insights into the electronic structure and dynamics of these systems.

- **Tunnel ionization:** Tunnel ionization is the process by which an electron escapes from an atom or molecule in the presence of a strong electromagnetic field. The process is described by quantum mechanics and was first proposed in 1928 by Fowler [25] for the case of ionization in metals. Oppenheimer also discussed multiple strong external field interactions with hydrogen and hydrogen-like atoms [26, 27]. The ADK theory [28], which considered the non-hydrogen-like poly electron atom, was significant in explaining tunnel ionization. The KFR theory [15, 29, 30], which was developed from the ADK theory, includes multiple atomic centers and takes into account the suppression of ionization rate in some molecules due to interference between atomic centers and the shape of the valence orbitals. While these theories have been successful in explaining experimental results for atoms, their predictions have been shown to deviate for polyatomic molecules.
- **Over the barrier ionization:** Over the barrier ionization is a process in which an electron is able to overcome the potential energy barrier of an atom or molecule and escape into the continuum. This process is typically induced by the application of a strong external electric field, such as that generated by an ultrafast laser pulse. Ultrafast pulses are characterized by their extremely short duration, often on the order of femtoseconds or picoseconds. Research has shown that the use of ultrafast pulses can significantly enhance the efficiency of over-the-barrier ionization, as the intense electric field of the pulse is able to more effectively push the electron over the barrier ([31, 32]). This has provided valuable insights into the mechanisms of over-the-barrier ionization and the role of the external electric field in driving the process. In particular, it has been demonstrated that the electric field of the ultrafast pulse can significantly modify the trajectory of the escaping electron, leading to the production of high-energy electrons

and the generation of non-thermal distributions [33]. Overall, the use of ultrafast pulses in over-the-barrier ionization has proven to be a powerful tool for the controlled ionization of atoms and molecules and the study of ultrafast electron dynamics.

The temporal dependence of the strong field ionization can be untangled by using an ultrashort probe.

### 1.1.2 Ultrafast dynamics in atoms and molecules

At the molecular level, processes are in the ultrafast time domain (ps to as). A shorter probe pulse than the event duration is needed to probe the processes in the time domain. This requirement can be understood through a frames-per-second (FPS) device that captures extremely fast-moving objects. As an example, we can consider the human vision, many experts claim that the human eye can see between 30 to 60 frames per second which means that we can observe a running horse quite well but not a bullet traveling at 300 km/s. To observe a high-speeding train or a fast-moving object, we need sophisticated instruments such as a camera that operates at higher frames per second compared to an eye. Similarly, we need an ultrafast light pulse to probe the molecular-level processes, which are of the pico- to atto-second scales as shown in Figure 1.1. Therefore there is a need to use ultra-short pulses and a new scheme/spectrometer that can image the ultrafast event. One of the established techniques is pump-probe spectroscopy. In this technique, a pump prepares the molecule in excited or ionized states, and another pulse probes the evolution in the time domain. In this pump-probe scheme, we can detect either the electron/ion or even photons. Various electron/ion spectrometers have been developed in the last few decades. Some key instruments are discussed here.

A mass spectrometer is used to understand molecular dynamics and their constituents. A mass spectrometer detects the charged ions based on their mass-to-charge ratio( $m/q$ ). Since 1955 [34], mass spectrometers have evolved from simple time-of-flight mass spectrometer to Recoil-ion electron momentum spectrometer and powerful Velocity Map Imaging mass spectrometer (VMI).

These VMI spectrometers have been used to measure with high precision of the momentum and angular distribution of both ions and electrons individually. With its advent in 1997 [35] VMI technique has been used extensively, from atoms[36, 37], simple molecules[38, 39] to ring-opening cyclic molecules[40, 41]. Several advancements have been made to the basic design to enhance the resolution of the momentum of the ions and electrons [42, 43]. Very recently, VMI has been used in the measurements involving two-color fields to understand the attosecond delayed processes and orbital selective processes [44, 45].

### 1.1.3 Quantum control of molecular reactions

Quantum coherent control could have been as simple as identifying the normal mode frequency of the targeted bond and then pumping with the laser tuned with that frequency to break the bond. This process of resonance-enhanced ionization is compelling for small molecules but with bigger molecules, the locally incident energy redistributes all over the molecule. This redistribution of energy eclipses selectivity and demands better ways for quantum coherent control [46]. Coherent control of molecular reactions has been observed as a function of wavelength [47, 48], intensity [49], temporal shaping [50, 51], polarization [52], OAM [53, 54], two-color [55] parameters and many more parameters. As suggested by theory, the quantum control of chemical reactions is the result of the excitation, which is completely dependent on the phase and amplitude of the incident radiation [56].

### 1.1.4 Two-color laser field-induced ionization

Two-colour photoionization has been proven to be a very effective method in discerning the ultrashort (from sub-femtoseconds to even attoseconds) dynamics of the atomic and molecular systems [57, 58, 59]. Compared to single-color pulses, the two-color method has been found to have more parameters, such as the intensity of both colors, relative phases, and relative polarizations, to study molecular dynamics. Several theories have studied the features of the two-color

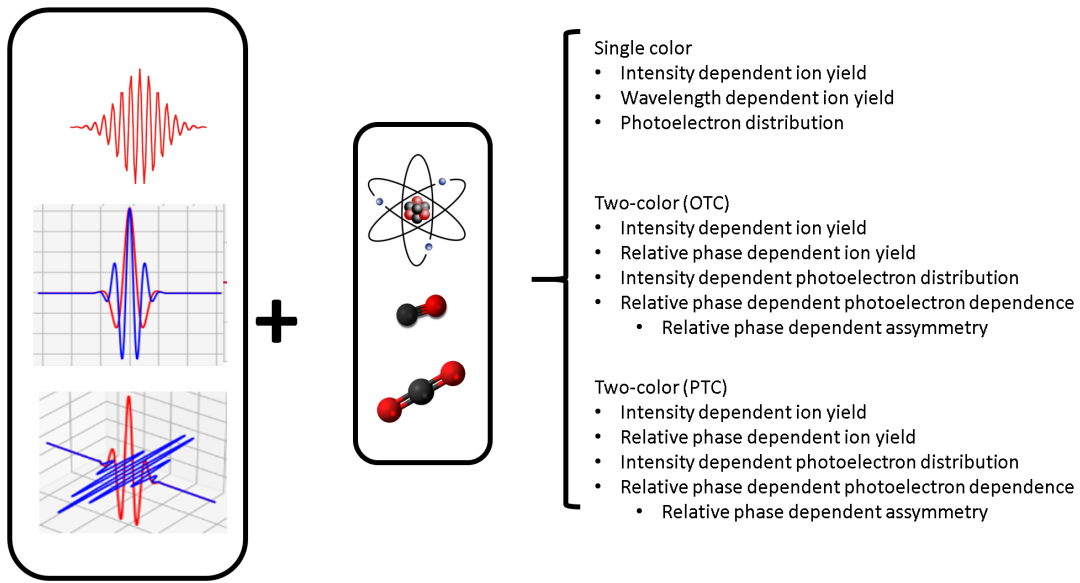


Figure 1.3: Schematic of single and two-color fields interacting with atoms, di- and tri-atomic molecules.

fields [60, 61, 62]. The tunneled electron has been observed to be steered by the two-color fields. The control of the parameters mentioned above, the photoelectron interference in both spatial and temporal regimes [63], the electron-electron correlation of Non-sequential double ionization (NSDI), and fragmentation induced in molecular dynamics have been observed. It has also been observed that electron spin polarization could be controlled by using Orthogonal Two-Color (OTC) fields [64, 65]. Two-color fields have also been used to orient the molecules and study the processes [66, 67].

### 1.1.5 Our Focus: Objectives of thesis

This thesis focuses on the strong-field ionization of atoms and molecules induced by single-color and two-color laser fields. For this study, we performed the photoionization experiments of Ar, Xe, N<sub>2</sub>, CO, and CO<sub>2</sub> samples in a Velocity Map Imaging Spectrometer. The ion's yield was measured as a function of laser parameters such as intensity, wavelength, and polarization for the single-color ionization case. In the case of two-color induced photoionization, we recorded the ion's yield as a function of intensity ratio and relative phase. We observed that the ion yield varies as a function of laser parameters. We performed the

semi-classical electron trajectories simulation to explain the observed experimental results. The revisiting electron may further ionize the parent ion. We modulated the electron trajectories using two-color and investigated their effect on molecular fragmentation. The objectives of the thesis are listed below.

- Study the two-color photoionization of atoms: Investigates the two-color intensity and phase influences on the ionization of atoms.
- Study the two-color (OTC/PTC) strong-field photoionization of diatomic and triatomic molecules: Investigate the fragments yield as a function of relative phase and intensity ratio.
- Study the photoelectron momentum distribution (PEMD) induced by a two-color field. Further Two-color induced asymmetry in PEMD is investigated.
- Simulate the tunnel electron trajectories in the single-color and two-color laser fields and estimate the revisiting kinetic energy and angle in a two-color field.

The objective of the thesis works is summarized in Figure 1.3.

## 1.2 Thesis Outline

This thesis has six chapters. The outline of the thesis is given below:

### Introduction

In this current chapter, the motivation, the principle of the strong field ionization, and the ultrafast perspective of the atoms and molecules are discussed. The basic principles and the importance of the temporal studies of atomic/molecular reactions are discussed in detail. The need for techniques and instruments used for probing the processes are introduced and explained in detail in the methodology chapter.

## Methodology

In this chapter, the methods and instruments employed for the current research are discussed in detail. The principle, characterization, and mathematical representation of femtosecond pulses, as necessary, are explained. Sample preparation for the light-matter interactions has been delved upon. The principle of operation, simulation, construction, and calibration of the time-of-flight mass spectrometer, and a VMI spectrometer which was used throughout the research, has been explained in detail. The generation of second harmonic pulses and different techniques of calibrating and controlling the relative phase of the two-color fields is explained in detail. The theoretical technique for electron trajectory in the presence of an intense ultrafast light pulse is explained in detail.

## Strong field ionization of atoms

In this chapter, the study on the strong field ionization of Argon and Xenon was performed at various single and two-color laser parameters. The ionization yield as a function of laser intensity is studied for a single color. It has been observed that the experimental results fitted well with the ADK and PPT theory at high enough intensities. The strong field ionization in the presence of circularly polarized light is also studied and explained effectively.

The two-color orthogonal and parallel polarized intensity dependence of single and doubly charged photoion yield is discussed in detail for both Xenon and Argon. The production of ions in relation to the relative phase of the OTC and PTC fields is examined in depth. An oscillatory trend in ions yield is observed as the relative phase is varied. Further, the photoelectron distribution of single color at FW (Fundamental wavelength) and SH (Second Harmonic) at different intensities was performed along with the OTC and PTC varying both intensity and phase. The observed trend in the yield of ions as a function of intensity and relative phase is explained using simulation results.

## Strong field ionization of diatomic molecules

In this chapter, the homo-(N<sub>2</sub>) and hetero-nuclear (CO) diatomic photoionization by two-color laser field (OTC and PTC) and the role of intensity and phase on the ion yield is investigated. The fragments yield as a function of intensity and relative phase yielded interesting results. Asymmetry in the photoelectron distribution is studied. We observed that the homo- and hetero-nuclear nature of the molecule have a unique influence on the photoelectron distribution and the asymmetry parameter. The observed results are explained based on the simulated results.

## Strong field ionization of triatomic molecules

In this chapter, the triatomic molecule (CO<sub>2</sub>) is examined with single and two-color fields. A detailed investigation of the photoionization of CO<sub>2</sub> and its fragments have been performed as a function of intensity, wavelength, polarization, and pulse duration in the presence of single color. The knee structure associated with Non-sequential double ionization (NSDI) is observed in the yield of parent and fragment ions as the laser intensity is varied. Further, two-color photoionization of CO<sub>2</sub> is discussed in detail in this chapter.

### 1.2.1 Summary and Future works

In this chapter, the key findings on the single-color and two-color photoionization of atoms (Ar & Xe), diatomic molecules (N<sub>2</sub> & CO), and triatomic molecules (CO<sub>2</sub>) are discussed.

The future plans to investigate polyatomic and cyclic molecules in the presence of not only OTC/PTC but also bi-circular fields to understand the revisiting electron-induced processes are discussed. Also, studying the HHG spectra in the presence of two-color will strengthen our understanding of revisiting induced processes, which I would like to do in the near future. Finally, my research gives a new pathway to control molecular dissociative reactions using a two-color field.



# Chapter 2

## Methodology

This chapter introduces all the experimental techniques, data acquisition schemes, data analysis methodology, and theoretical/simulation schemes used in this thesis. For thesis work, I developed a two-color pump-probe type setup. Further, I contributed in the development of a new multi-plate Velocity Map Imaging Spectrometer. PRL's femtosecond laser system produces 25 fs femtosecond pulses at 1KHz and a wavelength of 800 nm light pulses used in the thesis. We have developed a code for the ADK ionization rate and also performed a simulation of tunnel electrons in the two-color laser field. The experimental results are interpreted based on theoretical/simulation results. The details of experimental techniques/theoretical details are discussed below.

### 2.1 Introduction

The advent of femtosecond lasers opened an opportunity to chase the dynamical process in molecules that occurs in the femtosecond time domain, such as vibrational or rotational dynamics. The electron dynamics in atoms/molecules are in the attosecond time domain. Thus, with femtosecond laser pulses, chasing and controlling its dynamics is difficult due to the time resolution issue. Attosecond light pulses may help on this front, which is a challenging scheme, growing field, and beyond the scope of this thesis's works/objectives. Alternatively, the two-color scheme has emerged as a powerful scheme to probe and modulate the wavepackets in the attosecond time domain by adjusting the relative phase of the

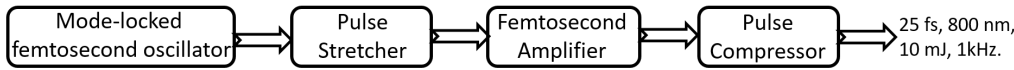


Figure 2.1: Schematic femtolaser

two-color field. The amplitude of both fields may also affect the electron trajectories in the field and thus influence the revisiting induced processes. In addition to the femtosecond laser and utilizing these laser pulses in a two-color scheme, suitable electron/ion spectrometers are also needed for ultrafast research. In this thesis, I have used the in-house developed Velocity Map Imaging Spectrometer. Here, I am introducing femtosecond laser, VMI spectrometer, two-color setup, etc., used in the thesis.

## 2.2 Ultrafast Lasers

Gerard Mourou and Donna Strickland shared their 2018 Nobel prize for the invention of chirped pulse amplification [68]. They demonstrated the generation of the shortest and most intense laser pulses known to mankind. Chirped pulse amplification fundamentally consists of a mode-locked oscillator, a light pulse stretcher, an amplifier, and a pulse compressor. A typical femtosecond laser is represented in Figure 2.1. The concept of mode-locking is vital for generating femtosecond pulses.

### 2.2.1 Mode-locked femtosecond oscillator

Detail of mode-locking techniques is available in the literature [69, 70, 71, 72] and also discussed in my book chapter [73]. An oscillator is broadly made up of four crucial components, optical resonator/cavity, pump source gain media and finally a negative dispersion component. Superficially the working of the oscillator is as follows, the pump source excites the gain media (usually a Ti:Sapphire crystal) to emit a broad band of radiation into the optical resonator/cavity comprised of a set of mirrors forming standing waves/modes. These modes may not have a constant phase with each other and oscillate autonomously, the process of fixing the phase relation among the modes is termed mode-locking. There are two

broad ways, named active mode locking and pasive mode locking, in which we can achieve the fixed phase relationship between the modes of the laser cavity. Active mode-locking employs a modulator, such as electro-optic or acousto-optic, with an external signal, while in passive mode-locking, a saturable absorber behaves as a modulator. An alternative method of modelocking is the Kerr modelocking which is based on the Kerr effect based mode's phase stabilization. The PRL's femtosecond laser (Coherent make) is based on the passive Kerr mode locking system.

### **2.2.2 Stretcher/Compressor of femtosecond laser**

The femtosecond pulse from the oscillator cannot be directly amplified, as the gain media (Ti:Sapphire crystal) in the amlifier may be damaged due to the high peak powers at low pulse durations. Therefore, conventionally a pair of diffraction gratings are used to stretch/compress pulses temporally by introducing a phase among the different modes by dispersion. The ultrashort femtosecond pulses can be stretched (chirped) to nanoseconds in the stretching unit of the femtosecond laser. The stretcher unit gives a positive chirp (phase-mismatched), reducing the peak power during amplification. After amplification, the compressor gives a negative chirp to the positively chirped pulse (phase-matched). In order to enhance the effects of stretching the laser pulse may be reflected multiple times to obtain the desired pulse duration. The process of amplification is relatively straightforward and is briefly explained further below.

### **2.2.3 Amplifier of femtosecond laser**

The output of the oscillator (termed a seed pulse) after stretchering, passed through an amplifier to produce a high-powered laser beam. There are two schemes for amplification, regen amplification and multipass amplification of stretched pulses. The Regen amplification is similar to the femtosecond oscillator, discussed in my book chapter. In multi-pass amplification, stretched pulses get amplified in each pass through the Ti: Sapphire crystal. Depending on the output power of the laser and design, most commercial multipass amplifiers have

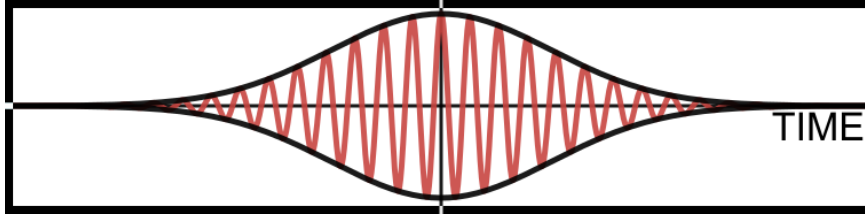


Figure 2.2: Graphical representation of gaussian ultrashort pulse.

3-14 times pass-based amplification. The PRL's femtosecond laser is based on a Regen amplifier which produces 10 mJ at 1 kHz, 800 nm, 25 fs pulses.

## 2.3 Pulse Characterisation

Ultrafast pulse characterization implies the estimation of pulse duration and phase of femtosecond pulses. For long pulses (100's fs), the characterization schemes are based on the auto-correlation type setup in which a femtosecond pulse is split into two pulses, and the delay between both pulses (reference pulse and unknown pulse) is probed.

A mathematical representation of the gaussian ultrashort pulse is,

$$E(t) = E_0 e^{-4 \ln(2) \left(\frac{t^2}{\tau^2}\right)} e^{i(\omega t - \phi(t))} \quad (2.1)$$

where,  $E_0$  is the peak electric field of the pulse,  $\tau$  is the FWHM of the ultrashort pulse,  $\omega$  is the wavelength of the carrier pulse represented in red (Figure 2.2) and  $\phi(t)$  is the Carrier-envelope phase.

Some of widely used pulse characterization techniques are listed below:

- Intensity autocorrelation
- Field autocorrelation
- FROG
- SPIDER

Intensity autocorrelation and field autocorrelation are two different ways of characterizing ultrashort laser pulses. Field autocorrelation measures

the temporal coherence of the electric field of a laser pulse, while intensity autocorrelation measures the temporal coherence of the intensity of the laser pulse. Field autocorrelation is typically used to measure the duration of ultrashort laser pulses, as it is sensitive to the phase and amplitude of the electric field. It is typically performed by mixing the electric field of the laser pulse in a nonlinear medium with a delayed version of itself and measuring the resulting intensity at the output. The temporal coherence of the electric field is then determined by the shape of the resulting intensity profile.

Intensity autocorrelation, on the other hand, is less sensitive to the phase and amplitude of the electric field but is more sensitive to the intensity and energy of the laser pulse. It is typically performed by mixing the intensity of the laser pulse with a delayed version of itself and measuring the resulting intensity at the output. The temporal coherence of the intensity is then determined by the shape of the resulting intensity profile.

Both field autocorrelation and intensity autocorrelation are commonly used to characterize the ultrashort laser pulses, briefly discussed in the below sections.

### 2.3.1 Field auto-correlation

Field auto-correlation techniques are used to measure the temporal properties of ultrafast laser pulses. These techniques are based on the observation that the electric field of an ultrafast pulse is correlated to itself at different times. The degree of correlation can be quantified by the degree of overlap between two copies of the pulse, which is known as the autocorrelation function. The autocorrelation function can be measured using various techniques, such as frequency-resolved optical gating (FROG) [74], spectral phase interferometry for direct electric-field reconstruction (SPIDER) [75] etc.

$$I_{\text{field}}(z) = \int_{-\infty}^{\infty} (E(t) + E(t+z))^2 dt \quad (2.2)$$

The crossterm is the auto-correlation term  $I_{\text{AC}}(z) = \int_{-\infty}^{\infty} E(t)E^*(t+z)dt$ .

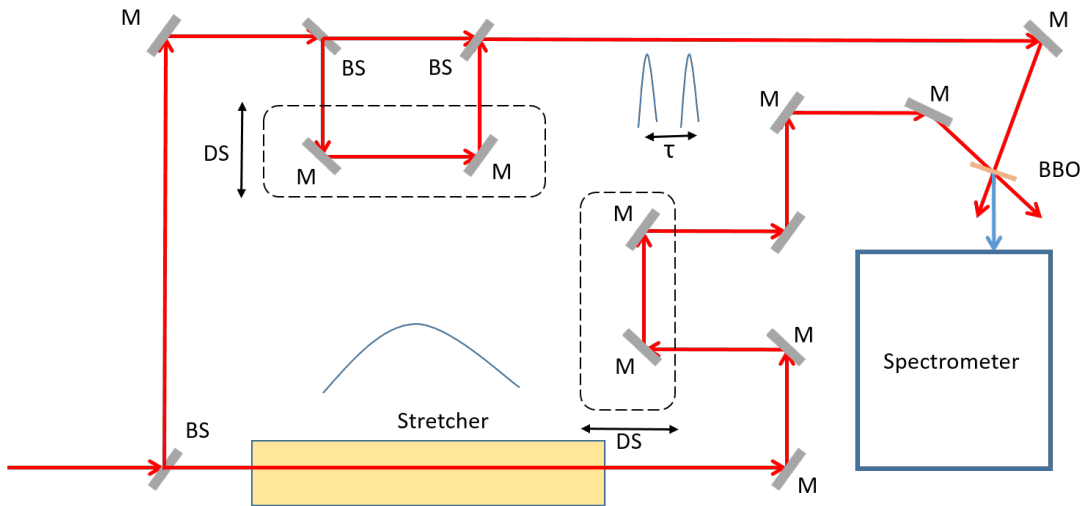


Figure 2.3: Schematic representation of SPIDER. M corresponds to mirrors, BS corresponds to Beams plitters, and DS corresponds to delay stage

### 2.3.2 Intensity auto-correlation

Similar to field correlation, the reference and probe pulses are focused onto a second harmonic Generation (SHG) crystal in this technique. Only the Second Harmonic signal is measured using a power meter or photomultiplier as a function of delay. Again, this technique cannot estimate the spectral phase of pulses.

### 2.3.3 Spectral Phase Interferometry for Direct Electric-field Reconstruction (SPIDER)

Spectral Phase Interferometry for Direct Electric-field Reconstruction was a novel interferometric technique invented by Iaconis and Walmsley in 1998 [76]. It is a technique that measures the spectral intensity and phase by spectral shearing interferometry. This technique can characterize pulse widths shorter than  $10^{-11}$  s. Figure 2.3 shows a schematic diagram of SPIDER. The test pulse is split using the beam splitter (BS), a pulse passing through a glass slab or a pair of gratings to chirp from fs to ps, while the unchirped pulse is passed through a mismatched Michelson interferometer with a time delayed ( $\tau$ ) pair of pulses. The pair of unchirped pulses are interfaced with a nonlinear crystal (BBO) with the

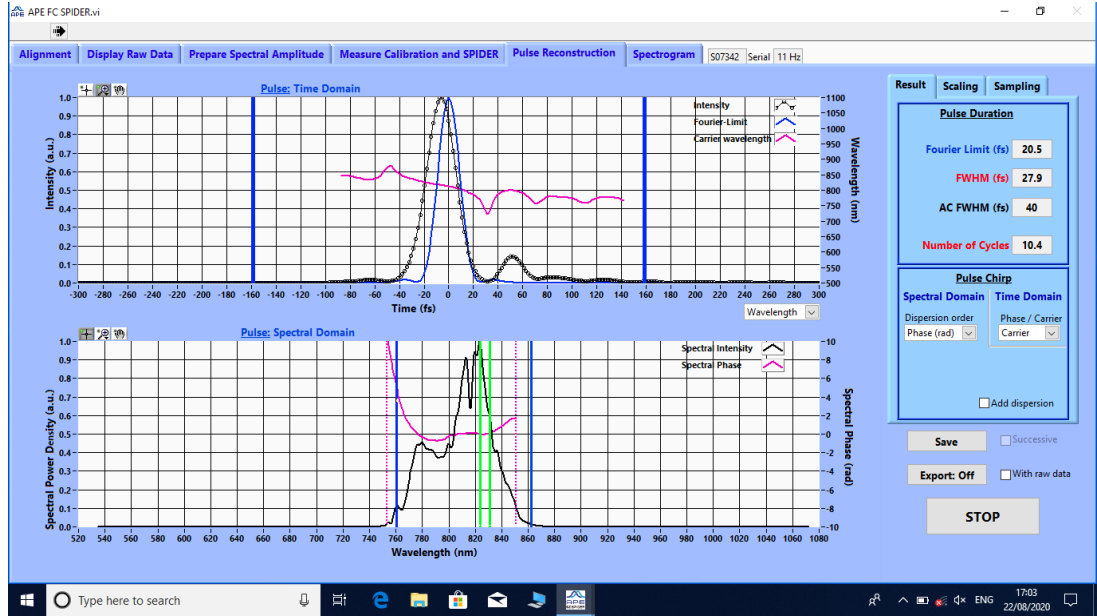


Figure 2.4: Femtosecond pulse characterization using PRL’s SPIDER.

chirped pulses. The unconverted blue pulses have different central frequencies (spectrally sheared) since the pair interacts with different regions of the chirped pulse. An interferogram is obtained using a spectrometer. The spectral phase is retrieved by an inversion algorithm on comparing the obtained interferogram with the pre-recorded (Calibrated) interferogram.

The pulse characterization of PRL’s femtosecond laser using SPIDER is shown in Figure 2.4. The pulse duration is 27.9 fs. The spectrum phase variation is clearly seen in the Figure.

Now, the ion/electron spectrometer used in the thesis is discussed here. All measurements were performed using a VMI spectrometer. Before describing the principle and detail of our VMI spectrometer, here I would like to introduce the basics of the Time of flight mass spectrometer. This discussion will help to understand the TOF mode of the VMI spectrometer.

## 2.4 Time of Flight Mass Spectrometer

A typical time-of-flight mass spectrometer works by differentiating ions reaching the detector at different times based on their mass-to-charge ratio. A typical linear TOF mass spectrometer is made of a repeller plate, extractor plate, and

a drift region. The region between the repeller and extractor plate is called the "interaction region." For best resolution, the separation between the repeller, extractor plates, and the length of the drift tube is optimized in simulation using McLaren's space focusing condition [77].

To illustrate the dependence of the mass-to-charge ratio on the time-of-flight, consider the TOF-MS as shown in figure 2.5. The ion of charge 'q' and mass 'm' travels a distance 'S' under the influence of a static electric field 'E<sub>s</sub>.' Considering ions with zero initial momentum, the time-of-flight 'T' can be written as follows where t<sub>s</sub> is the time of the ion spent in the presence of the static field, and t<sub>d</sub> is the time spent in the drift region.

$$T = t_s + t_D + T_0 \quad (2.3)$$

where T<sub>0</sub> is the start time which here is considered to be 0,  $t_s = \sqrt{\frac{2mS}{qE_s}}$ ,  $t_D = D/V$  with D being the length of the drift region and V is the velocity of the ion.

$$V = \frac{q}{m} E_s t_s = \frac{q}{m} E_s \sqrt{\frac{2mS}{qE_s}} = \sqrt{2S} \sqrt{\frac{qE_s}{m}} \quad (2.4)$$

resulting into

$$\begin{aligned} T &= t_s + \frac{Dm}{qE_s t_s} \\ &= \left( \frac{2S + D}{\sqrt{2S}} \right) \sqrt{\frac{m}{q}} \sqrt{\frac{1}{E_s}} \end{aligned} \quad (2.5)$$

Therefore,

$$\begin{aligned} \text{TOF} &\propto \sqrt{\frac{m}{q}} \\ \implies \text{TOF} &= a \sqrt{\frac{m}{q}} + b \end{aligned} \quad (2.6)$$

Similar to the single-field mass-spectrometer, the multi-field TOF mass spectrometer also has a linear dependence of time-of-flight with that of  $\sqrt{\frac{m}{q}}$ .

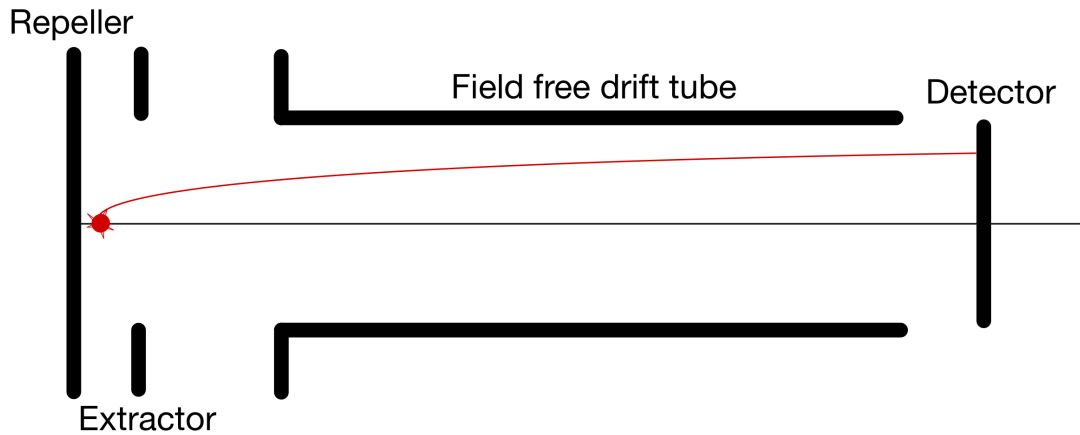


Figure 2.5: Schematic of Time-of-flight mass spectrometer

The current study employs an 11-plate mass spectrometer (VMI operated in TOF mode) to perform multiple time-of-flight measurements. A z-stacked double-MCP in a chevron configuration is used as a detector. The signal from the detector (MCP-back or screen) was decoupled using a homemade decoupler box and later connected to an analog-to-digital converting high-speed card (TDC8HP) through a Constant Fraction Discriminator (CFD). An amplifier was used before the CFD.

TOF Calibration can be performed using the simulation/calculation for a known applied electrostatic field and other parameters such as  $s$ ,  $d$ , and  $D$ . Another scheme of calibration is using the Ar or Xe in the TOF spectrometer and performing the photoionization experiment. The ions in the TOF spectrum can be identified as a function of time-of-flight value. In the current work, we have used Ar and Xe for calibration and obtained the calibration equation. For example, the Ar photoionization was performed at laser intensity  $0.69 \text{ PW/cm}^2$ . Variables 'a' and 'b' are obtained using the linear fitting of known ( $\sqrt{\frac{m}{q}}$ ) ions as shown in Figure 2.6. The calibrated time-of-flight spectra are plotted in figure 2.7.

## 2.5 Velocity-Map Imaging

Eppink and Parker in 1997 [78] developed a new electron/ion imaging technique which was an extension and an improved version of the ion imaging technique

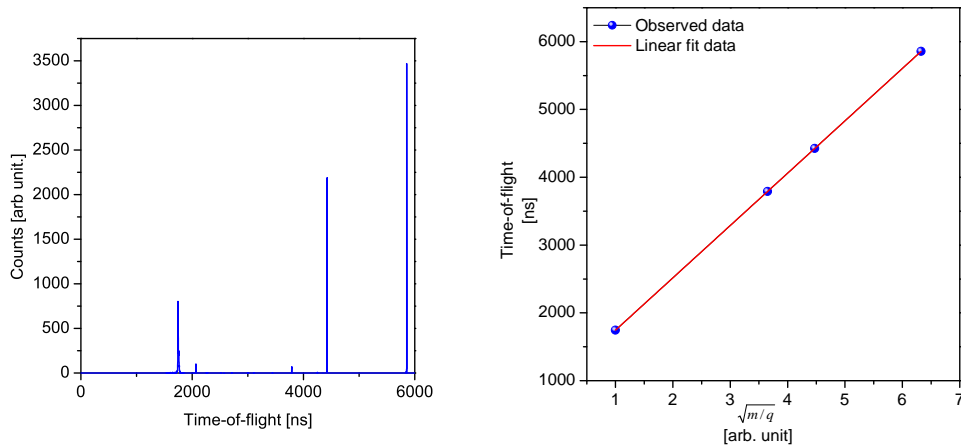


Figure 2.6: [left] Uncalibrated TOF spectrum of Argon, [right] the calibration curve based on the TOF of Argon.

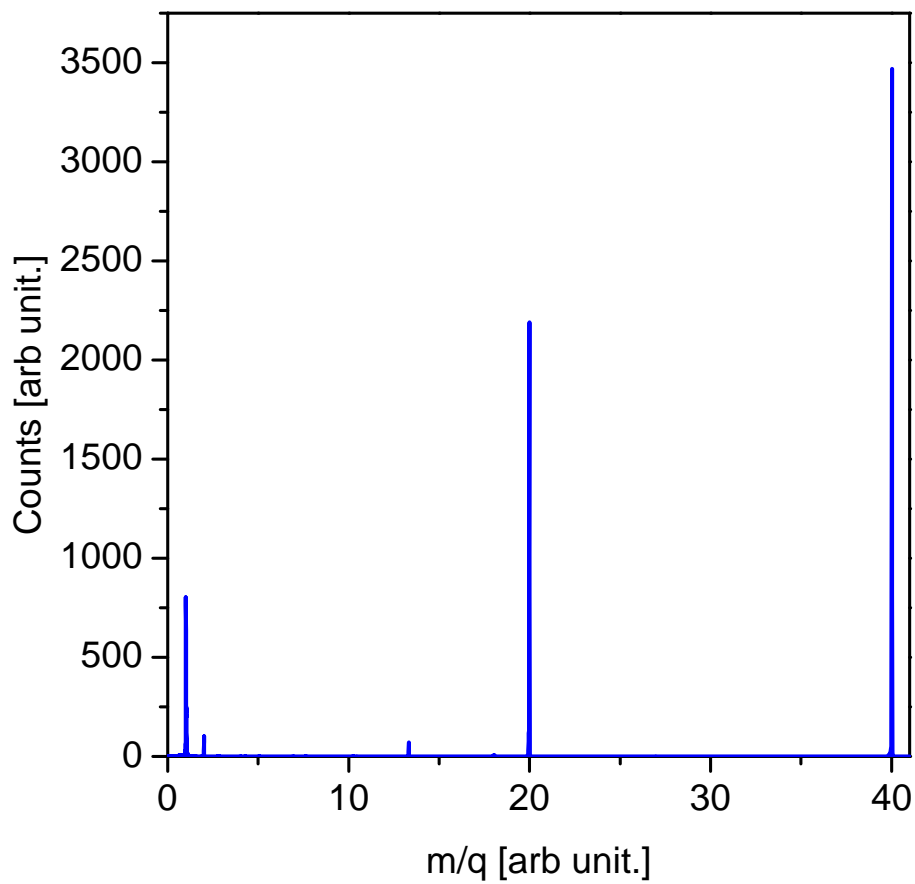


Figure 2.7: Calibrated TOF spectrum of Argon obtained at laser intensity 0.69 PW/cm<sup>2</sup>.

invented by David Chandler and Paul Houston in 1987 [79]. This VMI maps the electron or ions based on their velocity vectors. The potential applied to the electrodes is such that charged species with equal kinetic energies are projected onto a ring. Different kinetic energies are projected onto different concentric rings, whose radii are uniquely related to the kinetic energy of the corresponding charged species. The VMI spectrometer has a  $4\pi$  solid angle collection efficiency. The VMI can be used as a time-of-flight mass spectrometer with the correct choice of potentials. Further, it can be used as a photoelectron spectrometer/photoelectron imaging spectrometer.

Typically a VMI spectrometer consists of 3 regions, the ionization region, the focusing region, and the field-free drift region. The ionization region where the actual light-matter interaction takes place in the center of the Extractor and repeller plates which are maintained at high potentials(kV) for a complete collection of charged species. The focusing region is comprised of an extractor and focusing electrodes. A non-uniform electric field is maintained to allow electro-static focusing and control of the spectrometer's resolution. Finally, a drift-free region is for better spatial and temporal resolution. The charged species is collected after the drift region using a 2D detector (MCP-phosphor and imaging camera). Our homemade VMI spectrometer is a Thick Lens Velocity Map Imaging spectrometer (TL-VMI), considering that we employ nine plates (out of 11) for finer resolution of the observed charged species. A brief explanation of the simulation, construction, and assembly is presented below.

### 2.5.1 Simulation

Charged particle simulation in SIMION was performed before fabricating the components like electrodes and a drift tube. A SIMION workbench was created with actual measurements of the detector size, its position, and the position of the ionization region. Further, multiple plates (electrodes) are added at specific positions, and potentials are applied accordingly to create a non-uniform electric field. Charged particles with specific kinetic energies were carefully assigned their position and velocity vectors and were allowed to fly in the presence of potentials.

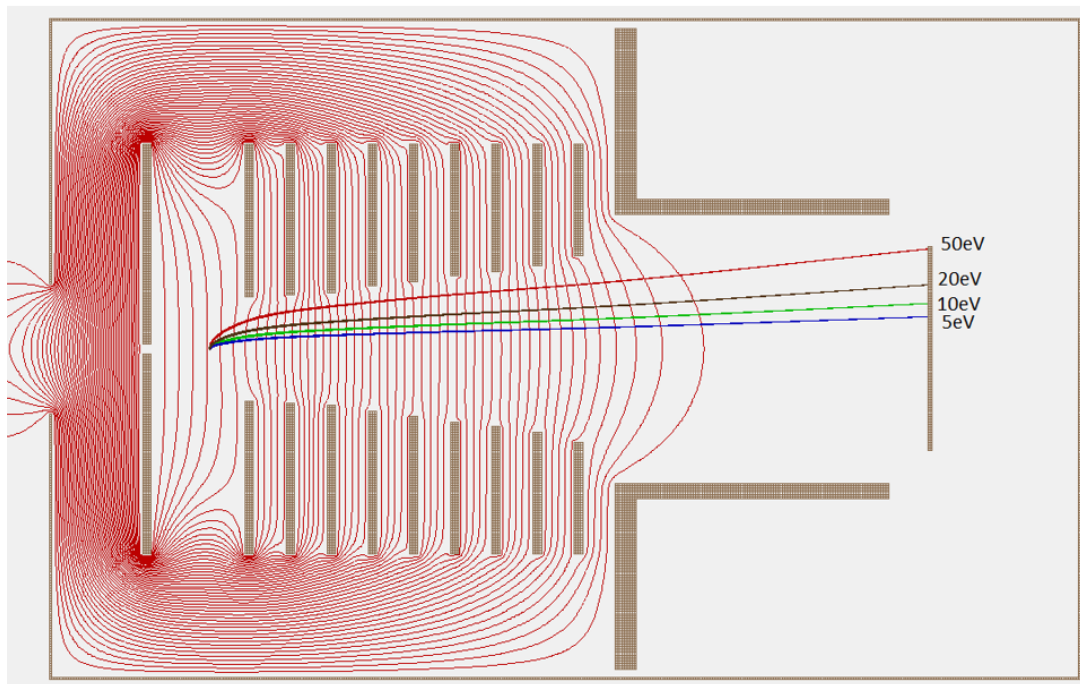


Figure 2.8: Charged particle trajectories simulation for construction of Multi-plate Velocity Map Imaging Spectrometer. The electrons with KE of 5eV, 10eV, 20eV, and 50eV are projected (focused) at the detector for the given electrodes' potential. The simulation was performed in SIMION software.

Figure [2.8] shows the simulated VMI results, like electron trajectories in a given electrode and the potentials in the focusing mode. It was observed that the third plate ('focusing plate' 3rd plate from repeller ) is crucial in the resolution of the charged species; the charged species can be focused within or beyond the detector. The potentials are optimized to have the most charged species focused on the detector.

### 2.5.2 Construction and Assembly of multi-plate Velocity Map Imaging Spectrometer, mounted on CF200 flange

Based on the simulation, the VMI spectrometer was designed and fabricated in-house. Space grade Aluminium - 314 was used for the electrode plates and the rods to support the stack of electrodes from the flange. Since the degassing of Aluminium - 314 material is very low, thus it is suitable for ultra-high vacuum. The electrodes were separated using custom-made, tightly gripped ceramic spac-

ers. The ceramic spacers insulate the electrodes from the body of the vacuum chamber and allow the electrodes to attain floating potentials. The photograph of the spectrometer is shown in Figure [2.9] before the installation of the detector. The repeller was independently connected to an SRS-High Voltage power supply capable of supplying up to 20kV. The extractor and Focusing electrode are independently connected to the NIM power supply, which can be toggled between the polarity and can supply voltage with high precision up to 6kV. The remaining nine plates (including the drift region) are connected to each other using high-rated resistors, maintaining the required potential difference. The vacuum was maintained at around  $10^{-13}$  bar, while during operation, the pressure dropped to about  $10^{-10}$  bars. A  $\mu$ -metal shielding was installed around the VMI spectrometer to restrict or reduce the effect of the earth's magnetic fields on the low-energy electrons. A simulation was performed to estimate the thickness of mu-metal based on the available information on Earth's magnetic field at Ahmedabad. This simulation was performed in COMSOL software.

### 2.5.3 Calibration of the VMI spectrometer

Based on the applied potentials on the electrodes, the different KE electrons will hit the detector at different places on the detector. As discussed, a ring will be formed on the detector for a fixed KE of photoelectrons. To calibrate this, we have to find out the relation between the kinetic energy of the photoelectron as a function of the radius of a ring in pixels. Here, we have used the Xenon to calibrate the spectrometer as it has unique  $P_{1/2}$  and  $P_{3/2}$  rings on the VMI images. Using 800 nm for the strong field ionization of Xenon, it is compared with the 400 nm VMI images. Since the single photon energy of 400 nm is precisely double that of 800 nm, the VMI images are compared and calibrated. The first ring of the 400 nm VMI image is supposed to be equal to that of the second ring of the 800 nm VMI image. Similarly, the second ring of the 400 nm VMI image is compared with the fourth ring of the 800 nm. The pixel length from the center (zero energy electrons) to the rings is calculated and compared for both colored fields. In the focusing mode of VMI, we obtained the equation

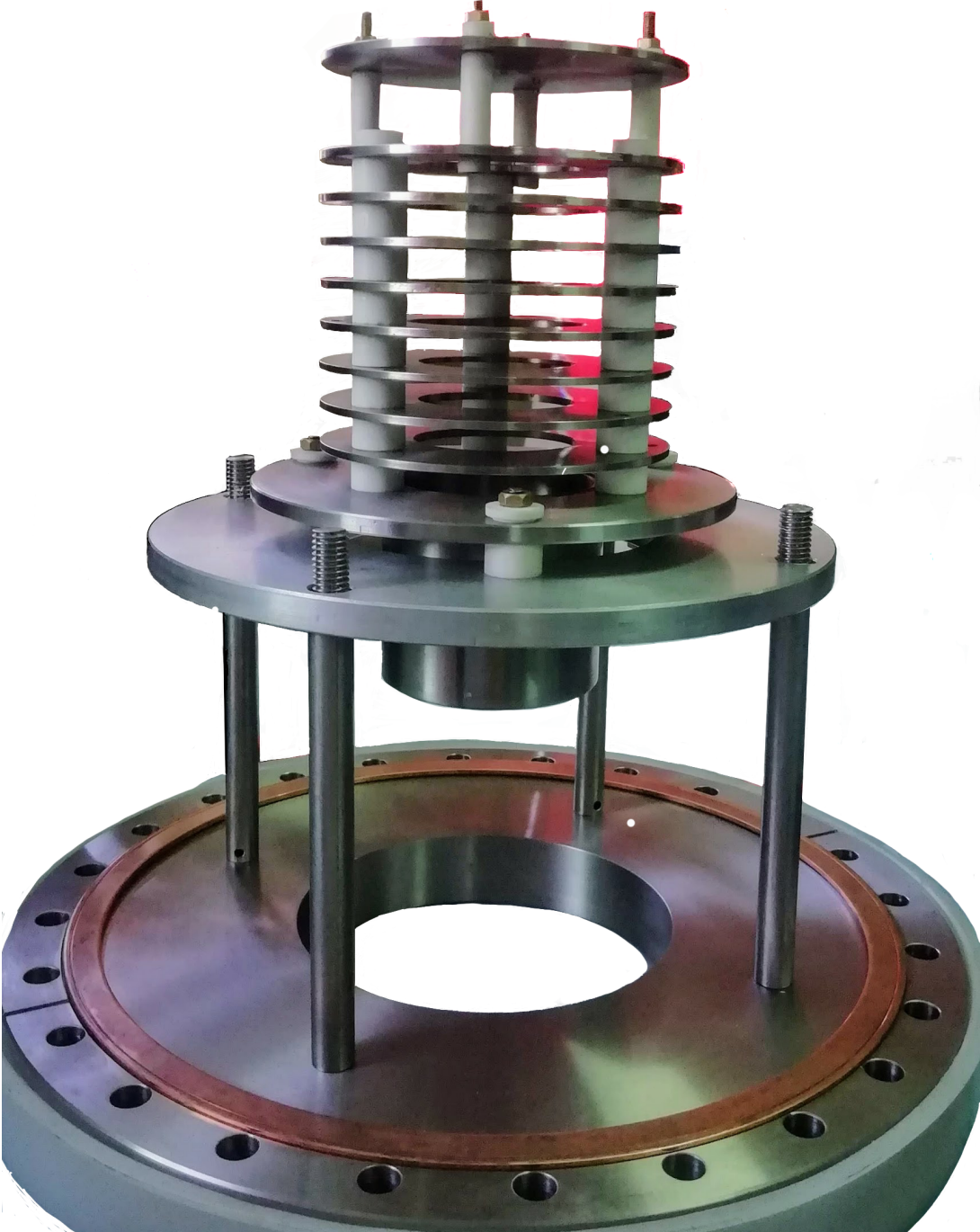


Figure 2.9: VMI electrode assembly

for calibration. It is observed that the square of the radius of the VMI images is directly proportional to the energy of the particles on the ring.

The unknown constants of the equations  $r^2 = A + BE$  are calculated by appropriate simultaneous equations. Each ring on the VMI image represents momentum along x and y. A 3-dimensional plot of  $p_x$ ,  $p_y$  and  $p_z$  are calibrated with the method as mentioned above with the Energy (E) representing  $\sqrt{p_x^2 + p_y^2 + p_z^2}$ . Since  $p_z$  is in the plane, a plot of  $p_x$  and  $p_y$  with atomic units is the calibrated VMI image. A relation between the momenta either  $p_x$  and  $p_y$  to the pixels on the VMI image is obtained and used for calibration.

## 2.6 Two-color setup

In the thesis, we developed three types of two-color setups. Three methods are discussed below.

- Two-color pump-probe type setup
- Wedge mirrors based two-color setup
- Calcite plate based two-color setup

In all three setups, getting overlap in space and time between FW and SH is challenging; thus, here we are discussing our scheme to achieve the overlap.

### 2.6.1 Overlap confirmation by detecting the Third Harmonic Generation

The third harmonic (TH) generation of 800 nm corresponds to 266 nm. It can be generated by temporally and spatially overlapping the FW and SH onto a third harmonic generating (BBO) crystal. The bunch of FW, SH, and TH are incident on a harmonic separator, which reflects the TH and allows FW and SH to pass through. The TH is in the UV regime, which was detected using a spectrometer. The yield of TH is about 15% of that of SH. Detection of the TH signal can validate the temporal overlap of FW and SH and can also be used as a strategy

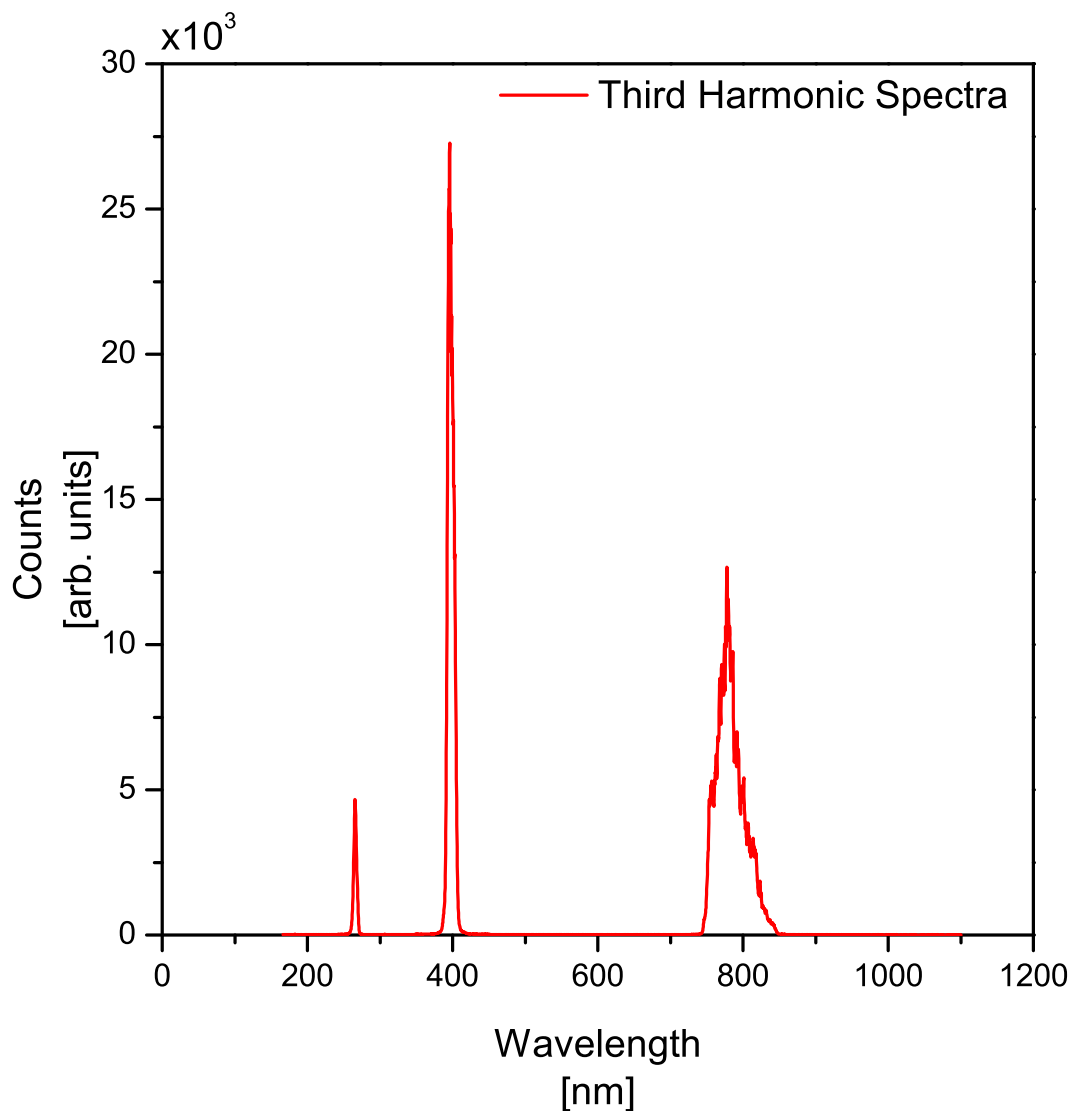


Figure 2.10: Third Harmonic detection using a spectrometer. FW, SH, and TH peaks are observed at the overlap of FW and SH.

for cross-correlation to measure the pulse duration of SH. The integrated yield of TH is plotted against the delay in FW and SH paths and is shown in Figure [2.11]. This plot is obtained by integrating the TH yield as visible in Figure 2.10.

In all setups, we have to create a delay between two colors and observe that the results are consistent and reproducible, and all three setups give the same scientific results. We have verified with measurement on Xenon, and results on photoelectron yield as a function of delay are discussed here. This effort is made to ensure that there are no experimental artifacts or issues with any data, as it has been checked by three different schemes. Further, it helps us to calibrate the

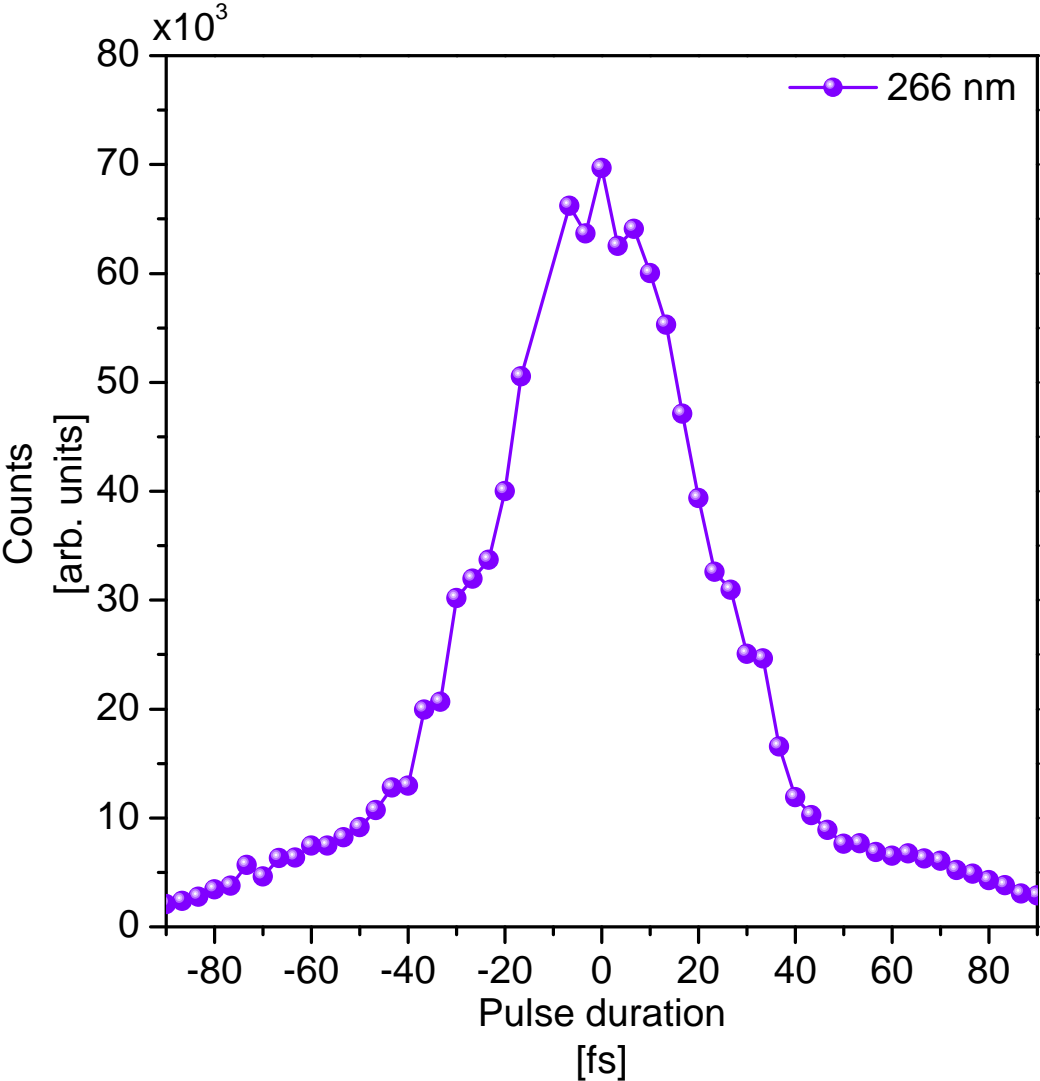


Figure 2.11: Yield of Third Harmonic Generation as a function of the delay between FW and SH.

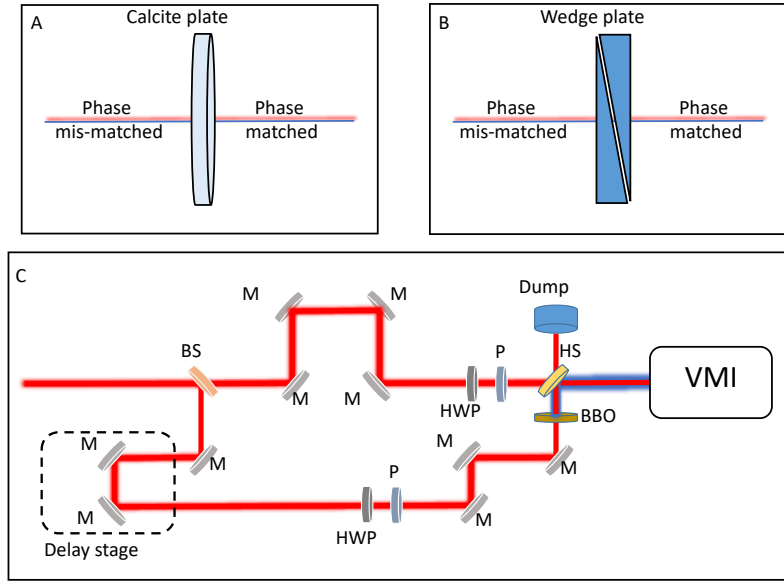


Figure 2.12: Schematic of two-color setup, [A] Calcite-based two-color setup, [B] Wedge mirrors based two-color setup, [C] Pump-probe type two-color setup

ion yield oscillation. Below, we briefly describe all three setups.

## 2.6.2 Pump-probe method

The Fundamental Wave (FW) is split into two pulses using a 70:30 beam splitter as shown in Figure 2.12. The path with power (70%) is tagged as the "probe" path, while the other one is tagged as the "pump" path. Two sets of half-wave plates and a Polarizer (P) are used to control power and polarization. A motorized linear stage (Newport XPS) is used to create a path difference in the pump-probe path. The pump and probe paths are combined at the (HS) harmonic separator. The paths of the pump and probe are adjusted to be equal and confirmed with a type-1 BBO crystal of 100 $\mu\text{m}$  thickness (beyond HS). After ensuring the paths of FW-FW are equal, A type-1  $\beta$ - Barium Borate second harmonic generation (SHG) crystal of thickness 100 $\mu\text{m}$  is used to generate 400 nm. The SH and FW pulses are spatially and temporally overlapped on the BBO THG crystal, and the TH signal is measured using an optical spectrometer (Avantes). Inside the vacuum chamber, the overlap can be confirmed by monitoring the amplification in the yield of ions in the time-of-flight spectrum. The phase dependent photoelectron yield in both orthogonal and parallel polarizations is

obtained and is shown in the Figure 2.13(bottom) and Figure 2.14(bottom)

### 2.6.3 Wedge-plate method

A pair of BK7, AR coated  $8^\circ$  wedge plates are used to set up a delay between FW and SH as shown in Figure 2.12. One wedge is mounted on the linear stage (piezo-controlled), while the other is static. We verified the temporal overlap by measuring the THG signal outside the VMI setup and for overlap inside the VMI chamber, the amplification in ions yield in the time of flight spectrum is monitored. We developed a LabVIEW program to integrate the linear stage with the CCD camera. A delay resolution of the linear stage was of 5 nm is possible in the used setup. A resolution of  $13.6\mu\text{m}$  of relative delay was used to measure the Xe photoelectrons as a function of delay as shown in the Figure 2.13(middle) and Figure 2.14(middle). The change in pulse duration on the introduction of the wedge plate stretches the pulse for about 3 fs.

### 2.6.4 Compensation plate

A tilt of the compensation plate of calcite (EKSMA optics FKE-800-020-M) can be used to introduce and control the delay between FW and SH. The compensation plate is mounted on a piezo-controlled circular nano positioner (Attocube ECR 3030). A compensation plate equilibrates the mutually perpendicular FW and SH beams. The chirp induced by the compensation plate onto the FW was found to be 1- 2 fs. A resolution of 0.163 m deg was used to observe the oscillation of photoelectron yield from the Xe sample with similar powers used in the other two schemes as shown in the Figure 2.13(top) and Figure 2.14(top).

## 2.7 Classical Electron Trajectories

In strong-field ionization induced by intense laser pulses, the tunneling electron follows the laser field, and it may revisit to parent ion as described by a three-step model of Paul Corkum[80]. This revisit electron may initiate many

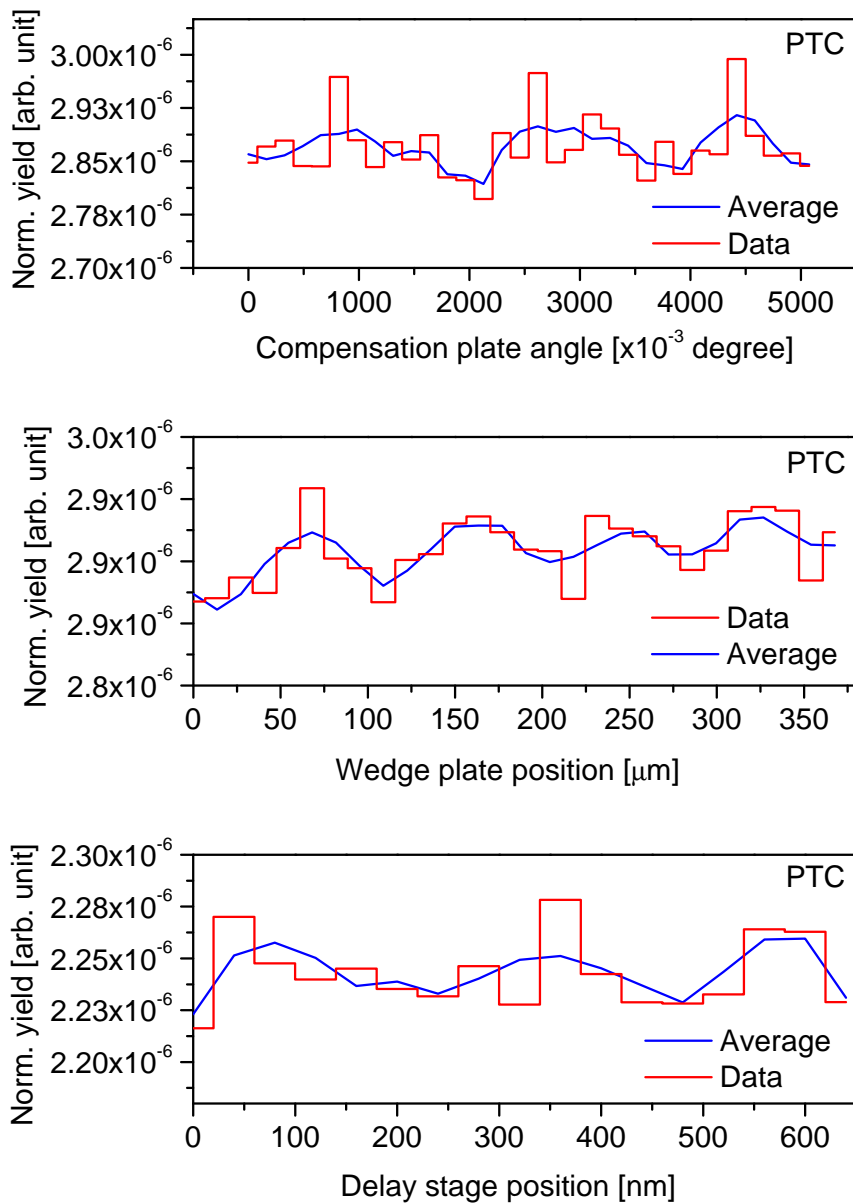


Figure 2.13: Photoelectron yield as a function of delay in all three setups in PTC

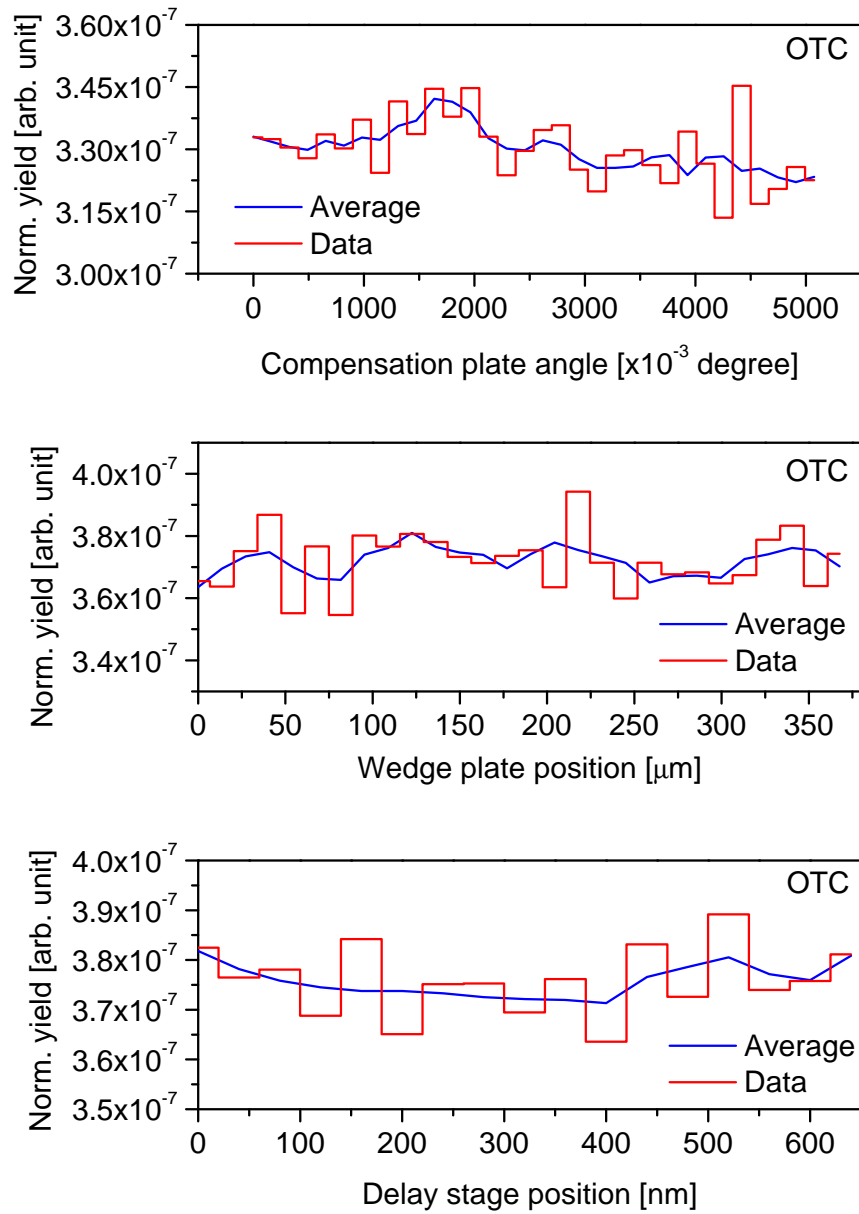


Figure 2.14: Photoelectron yield as a function of delay in all three setups in OTC.

processes, such as Nonsequential double ionization (NSDI), High Harmonic Generation (HHG), ultrafast photoelectron holography, etc.

The computation of electron trajectories is comprised of 2 parts: quantum treatment of the electron dynamics within the atomic and molecular systems and semi-classical electron trajectory computation of electrons in the presence of intense electromagnetic fields. The quantum analysis of the electron dynamics within the atomic and molecular systems can be performed by solving Schrodinger's equation. In the semi-classical electron trajectory calculation, electron position, the kinetic energy of the electron, and its ionization time can be treated as the initial conditions. The electron trajectories can be calculated by solving the equation of motion.

$$m_e \frac{d^2 y}{dt^2} = -e E_{field} \quad (2.7)$$

where  $m_e$  is the mass,  $e$  is the charge of the electron,  $E_{field}$  is the electric field of laser, and  $\frac{d^2 y}{dt^2}$  is the acceleration of the electron in the field in the derivative form of the electron position.

The double integration of Eqn [5.1] can give the electrons' position and velocity. The velocity and the position of the electron at the instant of tunnel ionization can be considered to be 0, which are the boundary conditions for solving the above integration.

### 2.7.1 Single color Field

A pulsed electric field representing an ultrashort electromagnetic pulse represented in Eqn[2.8] is considered as the source for the electric field. The  $\cos^2$  term defines the envelope of the pulse, while the  $\sin$  term represents the carrier of the pulse.

$$E_{field} = A \sin(\alpha + \omega(t + \eta)) \cos^2(k\omega(t + \eta)) \quad (2.8)$$

$A$  represents the amplitude of the electric field,  $\omega$  represents the wavelength of the electric field,  $\alpha$  represents the carrier-envelope phase,  $k$  represents a constant that is governed by the pulse duration and  $\eta$  represents the time offset

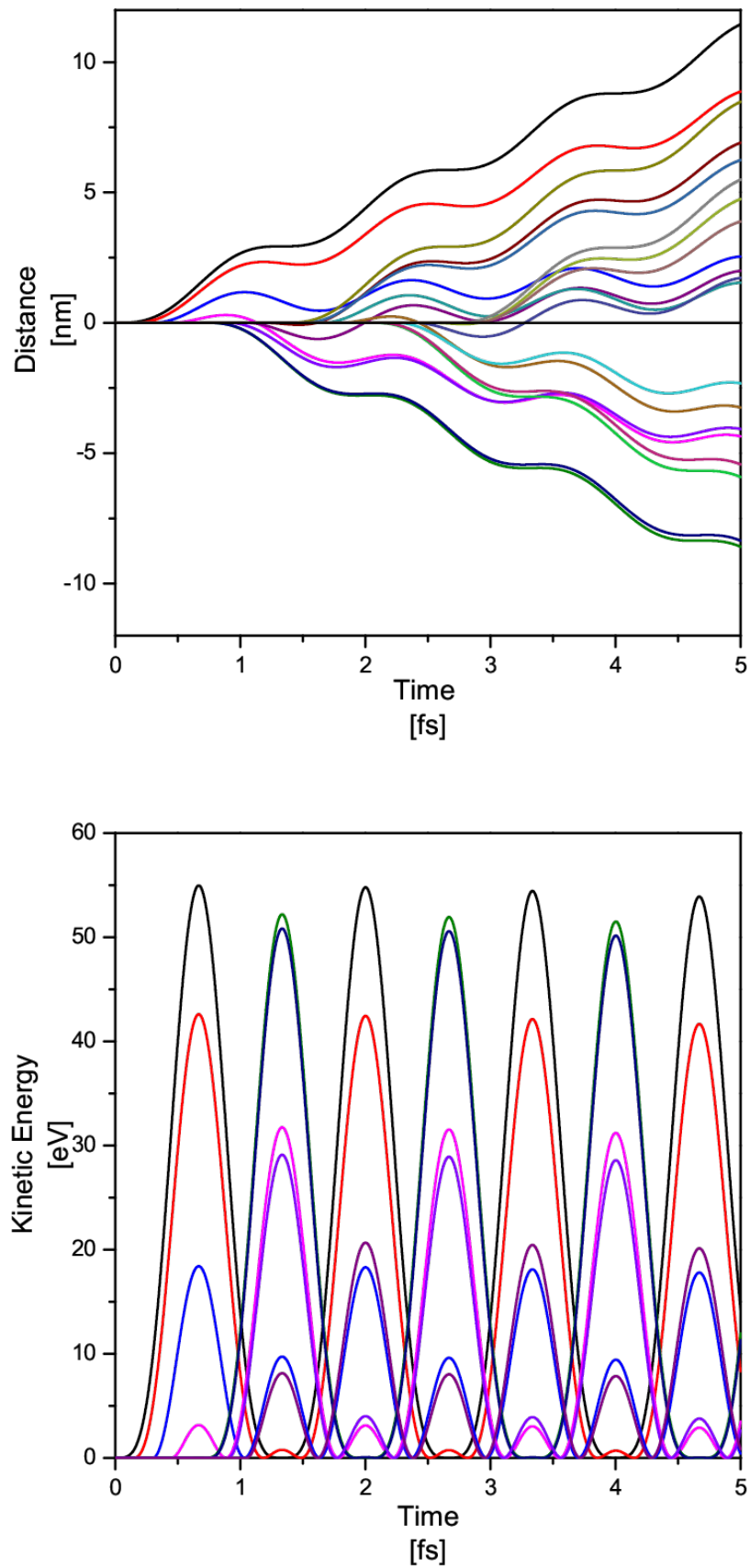


Figure 2.15: [top] 20 Electron trajectories at different birth times in the presence of 400 nm electric field, with peak power  $0.46 \text{ PW/cm}^2$ . [bottom] The kinetic energy of the electron at every instant (5 as). The color codes of the kinetic energy of the electrons correspond to their electron trajectories.

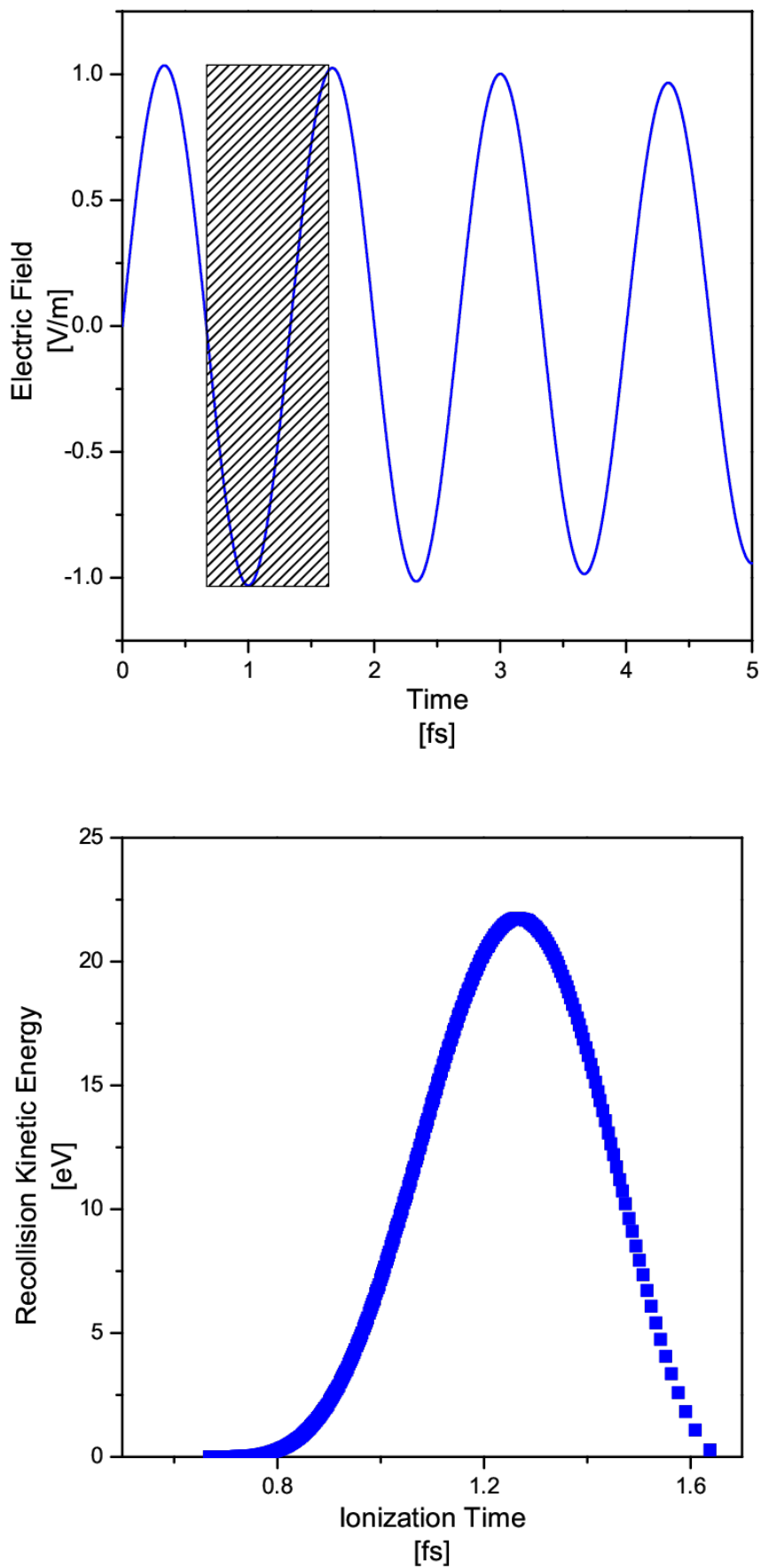


Figure 2.16: [top]The shaded region in the left panel represents the range of birth times over the electric field of the 400 nm pulse, with peak power  $0.46 \text{ PW/cm}^2$ . [bottom] The recollision kinetic energy of the electrons with different birth times.

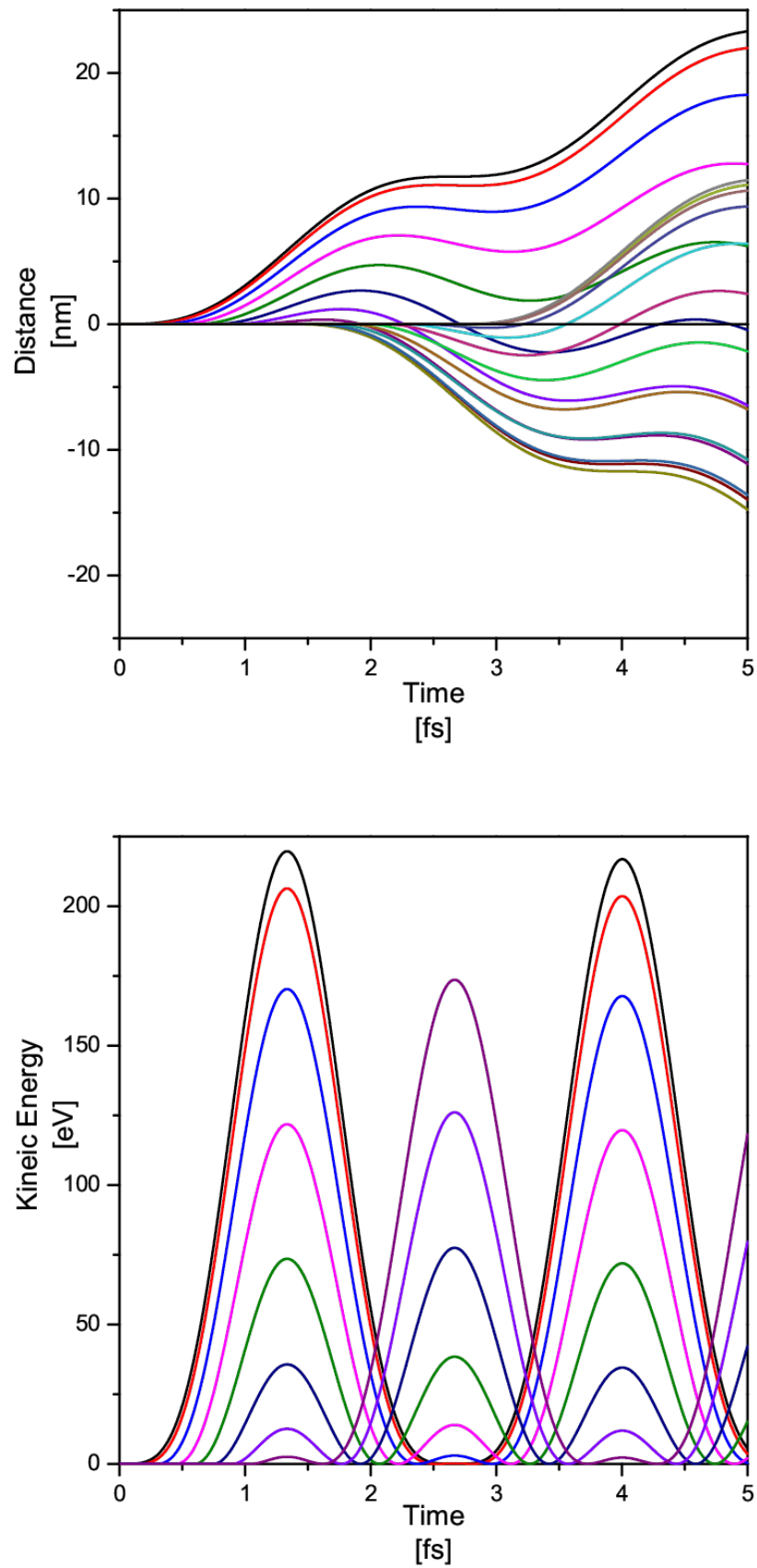


Figure 2.17: [top] 20 Electron trajectories at different birth times [left] in the presence of 800 nm electric field, with peak power  $0.46 \text{ PW/cm}^2$ . [bottom] The kinetic energy of the electron at every instant (5 as). The color codes of the kinetic energy of the electrons correspond to their electron trajectories.

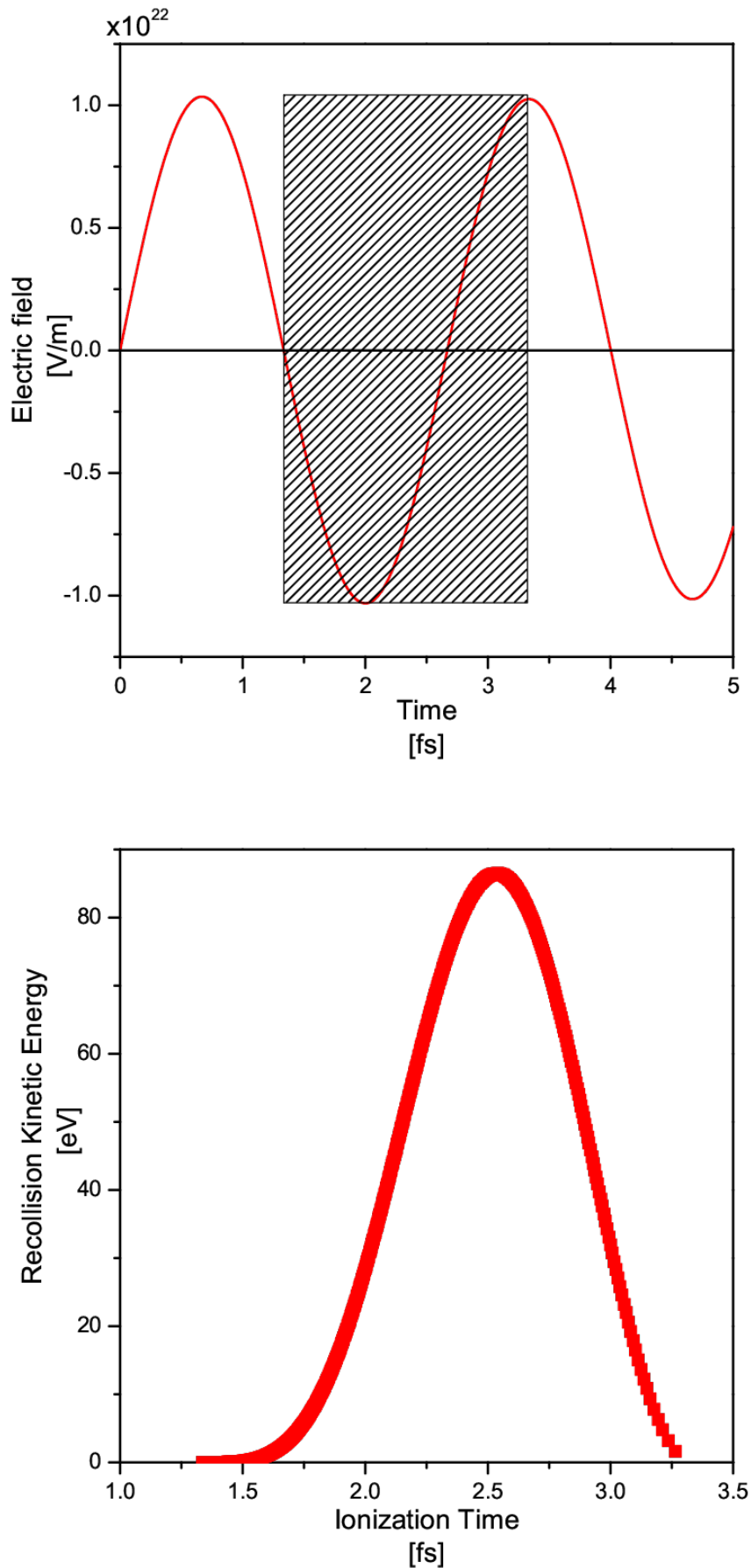


Figure 2.18: [top] The shaded region in the left panel represents the range of birth times over the electric field of the 800 nm pulse, with peak power  $0.46 \text{ PW/cm}^2$ . [bottom] The recollision kinetic energy of the electrons with different birth times.

of the wave on the time axis. Eqn[2.8] is used in equation Eqn[5.1] and solved with boundary conditions that the position and velocity are 0 at birth-time. The birthtimes are varied for half a cycle of the wavelength( $\omega$ ), and the corresponding kinetic energy of revisiting electrons is computed and plotted. It is clearly observed that the electrons with birth time lie in the shaded region of Figure [2.16 and 2.18](top panel) have trajectories returning back to the center, while the other birth times' have direct electron trajectories. The trajectories of the electron based on birth time have been plotted and shown in Figure [2.15 and 2.17]. The kinetic energy of the electron has been computed by getting the velocity of the electron at the instant of revisit and has been plotted in Figure [2.16 and 2.18] (bottom panel). The resolution of the birth time was 1 as ( $\times 10^{-18}s$ ), while the trajectory has been computed with a resolution of 5 as.

For simplicity, only a select number of trajectories have been shown in Figure [2.15]. The bottom panel of the figure represents the kinetic energy of the electrons at every instant (5 as). The color code of the trajectories (top panel) corresponds to their kinetic energies at every instant. It can be observed from Figure [2.15](bottom panel) that the kinetic energy of the electron at some instants is as high as 55 eV. The kinetic energy is maximum when the field is about half the maximum amplitude, and the kinetic energy drops to 0 when the field flips and the electron is driven in the opposite direction. It can also be observed that for some unique birth times, the electron revisits the nuclear centers more than once. This is usually employed to explain intercycle interferences, electron diffraction, and other self-probing techniques. The first revisiting kinetic energy of the trajectories is plotted against the electron birthtimes. The maximum kinetic energy is  $3.17 U_p$  [20] for corresponding wavelength and intensity [as described in equation [2.9]. In comparison, the second harmonic (400 nm) has a relatively lower maximum kinetic energy, almost four times lower than the fundamental harmonic (800 nm). It was also observed that the probability of the recollision increases with the increase in the wavelength of the incident radiation(electric field)[81].

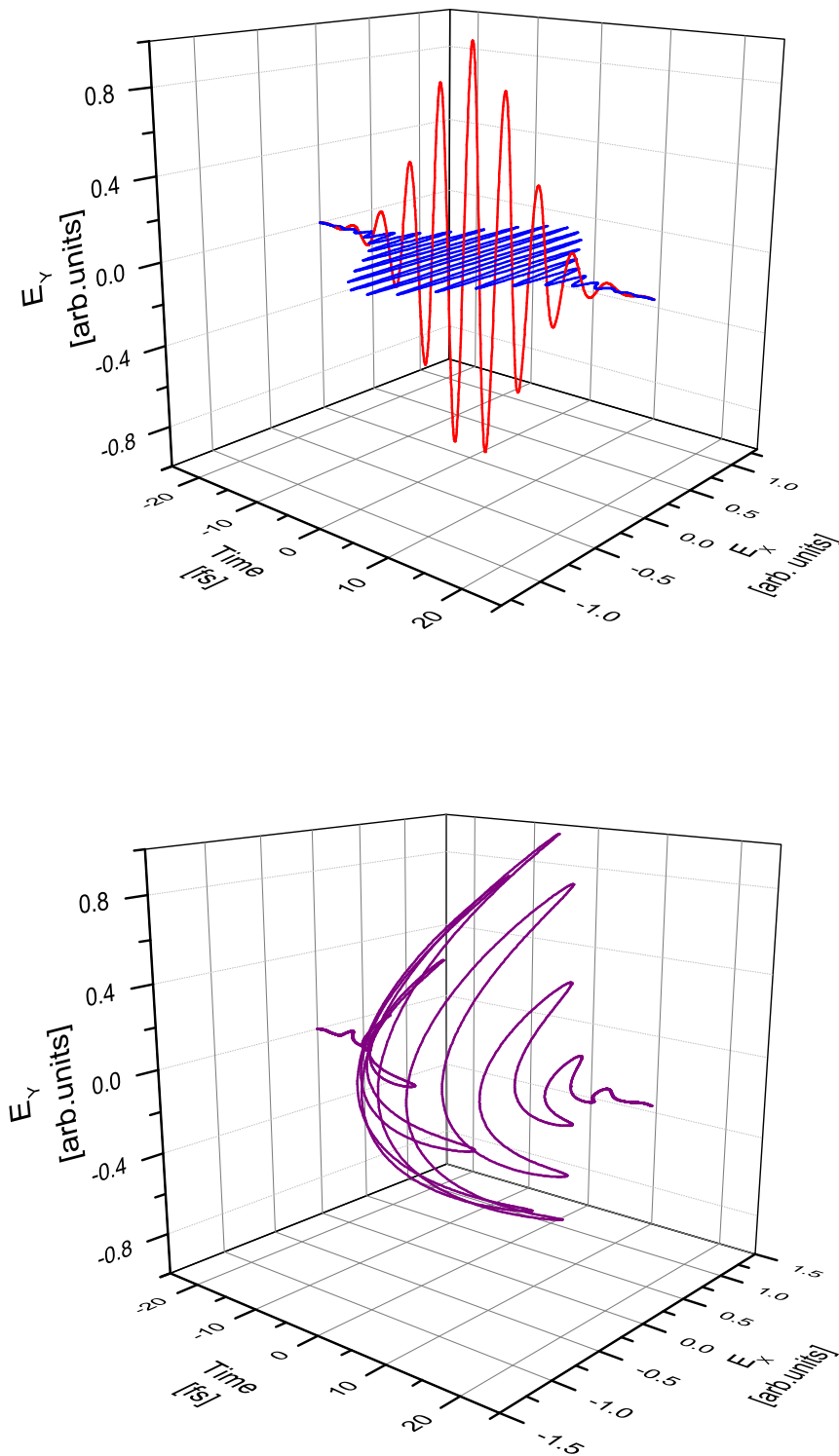


Figure 2.19: Top panel represents the 800 nm and 400 nm two-color fields. The bottom panel represents the resultant of orthogonal two-color fields.

$$U_p = 9.3 \times 10^{-5} I [PW/cm^2] \lambda^2 [nm] \quad (2.9)$$

### 2.7.2 Orthogonal two-colored linearly polarized fields

The equation of motion of the electron in the presence of the superposition of a pulse with wavelength ( $\omega$ ) and its second harmonic ( $2\omega$ ) orthogonal to each other can be represented in Equation [2.10].

$$m_e \left[ \frac{d^2x}{dt^2} \hat{x} + \frac{d^2y}{dt^2} \hat{y} \right] = [eA_{800} \sin(\omega_{800}(t + \eta_{800})) \cos^2(k_{800}\omega_{800}(t + \eta_{800}))] \hat{x} + [eA_{400} \sin(\omega_{400}(t + \eta_{400})) \cos^2(k_{400}\omega_{400}(t + \eta_{400}))] \hat{y} \quad (2.10)$$

Figure [2.19] represents the two-color orthogonal fields graphically at equal intensities [top panel] and their resultant at 0 phase [bottom panel]. The hemispherical resultant field distribution changes according to the phase. The return probability of the electron trajectories is reduced drastically, and only certain trajectories are allowed and can be selected by choice of peak powers and their relative phases.

Solving the above equation with similar boundary conditions as above, the trajectories of the electrons have been plotted accordingly. The trajectories having coordinates  $x, y = 0$ , at the same instant are considered as the revisit of the electron. Corresponding velocity vectors are tabulated. The velocity vectors are used to compute the kinetic energy and the angle of a revisit.

### 2.7.3 Parallel two-colored linearly polarized fields

Similar to OTC, the equation of motion of the electron in the superposition of a pulse with a wavelength ( $\omega$ ) and its second harmonic ( $2\omega$ ) parallel to each other is represented in Eqn[2.11].

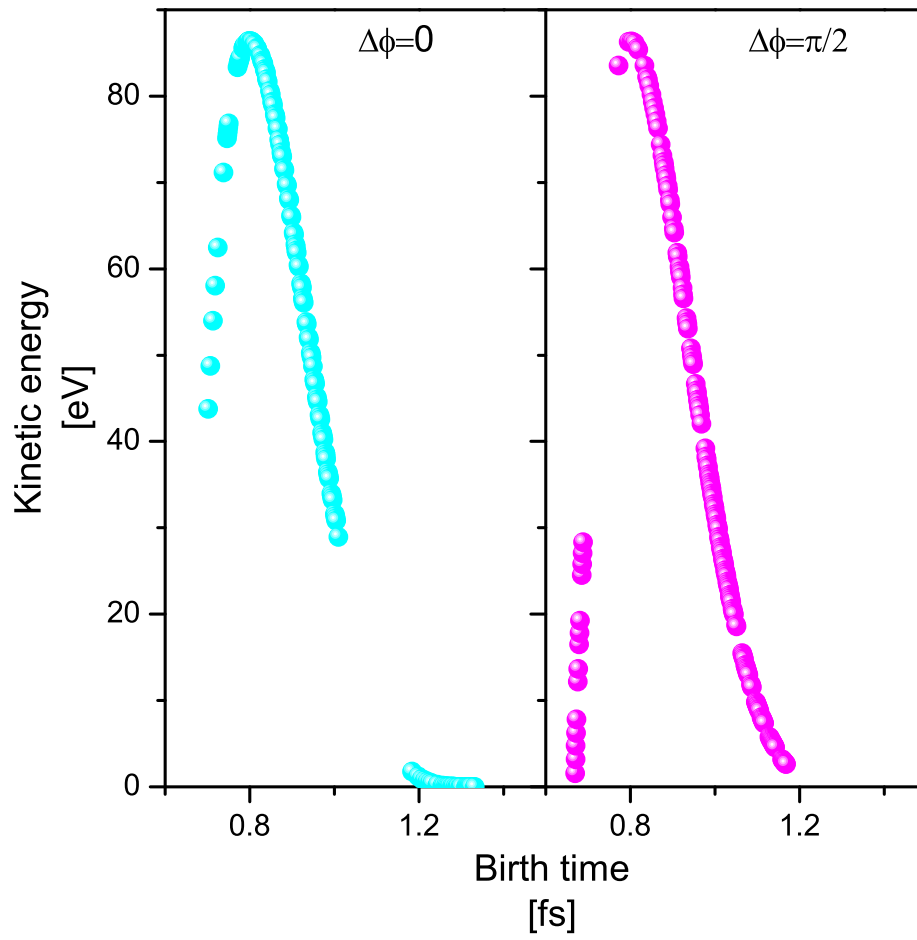


Figure 2.20: Maximum kinetic energy of the revisiting electron in the presence of OTC fields as a function of the birth-time.

$$m_e \left[ \frac{d^2 \hat{y}}{dt^2} \right] = \left[ eA_{800} \sin(\omega_{800}(t + \eta_{800})) \cos^2(k_{800}\omega_{800}(t + \eta_{800})) + eA_{400} \sin(\omega_{400}(t + \eta_{400})) \cos^2(k_{400}\omega_{400}(t + \eta_{400})) \right] \hat{y} \quad (2.11)$$

Graphically the resultant of the parallel two-colored linearly polarized field is shown in Figure [2.21], associated with kinetic energies of different birth times is shown in figure [2.22]. These simulated results give us a clear idea about revisiting electrons and their kinetic energy. These revisiting electrons may induce excitation/ionization and may also affect the fragmentation process of molecules. The results of revisiting electron-induced processes are discussed in the next chapters [3-5].

## 2.8 Theoretical ADK modelling

The ionization rate for  $\text{Ar}^+$  is theoretically obtained using the Ammosov-Delone-Krainov (ADK) theory. The rate of tunneling ionization for an atom can be expressed as [1]:

$$\omega_{ADK}(F) = C_{n^*l}^2 f(l, m) I_p \left( \frac{2}{F n^{*3}} \right)^{2n^* - |m| - 1} \quad (2.12)$$

where,

$$f(l, m) = \frac{(2l + 1)(l + |m|)!}{2^{|m|} |m|! (l - |m|)!} \quad (2.13)$$

In the following equation,  $n^* = 1/\sqrt{I_p}$  where  $I_p$  is the ionization potential for the given valence orbital,  $F$  is the field strength, and  $l$  and  $m$  are the azimuthal and magnetic quantum numbers respectively with respect to the quantization axis which is given by the direction of the laser polarization.

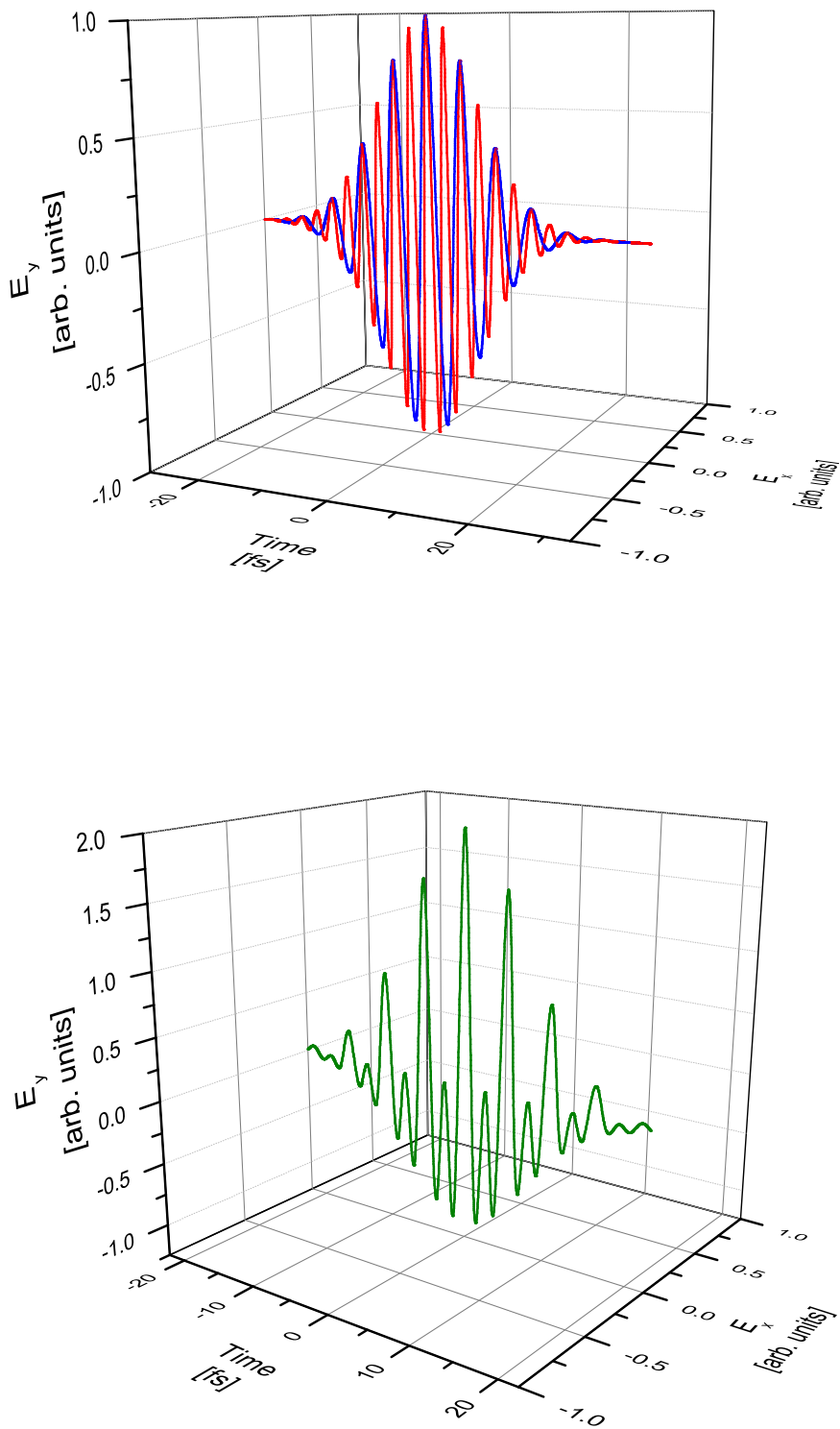


Figure 2.21: Top panel represents the 800 nm and 400 nm two-color fields. The bottom panel represents the resultant of parallel two-color fields.

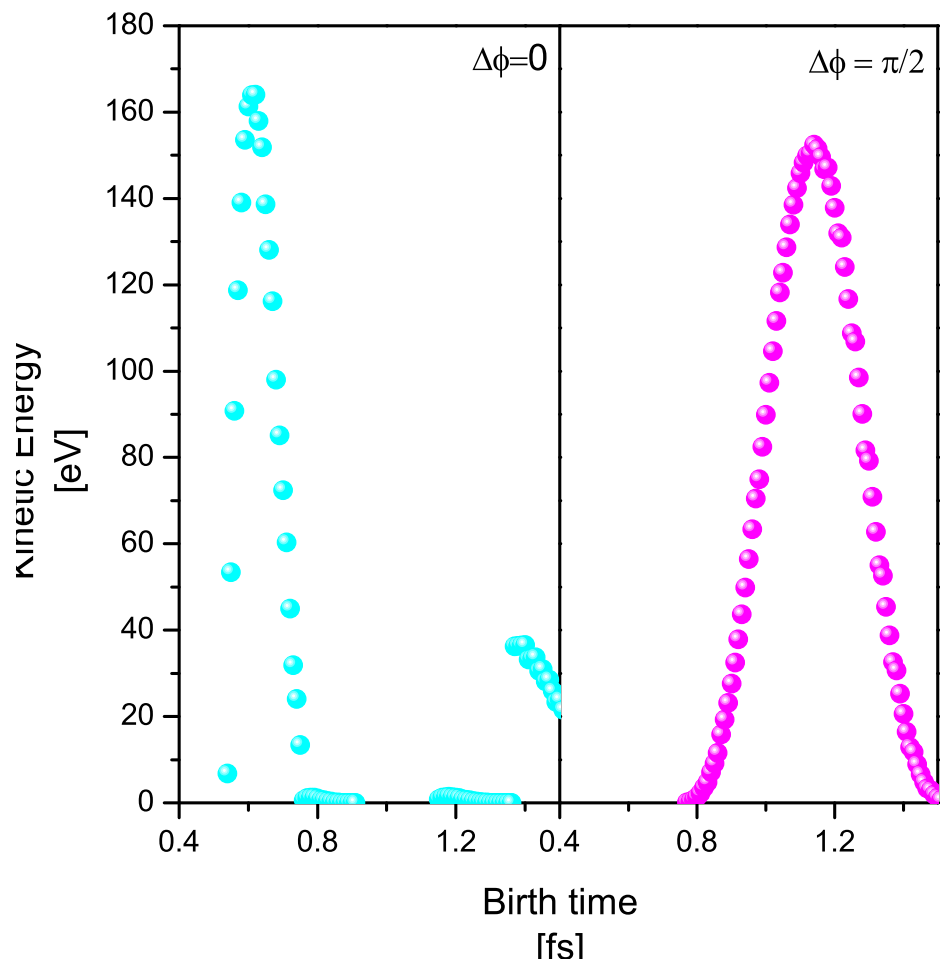


Figure 2.22: Maximum kinetic energy of the revisiting electron in the presence of PTC fields as a function of the birth-time.

Atom	$I_p(\text{eV})$	$C_{n^*l^*}^2$
Ar	15.79	4.116

Table 2.1: The parameters used in the theoretical model of ADK for Ar from Ref. [1] are given below.

Here,

$$C_{n^*l^*}^2 = \frac{2^{2n^*}}{n^*\Gamma(n^* + l^* + 1)\Gamma(n^* - l^*)} \quad (2.14)$$

The values of  $C_{n^*l^*}^2$  and  $I_p$  used in the calculations are tabulated in in Table 2.1.

In a pulsed laser field, the electric field has the form of [82]:

$$F(\mathbf{t}, r, z) = F_0 \exp(-2 \ln 2 t^2 / \tau^2) \exp(-2 \ln 2 r^2 / W(z)^2) \quad (2.15)$$

where  $F_0$  is the peak strength of the laser field and  $\tau$  is the FWHM of the laser pulse.

$$W(z) = w_0 \sqrt{1 + z^2 / z_R^2} \quad (2.16)$$

where  $w_0$  is the spot size and  $z_R$  is the Rayleigh range, is defined by  $\pi w_0^2 / \lambda$  where  $\lambda$  is the wavelength of the laser pulse.

The ionization probability is given by [16, 82]:-

$$P = 1 - \exp \int w(F(\mathbf{t}, r, z)) dt \quad (2.17)$$

Theoretical ionization rate is written using the in-house developed MATLAB programming. The focal volume averaging was included in the program by integrating over the spatial components (i.e., integrating over  $r$  and  $z$ ), where  $r$  varies from  $-45 \mu\text{m}$  to  $45 \mu\text{m}$  and  $z$  varies from  $0$  to  $z_R$ . The Rayleigh range calculated ( $z_R$ ) here was  $1.57 \text{ mm}$  for the beam spot size ( $w_0$ ) of  $20 \mu\text{m}$ . The ionization probability here was integrated from a time delay of  $-15 \text{ fs}$  to  $15 \text{ fs}$ . The theoretical ADK curve of  $Ar^+$  is shown in Figure 2.23.

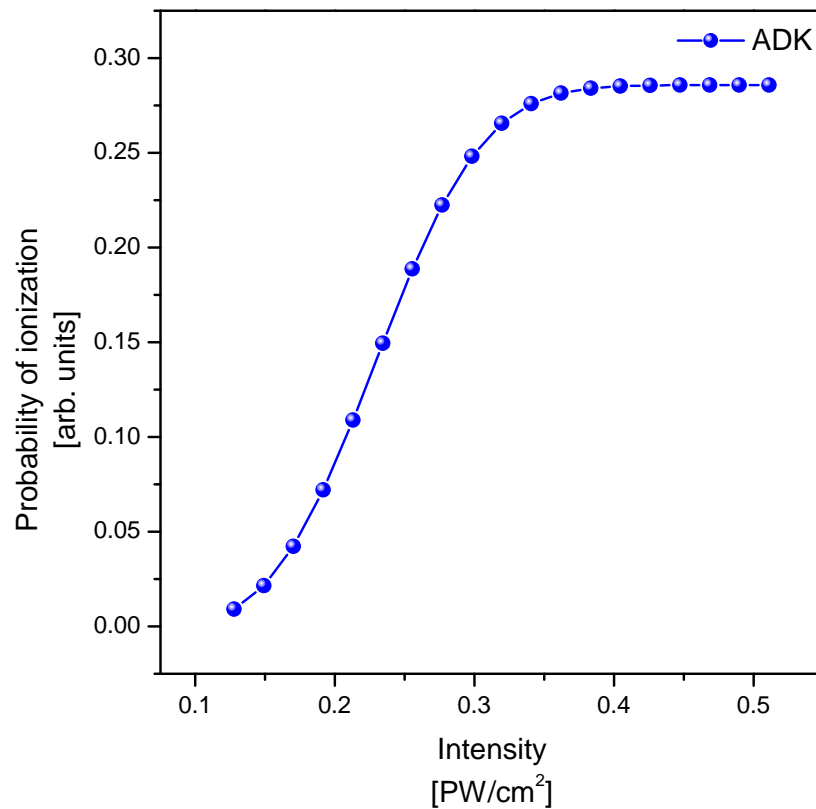


Figure 2.23: Theoretical ionization probability of  $\text{Ar}^+$  using ADK model

## 2.9 Summary and Conclusions

In this methodology chapter, we discussed all the experimental techniques and simulations used in this thesis. For this thesis work, the development of a new VMI setup and two-color pump-probe setup are discussed in detail. Further, the calibration scheme of VMI, the data acquisition scheme for ion yield as a function of intensity and relative phase, is also introduced. The classical tunnel electron trajectories simulations and ADK theory simulation are also discussed in this chapter.



# Chapter 3

## Single-color and two-color induced ionization of atoms: Argon and Xenon

The strong-field ionization of atoms (Ar, Xe) using single-color and two-color laser fields are discussed in this chapter. In the case of single-color-induced photoionization, the intensity dependence on the ion yield is investigated in detail. The ADK ionization rate is compared with the experimental results. To investigate how revisiting electrons affect the ionization rate, we have performed two-color-induced photoionization of Ar and Xe. We have measured the ions yield as a function of intensity and relative phase of Fundamental Wave (FW) and Second Harmonic (SH). Two-color fields modulate the revisiting electron trajectories, and the signature is seen in the ion yield. Further, the asymmetry in momentum distribution is obtained to understand the two-color induced modulation of tunnel electron trajectories.

### 3.1 Introduction

Chasing the electrons and nuclear dynamics in molecular photodissociation and controlling the outcome of the molecular reaction is one of the prime aims of ultrafast atomic, molecular and optical physics. The development of ultrafast laser

and modern experimental techniques like pump-probe combined with Velocity Map Imaging Spectrometer and Cold Target Recoil Ion Momentum Spectrometer have given a possible option to probe the ultrafast dynamics and even control them. The available commercial femtosecond laser produce pulse of about 20 fs or even less up to 5 fs with the hollow core fiber compression technique. Electron dynamics in atoms or molecules are in the attosecond time scale, and nuclear dynamics is in the picosecond to femtosecond range. Thus, the femtosecond pulses can probe and control the molecule's nuclear dynamics, but attosecond light pulses are needed to chase electrons. The last few decades have witnessed many scientific developments in the field of ultrafast science, like the development of attosecond pulses using High Harmonic Generation [83], [84], Time-resolved holography with photoelectron [85], Ångström- and femtosecond-scale atomic motion movie [86], molecular orbital tomography (MOT) [87], etc.

The two-color field-induced ionization scheme has emerged as a powerful technique to control electron dynamics. In a two-color field scheme, the polarization of both fields can be chosen as orthogonally polarized two-color (OTC) or parallel polarized two-color (PTC). Both schemes have been successfully used in the past decade to demonstrate electron dynamics control. For example, double-slit interference temporal control [88], Coulomb effect on photoelectron momentum distribution [89], intracycle interference (between electron wave packets ionized within the same laser cycle) [90], and electron correlation in Non-sequential double ionization (NSDI) [88], [91], [92].

In this study, we report the yield of singly and doubly ionized Argon induced by a two-color as a function of relative delay (phase) with attosecond resolution. We investigated the power ratio of FW and SH as a function of ionization yield and observed the unique trend of doubly ionized Argon. Further, photoelectron momentum distribution at different relative phases is obtained to understand the modulation induced by the two-color field.

## 3.2 Methodology

Detail of the laser, spectrometer and experimental scheme is discussed in Chapter 2: Methodology. Here, we briefly described the experimental parameters used in the strong-field ionization of  $\text{CO}_2$ .

### 3.2.1 Single color photoionization experiment

The strong field photo-ionization of Ar has been studied using femtosecond laser pulses in combination with a home-built multi-plate Velocity Map Imaging (VMI) Spectrometer. An Argon gas of about 6 bars is used through the pulsing valve (Parker) with an opening of 1000 microns. The laser pulse (29 fs, 1 kHz, 800 nm) interacts with the Argon gas beam in the interaction region of the VMI spectrometer. For ion yield measurements, the VMI was operated in Time-of-flight (TOF) mode. The TOF spectrum at given laser intensity was recorded and analyzed. In this study, the laser intensity varies from 0.10 to 0.70  $\text{PW}/\text{cm}^2$ .

During the experiments, the pulse duration was monitored using a commercial SPIDER (FC-SPIDER, APE Germany) unit. Previously, we reported the pulse characterization [93], [94] and also discussed it in the methodology chapter.

### 3.2.2 Two-color photoionization experiment

Photoionization of Argon by a two-color field is performed in a VMI spectrometer. The experimental setup can be categorized into two parts: the velocity map imaging spectrometer and the optical setup, which includes the laser system, SPIDER, and  $\omega - 2\omega$  generation. The laser system used for the experiment was a Coherent Ti: Sapphire femtosecond laser whose central wavelength is 800 nm, pulse duration of 26 fs with pulse energy of 10 mJ at a 1 kHz repetition rate.

The optical setup has a Mach-Zehnder interferometer setup in which one arm is for the fundamental wave(FW) at 800 nm, and the other is for the second harmonic (SH) at 400 nm. A type-I  $\beta$ -BBO of  $100\mu\text{m}$ (Eksma-Optics) is used in the SH arm to generate a second harmonic with approximately 12% efficiency. The power of individual paths is controlled by the half-wave plate and

a polarizer combination.

A delay stage in the 400 nm path is used to make the path lengths equal. An Avantes spectrometer is used to measure the THG, and the delay stage is fixed at the point where THG(266nm) is maximum, ensuring the temporal overlap of 400 nm and 800 nm within  $1\mu\text{m}$  resolution outside the VMI chamber. A  $\text{CaF}_2$  window is also placed before the THG generation so that the optical path lengths of the 400 and 800 nm inside the  $\text{CaF}_2$  window are also taken into account while finding their temporal overlap. The Orthogonal/Parallel Two-Color(OTC/PTC) configuration is obtained by adjusting the polarizers in both paths suitably. The phase between the FW and the SP is adjusted by the Newport XML350-S delay stage, which has a resolution of 1nm in the 400 nm path, and polarizers in both paths are used to adjust various intensity ratio combinations. The delay stage is moved at a 20nm interval corresponding to 133.33 attoseconds temporally during the experiment.

### 3.2.3 ADK ionization rate

We have obtained the ADK ionization rate of Argon at the used laser intensities ( $0.1 - 0.7 \times \text{PW}/\text{cm}^2$ ). The detail of ADK mathematical expression, parameters used, etc., is discussed in the methodology chapter.

## 3.3 Results and Discussions

### [A] Two-color laser field-induced photoionization of Argon

#### 3.3.1 Single and two-color field-induced ionization of Argon: Intensity dependence

Figure 3.1 [top] shows the  $\text{Ar}^+$  and  $\text{Ar}^{2+}$  yields as a function of single-color (800 nm, FW) laser intensity. The yield of  $\text{Ar}^+$  is increasing in the laser intensity range of  $0.11$  to  $0.4 \times 10^{14} \text{ W}/\text{cm}^2$  and saturates beyond  $0.4 \times 10^{14} \text{ W}/\text{cm}^2$ . A

similar increasing trend in  $\text{Ar}^{2+}$  is also observed, which saturates at about  $0.5 \times 10^{14} \text{ W/cm}^2$ . The ionization rate of  $\text{Ar}^+$  obtained using ADK calculation is also shown in the same figure. It is interesting to see that the ADK ionization rate (black curve, normalized with a factor of 3.5) agrees well with the experimental result at high intensities (above  $0.4 \times 10^{14} \text{ W/cm}^2$ ). It shows some deviation at low intensities (MPI regime) where the ADK breakdown [95]. The deviation in ADK rate from the experimental result (factor 3.5) is possibly due to various processes like sequential double ionization (SDI) or non-sequential double ionization (NSDI) and enhanced ionization (Freeman resonances), which are not incorporated in ADK calculations. Similar trends in  $\text{Ar}^+$  and deviation of ADK ionization rate at low intensities have also been found previously [96] but not much work is reported on the  $\text{Ar}^{2+}$  trend. However, the ion yield ratio ( $\text{Ar}^{2+}/\text{Ar}^+$ ) as a function of laser intensity has been used earlier to understand the NSDI [96, 97]. The observed single-color induced  $\text{Ar}^+$  yield as a function of laser intensity will be compared to the similar yield plot induced by a two-color field. The two-color field (Parallel polarization Two-Color (PTC) field) induced ion yield trend may completely deviate from the single-color case as a combination of laser intensities and relative phase may influence the ionization yield. Here, we investigate the ion yield trend as a function of two-color laser intensity and relative phase.

The  $\text{Ar}^+$  and  $\text{Ar}^{2+}$  yield as a function of two-color laser intensity is shown in Figure 3.1 [bottom]. This plot is obtained at a fixed  $0.25 \text{ PW/cm}^2$  of SH intensity while varying the 800 nm intensity from  $0.05$  to  $0.38 \text{ PW/cm}^2$ . As both colors contribute to ionization, the resultant effect on ion yield may have a different trend than the single-color-induced ion yield trend. Interestingly, we can see the different trends in the ion yield of  $\text{Ar}^+$  and  $\text{Ar}^{2+}$  in the case of two-color (PTC) fields. In the  $0.3 \times 10^{14} \text{ W/cm}^2$  to  $0.4 \times 10^{14} \text{ W/cm}^2$ , the yield of  $\text{Ar}^+$  is constant and  $\text{Ar}^{2+}$  yield is slightly decreasing. Beyond the  $0.4 \times 10^{14} \text{ W/cm}^2$ , the yield of  $\text{Ar}^{2+}$  is increasing and the yield of  $\text{Ar}^+$  is decreasing and beyond  $0.5 \times 10^{14} \text{ W/cm}^2$ , both the  $\text{Ar}^+$  and  $\text{Ar}^{2+}$  ions yield saturates. This trend is due to two-color (PTC) induced ionization in which the enhanced double ionization and depletion of singly ionized Ar occur in the range of  $0.40 - 0.55 \times 10^{14}$

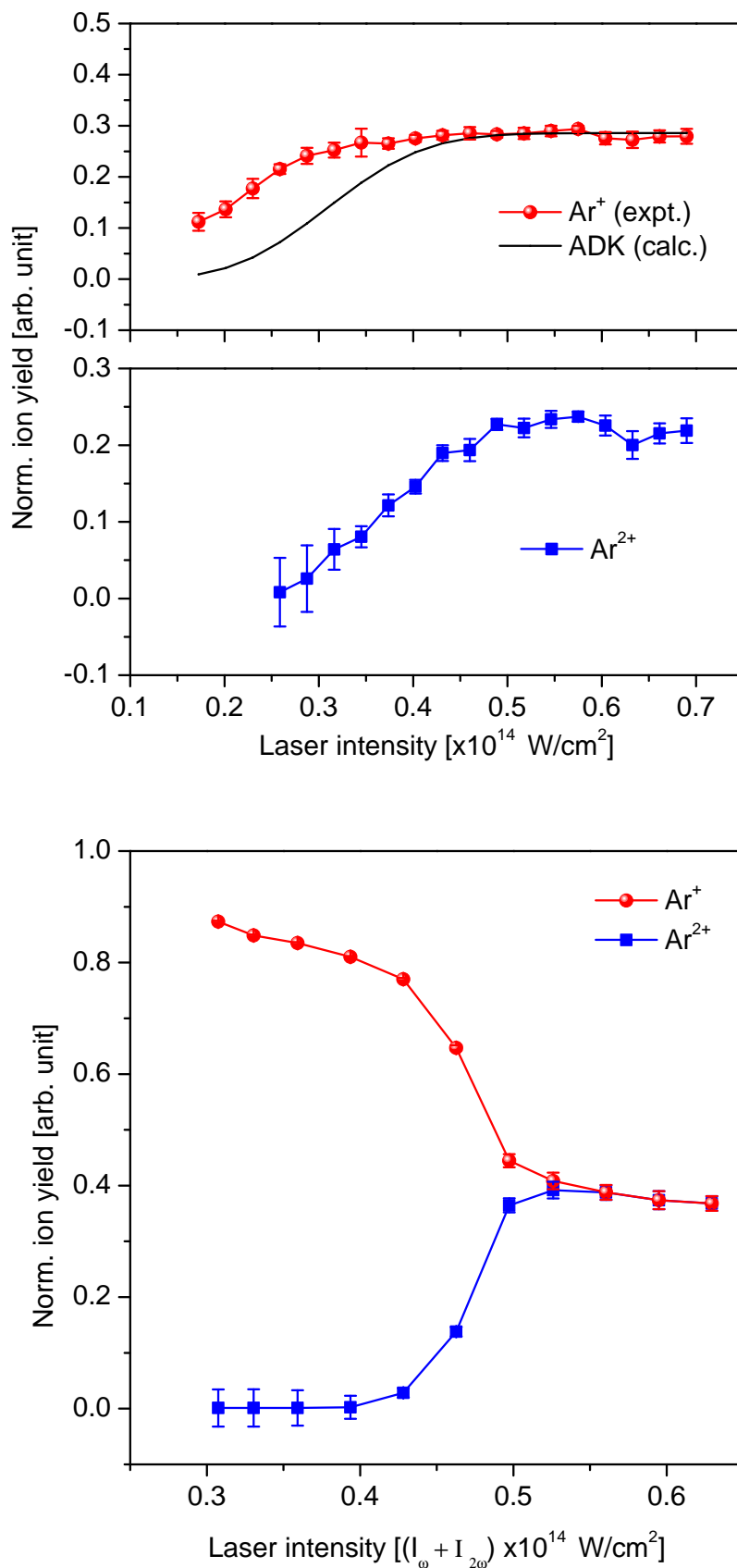


Figure 3.1: [Top] Ion yield of  $\text{Ar}^+$  (red),  $\text{Ar}^{2+}$  (blue) and the ADK calculated ion yield of  $\text{Ar}^+$  (black line) as a function of intensity of single color 800 nm is compared with the ion yield of [bottom]  $\text{Ar}^+$  (red) and  $\text{Ar}^{2+}$  (blue) as a function of the intensity of PTC (800 nm and 400 nm) pulses.

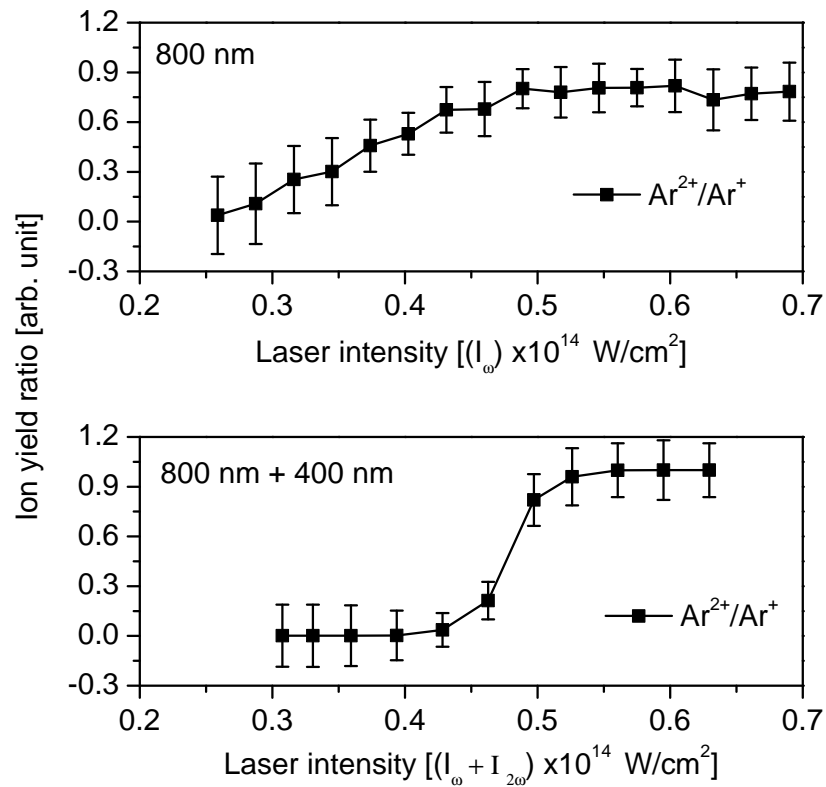


Figure 3.2: Photo-ionization of Argon using intense femtosecond laser pulses as a function of laser intensity.

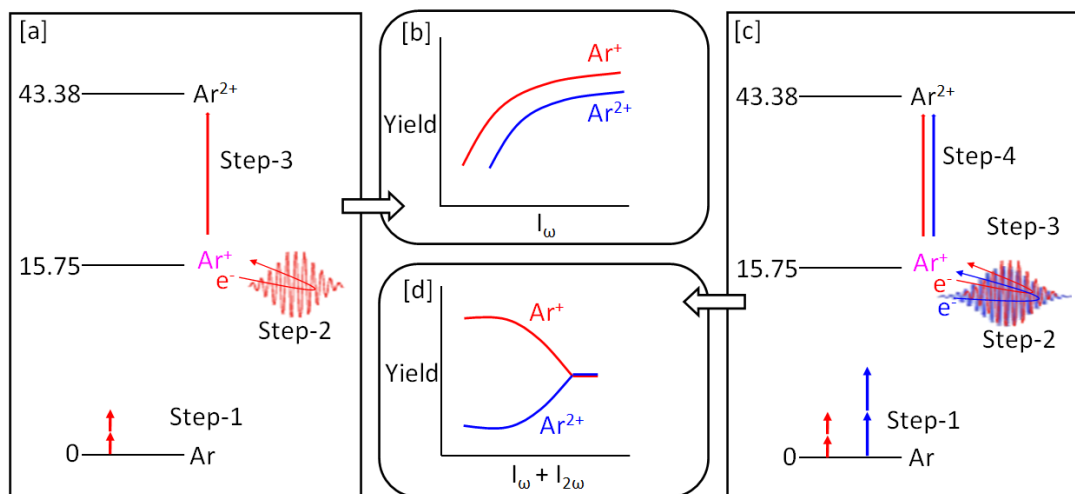


Figure 3.3: A scheme of two-color processes

$\text{W}/\text{cm}^2$  of the sum of both colors intensity. This trend is completely different from the single-color-induced ionization in the same intensity value. In the case of single color induced ionization, the ion yield ratio (e. g.  $\text{Ar}^{2+}/\text{Ar}^+$ ) is usually used to interpret the enhanced doubly ionization induced by revisiting electrons [80, 98, 99]. We also plotted the ion yield ratio for single-color and two-color photoionization, and the results are shown in Figure 3.2. The top panel of the figure is the ion yield ratio ( $\text{Ar}^{2+}/\text{Ar}^+$ ) as a function of laser intensity obtained with a single color (800 nm). The ion yield ratio ( $\text{Ar}^{2+}/\text{Ar}^+$ ) is gradually increasing as a function of intensity and saturates beyond the  $0.5 \times 10^{14} \text{ W}/\text{cm}^2$ . In the bottom panel of the figure, an ion yield ratio ( $\text{Ar}^{2+}/\text{Ar}^+$ ) as a function of the sum of the intensity of two-color (800 nm + 400 nm) is shown.

Interestingly, a unique trend in ion yield ratio is observed in the case of two-color (PTC) photoionization. This kind of trend is never reported. This sudden enhanced double ionization due to the two-color (PTC) field is possible to understand based on the tunnel electron recollision. In a single-color field, the tunneling electron revisits to parent, and the probability of revisit depends on the nature of laser pulses that guide the electrons. It is now accepted that processes like HHG, NSDI, etc., are due to the revisiting electrons. The NSDI or RESI processes have been studied previously mostly by single-color (FW) photoionization. Here, we found similar to the NSDI process but in the two-color field where electron return probability depends on the intensity and relative phase of two-color, which may modulate the electron trajectories. To explain the observed trend, we have schematically shown (in figure 3.3 ) the possible processes which are most likely responsible for the observed enhanced double ionization of Argon.

### 3.3.2 Phase dependent two-color photoionization Argon: PTC & OTC

Like the intensity of a two-color field, the relative phase may also influence the ionization rate of Argon. In this section, our investigation of the phase-dependent two-color (PTC) ionization is discussed. The  $\text{Ar}^+$  yield as a function of relative

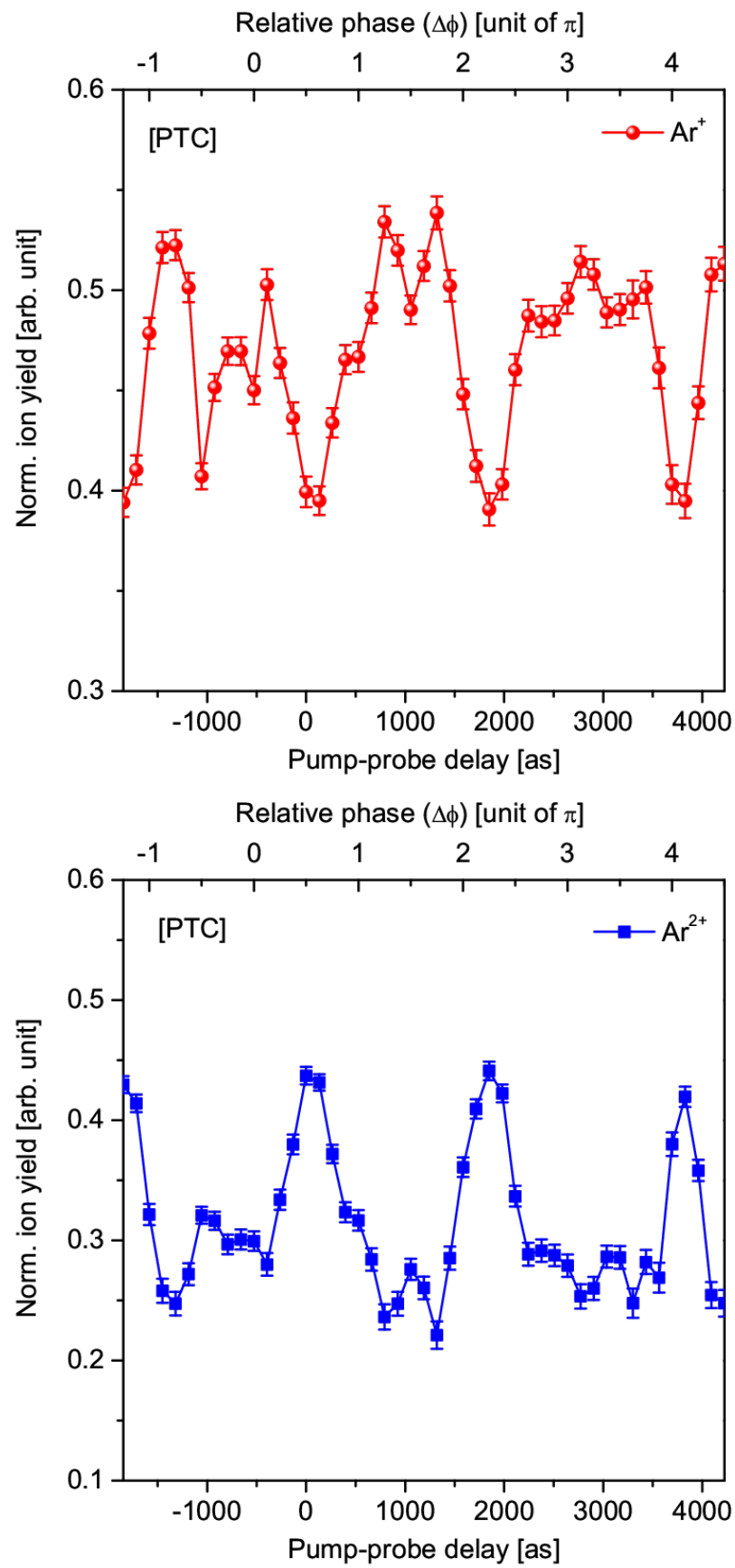


Figure 3.4:  $\text{Ar}^{2+}$  and  $\text{Ar}^+$  ions yield as a function of relative phase at intensity ratio ( $I_{SP}/I_{FP}=0.65$ )

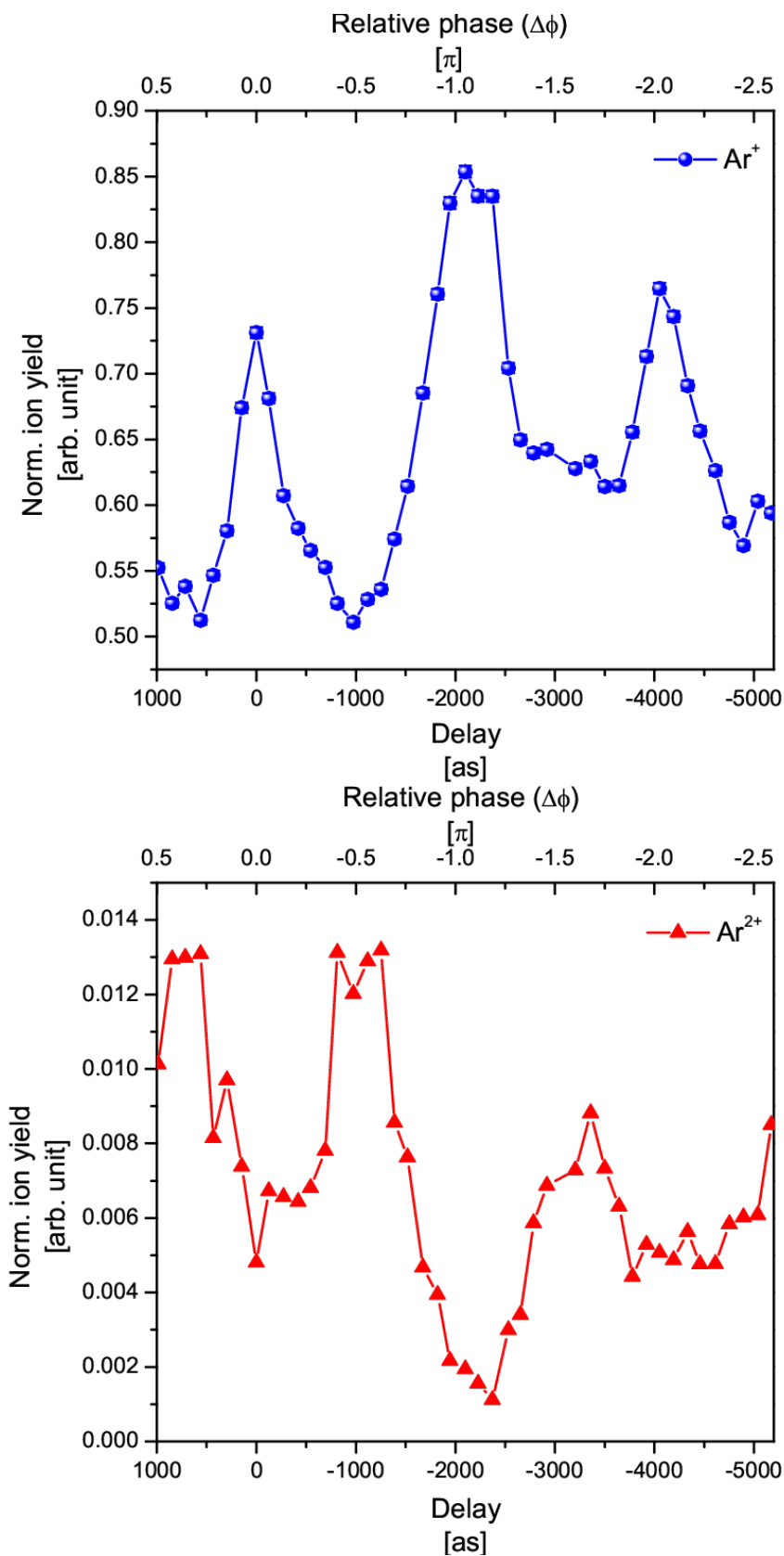


Figure 3.5: Two-color (OTC) induced  $\text{Ar}^{2+}$  and  $\text{Ar}^+$  ions yield as a function of relative phase at intensity ratio ( $I_{SP}/I_{FP}=0.65$ ).

phase is shown in the top panel of figure 3.4 and the yield of  $\text{Ar}^{2+}$  as a relative phase is shown in the bottom panel of the same figure. The variation in yield of  $\text{Ar}^+$  and  $\text{Ar}^{2+}$  is clearly seen. Both ion yields are oscillatory in nature and have a periodicity of  $\pi$ . Interestingly, the  $\text{Ar}^+$  and  $\text{Ar}^{2+}$  yields are anti-correlated. Here anti-correlation means that when  $\text{Ar}^+$  yield is high, then  $\text{Ar}^{2+}$  is low. This observation suggests that at a given relative phase, the  $\text{Ar}^+$  yield is converted to the  $\text{Ar}^{2+}$  induced by a two-color field. At the used intensity, the TI is possible by FW, and MPI is by SH. Thus, at a given relative phase, both TI and MPI are contributing to the yield of  $\text{Ar}^+$  and  $\text{Ar}^{2+}$  ions. Further, the electron revisit to the parent ion may also efficiently contribute to excitation or ionization and, thus, the depletion of single ionized Argon and enhancement in double ionization is most likely, which explains the observed anti-correlation trend.

The two-color (OTC) induced photoionization of Argon is also studied. The  $\text{Ar}^+$  and  $\text{Ar}^{2+}$  yield as a function of relative phase in case of OTC field is shown in figure 3.5. The yield of  $\text{Ar}^+$  and  $\text{Ar}^{2+}$  are oscillatory and have a period of  $\pi$ . The  $\text{Ar}^{2+}$  yield is low compared to  $\text{Ar}^+$ . The  $\text{Ar}^+$  and  $\text{Ar}^{2+}$  yield trends are anti-correlated, similar to the PTC case (figure 3.4), suggesting a similar mechanism of doubly ionized Argon formation in the two-color field. A classical trajectory simulation (discussed in the methodology chapter) advocates revisiting electron-induced double ionization.

Here, we studied the two-color induced photoionization of Argon as a function of intensity and relative phase. We observed that the ion yield is sensitive to the intensity and phase. Now we extend our study to photoelectrons. The findings on photoelectrons are discussed in the next section.

### 3.3.3 Two-color (PTC) induced Photoelectron Momentum Distribution: Argon

The photoelectron momentum distribution (PEMD) of Argon induced by a two-color (PTC) field at  $I_{800} = 0.24 \text{ PW/cm}^2$  and  $I_{400} = 0.12 \text{ PW/cm}^2$  is shown in Figure [3.6], both SH and FW polarization was along the x-axis (parallel to detector plane). Photoelectron distribution at relative phase 0 is shown in the

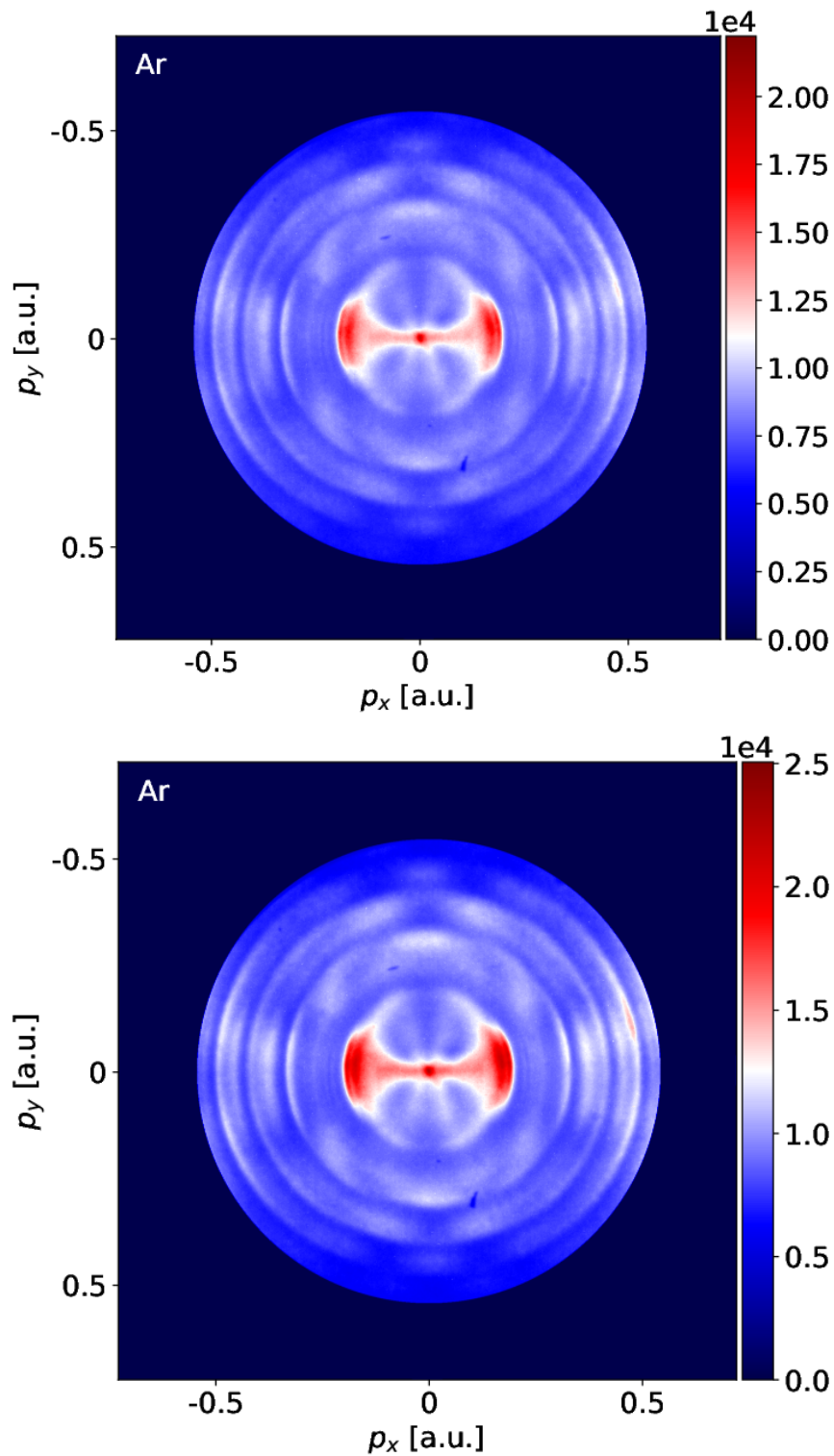


Figure 3.6: Photoelectron momentum distributions of Ar induced by Two-color parallel polarized field at laser intensity ratio of 2 ( $I_{SP}/I_{FP} = 2$ ), [top] at relative phase 0, [bottom] at relative phase  $\pi/2$ . Polarization of both fields was in the detector plane.

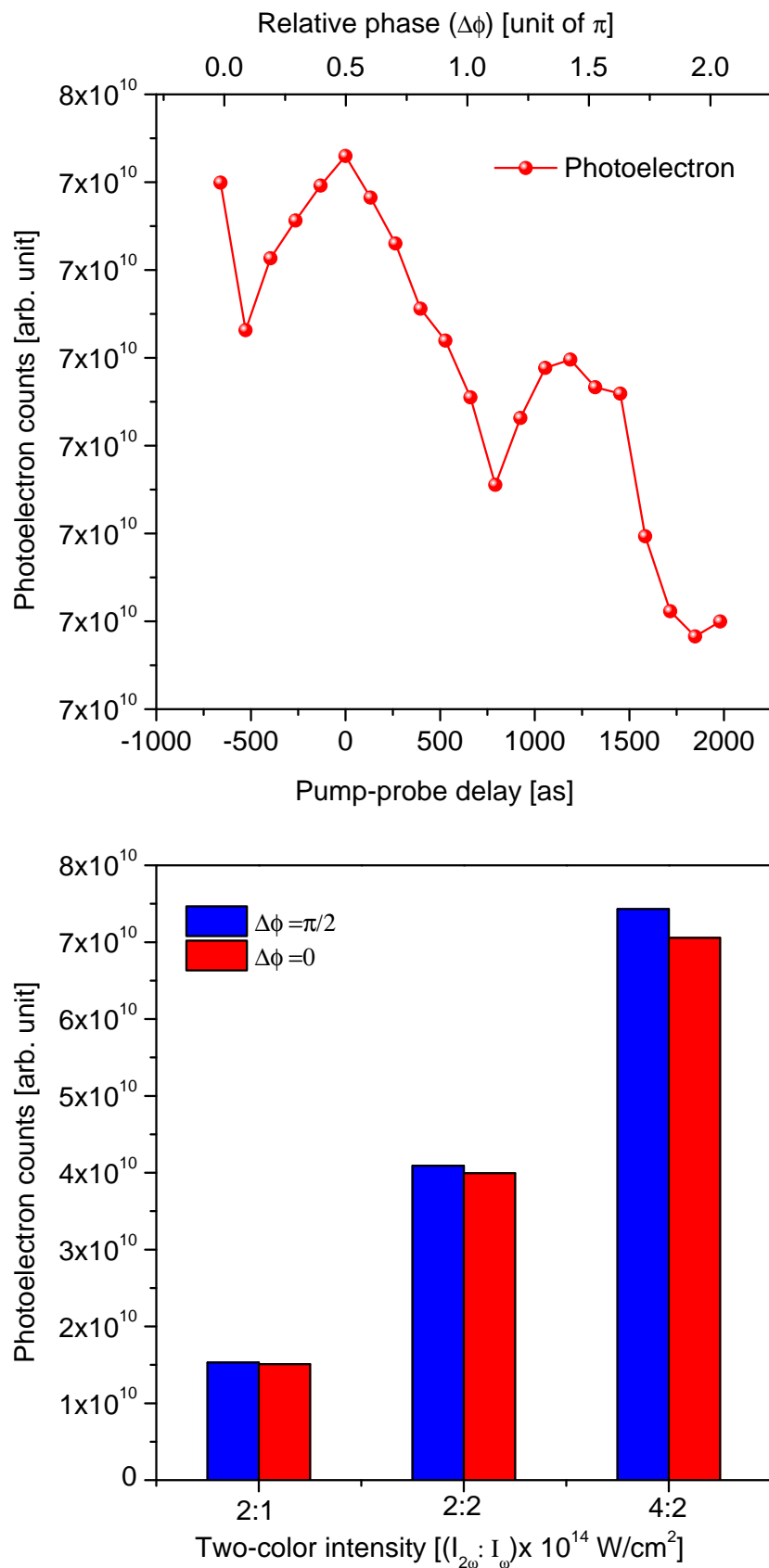


Figure 3.7: [top] Photoelectron yield as a function of delay or relative phase between 800 nm and 400 nm. [bottom] The photoelectron yield at three different intensity ratios ( $I_{SP}/I_{FP}$ ). The yield at the relative phase at 0 and  $\pi/2$  is also shown in this figure.

top panel, and the photoelectron distribution at a relative phase at  $\pi/2$  is shown in the bottom panel of this figure. The intensity of photoelectrons along the polarization axis is maximum in both PEMD images. The ATI structure and sub-structures are clearly visible in the PEMD images. The radial pattern (ATI-rings) for single and two colors has been reported by other groups [100, 101, 102], and similar structures have been observed here. The observed unique "bouquet" shape structure and the ring structures by multiphoton absorption have also been interpreted theoretically [102]. The clear amplification in the intensity can be observed in the PEMD of  $\pi/2$  (color bar). The narrow sub-structures above 0.2 a.u. are likely due to the freeman resonances [102]. The PEMD is distinguished into 2 major contributions. Firstly, the electron momentum density beyond 0.2 a.u., which has been attributed to (n+1)resonance-enhanced ionization via intermediate Rydberg states. Secondly, the structures below 0.2 a.u. are the low-energy spectra, and the bouquet (fan) in the low-energy region increases or decreases by one unit based on the intensity of the applied field. This low energy structure is not due to the rescattering of indirect electrons, but a consequence of the long-range coulomb potential effect [103]. The two-color fields may also influence the PEMD. To understand the two-color fields, we have investigated the photoelectrons as a function of intensity and phase.

Figure [3.7] [top] displays the photoelectron yield as a function of relative delay between 800 nm and 400 nm pulses, recorded with a step size of 132 as ( $\pm 13$  as) using a precision motorized stage (Newport's XPS). The observed oscillation has a period of 1.3 fs, with optical cycle of 400 nm. The delay can also be interpreted as the relative phase between FW and SH, shown in this figure's [top] axis. The period of  $\pi$  for the oscillations of the photoelectrons is similar to the ion yield defined above (Figure [3.4] and Figure [3.5]).

To understand the two-color intensity dependence on the total photoelectron yield, the photoelectron yield at relative phases 0 and  $\pi/2$  has been illustrated in the bottom panel of Figure [3.7]. The bar plot indicated the yield of the photoelectrons at both relative phases for 2:1 ( $I_{FW} = 0.24 \text{ PW/cm}^2$  ( $\gamma = 0.73$ ),  $I_{SH} = 0.12 \text{ PW/cm}^2$  ( $\gamma = 2.14$ )), 2:2 ( $I_{FW} = 0.24 \text{ PW/cm}^2$  ( $\gamma = 0.731$ ),  $I_{SH} = 0.24 \text{ PW/cm}^2$  ( $\gamma = 1.462$ )) and 4:2 ( $I_{FW} = 0.46 \text{ PW/cm}^2$  ( $\gamma = 0.54$ ),  $I_{SH}$

$= 0.24 \text{ PW/cm}^2$  ( $\gamma = 1.46$ ). The  $\gamma$  values for the range of intensities indicate that FW is in the domain of tunnel ionization while SH is in the multiphoton ionization regime. It is clear from the bar plot that the photoelectron yield at relative phase  $\pi/2$  is relatively higher compared to phase 0. We observed that the photoelectron yield is increasing at intensities 2:1 to 4:2 of the two-color field. We learned that the intensity and the relative phase of two-color fields influence the ionization and, thus, the yield of photoelectrons. The two-color field may also affect the photoelectron momentum distribution (PEMD). In figure 3.6, the variation in PEMD at relative phase 0 and at  $\pi$  is not significant. To understand how the two-color field affects the PEMD, an asymmetry parameter analysis of PEMD induced by two-color field analysis is needed.

The asymmetry parameter defined in equation [5.15] can confirm the induced asymmetry by a two-color field. Asymmetry along  $p_x$  has been evaluated at  $p_y = 0$ , Similarly, asymmetry along  $p_y$  can be obtained at  $p_x = 0$ . The asymmetry between two pixels is determined by selecting one pixel (intensity) along the x-axis to the right of the center with intensity  $I_X$  and a matching equidistant pixel (intensity) to the left of the center with intensity  $I_{X'}$ .

$$\text{Asymmetry}(p_x) = \frac{I_X - I_{X'}}{I_X + I_{X'}} \quad (3.1)$$

Here, asymmetry along  $p_y$  is defined using the asymmetry parameter defined in the equation [5.15]. The  $I_x$  is the intensity of a pixel along the x-axis ( $p_y = 0$ ) lying to the right of the center (zero-energy), while  $I_{x'}$  is the intensity at equidistant on the other side of the center of the image.

In Figure [3.8], the asymmetry parameter as a function of  $p_x$  at relative phase 0,  $\pi/2$  for PEMD of  $I_{\omega+2\omega} - I_{\omega}$  as well as for 400 nm ( $I_{2\omega}$ ) are shown and compared. Here, the asymmetry of 400 nm is considered as a reference, where asymmetry must be zero (observed asymmetry in 400 nm is less than 0.1 and probably due to experimental artifact). It is important to mention that no spatial efficiency correction is performed in this MCP detector.

The asymmetry along the polarization axis (x-axis) shows a significant modulation beyond 0.2 a.u and no modulation till around 0.22 a.u. This obser-

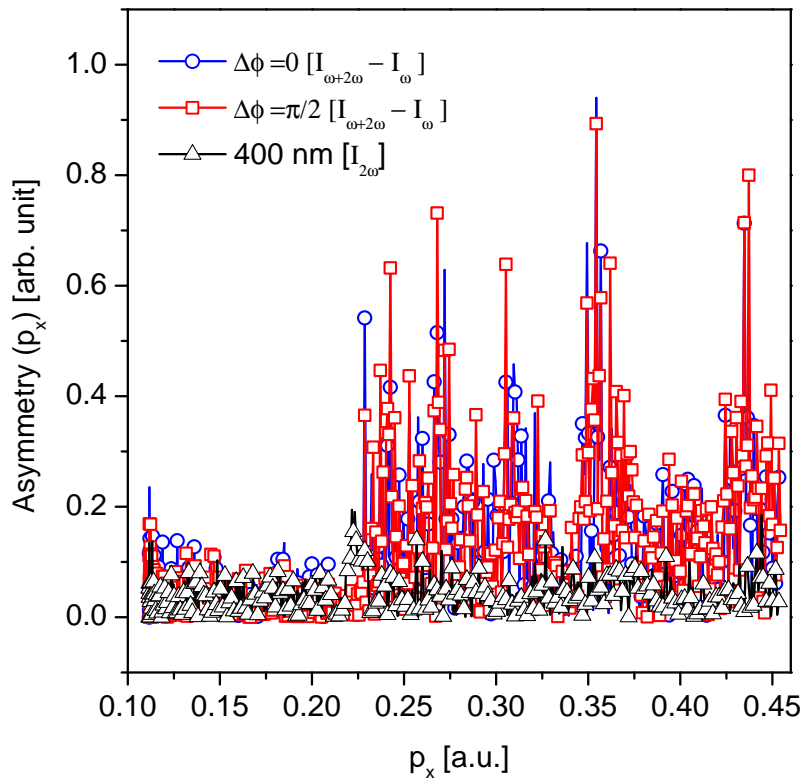


Figure 3.8: Asymmetry in  $p_x$  as a function of laser intensity ratio.

variation is consistent with published work [102], which explains based on the low variation in the long-range coulomb potential. It is observed that the modulation in the asymmetry of both 0 and  $\pi/2$  is maximum in the resonance-enhanced region. The tunneling ionization of 800 nm and the multiphoton regime of 400 nm modulates the electrons, which are resonance-enhanced ionization via intermediate Rydberg states.

### 3.3.4 Two-color (OTC) induced Photoelectron Momentum Distribution: Argon

The photoelectron momentum distribution of Argon induced by a two-color field at  $I_{800} = 0.24 \text{ PW/cm}^2$  and  $I_{400} = 0.12 \text{ PW/cm}^2$  is shown in Figure [3.9], the FW polarization was along the x-axis (parallel to detector plane) while the SH was along the detector. In the top panel, photoelectron distribution at a relative phase of 0, and in the bottom panel, the PEMD at a relative phase  $\pi/2$  is shown. The PEMD at both relative phases indicates that the streaking of the electrons

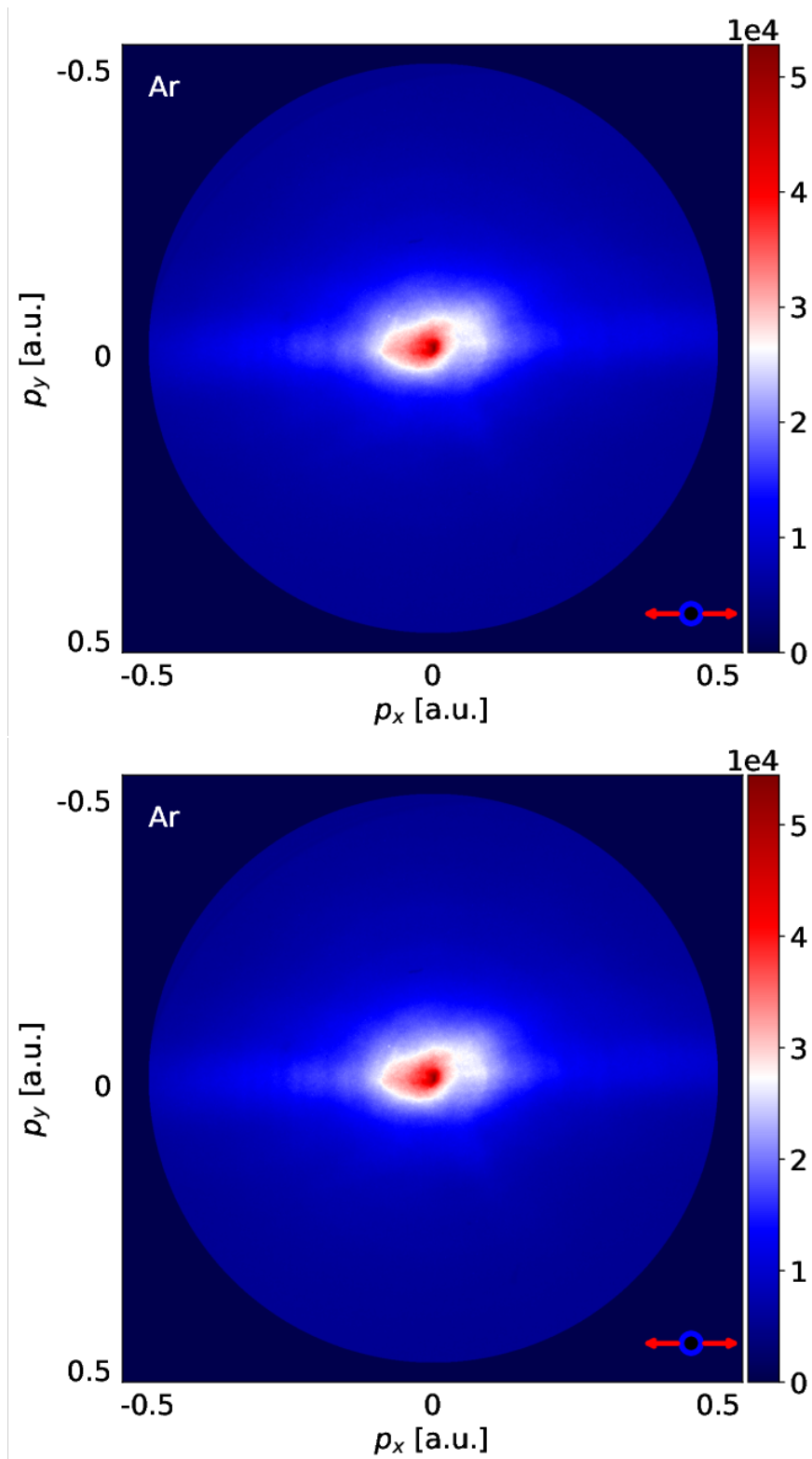


Figure 3.9: Photoelectron momentum distributions of Ar induced by Two-color Orthogonal polarized field at laser intensity ratio of 2 ( $I_{SP}/I_{FP} = 2$ ), [top] at relative phase 0, [bottom] at relative phase  $\pi/2$ .

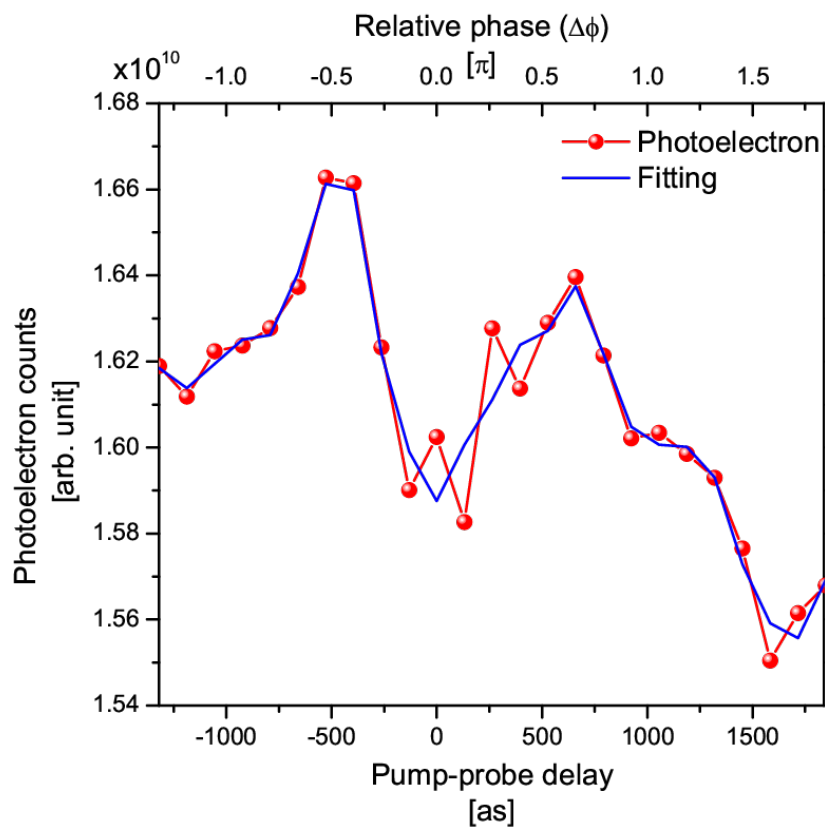


Figure 3.10: Photoelectron yield as a function of delay or relative phase between 800 nm and 400 nm. Red points are experimental data points. The blue line is based on fittings.

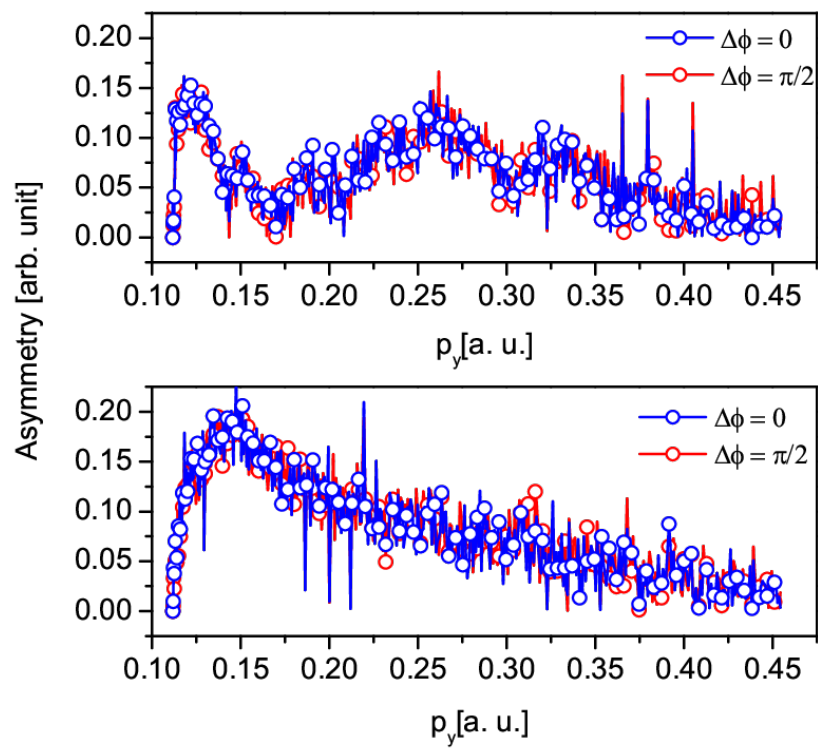


Figure 3.11: Asymmetry in  $p_x$  and  $p_y$  as a function of relative phases at 0 and  $\pi/2$ .

due to the  $0.24 \text{ PW/cm}^2$  shows very low variation in PEMD at both relative phases. The ATI rings and internal substructures observed in the PTC are also absent in OTC.

We now extend our study to the photoelectron yield analysis as a function of relative phase. Although at two relative phases, the variation in PEMD is not much, both PEMDs look similar in Figure 3.9, it is expected that the total photoelectron yield varies with relative phase due to ionization rate variation. The photoelectron yield as a function of relative phase (delay between 800 nm and 400 nm) is shown in figure 3.10. An oscillatory trend in yield is observed. This trend is similar to the photoelectron yield induced by PTC fields. The oscillation has a period of  $\pi$ . This observation suggests that the relative phase plays a role in two-color (OTC) induced ionization. Further, the OTC two-color may also influence the photoelectron momentum distribution. To understand the OTC-induced effect on photoelectron momentum distribution, an asymmetry parameter analysis is performed here, similar to PTC. The asymmetry parameter, defined in equation [5.15], is used to obtain the asymmetry along  $p_x$  and along  $p_y$ . The asymmetry parameter as a function of  $p_x$  is shown in top panel of figure 3.11 at relative phase 0 and at  $\pi/2$ . In the bottom panel of the same figure, the asymmetry along  $p_y$  at relative phase 0 and at  $\pi/2$  is shown. Asymmetry in both  $p_x$  and  $p_y$  has dominant variation in the low energy region (below 0.35 a. u.). The asymmetry at the relative phase of 0 and at  $\pi/2$  along  $p_x$  and  $p_y$  are the same. The observed variation in asymmetry along  $p_x$  and along  $p_y$  is due to the OTC field, which modulates the photoelectron trajectories.

## [B] Two-color laser field-induced photoionization of Xenon

In this section, we will present the key findings on the two-color photoionization of the Xenon atom. A study on two-color photoionization on Xenon is performed using a Velocity Map Imaging spectrometer and a pump-probe type setup. The experimental setup is the same as used in Argon (previous section). This study

focuses on photoion yield as a function of relative phase, photoelectron momentum distribution, and asymmetry due to the two-color field.

### 3.3.5 Phase dependent two-color photoionization Xenon: PTC & OTC

The two-color photoionization Xenon with PTC and OTC laser field is performed at the intensity of  $I_{800} = 0.09 \text{ PW/cm}^2$  and  $I_{400} = 0.03 \text{ PW/cm}^2$ . At this intensity, the yield of doubly ionized Xenon in time-of-flight mass spectrum was negligible. Thus phase dependence analysis is based on the yield of singly ionized Xenon. The singly ionized Xenon ( $m/q = 128.6 \text{ amu}$ ) yield induced by PTC as a function of relative phase is shown in the top panel of figure 3.12. An oscillation in the yield is clearly seen in this plot. This result is similar to the  $\text{Ar}^+$  yield and has the periodicity of  $\pi$ .

To see the oscillation in yield of Xenon ion induced by two-color (OTC) fields, we have performed a photoionization experiment with OTC, and the result is displayed in the bottom panel of figure 3.12. We can see the yield trend, which is sensitive to the relative phase. The  $\text{Xe}^+$  yield is oscillatory with a period of  $\pi$ . It is interesting to see the oscillatory trend in the PTC is different (out of phase/anti-correlated) than in the OTC case. This observation is directly linked to the two-color ionization and the electron revisit-induced processes which produce the  $\text{Xe}^+$  in OTC and PTC.

### 3.3.6 Two-color (PTC) induced Photoelectron Momentum Distribution: Xenon

Photoelectron momentum distribution (PEMD) of Xe induced by a two-color (PTC) field at  $0.03 \text{ PW/cm}^2$  SH and  $0.09 \text{ PW/cm}^2$  FW is shown in figure 3.13. The PEMD at relative phase 0 is shown in the top panel of the figure, and at a relative phase of  $\pi/2$  is displayed in the bottom panel. The ATI and sub-structure (due to Freeman resonance) are visible in both PEMDs. At two different relative phases, both PEMDs are appearing similar, and thus, further analysis is needed

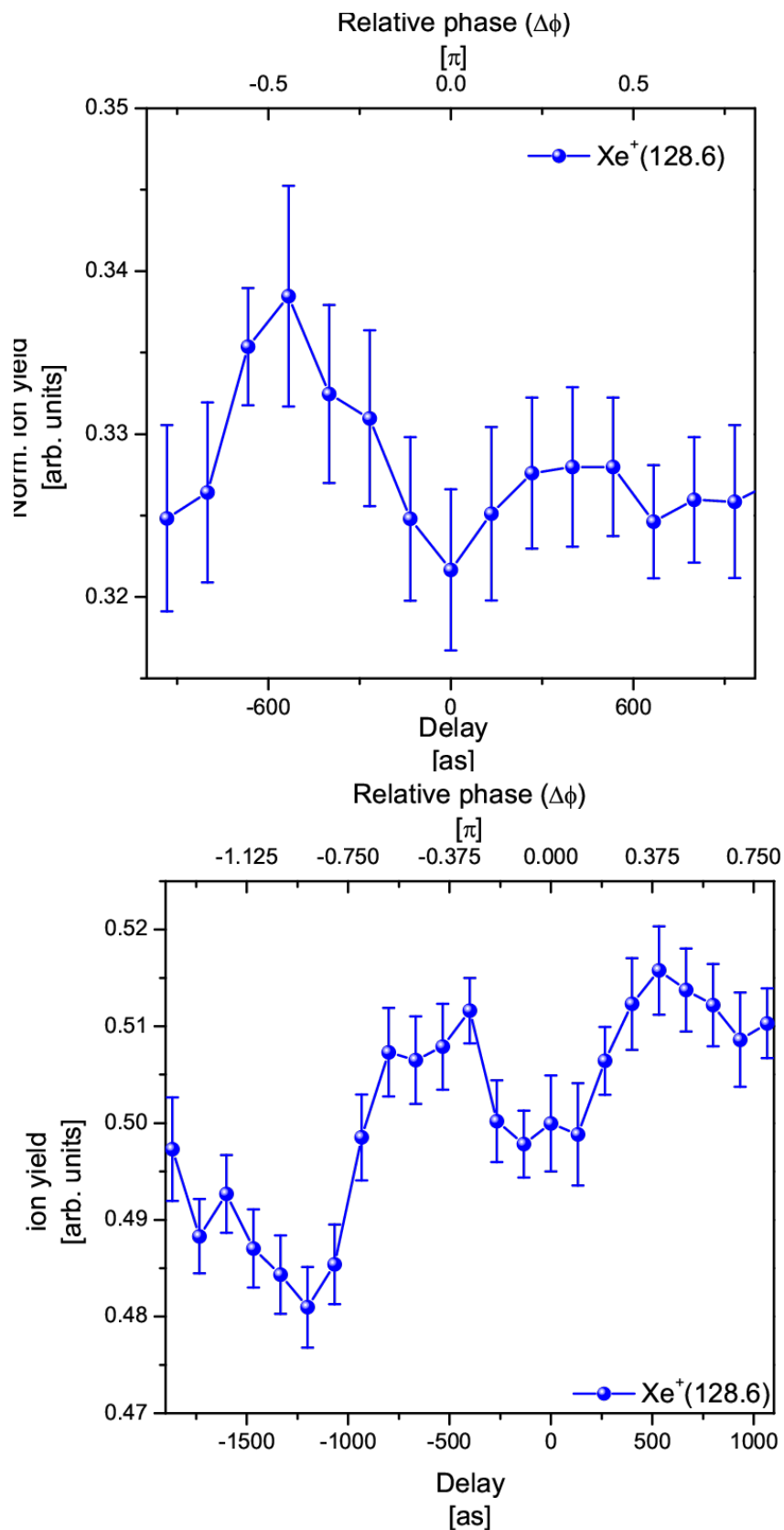


Figure 3.12: Xe<sup>+</sup> ions yield as a function of relative phase, at  $I_{800} = 0.09 \text{ PW}/\text{cm}^2$  and  $I_{400} = 0.03 \text{ PW}/\text{cm}^2$ . The polarization of FW and SH are parallel [top panel], and orthogonal [bottom panel].

to confirm that the relative phase affects the ionization rate and photoelectron yield. The total yield of photoelectrons is obtained by integrating the PEMD at a fixed relative phase. The photoelectron yield as a function of relative phase (delay between FW and SH) is represented in Figure 3.14. The red points are experimental results and the blue line is from Savitzky–Golay filter fitting. The photoelectron yield is oscillatory as a function of relative phase and it has a period of  $\pi$ , similar to Argon’s photoelectron yield. The observation supports the phase dependence on the ionization rate.

Next, we investigate the two-color effect on the photoelectron momentum distribution. The two-color PTC field may induce the asymmetry although it is not clear from figure 3.13. Thus, we performed the asymmetry parameter analysis. The asymmetry parameter is defined above in this chapter. The same formula has been used here to obtain the asymmetry parameter as a function of  $p_x$  or  $p_x$ .

The asymmetry parameter at relative phases 0 and  $\pi/2$  along  $p_x$  and  $p_y$  of PEMD is displayed in Figure 3.15. The asymmetry along  $p_x$  has a high variation, while the asymmetry along  $p_y$  is almost uniform. The low energy asymmetry within 0.3 a.u, along  $p_x$ , is possibly due to the two-color effect and the Coulomb effect on photoelectrons.

### 3.3.7 Two-color (OTC) induced Photoelectron Momentum Distribution: Xenon

The photoelectron momentum distribution of Xe induced by two-color (OTC) fields at 0.03 PW/cm<sup>2</sup> SH and 0.09 PW/cm<sup>2</sup> FW is shown in Figure 3.16. PEMD in the presence of SH [Top, left] shows few ATI rings, while the PEMD with FW [top, right] exhibits multiple ATI rings and also low-energy electron structures. The polarization of SH for the PEMD is perpendicular to the detector, while the polarization of FW is parallel to the detector. The intensity of 800 nm is sufficiently high enough to contribute to (9+1) photon ionization of Xenon [104]. In the two-color PEMD at phases 0 [bottom, left] and  $\pi/2$  [bottom, right], the electrons streaked due to the low SH field affect not only the low-energy

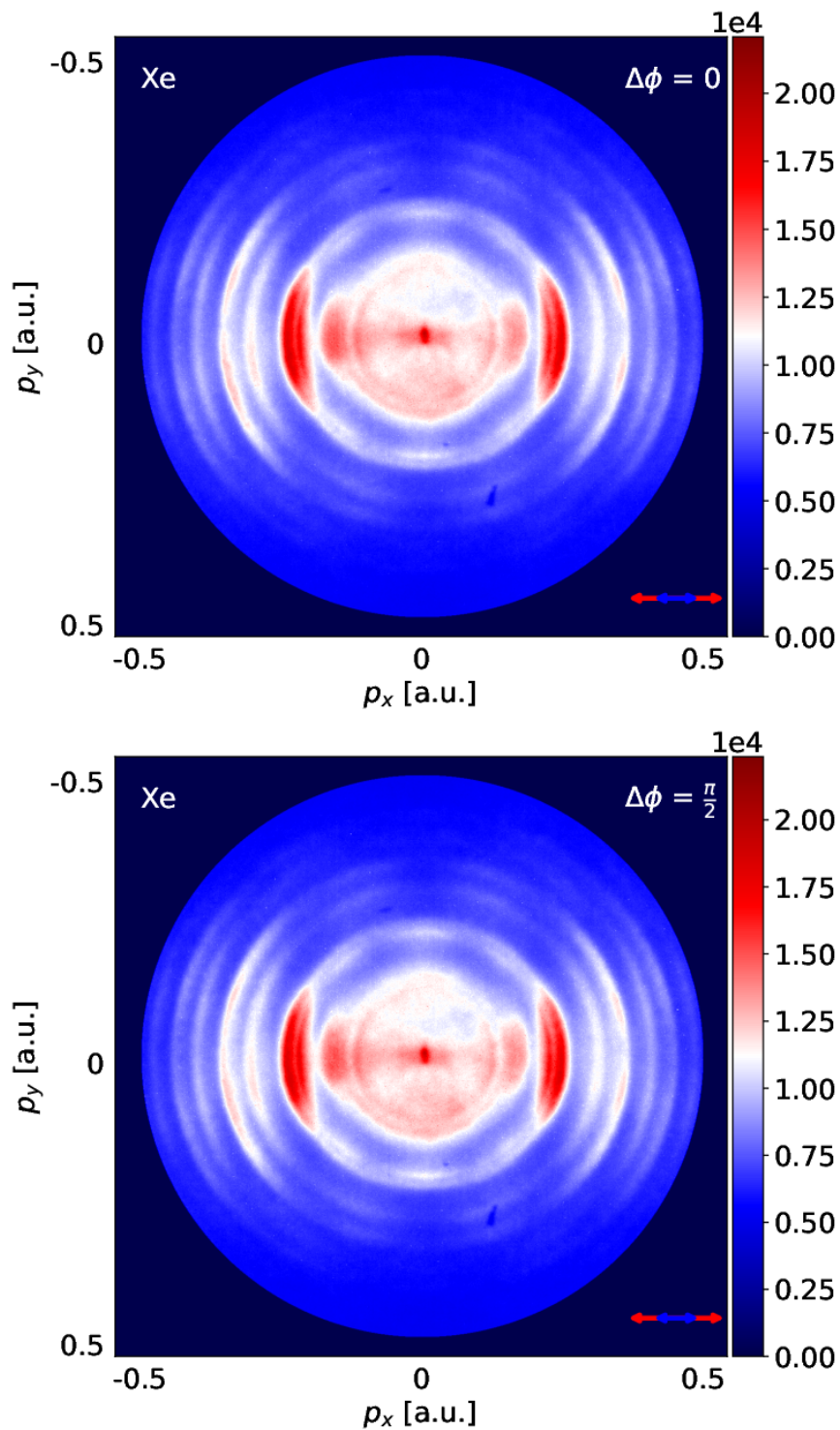


Figure 3.13: Photoelectron momentum distributions of Xe induced by Two-color parallel polarized field at laser intensity ratio of 3 ( $I_{FW}/I_{SH} = 3$ ), [top] at relative phase 0, [bottom] at relative phase  $\pi/2$ . Polarization of both fields was in the detector plane.

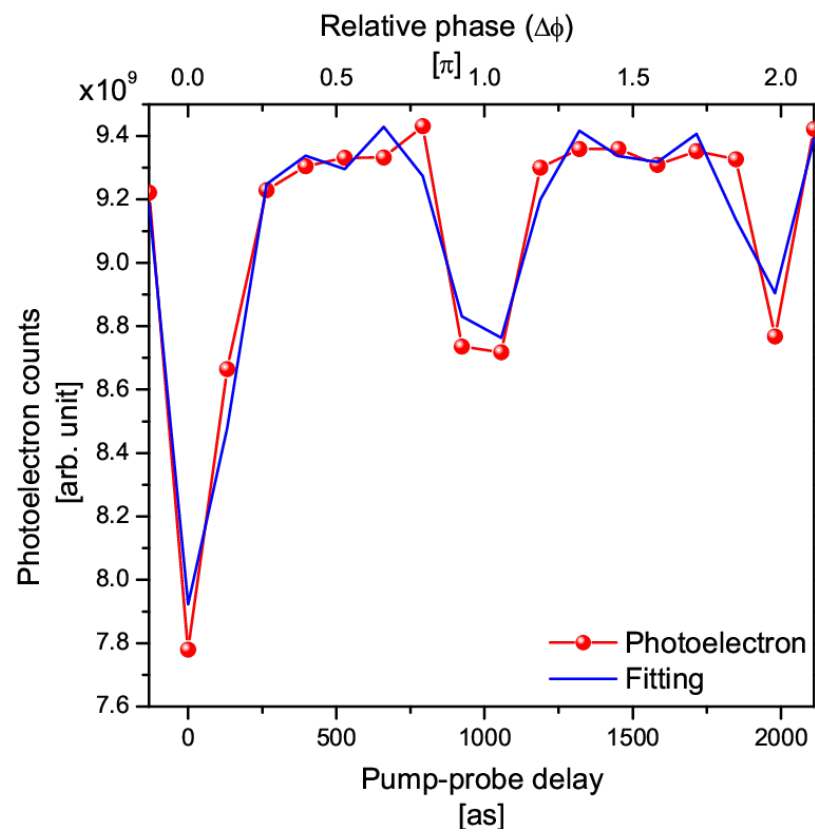


Figure 3.14: Photoelectron yield as a function of relative phase, at  $I_{800} = 0.09$   $PW/cm^2$  and  $I_{400} = 0.03$   $PW/cm^2$ .

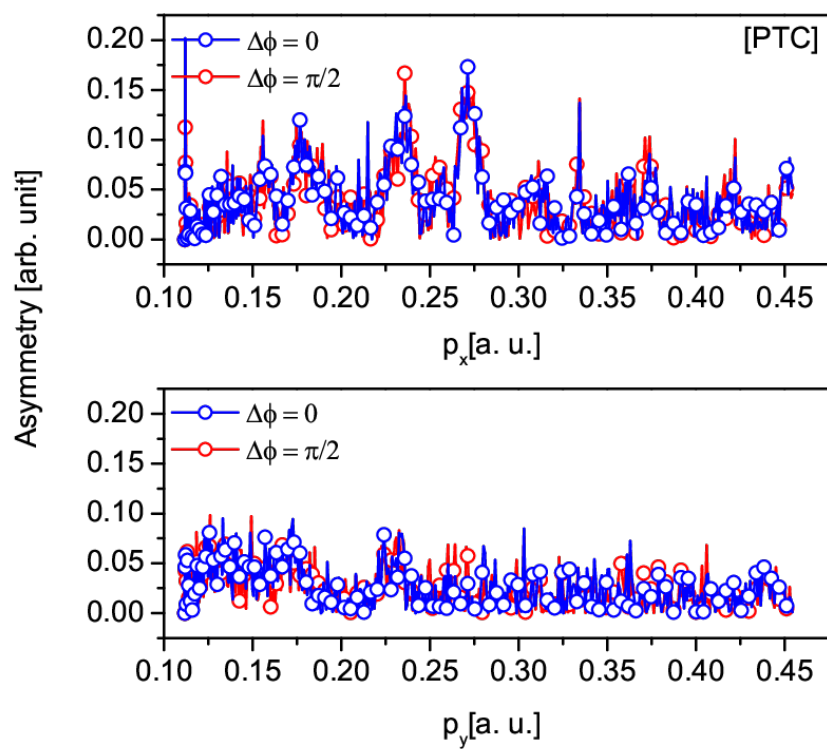


Figure 3.15: Asymmetry along  $p_x$  and  $p_y$  induced by two-color (PTC) field at 0 and  $\pi$  of relative phase.

structures but also the ATI distribution. The intensity of photoelectrons is high at relative phase  $\pi/2$  compared to 0, but the structure appeared similar. We now analyzed the photoelectron yield as a function of relative phase and also the asymmetry due to the two-color field.

The photoelectron yield as a function of relative phase or delay is presented in Figure 3.17. The delay is of the order of attoseconds. The yield is oscillating with a period of  $\pi$ , similar to previous findings on Argon.

Now, we analyzed the asymmetry parameter to know the possible asymmetry in photoelectron momentum distribution by OTC field.

The asymmetry parameter at a relative phase of 0 and  $\pi/2$  as a function of  $p_x$  or  $p_y$  are shown in Figure 3.16. Interestingly, the asymmetry along  $p_x$  is significantly modulated beyond 0.25 a.u. But the asymmetry along  $y$  is relatively constant. At a relative phase of 0 and at  $\pi/2$ , the asymmetry parameter variation is similar. The observed asymmetry along  $p_x$  or  $p_y$  is due to a two-color (OTC) induced effect on the photoelectron momentum distributions.

### 3.4 Summary and Conclusions

A study of two-color (PTC and OTC) laser fields induced photoionization of atoms (Argon and Xenon) is performed. In Argon, we investigated the ionization yield as a function of intensity and relative phase. We further investigated the photoelectron momentum distribution at two different phases and the photoelectron yield as a function of the relative phase. We observed that the photoelectron yield is oscillatory in nature and has a period of  $\pi$ . Further, a unique asymmetry variation along  $p_x$  and  $p_y$  is observed. The observed results are due to two-color fields and different than the single-color photoionization.

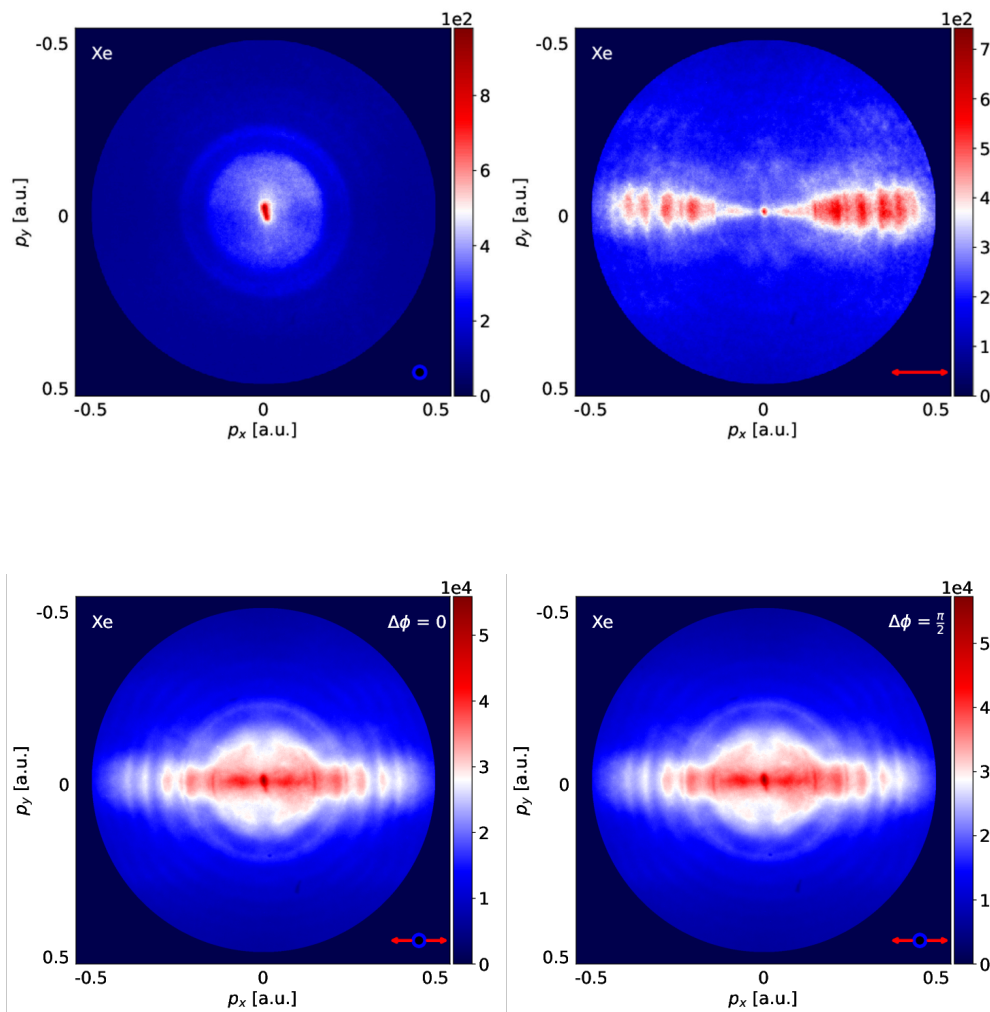


Figure 3.16: Photoelectron momentum distributions of Xe induced by FW (800 nm) [top, left], SH (400 nm) [top, right] and by Two-color orthogonally polarized field at laser intensity ratio of 3 ( $I_{FP}/I_{SP} = 3$ ), [bottom, left] at relative phase 0, [bottom, right] at relative phase  $\pi/2$ .

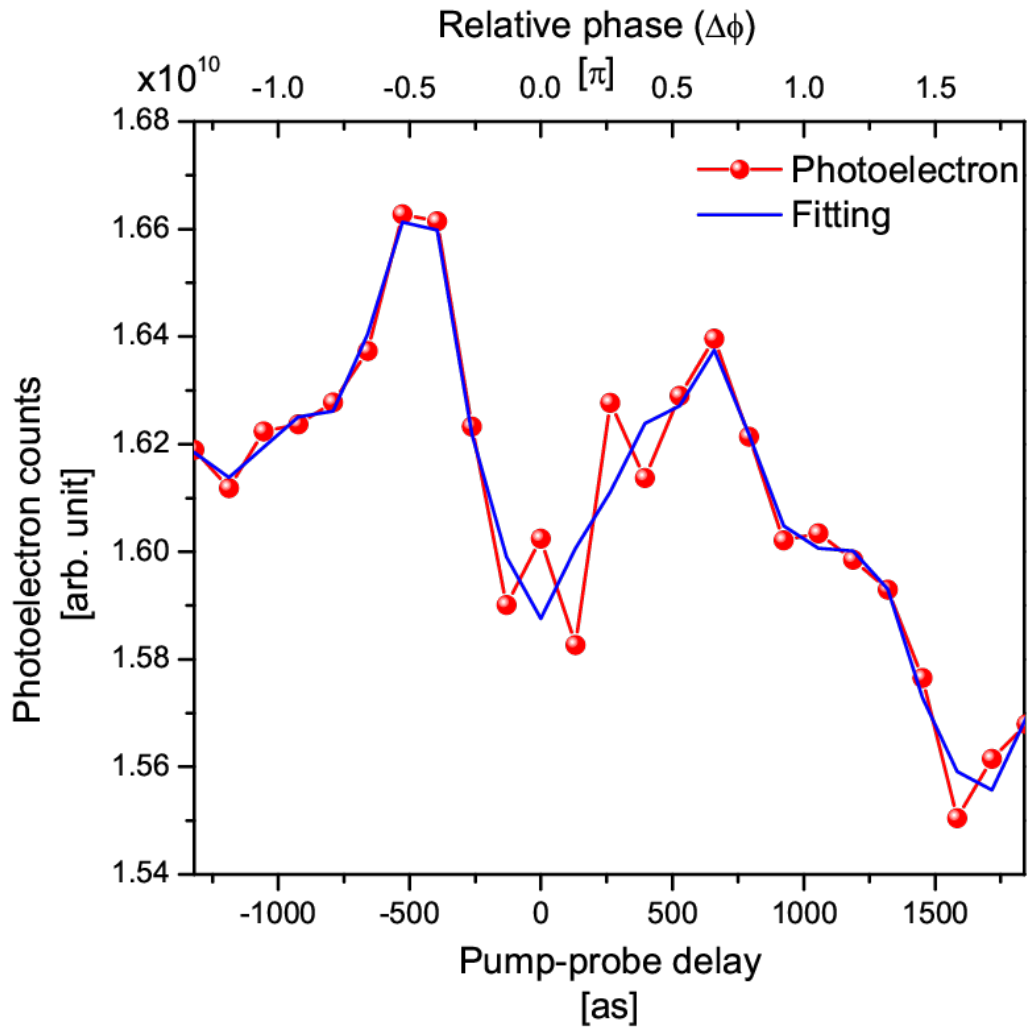


Figure 3.17: Photoelectron yield of Xe at intensities of FW and SH at 0.09 and 0.03 PW/cm<sup>2</sup> respectively, as a function of delay or relative phase between 800 nm and 400 nm. The polarizations of FW and SH are orthogonal to each other.

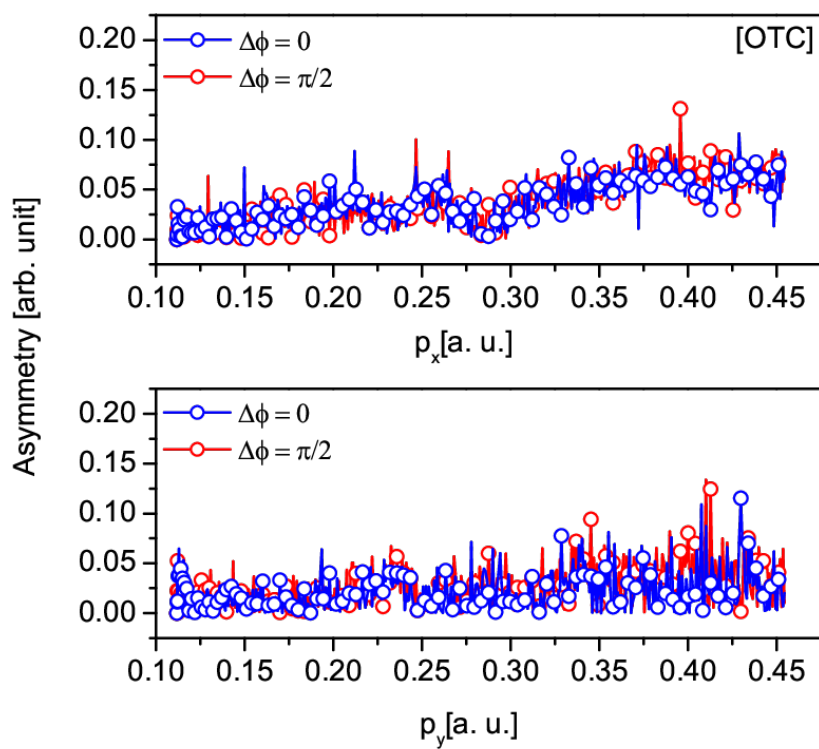


Figure 3.18: Asymmetry along  $p_x$  and  $p_y$  induced by two-color (OTC) field at 0 and  $\pi$  of relative phase.

# Chapter 4

## Single-color and two-color induced strong-field ionization of diatomic molecules: $\text{N}_2$ and CO

This chapter presents the new results on strong-field ionization of homo- and hetero-nuclear  $\text{N}_2$  and CO molecules using a two-color field. In this study, we have measured the ions yield as a function of relative phase at a fixed intensity ratio of Fundamental Wave (FW) and Second Harmonic (SH). Two-color fields may influence the revisiting electron trajectories, and the molecular structural effect like homo or hetero type of diatomic molecule may uniquely affect the revisiting electron. Thus we can see these effects in photoelectron momentum distribution. Further, the asymmetry in momentum distribution in  $\text{N}_2$  may differ from the asymmetry in CO due to the molecular effect and the two-color induced effect on trajectories. Detail study on these points is performed and reported in this chapter.

### 4.1 Introduction

Coherent control using two-color laser pulses to manipulate the nuclear and electron dynamics during strong-field ionization may modify the dissociative ion yield. This approach may also provide insights into the molecular structure, and

the tunneling process [105, 106, 107, 108]. The use of two-color laser pulses to shape the laser field has been described as an effective method for modulating electron dynamics through the control of the phase and amplitude of the fields. This technique has been shown to be successful in controlling electron-induced processes [44].

The electric field of the two-color field is the sum of both color fields. In the OTC two-color field case, the electric field is represented by  $\mathbf{E}(t) = E_0[f_1(t)\cos(\omega_1 t)\hat{\mathbf{z}} + \beta f_2(t)\cos(\omega_2 t + \Delta\phi)\hat{\mathbf{x}}]$ , where  $\beta$  is the relative electric field strengths and  $\phi$  is the relative phases between the two-color fields. The  $\omega_2$  can act as a control pulse or a probe with  $\beta < 1$ , while the ionization remained unaffected [109]. If  $\beta$  is comparable to one, and the intensity of  $\omega_2$  is high enough to ionize, the interplay of the two fields modulates the ionization. The asymmetric photoelectron momentum distribution in the presence of two-color fields is a function of the amplitude and the relative phase against the symmetric nature of the photoelectron momentum distribution in the presence of the single-color field. The electron trajectories interferences of direct and indirect electrons are perturbed by the presence of the second Harmonic field. The perturbation in the intracycle fringes can be controlled by the relative phase of the two color fields[105]. The tunneling process of the electron can be studied with orthogonal [109, 110] and parallel [111, 112] two-color fields. Quantum control of the molecular electron wavepackets by OTC streaking is reported here [88].

In this chapter, the study on two-color strong field ionization of homo- and hetero-nuclear diatomic molecules N<sub>2</sub> and CO is discussed. An ion yield study of the molecules as a function of intensity and phase of the FW and SH fields is studied in detail. The ionization and fragmentation of the molecules as a function of the kinetic energy of the returning electrons are studied thoroughly. The photoelectron momentum distribution and the asymmetry parameter analysis are performed for both CO and N<sub>2</sub>.

## 4.2 Two-color Experimental scheme

Two-color Strong field ionization of  $N_2$  and CO diatomic molecules are studied with a VMI spectrometer and a two-color pump-probe type setup. The detail of the VMI setup is discussed in the methodology chapter. Here we give the details of the scheme used in experiments like the data acquisition parameters, calibration, data analysis methodology, and simulation.

The experimental setup shown in Figure [4.1] consists of a laser system, a unit for generating  $\omega + 2\omega$ , and a spectrometer for ion and electron detection. The laser system used in this thesis was a Ti: Sapphire femtosecond laser, which generates ultra-short pulses of light with a central wavelength of 800 nm and a pulse duration of 26 fs. The laser had a maximum per pulse energy of 10 mJ and a repetition rate of 1 kHz. In the experimental setup, the laser beam was split into two paths. One path was used to pump an optical parametric amplifier (OPA) in order to achieve tunability in the infrared region. The remaining pulse was employed for a two-color photoionization experiment. The Carrier Envelope Phase (CEP) of the amplifier was not locked in this study. In addition to the laser system, the experimental setup included a module for generating  $\omega - 2\omega$  in a pump-probe configuration. This unit allowed us to study the electron dynamics in the molecule during strong-field ionization. A commercial pulse characterization setup known as a spectral phase interferometer (SPIDER) was used to continuously monitor the pulse width of the laser during the experiment. The pulse characterization of PRL's femtosecond laser has been reported recently [73] and also discussed briefly in the methodology chapter.

### 4.2.1 Two-color femtosecond laser fields

Two-color setup is shown in Figure 4.1([c]). The laser beam, FW (800 nm), is split using an 80:20 beam splitter. The 80% path is named as the probe, which can be delayed with respect to the 20% pump using a precision motorized linear stage. To control the laser power and polarization, a set of Half Wave Plate (HWP) and Polarizer (P) is used in both paths. A 100  $\mu\text{m}$  type-1 phase matching  $\beta$ -barium borate (BBO) crystal was used in the probe path for 400

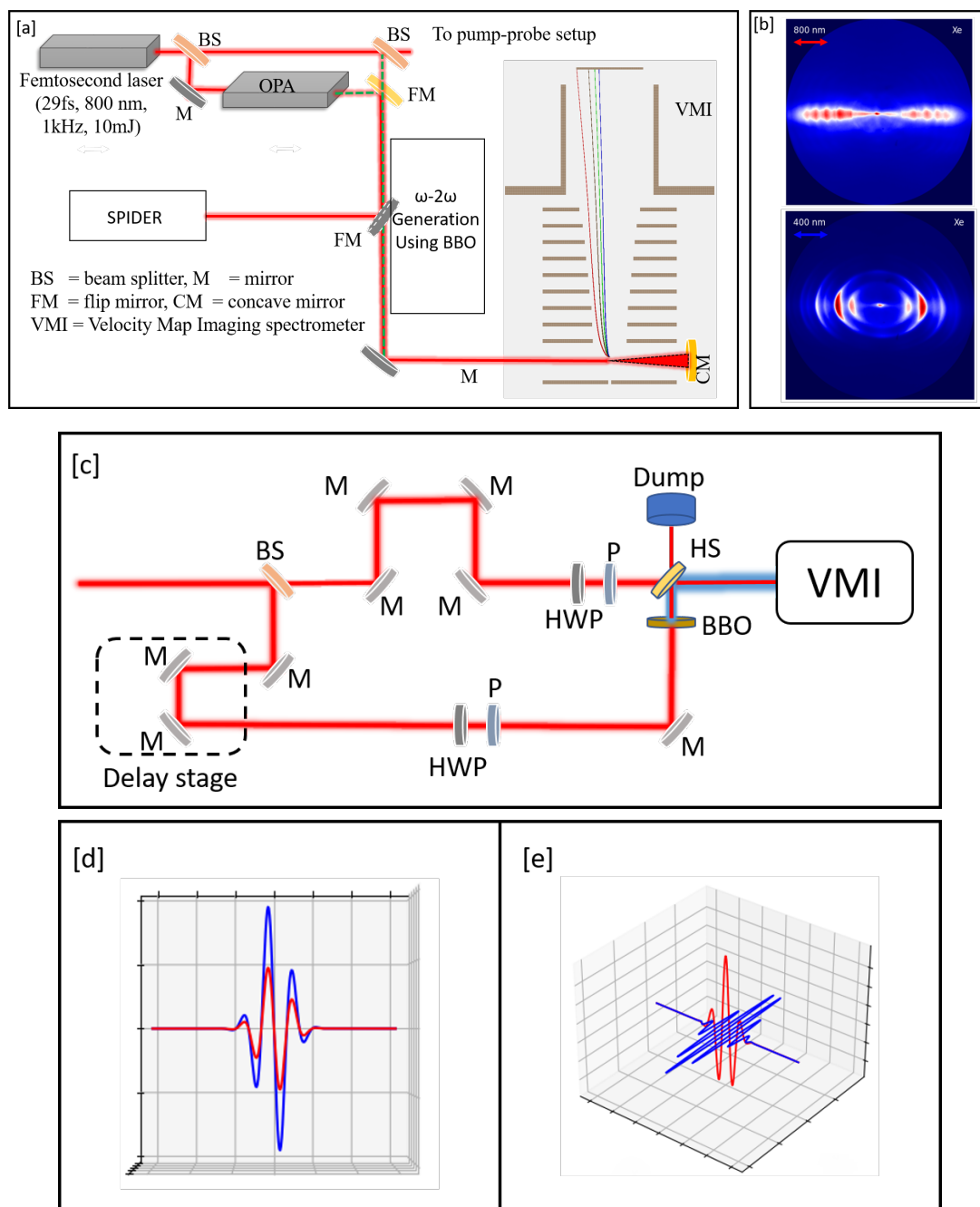


Figure 4.1: [a] An experimental setup scheme, [b] the photoelectron VMI spectrum of Xenon at 800 nm and 400 nm wavelength, [c] Two-Color (OTC) and Two-Color (PTC) laser pulses generation scheme, [d, e] pictorial sketch of OTC, and PTC laser fields. HWP: Half Wave Plate, M: Mirror, BBO:  $\beta$ -barium borate crystal, HS: Harmonic Separator.

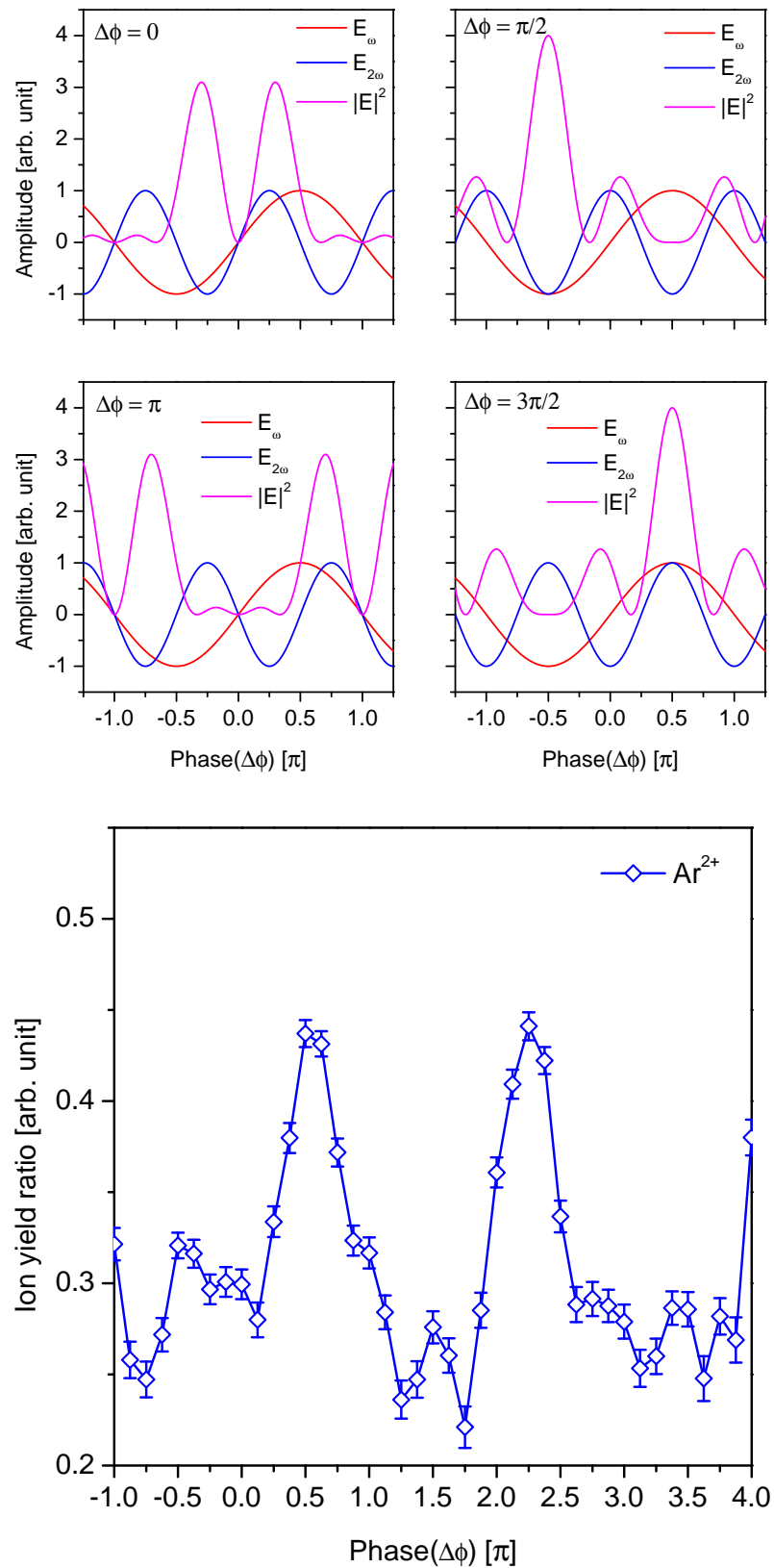


Figure 4.2: [Top][a] Electric field of 800 nm, (FW) (in red), 400 nm (SH) (in blue) and the intensity of the sum of the two-color fields (in pink) at phase delays between 0 and  $3\pi/2$ , [Bottom] The yield of  $\text{Ar}^{2+}$  as a function of the relative phase at intensity ratio  $I_{2\omega}/I_\omega = 1$ , where  $I_\omega = I_{2\omega} = 0.45 \text{ PW}/\text{cm}^2$ . The error bars are estimated from the observed counts.

nm generation. The 400 nm generation efficiency is about 12%. A harmonic separator (HS) is used for reflecting the 400 nm pulse and allowing the 800 nm pulse. After the HS, the 800 and 400 nm pulses are focused in the VMI spectrometer. The overlap between the probe and pump outside the vacuum chamber is achieved by the delay stage. This overlap is confirmed by measuring the third harmonic (266 nm) using an optical handheld spectrometer. Further, the overlap in the VMI chamber is confirmed by checking the TOF peak as a function of delay. By adjusting the individual polarizer of the 800 and 400 nm beams, the OTC and PTC laser fields are generated.

The VMI spectrometer is used to record the photoelectron distribution and the time-of-flight spectrum of photoions at different laser parameters. In VMI, the detector is a dual-stacked MCP with a phosphor screen (P47), and a scientific CMOS camera (PCO.EDGE 5.5) has been used to record the images from the phosphor screen. The MCP detector is maintained at a potential difference of 2000 V, and the phosphor-screen is maintained at 5250 V for bright and sharp images. For the time-of-flight spectrum measurement, a signal from the screen is taken through a homemade decoupler box and fed to the Roentdek FAMP and CFD 8c which converted to NIM signals. The NIM signals through lemo cables are sent to the TDC8HP (Roentdek) card, where they are read and binned. The triggering of the TDC8HP card for TOF measurements was done from the sync out of the femtosecond laser.

The gas chamber was maintained at  $5 \times 10^{-11}$  bar, and the Velocity Map Imaging (VMI) vacuum chamber was maintained at a pressure of  $4 \times 10^{-12}$  bar. During measurement, the pressure in the gas chamber was at  $5 \times 10^{-8}$  bar, and the VMI chamber was at about  $2 \times 10^{-10}$  bar.

The spot size and average power measurement were performed to estimate the laser intensity. The beam's spot size was 40  $\mu\text{m}$ , which was measured using the Gentec beam profiler.

The Parker valve was used to produce the supersonically cooled molecular beams. The valve was operated at 250 Hz having an orifice of 1 mm diameter. A skimmer of 1.01 mm orifice was installed in the zone of the silence of the molecular beam. Using a trigger signal, a delay was applied to the pulse valve

for overlapping the pulsed laser and molecular beams at the interaction region.

### 4.2.2 Data acquisition scheme

Data acquisition was performed with the TOF mode and the VMI mode of the VMI spectrometer. The TOF spectrum measurement was performed at various relative phases for OTC and PTC with the laser intensity ratio  $I_{SH}/I_{FW}=0.5$ , where  $I_{SH} = 0.23 \text{ PW/cm}^2$  and  $I_{FW} = 0.46 \text{ PW/cm}^2$ . At the same intensity, the photoelectron spectra are also measured and later analyzed.

### 4.2.3 Data analysis scheme

The time-of-flight (TOF) calibration was carried out using the strong-field ionization of Xenon. The ion yields of ionized  $\text{N}_2$ ,  $\text{CO}$ , and their fragments were obtained from the calibrated TOF spectrum by integrating the ion peaks. In the mass spectra of nitrogen, the peaks at  $m/q = 14$ , may represent either charged molecular ions  $\text{N}_2^{2+}$  or  $\text{N}^+$ . However, the broad full width at half maximum (FWHM) of these peaks suggests that they likely correspond to  $\text{N}^+$ . Further, the higher charged fragments from multiply ionized  $\text{N}_2$  are not observed in mass spectrum

In the experiment, the relative phase between 800 and 400 nm was achieved by using a pump-probe scheme. Time-of-flight measurements were recorded as a function of pump-probe delay, with a step size of  $20 \text{ nm} \pm 1 \text{ nm}$  ( $132 \text{ as} \pm 6.6 \text{ as}$ ) and a range of  $2 \text{ } \mu\text{m}$  ( $13.2 \text{ fs}$ ). Additionally, a photoelectron spectrum (VMI image) was recorded for 125000 shots/step as a function of pump-probe delay, using the same step size. The relative phase is assigned to the pump-probe delay.

Figure 4.2[left] shows the electric fields of the 800 nm and 400 nm and the intensity of both (sum of both colors) fields.

$$I = (|E_{0,800}\cos(\omega_{800}t) + E_{0,400}\cos(\omega_{400}t + \Delta\phi)|)^2 \quad (4.1)$$

Ionization by an intense laser field depends on the amplitude of the laser electric field [113], [114]. Further, in the case of two-color fields, the net

electric field is influenced by the relative phase of the FW and SH, peaking with a period of  $\pi$ . This period of  $\pi$  has been reported previously in the ionization of Neon. The ionization yield of Ne<sup>2+</sup> is reported to have oscillations having a period of  $\pi$ . Further, the yield is peaking at a relative phase of odd multiples of  $\pi/2$  [91]. This finding was also confirmed by tunneling theory [115].

To calibrate the relative phase, we performed the photoionization of Argon by two-color fields and measured the TOF spectra as a function of delay between FW and SH. The yield of Ar<sup>2+</sup> obtained by integrating the peak is plotted as a function of delay. The oscillation in ion yield at a delay of about 1.32 fs has been observed. We have calibrated the delay of this observed oscillation in terms of phase. The yield of Ar<sup>2+</sup> with the relative phase is shown in Figure [4.2][right]. Similarly to this, we have calibrated for the ion yield of N<sub>2</sub> and CO.

#### 4.2.4 Semi-classical tunnel electrons trajectory simulations: In two-color fields

We have simulated the tunnel electron trajectories in the two-color (OTC and PTC) fields and obtained the electron kinetic energy. The detail of the simulation scheme is discussed in the methodology chapter. Here, we briefly summarize the key equations used in the simulation for N<sub>2</sub> and CO. The femtosecond (ultrashort) pulse can be written as in the equation [4.2].

$$E_{field} = A \sin(\omega(\eta + t)) \cos^2(k\omega(\eta + t)) \quad (4.2)$$

where  $A$  is the electric field amplitude. The  $\omega$  is the angular frequency of the electric field, and the  $\eta$  represents the delay which can be introduced to the pulse. The  $\cos^2(k\omega t)$  represents the pulse envelope. The electron trajectories can be obtained by solving the equation of motion of an electron in a field [4.3]. In simulation, the Coulomb effect on the electron's trajectories is not considered.

$$m_e \frac{d^2y}{dt^2} = -eE_{field} \quad (4.3)$$

For two-color (orthogonally polarized, (OTC)) field, the equation [4.3]

can be rewritten as:

$$m_e \left[ \frac{d^2x}{dt^2} \hat{x} + \frac{d^2y}{dt^2} \hat{y} \right] = - \left[ [eA_{800} \sin(\omega_{800}(t + \eta_{800})) \cos^2(k_{800}\omega_{800}(t + \eta_{800}))] \hat{x} + [eA_{400} \sin(\omega_{400}(t + \eta_{400})) \cos^2(k_{400}\omega_{400}(t + \eta_{400}))] \hat{y} \right] \quad (4.4)$$

The electron's kinetic energy and the angle can be estimated by tracing the velocity along both components back to the origin. The kinetic energy of revisit electron  $E_{R,OTC}$  for the two-color (OTC) field is obtained using the equation [4.5], and the angle is defined as  $\tan^{-1}(\dot{y}/\dot{x})$ .

$$E_{R,OTC} = \frac{1}{2} m_e (\dot{x}^2 + \dot{y}^2) \quad (4.5)$$

For two-color (parallel polarized, (PTC)) field, the equation [4.3] can be written as:

$$m_e \left[ \frac{d^2y}{dt^2} \hat{y} \right] = - \left[ [eA_{800} \sin(\omega_{800}(t + \eta_{800})) \cos^2(k_{800}\omega_{800}(t + \eta_{800})) + eA_{400} \sin(\omega_{400}(t + \eta_{400})) \cos^2(k_{400}\omega_{400}(t + \eta_{400}))] \hat{y} \right] \quad (4.6)$$

The kinetic energy of revisit electron,  $E_{R,PTC}$  for the two-color (PTC) field can be obtained using the equation [4.7].

$$E_{R,PTC} = \frac{1}{2} m_e \dot{y}^2 \quad (4.7)$$

For trajectories simulations, we have computationally solved the equations [4.5] - [4.7] and obtained the kinetic energy and angle of revisiting electrons. Here, for the boundary conditions, the position of the electron and the momenta at ionization time (birth time) are assigned to be 0. The result of simulations of the two-color-induced modulation on electron trajectories are discussed in the

## 4.3 Results and Discussions

### 4.3.1 Two-color (PTC) fields induced ionization: intensity dependence on ion yield

The yield of N<sub>2</sub><sup>+</sup> and N<sup>+</sup> as a function of two-color (OTC) intensity ratio ( $I_{FW}/I_{SH}$ ) is shown in Figure 4.3. The intensity of SH ( $I_{SH}$ ) was 0.15 PW/cm<sup>2</sup> which was fixed throughout experiment and the intensity of FW ( $I_{FW}$ ) varied from 0.115 to 0.69. The yield of N<sub>2</sub><sup>+</sup> is increasing in range of 0.8 to 1.5 of intensity ratio, then decreasing till 2 and saturates beyond the 2.5 of intensity ratio. Interestingly, the yield of N<sup>+</sup> is always more compared to N<sub>2</sub><sup>+</sup>. It means that at the used intensity (0.15 PW/cm<sup>2</sup>), the ionized N<sub>2</sub> is in repulsive dissociate excited states which dissociates and produces more N<sup>+</sup> ions. Further, as intensity ratio is increasing, the yield of N<sup>+</sup> is increasing and peaking at around 2.5 of intensity ratio. Beyond, 2.5, the N<sup>+</sup> ion yield is decreasing. This observation is unique type and never reported earlier. The observation is possible to explain based on the processes involved at this laser intensity. The SH intensity is in MPI and FW intensity is in TI regime. Thus both ionization process are playing a role in excitation/ionization and fragmentation of ionized N<sub>2</sub>. Further, the tunnel electron travel in two-color field and revisit to the parent ion and may contribute in excitation/ionization.

The tunnel electron trajectory simulation for the electron trajectories in two-color (OTC) field is performed, discussed in Chapter 2. The revisiting KE is enough to further excite/ionized the N<sub>2</sub>. Most likely, at the intensity ratio of 2.5, the transfer of population from N<sub>2</sub><sup>+</sup> to doubly ionized N<sub>2</sub> is more due to electron revisit. This process is known as Non-sequential double ionization. As a result, the depletion of N<sub>2</sub><sup>+</sup> population is also expected which is clearly seen in the trend of N<sub>2</sub><sup>+</sup> yield. Beyond the 2.5 of ratio, the decreasing trend is possibly due to the further ionization/excitation which alter the fragmentation and reduce the production of N<sup>+</sup>.

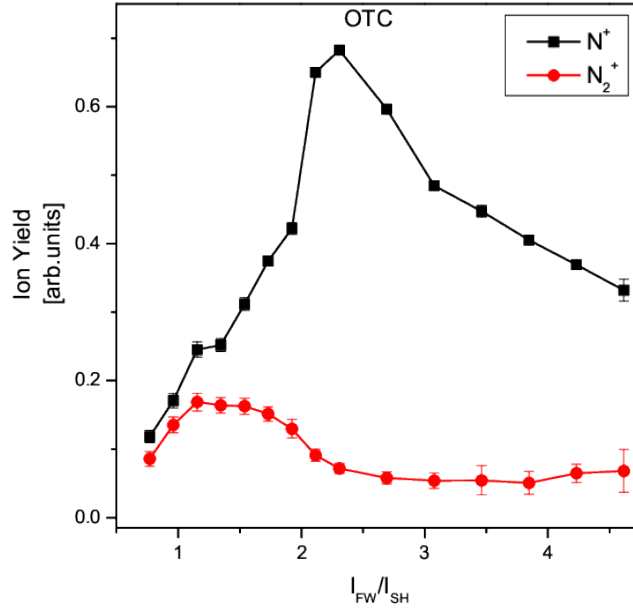


Figure 4.3: The yield of  $N_2^+$  and  $N^+$  ions with the ratio of FW to SH peak powers for OTC induced photoionization of  $N_2$ . At the ratio 1, the peak powers of FW and SH was maintained at  $0.149 \text{ PW/cm}^2$ .

The yield of  $CO^+$  and their singly and doubly charged fragments yield with variable intensity ratio is shown in Figure [4.4]. The  $CO^+$  yield trend is decreasing with increasing the intensity ratio. This trend is certainly different than the yield trend of  $N_2^+$ . Such trend variation is linked to the electronic structure of both molecules and revisiting electron induced processes. The  $O^+$  yield is more compared to  $C^+$ . Possibly, the  $1^2\Sigma^-$ ,  $2^2\Sigma^-$  of  $CO^+$  as well as the  $X^3\Pi$ ,  $3^3\Sigma^-$  are populated which produces  $O^+$  ions more in the ratio range of 0.8 to 4.0. Beyond this range, both the  $C^+$  and  $O^+$  yield is constant/saturates [116].

The doubly charged fragments ( $C^{2+}$  and  $O^{2+}$ ) yield with the intensity ratio is displayed in the bottom panel of the figure [4.4]. Interestingly, the  $O^{2+}$  yield is more compared to the  $C^{2+}$  yield. This trend is possibly due to recollision induced process populated the excited states multiply ionized CO which produces more  $O^{2+}$  in the intensity range of 0.8 to 3.5. Beyond this ratio, the  $O^{2+}$  yield start decreasing. It is interesting to see the rising trend of  $C^{2+}$  beyond 3.0 of intensity ratio, which indicates that the population in  $1\Pi$  and other states which producing the  $C^{2+}$  ions are as a function of intensity ratio [117].

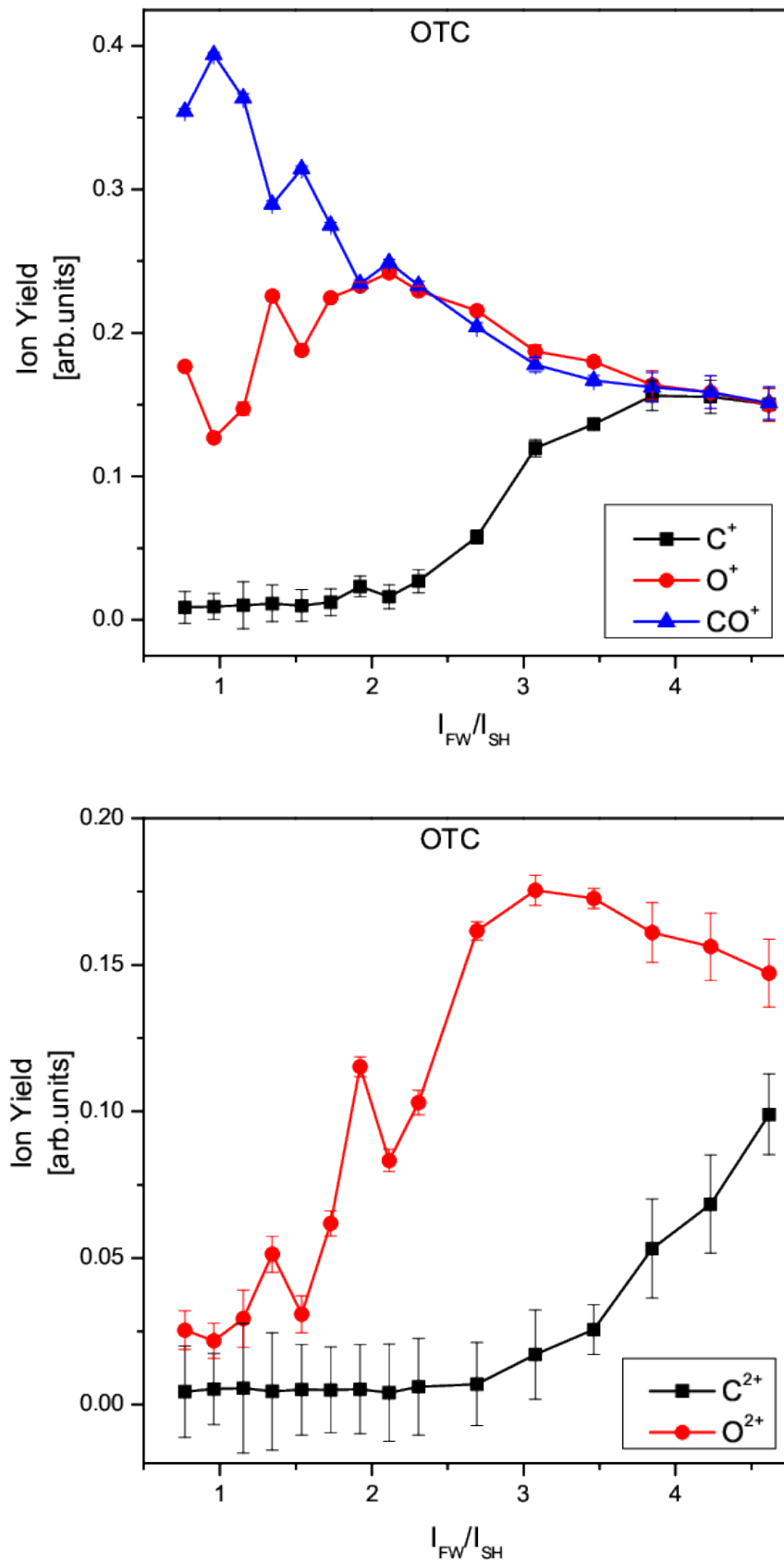


Figure 4.4: [top]The  $C^+$ ,  $O^+$  and  $CO^+$  ion yield and [Bottom]  $C^{2+}$ ,  $O^{2+}$  ion yields as a function of the ratio of FW to SH peak powers of OTC induced photoionization of CO. At the ratio 1, the peak powers of FW and SH was maintained at  $0.149 \text{ PW/cm}^2$

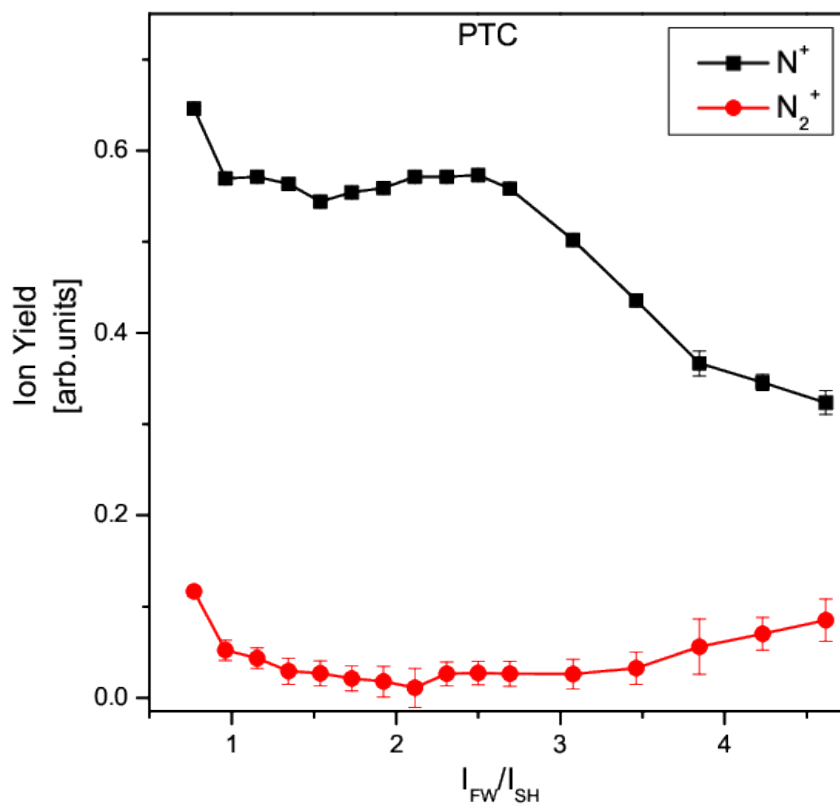


Figure 4.5: [The yield of  $N_2^+$  and  $N^+$  ions with the ratio of FW to SH peak powers of PTC induced photoionization of  $N_2$ .

The PTC induced photoionization of N<sub>2</sub> is investigated to see the role of intensity on the ionization and fragmentation trend. The intensity of SH ( $I_{SH}$ ) was 0.15 PW/cm<sup>2</sup> which was fixed throughout experiment and the intensity of FW ( $I_{FW}$ ) varied from 0.115 to 0.69 PW/cm<sup>2</sup>. The yield of N<sub>2</sub><sup>+</sup> and N<sup>+</sup> ions vs. the intensity ratio ( $I_{FW}/I_{SH}$ ) is presented in Figure 4.5. The N<sup>+</sup> yield is more about 5-times than the yield of N<sub>2</sub><sup>+</sup> in the range of 0.8-3.0 of intensity ratio. This high yield of N<sup>+</sup> suggest that that the used intensity is enough to populates multiple dissociative states which produces N<sup>+</sup> ions. As intensity ratio increases, the N<sup>+</sup> yield decreases and N<sub>2</sub><sup>+</sup> increases. This is expected as intensity of FW is decreasing and less dissociative states populates in ionized N<sub>2</sub>.

Interestingly, the N<sup>+</sup> and N<sub>2</sub><sup>+</sup> yield trend in the PTC is different compared to the OTC. We have simulated the tunnel electron trajectories and obtained the maximum KE of revisiting electrons at used intensity. We observed that the KE is more in case of PTC compared to OTC and thus it is expected that in PTC, the revisiting electron populates the dissociate states which produce more N<sup>+</sup>. The observed trend is due to electron revisit induced processes.

The intensity dependence PTC induced photoionization of CO<sub>2</sub> is investigated to see the role of intensity on the ionization and fragmentation trend. Here also, the intensity of SH ( $I_{SH}$ ) was 0.15 PW/cm<sup>2</sup> which was fixed throughout experiment and the intensity of FW ( $I_{FW}$ ) varied from 0.1 to 0.7 PW/cm<sup>2</sup>.

The singly ionized CO and its fragments (e. g. C<sup>+</sup> and O<sup>+</sup>) yields with the intensity ratio ( $I_{FW}/I_{SH}$ ) is shown in Figure 4.6. The CO<sup>+</sup>C<sup>+</sup>, O<sup>+</sup> and C<sup>+</sup> yield are more in 0.8 - 2.0 of intensity ratio. In this range, the O<sup>+</sup> yield is highest and other charged species like CO<sup>+</sup> and C<sup>+</sup> yield are comparable. This observation is due to the competing process like metastable CO<sup>+</sup> formation, the formation of more dissociative states of CO<sup>+</sup> by revisiting tunnel electron which produces these charged species. As the FW intensity decreases (intensity ratio increasing), the completing processes are not affected by the revisiting electron due to its low energy, which is not enough to excite or ionize the CO<sup>+</sup>.

The doubly charged fragments yields (C<sup>2+</sup> and O<sup>2+</sup>) with the laser intensity ratio is shown in the bottom panel of the figure 4.6. As expected, the yield of these fragments is low in the range of 0.8 - 2.0 of intensity ratio where

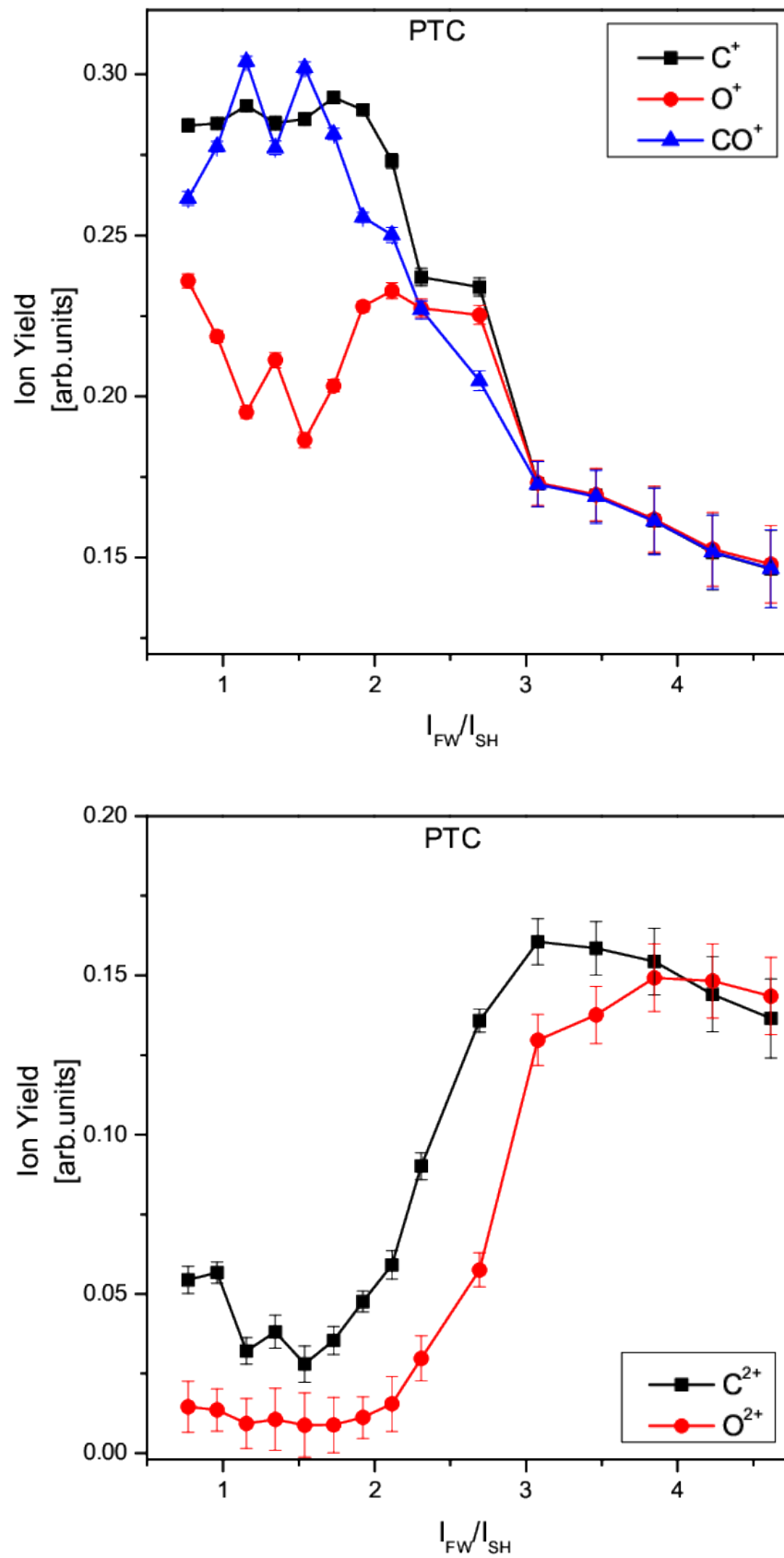


Figure 4.6: The  $C^+$ ,  $O^+$  and  $CO^+$  ion yield and [Bottom, right]  $C^{2+}$ ,  $O^{2+}$  ion yields as a function of the ratio of FW to SH peak powers of PTC induced photoionization of CO. At the ratio 1, the peak powers of FW and SH was maintained at  $0.149 \text{ PW/cm}^2$

singly charged species (CO<sup>+</sup>, C<sup>+</sup> and O<sup>+</sup>) yields are high (see top panel of the same figure). This trend is due to less formation of doubly or triply ionized CO which produces less doubly charged fragments. as intensity ratio increases, the yield of singly charged species decreases and doubly charged species increasing which means that the depletion of singly ionized states of CO and enhanced multiply ionization of CO.

### 4.3.2 Two-color (OTC) fields induced ionization: phase dependence on ion yield

The OTC induced photoionization of N<sub>2</sub> is discussed here. The yield of N<sub>2</sub><sup>+</sup> and N<sup>+</sup> ions at various relative phases are displayed in Figure [4.7] [top]. With peak intensities of I<sub>SH</sub> = 0.23PW/cm<sup>2</sup> and I<sub>FW</sub> = 0.46PW/cm<sup>2</sup>, this result was achieved at a laser intensity ratio (I<sub>SH</sub>/I<sub>FW</sub>) of 0.5. The oscillation has been observed as a function of the relative phase in the N<sub>2</sub><sup>+</sup> and N<sup>+</sup> ions yields. The period of oscillation is π. A similar oscillation has also been reported previously on N<sub>2</sub> molecule [118]. Interestingly, the parent (N<sub>2</sub><sup>+</sup>) and its fragment (N<sup>+</sup>) yields are anti-correlated, meaning that when the ion yield of one is low, the ion yield of the other is high. This "anti-correlated" yield trend has been experimentally checked and found to be reproducible.

The observed trend of inverse correlation between the yield of N<sub>2</sub><sup>+</sup> ions and N<sup>+</sup> fragment ions in this study is likely the result of the fragmentation of unstable N<sub>2</sub><sup>+</sup>, as described by equations [4.8, 4.9]. Previous research has shown that in photoionization experiments with a constant number density of molecules at the interaction region, the ion yields of a parent molecule and its fragments tend to be inversely related [119]. This trend is also observed in the current study. However, a different trend has been reported in other published research, with the ion yield of N<sub>2</sub><sup>+</sup> exhibiting an opposite relationship with the ion yields of N<sub>2</sub><sup>2+</sup> and N<sup>+</sup> at a laser intensity ratio of I<sub>SH</sub>/I<sub>FW</sub>=0.33 [118].



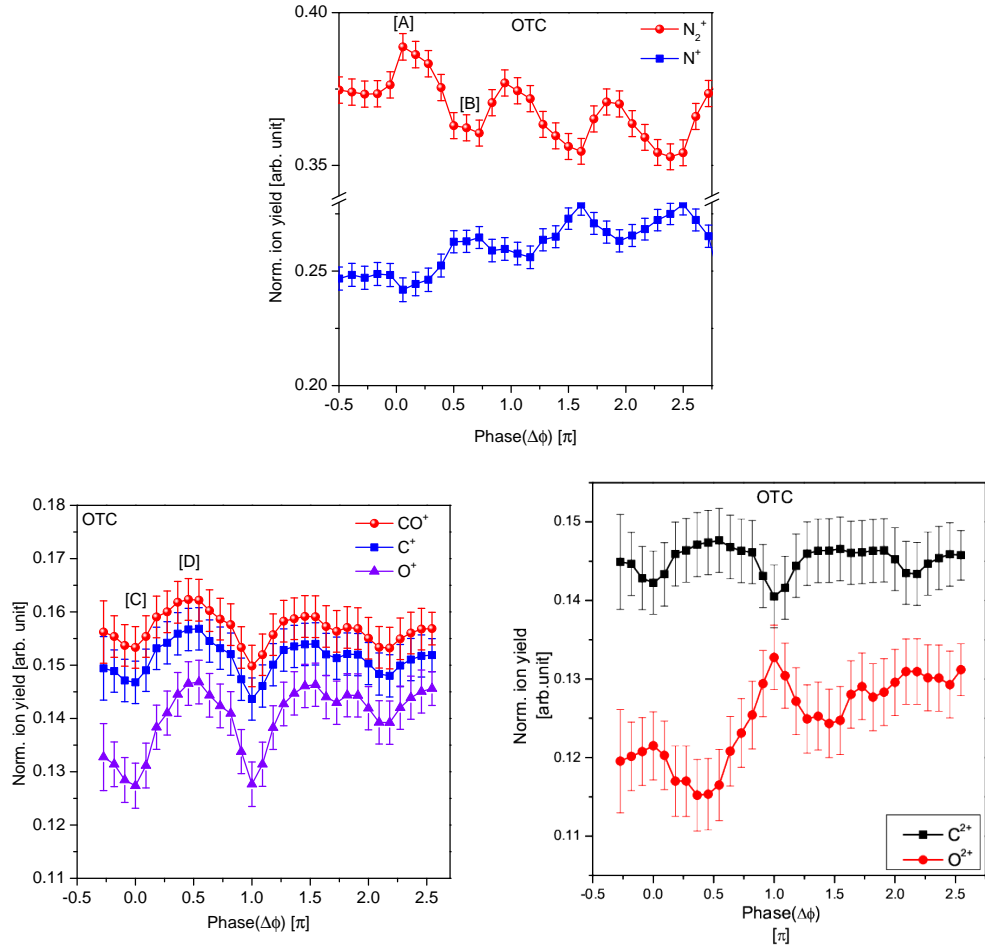


Figure 4.7: [top] The two-color laser field (OTC) induced photoionization of  $\text{N}_2$ . The yield of  $\text{N}_2^+$  and  $\text{N}^+$  ions is plotted as a function of the relative phase between the FW and SH. The intensity ratio in this experiment is  $I_{SH}/I_{FW} = 0.5$ . [bottom] The two-color laser field (OTC) induced ionization of  $\text{CO}$ . The yield of  $\text{CO}^+$ ,  $\text{C}^+$ , and  $\text{O}^+$  ions is plotted as a function of the relative phase between the FW and SH. The intensity ratio in this experiment is also  $I_{SH}/I_{FW} = 0.5$ .

In this study, the modulation depth (amplitude of oscillation) of ion yields was determined by fitting a Gaussian curve to a peak using Origin 7.0 software. The results showed that the modulation depth at an intensity ratio of  $I_{SH}/I_{FW} = 0.5$  was about 7-times greater than the modulation depth reported at an intensity ratio of  $I_{SH}/I_{FW} = 0.33$  in a previous study [118]. This suggests that the modulation depth of ion yields depends on the intensity ratio of the fundamental wave (FW) and the second harmonic (SH).

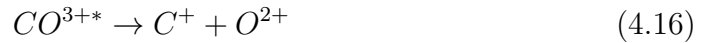
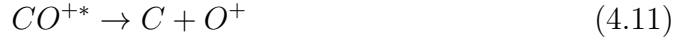
The bottom left panel of Figure [4.7] shows the ion yields of fragments C<sup>+</sup> and O<sup>+</sup> alongwith CO<sup>+</sup> with the variation of relative phase, induced by two-color laser field (OTC) at the same intensities of the fundamental wave (FW) and second harmonic (SH) used in the study of N<sub>2</sub>. The C<sup>+</sup> and O<sup>+</sup> ions can be formed through dissociation reactions of singly or doubly ionized CO, as described in equations [4.10 - 4.14]. Like N<sub>2</sub>, the ion yields of CO<sup>+</sup> and its fragments oscillate with a period of  $\pi$ .

The bottom left panel of Figure [4.7] shows the ion yields of CO<sup>+</sup> and its singly charged fragments C<sup>+</sup> and O<sup>+</sup> as a function of relative phase, induced by two-color laser field (OTC) at the same intensities of the fundamental wave (FW) and second harmonic (SH) used in the study of N<sub>2</sub>. The ion yield of O<sup>+</sup> is lower (6%) compared to the C<sup>+</sup> yield, which can be attributed to the dissociative energies of the pathways leading to their formation. The dissociation energy of pathway (4.10) is about 22.369 eV, while the dissociation energy of pathway (4.11) is about 24.727 eV [120]. The significant difference in dissociation energy likely contributes to the higher fragmentation yield of C<sup>+</sup> over O<sup>+</sup>. The modulation depth of CO<sup>+</sup> and C<sup>+</sup> is about 5-7%, while the modulation depth of O<sup>+</sup> is about 3 times higher than that of CO<sup>+</sup>.

Doubly charged fragments such as C<sup>2+</sup> and O<sup>2+</sup> from doubly or multiply ionized CO have been observed in the TOF-spectrum of CO. Interestingly, at the same laser parameters, a doubly charged fragment like N<sup>2+</sup> is observed in the case of N<sub>2</sub>. This is likely due to the high Ionization potential of N<sub>2</sub> [IP: 15.58 eV] compared to CO [IP: 14.07 eV]. The doubly charged fragments yield of CO is shown in [Figure [4.7](bottom, right)]. Oscillation in the yield of C<sup>2+</sup> and O<sup>2+</sup> with the relative phase is visible in this plot and has a period of  $\pi$ . The oscillation

of  $C^{2+}$  yield has modulation depth of about 3-5%, and the modulation depth of  $O^{2+}$  oscillation is 5-7 %. Interestingly the yield of  $O^{2+}$  is lower compared to  $C^{2+}$ . This infers that the probability of  $O^{2+}$  formation through equation [4.14] from various excited states of  $CO^{2+}$  and also from triply ionized CO is less compared to the  $C^{2+}$  formation from through equation [4.13] and triply ionized CO molecules.

Figure [4.7] tell us that all ionic species are sensitive to relative phase, which suggest that the two-color field can be used to control the yield of dissociative reactions.



In these equations, the " \* " on ions represents the unstable ions.

Now, we study the two-color (PTC) field-induced ionization  $N_2$  and CO. The ions yield vs. the relative phase at intensity ratio of  $I_{SH}/I_{FW} = 0.5$  is shown in the figure [4.8]. As the FW electric field and SH electric field are in the same plane in the PTC but not in OTC, the resulting field along their polarization is stronger than in OTC. Interestingly, the  $CO^+$  and  $N_2^+$  yield trend oscillation have a period of  $\pi$ .  $N_2^+$  has a modulation depth that is over 1.5 times greater than  $N^+$ . As in the case of OTC, the parent and its fragment yield continue to exhibit an anti-correlation pattern. In Figure [4.8] [top] at  $1.1 \pi$ , a point from the oscillation trend deviates, which is possibly due to an experimental artifact. This is based on the fact that a similar deviation was not observed in other oscillations beyond  $2\pi$  of relative phase (not shown here).

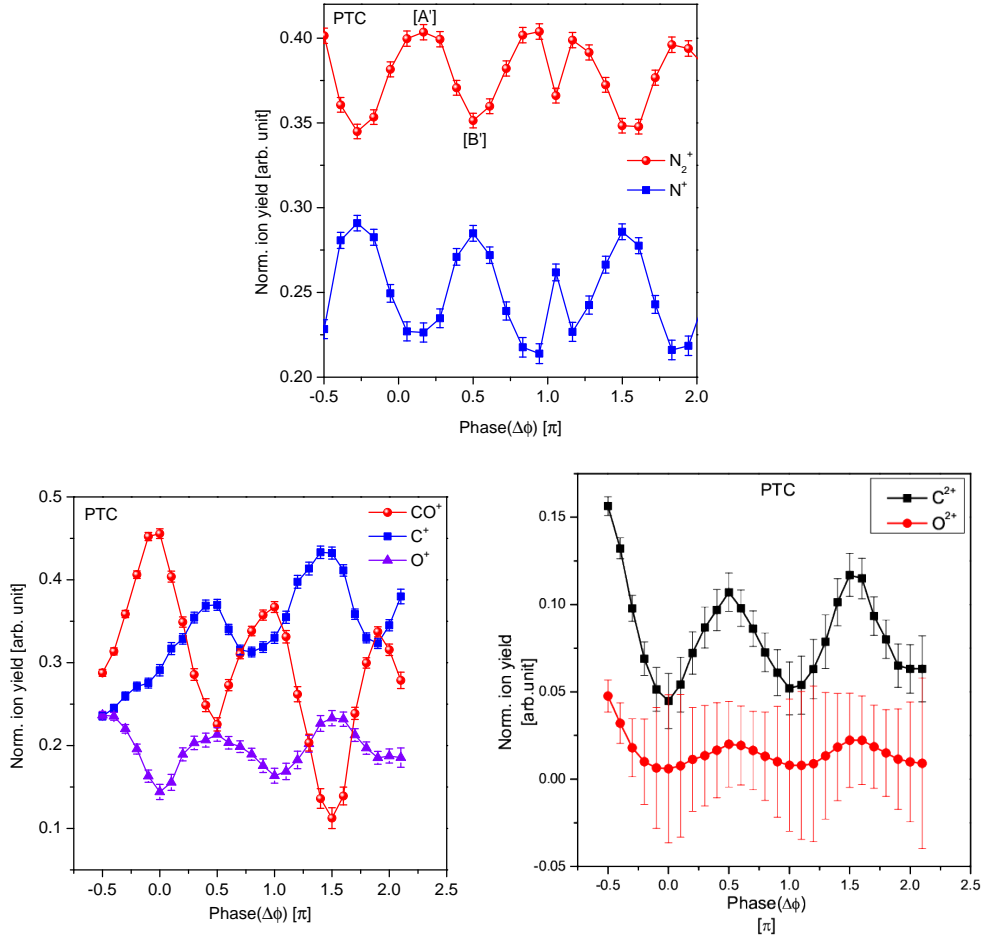


Figure 4.8: Two-color photoionization of N<sub>2</sub> and CO with parallel polarization and  $I_{SH}/I_{FW}=0.5$ . Both FW and SH polarizations are kept parallel to the detector plane. [left] Normalized N<sub>2</sub><sup>+</sup> ion yield as a function of the relative phase between SH and FW, [right] Normalized CO<sup>+</sup> ion yield as a function of the relative phase between SH and FW in units of degrees.

Figure [4.8](bottom, left)[121] displays the ions CO<sup>+</sup>, C<sup>+</sup>, and O<sup>+</sup> yield with the relative phase. Unexpectedly, an unique trend in the C<sup>+</sup> ion yield in the relative phase from  $-0.5\pi$  to 0 has been found. This trend deviates from the O<sup>+</sup> trend in the specified range, is possibly due to the low contrast in ion yield. It is interesting to note that the C<sup>+</sup> and O<sup>+</sup>'s ion yields are anti-correlated with CO<sup>+</sup>. The estimated modulation depth for CO<sup>+</sup> is about 60%. The modulation depth for fragments ions such as C<sup>+</sup> and O<sup>+</sup> are about 20-30 %.

The C<sup>2+</sup>, and O<sup>2+</sup> yield trend is shown in Figure [4.8](bottom, right). An oscillation with period of  $\pi$  is observed in the yield of C<sup>2+</sup>, and O<sup>2+</sup>. Further, the O<sup>2+</sup> yield is lower compared to the C<sup>2+</sup>, which is possible when the formation

probability of  $O^{2+}$  from various channels is low compared to the formation of  $C^{2+}$ . The modulation depth of  $C^{2+}$  is 1.4 times more than that of  $O^{2+}$ .

Oscillations in  $N_2^+$  and  $N^+$  yield are constant over the relative phase range. On other hand, the yield of  $CO^+$  is decreasing and the  $C^+$  and  $O^+$  yields are increasing. This trend of CO is possibly due to the two-color field effect on the ionization. Recent theoretical CO calculations conclude that the HOMO orbital is principally responsible for the two-color ionization [122]. The orbitals' contributions at the applied intensities may be the cause of the observed trend in CO. The SH intensity is  $0.23 PW/cm^2$ . The Keldysh value  $\gamma$  at this intensity is 1.43. Thus, the SH is in the multiphoton ionization (MPI) regime. The FW intensity is  $0.46 PW/cm^2$  which is in the tunneling region ( $\gamma = 0.51$ ). Thus, in two-color ionization, both fields contribute differently to the ionization of CO, and relative phase or intensity affects the fragmentation and the yield trend of  $CO^+$ ,  $C^+$ , and  $O^+$  ions.

In this study, it was found that the ion yields of  $N_2^+$  in OTC and PTC are similar, with comparable modulation depths. However, the  $CO^+$  yield in PTC was observed to be at least three times higher than in OTC, which suggests that the electric field may influence the recollision of electrons in the same plane, leading to an increased degree of ionization. Additionally, the yields of  $C^+$  and  $O^+$  ions in OTC were found to be correlated with  $CO^+$ , but this trend was not observed in the case of PTC. Also, the sensitivity of ion yields to the relative phase of the two-color field and the potential impact on photoelectron trajectories produced during ionization.

The results of the simulations on the revisiting electron kinetic energy in the two-color field are shown in the figure 4.9. In the case of a single-color (FW) field, the electron kinetic energy is about 83 eV (not including the binding energy of CO or  $N_2$ ). In the two-color field, the revisiting electron kinetic energy increases by about 50-65% in the case of a parallel two-color field (PTC) and 8-15% for the perpendicular two-color field (OTC). This increased revisiting electron energy can lead to further ionization of the parent ion through nonsequential double ionization (NSDI) or recollision-excitation-with-subsequent-ionization (RESI). These processes enhance double/multiple ionization and deplete the sin-

gle ionization rate of molecules, potentially affecting the fragmentation yield as the population of repulsive dissociative states is impacted by the revisiting electron-induced processes. The observed anti-correlation trend in N<sub>2</sub> with OTC (Figure 4.7, left) and in CO and N<sub>2</sub> with PTC (Figure 4.8) is likely due to the enhancement of double/multiple ionization followed by fragmentation and the depletion of single ionization yield. The low electron energy in the OTC case may not be sufficient to enhance double/multiple ionization and deplete the single ionization rate. It is worth noting that the available multiple curve crossings [123] in the potential energy curve of CO<sup>+</sup> and CO<sup>2+</sup> may impact the population in repulsive dissociative states, potentially leading to the observed correlation trend in CO with OTC. In PTC, the electron energy is high enough to overcome the effect of curve crossings, leading to different yields in OTC and PTC as a function of relative phases. The simulated results in Figure 4.9 suggest that the probability of revisiting-induced ionization is higher at a relative phase of  $\pi/2$  compared to a relative phase of 0, supporting the observed yield trend. In the case of OTC, simulation results show that fewer trajectories revisit at a relative phase of 0 compared to  $\pi/2$ , which is reflected in the observed ion yield.

The next section discusses the two-color field's effects on the photoelectron momentum distribution of N<sub>2</sub> and CO.

### 4.3.3 Two-color induced ionization: Photoelectron momentum distributions

The photoelectron momentum distributions (PEMDs) of N<sub>2</sub> and CO induced by OTC at a laser intensity ratio ( $I_{SH}/I_{FW} = 0.5$ ) with peak intensities of  $I_{SH} = 0.23$  PW/cm<sup>2</sup> and  $I_{FW} = 0.46$  PW/cm<sup>2</sup> are shown in Figure [4.10]. The PEMD at a relative phase of 0 is shown in the top left panel, while the PEMD at a relative phase of  $\pi/2$  is shown in the bottom left panel. Similarly, the PEMDs at relative phases of 0 and  $\pi/2$  for CO are shown in the top right and bottom right panels, respectively. At a relative phase of  $\Delta\phi = 0$ , the N<sub>2</sub> molecule has a lower ionization probability as the electric field directions of the FW and SH are in opposite directions, resulting in destructive interference of the streaking

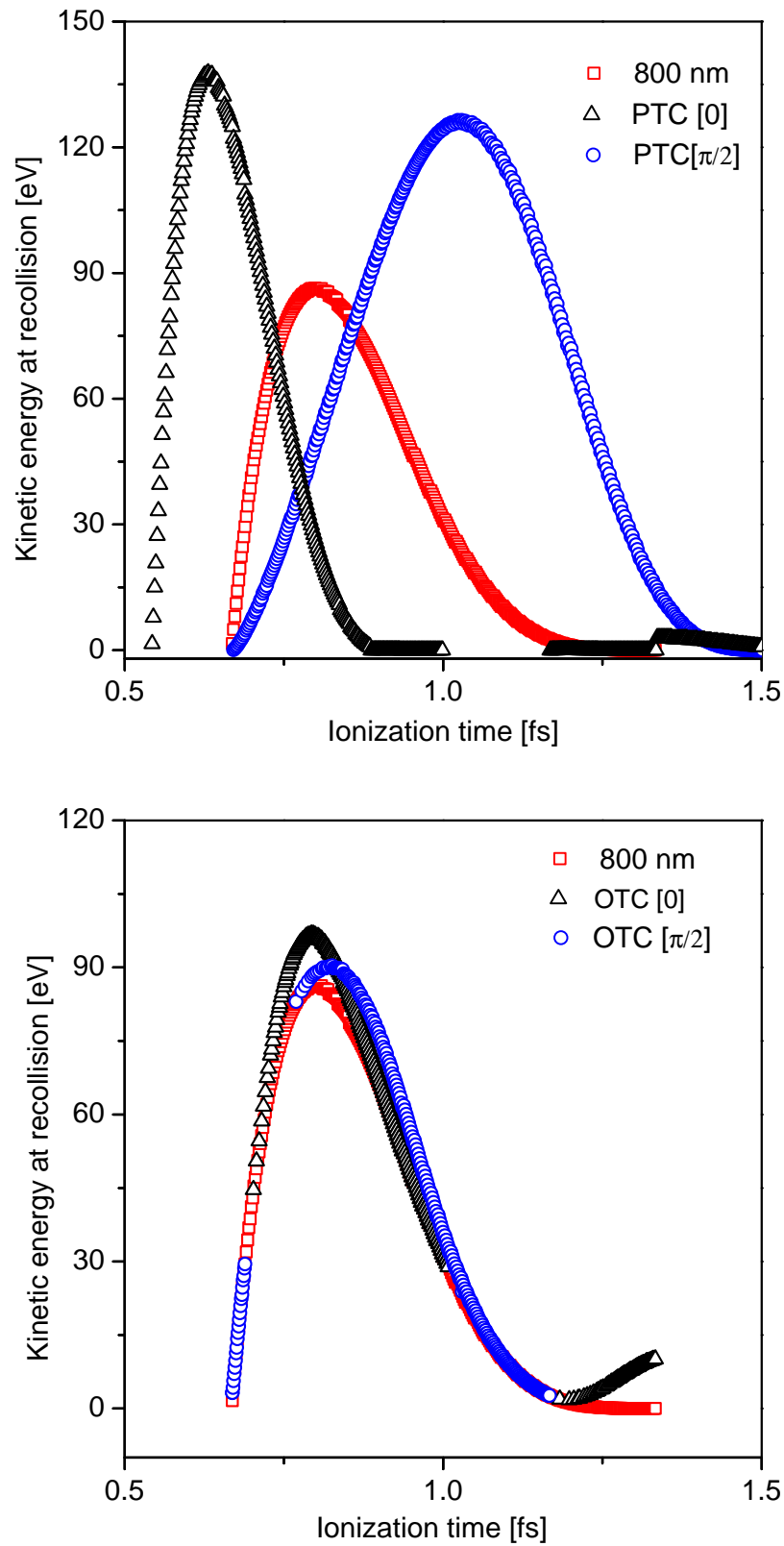


Figure 4.9: Classical electron trajectories simulation in the OTC and PTC field. [top] Revisiting electron kinetic energy as a function of birth time for PTC, [bottom] Revisiting electron kinetic energy as a function of birth time for OTC. Color/curve and relative phase in OTC or PTC are self-explained.

electron. However, at a relative phase of  $\pi/2$ , the electric fields are in the same direction, facilitating the interference of the electron and increasing the ionization probability [88]. The interference of electrons also depends on the alignment of the molecule and the contribution of molecular orbitals to ionization [124]. The electron momentum distributions induced by a two-color field can also be influenced by homo- and hetero-nuclear diatomic molecules, such as N<sub>2</sub> and CO [125], [126].

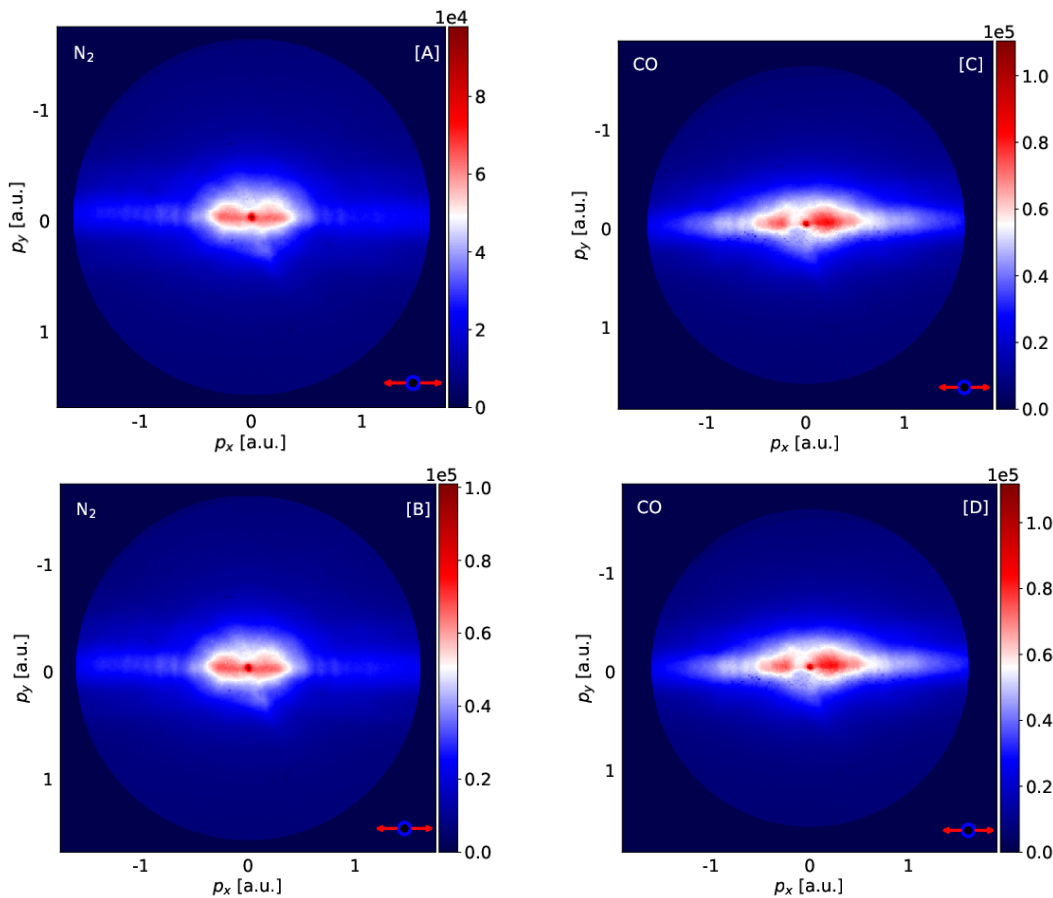


Figure 4.10: Two-color (OTC) induced photoelectron momentum distributions of CO and N<sub>2</sub> at  $I_{SH}/I_{FW} = 0.5$ , [top] PEMD at relative phase 0, [bottom] PEMD at relative phase  $\pi/2$ . In PEMD, visible dark spots are due to defects in the detector, should be ignored. The red arrow is parallel to the detector plane, and the blue circle is perpendicular to the detector plane.

The measured PEMD at the relative phase ( $\Delta\phi$ ) of 0 or  $\pi/2$  appears identical in N<sub>2</sub> or CO, indicating that the two-color field influence on PEMD is not significant at the used intensity ratio. On the other hand, a definite distinction between the PEMD of N<sub>2</sub> and the PEMD of CO has been noted.

This variation in PEMD may be caused by molecule orbital contributions, site-specific electron emissions and their trajectory variation in a two-color field, as well as molecular alignments [124], [127]. Furthermore, as demonstrated in a prior study using the two-color approach [44], the Coulomb potential might influence electron trajectories.

Our simulation shows that the two-color field influences the electron re-visit trajectories, which could lead to an asymmetry in the distribution of photoelectron momentum. Recently, the asymmetry in doubly differential momentum distributions for atoms (such as Argon) has been investigated theoretically and experimentally [128], while for  $\text{H}_2^+$  molecules, the asymmetry in photoelectron distribution is obtained using conventional trajectories, and TDSE simulations [129]. Here, we have examined the asymmetry parameter, which is defined in equation [4.17], to gain a knowledge of the impacts of two-color fields on the PEMD. Two-color induced asymmetry along  $p_x$  evaluated at  $p_y = 0$ , and vice versa for asymmetry along  $p_y$ . The asymmetry is determined by selecting one pixel along the x-axis to the right of the center with intensity  $I_X$  and a matching equidistant pixel to the left with intensity  $I_{X'}$ .

$$\text{Asymmetry}(p_x) = \frac{I_X - I_{X'}}{I_X + I_{X'}} \quad (4.17)$$

Figure [4.11] shows the OTC induced asymmetries in  $p_x$  and  $p_y$  at the relative phase 0 and  $\pi/2$  in  $\text{N}_2$  and CO. The detection efficiency correction as a function of the position is not performed in present study. The same detector parameters are used for the measured PEMDs for OTC/PTC. The measured asymmetry parameter in  $p_x$  and  $p_y$  exhibits the same pattern at 0 and  $\pi/2$ . We noticed that there is not much change in the asymmetry parameter between 0 and  $\pi/2$ . our observed finding is consistent with previously published research [130] work. The asymmetry parameter's modulation along  $p_x$  and  $p_y$  differs and is dependent on the nature of the molecule.

In Figure [4.11], the asymmetry of the electron momentum distributions in the  $\text{N}_2$  molecule when exposed to OTC laser fields is shown. The top left panel shows the asymmetry along the  $p_x$  axis, which varies from  $10^{-5}$  to 0.09, and the

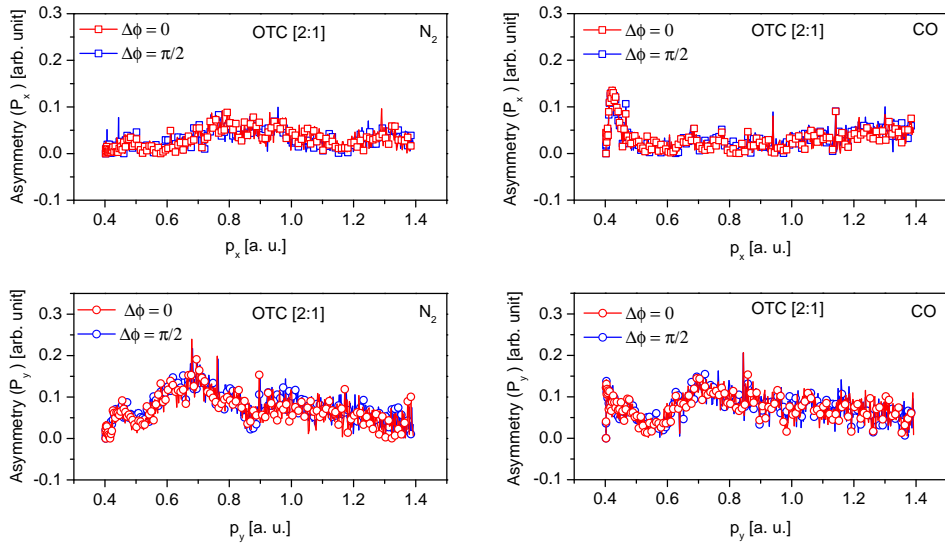


Figure 4.11: OTC field induced asymmetry in  $p_x$  and  $p_y$  at  $I_{SH}/I_{FW} = 0.5$ , at a relative phase of 0 and  $\pi/2$ . The statistical error (maximum) in the asymmetry is about 0.6%, estimated from counts/pixel. The counts/pixel are about  $10^5$ .

bottom left panel shows the asymmetry along the  $p_y$  axis, which varies from  $10^{-4}$  to 0.24. The modulation of the asymmetry parameter is most pronounced at around 0.7 atomic units (a. u.) for both relative phases. The modulation is noticeable up to  $p_x$  or  $p_y$  values of less than 1 a. u., but becomes less significant beyond this value. In CO, the asymmetry along the  $p_x$  axis (top right panel) varies from  $10^{-5}$  to 0.14, and the asymmetry along the  $p_y$  axis (bottom right panel) varies from  $10^{-3}$  to 0.21. The modulation of the asymmetry parameter peaks at around 0.7 a. u. for both relative phases. Interestingly, the asymmetry for both  $p_x$  and  $p_y$  in CO peaks at around 0.5 a. u., a behaviour not observed in N<sub>2</sub>. However, similar to N<sub>2</sub>, the fluctuation in the  $p_y$  axis is more significant than in the  $p_x$  axis. The observed variation in the asymmetry parameter may be due to the Coulomb effect, the modulation of electron trajectories by the two-color field, and the contribution of molecular orbitals.

The PEMD of N<sub>2</sub> and CO induced by PTC at a laser intensity ratio of  $I_{SH}/I_{FW} = 0.5$  are shown in Figure 4.12, with the relative phase set to 0 [B] and  $\pi/2$  [A]. The PEMD of N<sub>2</sub> appears to be distinct from that of CO, which can be attributed to the differences in the ionization processes, molecular orbital contributions, and modulation of photoelectron trajectories. At the same intensity ratio, the lobes in the PEMD of CO are more pronounced than those

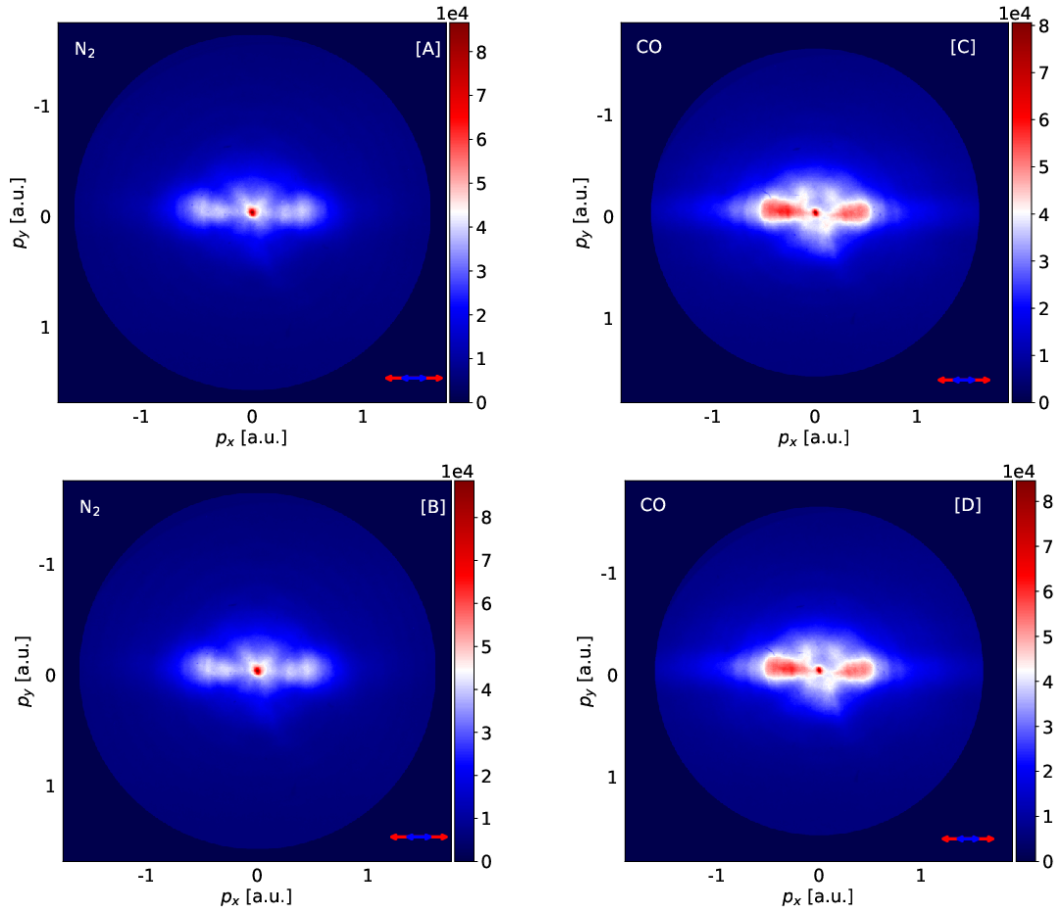


Figure 4.12: Photoelectron momentum distributions of CO and N<sub>2</sub> induced by PTC at laser intensity ratio of 0.5 ( $I_{SH}/I_{FW} = 0.5$ ), [top] at relative phase 0 deg, [bottom] at relative phase  $\pi/2$ . Visible dark spots in the image are due to defects in the detector and should be ignored. Both blue and red arrows are parallel to the detector plane.

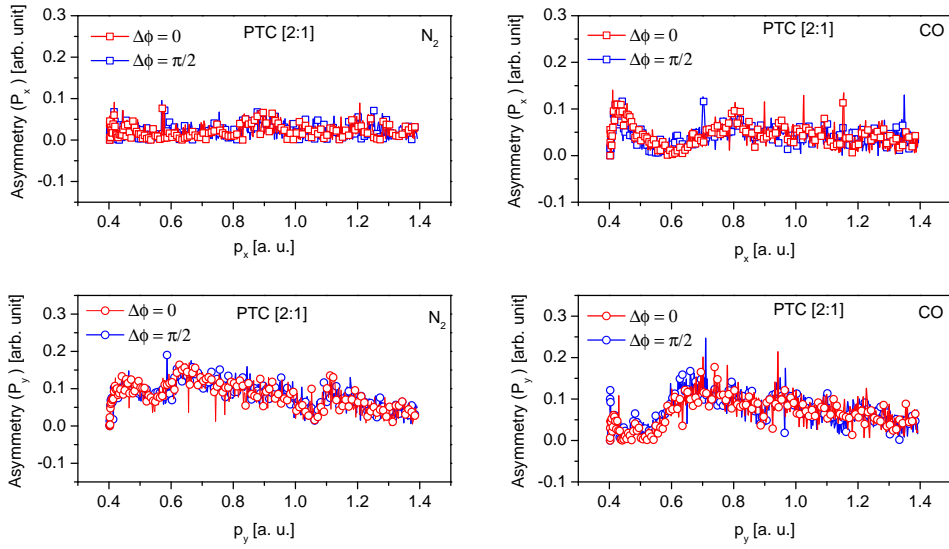


Figure 4.13: Asymmetry in  $p_x$  and  $p_y$  induced by PTC field at  $I_{SH}/I_{FW} = 0.5$ , at relative phase of 0 and  $\pi/2$ . The maximum statistical error in the asymmetry is about 0.8% estimated from counts/pixel. The counts/pixel are about  $10^5$ .

in the PEMD of N<sub>2</sub>. Additionally, the momentum spread along the  $p_y$  axis is higher in CO compared to N<sub>2</sub>.

The parallel two-color electric field at a relative phase of  $\pi/2$  results in electrons being released in the same direction as the electric field from both the 800 nm and 400 nm wavelengths. Previous research has shown that the modulation of the two-color field on low energy (non-scattering) and high energy (rescattering) electrons can differ based on the angle of emission relative to the polarization [131]. In this study, the random orientation of N<sub>2</sub> and CO molecules makes it difficult to distinguish the individual effects of the electric field, Coulomb effect, and electron emission relative to polarization on the modulation of electron trajectories. However, the resulting asymmetry in the momentum distribution can still be observed.

Figure [4.13] illustrates the asymmetry in  $p_x$  and  $p_y$  induced by the PTC field in N<sub>2</sub> and CO at relative phase 0 and  $\pi/2$ . In both molecules, the variation in the asymmetry at the relative phases of 0 and  $\pi/2$  is much. Modulations in asymmetry along  $p_x$  and  $p_y$  are clearly visible in both N<sub>2</sub> and CO. The observed trend in the asymmetry of both molecules is possibly due to the two-color induced modulation on the tunneling electron revisiting trajectories.

From Figure [4.13], we can estimate the asymmetry value. The asym-

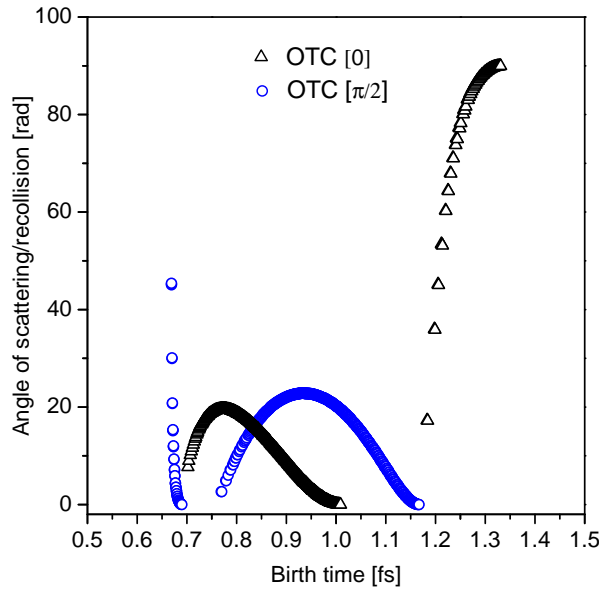


Figure 4.14: Classical-electron trajectory simulation in the OTC field. The black curve represents the electron revisit angle at the relative phase of 0, and the blue curve is at the relative phase of  $\pi/2$ .

metry of  $N_2$  along  $p_x$  [top, left] varies from  $10^{-5}$  to 0.09, whereas that along  $p_y$  [bottom, left] varies from  $10^{-3}$  to 0.17. For both phases, this asymmetry peak is at about 0.7 a.u. For  $p_y$ , the modulation is significant, whereas for  $p_x$ , it is nonexistent. For CO, the  $p_x$  and  $p_y$  varies from  $10^{-4}$  to 0.14 and 0.21, respectively. For both OTC and PTC, the asymmetry peak is at 0.7 a.u. Interestingly, the peak at 0.5 a.u. was considerable in OTC but nearly completely suppressed in PTC's  $p_y$ . Additionally, the peak for OTC at about 0.7 a.u. appears to be similar to PTC. Finally, we compare the OTC and PTC influence on the PEMD and the asymmetry modulation of  $N_2$  and CO. As expected, the OTC and PTC influence the PEMD of both molecules uniquely. The modulation in the asymmetry parameter induced by OTC and PTC is noticeable for the low energy electrons ( $p_x, p_y < 1$ ).

The electrons released during the parallel two-color electric field phase of  $\pi/2$  are influenced by both the 800 nm and 400 nm electric fields in the same direction. Previous research has shown that the modulation of the two-color field on low-energy electrons (non-scattering trajectories) is different from that on high-energy electrons (rescattering trajectories) based on the emission

angle of the electrons relative to the polarization [131]. In the current study, the orientation of N<sub>2</sub> and CO is random, making it difficult to distinguish the specific effects of the electron ejection relative to the polarization and the modulation of their trajectories by the field and Coulomb effect on the asymmetry parameter. However, the asymmetry in the PEMD induced by OTC can be challenging to interpret due to the complex 3D pattern of the resulting field. In an effort to understand the asymmetry in this case, we have analyzed the electron trajectories simulated in the OTC field. The revisiting angle of the electron in the case of OTC as a function of birth time is shown in Figure [4.14]. The birth times of the electrons at the relative phase of 0 range from approximately 0.7 fs to 1.35 fs, while the returning angle ranges from 0 to 90°. Similarly, the birth times at the relative phase of  $\pi/2$  have a range of 0.7 to 1.16 fs, while the revisiting angle is from 0 to 45°. From Figure [4.14] and Figure [4.10], it can be seen that the spread in revisiting angle is less ( $< 1^\circ$ ) for high energy electrons (beyond 90 eV) compared to low energy electrons (below 45 eV). Therefore, the observed variation in asymmetry in low energy electron momentum may be due to the modulation of revisiting angle in the two-color field. The simulation presented here is at the elementary level and does not consider the contribution of molecular orbitals to the PEMD or the Coulomb effect.

## 4.4 Conclusions

The present study investigates the strong-field ionization of N<sub>2</sub> and CO using two-color laser fields with orthogonal (OTC) and parallel (PTC) polarizations. The phase-dependent ion yield and fragmentation of these molecules were evaluated under both OTC and PTC conditions. It was found that the ion yield oscillates with a period of  $\pi$  for both CO and N<sub>2</sub>. The fragment ion yield was found to have an anti-correlated trend with the parent ions in the case of OTC in N<sub>2</sub>, but not in CO. In contrast, the CO<sup>+</sup> ion yield was found to be anti-correlated with its charged fragments in the case of PTC and was found to be three times higher than the OTC case. On the other hand, the anti-correlated oscillatory trend in the N<sub>2</sub><sup>+</sup> yield with fragment N<sup>+</sup> was found to be similar in both OTC and

PTC. The results of this study suggest that the ion yield is highly sensitive to the relative phase of the two-color field, and that the two-color field can be used to modulate electron trajectories and control the fragment ion yield of ionized molecules. Additionally, the photoelectron momentum distributions of CO and N<sub>2</sub> induced by OTC and PTC at relative phases of 0 and  $\pi/2$  were studied. It was found that the PEMD of N<sub>2</sub> is different from the PEMD of CO induced by the two-color fields and that this difference is likely due to molecular orbital contributions and the modulation of electron trajectories in the two-color field. The asymmetry parameter was also computed and analyzed for  $p_x$  and  $p_y$  at the relative phases of 0 and  $\pi/2$ . Variation in the asymmetry parameter was observed for both molecules under both OTC and PTC conditions, and classical electron trajectory simulations suggest that electron revisiting-induced processes in the two-color fields may influence the ion yield trend and the asymmetry in the photoelectrons.



# Chapter 5

## Strong-field ionization of CO<sub>2</sub>

The strong-field ionization of CO<sub>2</sub> using single-color and two-color laser fields is discussed in this chapter. In the case of single-color-induced photoionization, the intensity, wavelength, and pulse duration dependence on the yield on charged fragments are investigated in detail. Further, the Non-sequential double ionization (NSDI) is investigated, and found a knee structure in CO<sub>2</sub><sup>2+</sup>/CO<sub>2</sub><sup>+</sup> yield ratio and also in fragments. This observation is attributed to the revisiting tunnel electron induce processes in ionized CO<sub>2</sub>. To investigate how revisiting electrons affect the fragmentation yield, we have performed two-color induced photoionization of CO<sub>2</sub>. We have measured the ions yield as a function of relative phase at a fixed intensity ratio of Fundamental Wave (FW) and Second Harmonic (SH). Two-color fields modulate the revisiting electron trajectories, and the signature is seen in the fragments yield. Further, the asymmetry in momentum distribution is obtained to understand the two-color induced modulation of tunnel electron trajectories.

### 5.1 Introduction

The energy transfer to the bound electrons of atoms or molecules by the interaction of charged particles or photons initiates excitation or ionization. Such an excitation or ionization is the first step for any molecular dissociative reactions. The excitation or ionization of molecules induced by an intense laser field has been a research topic for over a few decades [132, 133, 134]. The ioniza-

tion of atoms or molecules is possible by the absorption of many photons. This process is called multiphoton ionization. The intense laser field can distort the Coulomb potential and subsequently ionize the molecule through tunneling. The multiphoton and tunneling ionization can be distinguished based on the Keldysh parameter defined as  $\gamma = I_p/2U_p$ , where  $I_p$  is the ionization potential, and  $U_p$  is the quiver energy of the free electron in the laser field. If  $\gamma > 1$ , then the multiphoton ionization (MPI) dominates, while for  $\gamma < 1$ , the tunneling ionization dominates. In the study of strong-field ionization of atoms and molecules, many new processes, such as Above threshold ionization [135], Sequential and Non-sequential double ionization [136, 137, 138, 139], and High Harmonic Generation [140, 141, 142], were discovered. These processes are directly linked with the absorption of excess photons by the bound electrons or the energy gained by the tunneling electron in the presence of a laser field and revisiting the parent ions. It was observed that electronic structures play a crucial role in revisiting electron-induced double ionization processes [143, 144, 145].

Non-sequential double ionization (NSDI) has continued to attract the attention of many physicists due to its manifestation of dynamical electron-electron correlation in ionization [139]. In early experiments [98, 146, 147, 148] on the strong-field ionization of noble-gas atoms, a characteristic knee structure was observed in the doubly by singly ion yield ratio as a function of the laser intensity. This knee structure has been interpreted as the enhancement of double ionization probabilities. Nowadays, it has been accepted that the inelastic recollision process is responsible for NSDI. Electron recollision processes in molecules may be complex to disentangle due to the presence of other atoms, additional degrees of freedom, molecular structure, and higher density of electronic states. Previously, many attempts have been made to understand the recollision induced-processes in small molecules, such as N<sub>2</sub>, CO<sub>2</sub>, C<sub>2</sub>H<sub>2</sub>, and C<sub>3</sub>H<sub>4</sub> and the signature of NSDI has been reported [149, 150, 151, 152]. Recently, the energy transfer in a recollision process in OCS has been studied, and its dependence on the impact parameter has been reported [153]. The multichannel contributions in the NSDI of CO<sub>2</sub> are also reported [154]. Further, the rescattering-induced dissociative and nondissociative double ionization from HOMO and HOMO-1 of CO<sub>2</sub>

has been studied using a reaction microscope [155]. The recollision-induced processes and their effect on the fragment yield are only explored a little. However, it is expected that the revisiting electron not only further ionizes the parent ion but also excites or alters the populations of multiple dissociative states. Thus, fragment yield may also be affected by the recollision processes. Further, the modulation of revisiting electron trajectories by a two-color field may also affect the fragmentation yield.

In the first part of this chapter, we report our new findings on the strong-field ionization of  $\text{CO}_2$  induced by femtosecond pulses. We examined the knee structure in  $\text{CO}_2^{2+}/\text{CO}_2^+$  as well as in the  $\text{C}^+$ ,  $\text{O}^+$ , and  $\text{CO}^+$  yields.

The second part of this chapter is focused on the two-color photoionization of  $\text{CO}_2$ . The two polarization schemes, viz., Orthogonal Two-Color (OTC) and Parallel Two-Color (PTC), have been used here. Further, the two-color intensity ratio dependence on fragmentation and the relative phase of the fragment yield are investigated in detail. Finally, the classical electron trajectories simulation is performed in Mathematica software to explain the experimentally observed results.

## 5.2 Experimental scheme

Detail of the laser, spectrometer and experimental scheme is discussed in Chapter 2: Methodology. Here, we briefly described the experimental parameters used in the strong-field ionization of  $\text{CO}_2$ .

### 5.2.1 Single-color photoionization experiment

The strong field photo-ionization of the  $\text{CO}_2$  molecule has been studied using femtosecond laser pulses in combination with a home-built multi-plate Velocity Map Imaging (VMI) Spectrometer. A gas mixture consisting of 20%  $\text{CO}_2$  and 80% Helium gas (buffer) to provide high pressure of about 2 bars is used through the pulsing valve (Parker) with an opening of 1000 microns. The laser pulse (29fs, 1kHz, 800 nm) interacts with  $\text{CO}_2$  molecules in the interaction region of

the VMI spectrometer. For ion yield measurements, the VMI was operated in Time-of-flight (TOF) mode. The TOF spectrum at given laser intensity was recorded and analyzed. In this study, the laser intensity varies from 0.10 to 0.30 PW/cm<sup>2</sup>.

During the experiments, the pulse duration of femtosecond laser pulses was monitored using the SPIDER unit. Detail of pulse characterization of PRL's femtosecond laser is available in previous publication [93], [94].

In addition to the laser intensity dependence on fragmentation, the wavelength and pulse duration dependence on ion yield is also performed. For the wavelength dependence study, TOF measurements at two wavelengths (800 nm and 400 nm) with the same laser intensity were performed.

For pulse duration dependence, the pulse width is increased by adding SF11 glass plates of different thicknesses. The stretched pulse shape and width are characterized using the SPIDER system, and results are reported in these [93][94] publications. The spatial beam profile (beam width  $\sim 13$  mm) and focus-spot ( $44 \mu\text{m}$ ) size are determined using the beam profiler system (Gentec-EO, USA).

### 5.2.2 Two-color photoionization experiment

Two-color photoionization of CO<sub>2</sub> was performed using a pump-probe type setup combined with the Velocity Map Imaging spectrometer. The Two-color pump-probe setup and VMI setup are discussed in chapter 2. Here we are describing the parameters in detail.

- **Two-color Intensity dependence on ion yield:** For this study, we fixed the SH power and varied the FW power.
- **Two-color relative phase dependence on ion yield:** The relative phase was achieved using a precision motorized stage (Newport's XPS). The TOF spectrum as a function of delay (relative phase) was recorded and analyzed.

- **Polarization combinations:** like OTC or PTC were obtained using a Half wave plate and polarizer.
- **Photoelectron momentum distribution (PEMD):** The two-color may modulate the tunnel electron trajectories and also introduce the asymmetry in photoelectron angular distribution. We recorded the PEMD as a function of relative phase and intensity and analyzed it to understand the two-color effect on photoelectrons.

Finally, to understand the observed results, we have performed the semi-classical tunnel electron trajectory simulation using equations [5.1, 5.2] and obtained the max kinetic energy of revisiting electrons as a function of birth/ionization time.

$$m_e \frac{d^2 \vec{y}}{dt^2} = -e \vec{E}_0 \sin(\omega t) \cos^2(k\omega t) \quad (5.1)$$

$$\left. \frac{d\vec{y}}{dt} \right|_0^{\vec{y}} = \frac{e \vec{E}_0 (\cos(\omega t) (-4k^2 + \cos(2k\omega t) + 1) + 2k \sin(\omega t) \sin(2k\omega t))}{2(4k^2 - 1) \omega m_e} \Bigg|_{t_{birth}}^t \quad (5.2)$$

$$\begin{aligned} \vec{y}(t) = \frac{e \vec{E}_0}{2(4k^2 - 1)^2 \omega^2 m_e} & \left[ -\sin(t\omega) \left( (4k^2 + 1) \cos(2kt\omega) + (1 - 4k^2)^2 \right) \right. \\ & \left. + 2(8k^4 - 6k^2 + 1) t\omega + 4k \cos(t\omega) \sin(2kt\omega) \right] \quad (5.3) \end{aligned}$$

## 5.3 Results

### [A] Single-color photoionization of CO<sub>2</sub>

#### 5.3.1 Intensity dependent single-color photoionization of CO<sub>2</sub>

The ion yield ratio (CO<sub>2</sub><sup>2+</sup>/CO<sub>2</sub><sup>+</sup>) as a function of laser intensity is shown in Figure 5.1. The laser intensity is varied from 0.1 PW/cm<sup>2</sup> to 0.3 PW/cm<sup>2</sup>. The saturation of the ion yield ratio appears beyond 0.2 PW/cm<sup>2</sup> of laser intensity.

Below the saturation, it is interesting to see the "knee" structure at about 0.15 PW/cm<sup>2</sup>. This knee structure is a characteristic of nonsequential double ionization (NSDI). The knee structure around the same laser intensity was found previously in CO<sub>2</sub> [156, 157].

The observed knee structure is possibly due to recollision-induced enhanced double ionization. Depending on laser intensity, the revisiting electrons carry different kinetic energy, which can excite or even further ionize the parent ion. In the present case, the tunneling ionization from the HOMO and HOMO-1 releases an electron, which travels in the field and gains energy from the field. While revisiting, it interacts with the bound electron of HOMO or HOMO-1 and

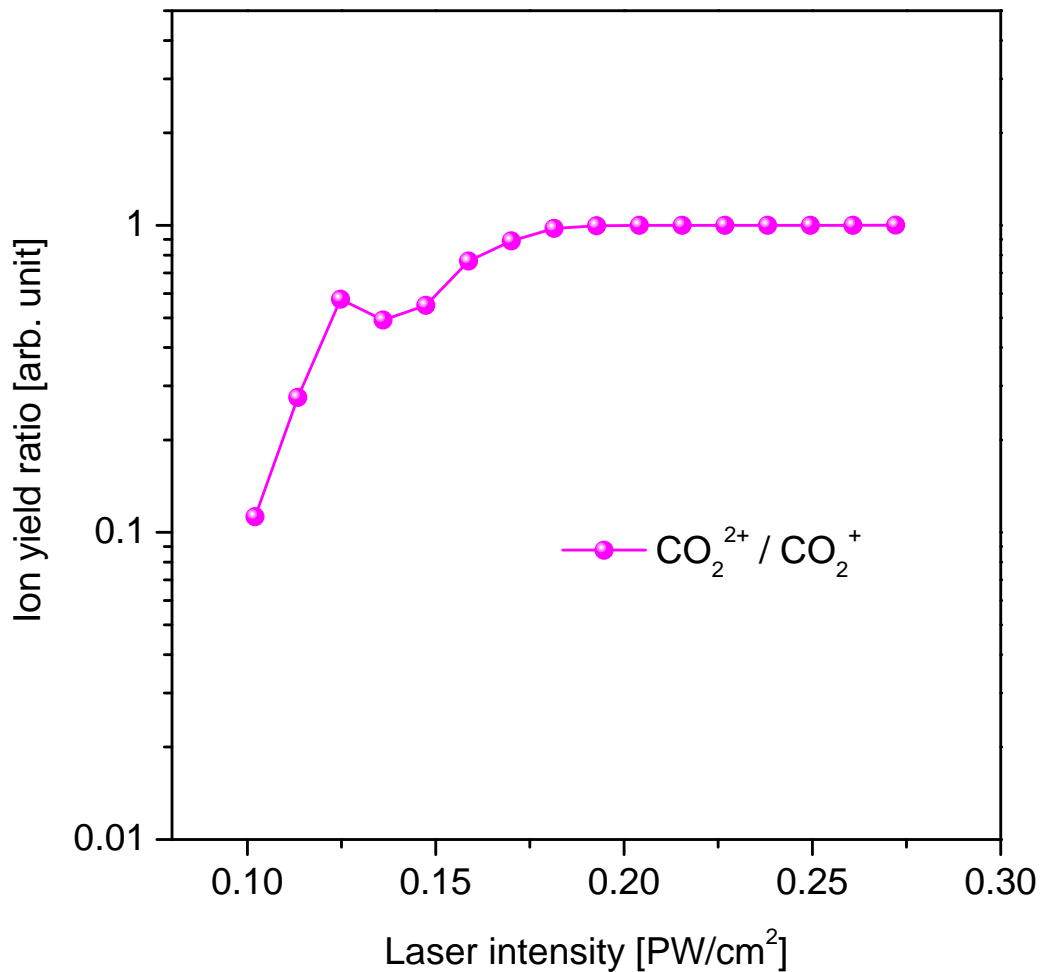


Figure 5.1: Ion yield ratio ( $\text{CO}_2^{2+}/\text{CO}_2^+$ ) as a function of laser intensities for linearly polarized light. The intensity-dependent experiments were carried out using 800 nm, 29 fs laser pulses.

excites the  $\text{CO}_2^+$  to a pre-dissociative state ( $\text{C } ^2\Sigma_g^+$ ) or further ionizes to  $\text{CO}_2^{2+}$ .

To understand the revisiting kinetic energy of electrons as a function of birth time (ionization time) and the laser intensity, a classical electron trajectories simulation was performed using equations [5.1 & 5.3], and results are plotted in Figure 5.2. The top panel of the figure shows that the maximum kinetic energy of the revisiting electron is about 26 eV at 0.14 PW/cm<sup>2</sup> of the laser intensity (at the knee structure). A similar plot is obtained at other laser intensities, and maximum kinetic energy as a function of laser intensity is shown in the bottom panel of the figure. Simulation reveals that the revisiting energy range is from 8 eV to 60 eV without considering the ionization potential of  $\text{CO}_2$  (13.8 eV). The revisiting electron kinetic energy is adequate to excite/ionize the  $\text{CO}_2^+$ . The observed knee structure can be understood from the revisiting electron-induced formation of  $\text{CO}_2^{2+}$ . The metastable band of  $\text{CO}_2^{2+}$  is lying in 25.0 to 27.5 eV from the ground state of  $\text{CO}_2^+$ . Possibly, the revisiting electron populates the bound state of  $\text{CO}_2^{2+}$  ( $^3\Sigma_g^-$ ,  $^1\Delta_g$ ) and metastable  $\text{CO}_2^{2+}$  through multiple pathways [154]. The efficient double ionization depletes the singly-charged-ion population, which leads to a knee structure in the observed laser intensity range.

Laser-induced strong-field ionization (MPI & Tunneling ionization) and revisiting electron-induced excitation/ionization can also populate multiple repulsive excited states of  $\text{CO}_2^+$  and  $\text{CO}_2^{2+}$ . The multiple dissociative states open up numerous fragmentation pathways. The observed yield of the  $\text{C}^+$ ,  $\text{O}^+$ ,  $\text{CO}^+$ ,  $\text{C}^{2+}$ , and  $\text{O}^{2+}$  ions are of different pathways of the singly or doubly ionized  $\text{CO}_2$  [158], [159], [160], [161], [162].

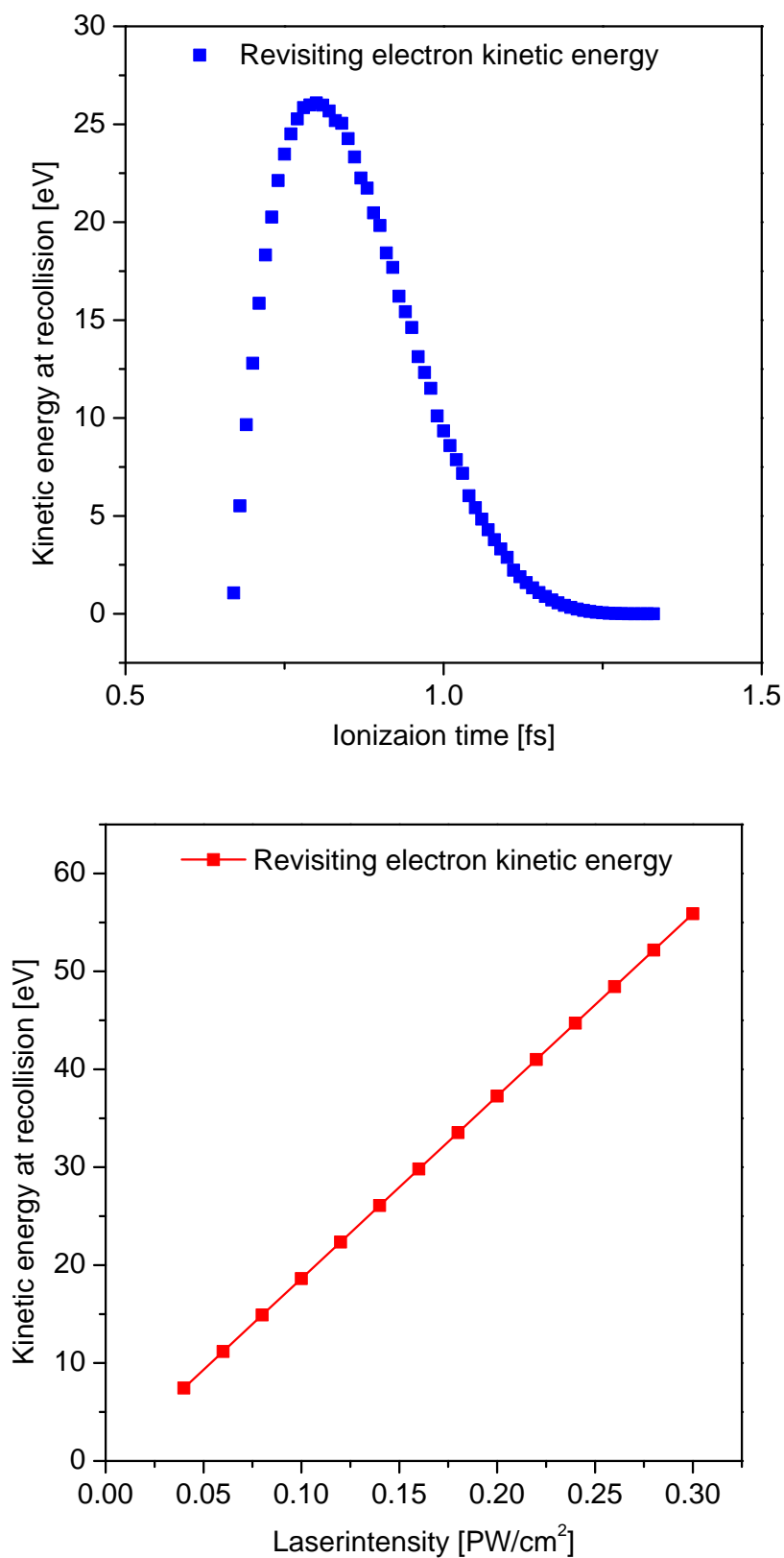
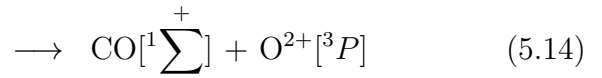
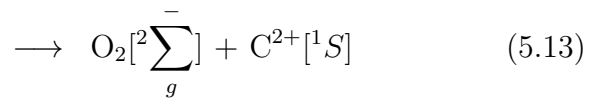
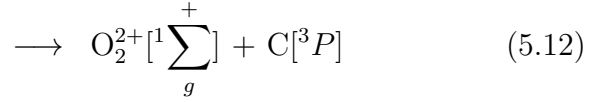
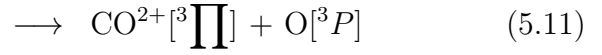
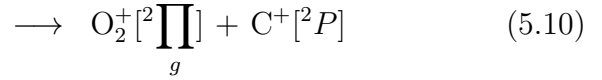
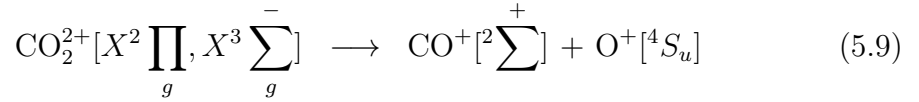
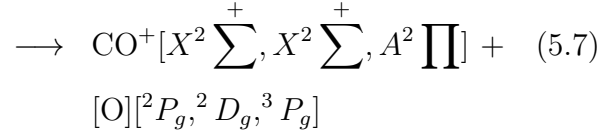
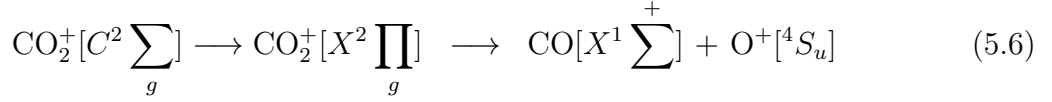
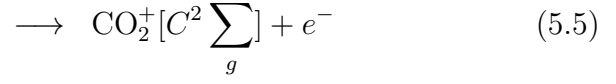
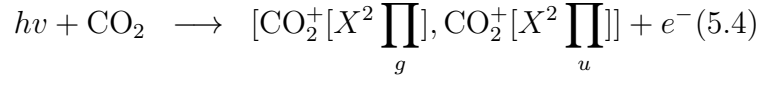


Figure 5.2: Classical electron trajectories simulation in laser field. [top] Revisiting electron kinetic energy as a function of ionization time. This plot is obtained at 0.15 PW/cm<sup>2</sup> of the laser intensity, [bottom] Revisiting electrons having maximum kinetic energy as a function of laser intensity.



Fragment ion yield of  $\text{C}^+$ ,  $\text{O}^+$ , and  $\text{CO}^+$  as a function of laser intensity is shown in the top panel of Figure 5.3. Interestingly, a knee structure is seen in these charged fragments yield. Such knee structure in fragment yield of  $\text{CO}_2$  has never been reported before and indicates that the revisiting electron influences the fragmentation. The dissociative or pre-dissociative channels of  $\text{CO}_2^+$  and  $\text{CO}_2^{2+}$  can contribute to the yield of  $\text{C}^+$ ,  $\text{O}^+$  and  $\text{CO}^+$ . The  $\text{O}^+$  yield is the highest, and the  $\text{C}^+$  yield is the lowest at all laser intensities. Interestingly, all  $\text{C}^+$ ,  $\text{O}^+$ , and  $\text{CO}^+$  yields follow a similar trend as a function of laser intensity.

The higher yield of O<sup>+</sup> is possible due to its efficient formation via channels ([5.6] & [5.9]) and also through other channels [163] from repulsive states of CO<sub>2</sub><sup>2+</sup>, which can be accessed by the revisiting electron. The CO<sup>+</sup> [ $X^2 \Sigma^+$ ,  $A^2 \Pi$ ] formation is possible from the pre-dissociative state of CO<sub>2</sub><sup>+</sup> [ $C^2 \Sigma_g$ ] (channel 5.7), and also from CO<sub>2</sub><sup>2+</sup> [ $X^2 \Pi_g$ ] through channel [5.9]. The formation of C<sup>+</sup> is possible from the pre-dissociative and dissociative channels of CO<sub>2</sub><sup>+</sup> channels [5.8] & dissociative state of CO<sub>2</sub><sup>2+</sup> channel [5.10]. The observed relative yield (O<sup>+</sup> > CO<sup>+</sup> > C<sup>+</sup>) is consistent with previous report [163]. The knee structure in the yield of singly charged fragments is possibly due to the enhanced metastable CO<sub>2</sub><sup>2+</sup> and inhibiting the dissociative state CO<sub>2</sub><sup>2+</sup> [ $X^2 \Pi_g$ ] formation, which does not produce singly charged fragments. Further, the depletion of the dissociative singly-charged-ion population of CO<sub>2</sub><sup>+</sup> contributes to the knee structure.

The C<sup>2+</sup>, and O<sup>2+</sup> ion yield as a function of laser intensity is shown in the [b] of the top panel of Figure 5.3. The CO<sup>2+</sup> ion is not observed in time-of-flight spectra (not shown here). Possibly, CO<sup>2+</sup> [ $X^3 \Pi$ ,  $^3 \Sigma^-$ ] states are repulsive in nature which dissociates into C<sup>+</sup> and O<sup>+</sup> ions [160, 164, 165]. Further, the formation of CO<sup>2+</sup> from the CO<sub>2</sub><sup>2+</sup> is unlikely due to the high energy barrier (48.71 eV) and, thus, not found also in the previous study on CO<sub>2</sub> induced by Ar<sup>2+</sup> impact [166]. A knee structure is also observed in the yield of C<sup>2+</sup> and O<sup>2+</sup> ions. This knee structure is possibly due to the revisiting electron effect on the fragmentation of CO<sub>2</sub><sup>2+</sup>. Further, the observed C<sup>2+</sup>, and O<sup>2+</sup> ion yield trend is unique in the sense that the O<sup>2+</sup> yield is more compared to C<sup>2+</sup> in the intensity range of 0.10 to 0.18 PW/cm<sup>2</sup> and beyond the 0.18 PW/cm<sup>2</sup>, the C<sup>2+</sup> is more, and both C<sup>2+</sup> and O<sup>2+</sup> have an increasing trend as a function of laser intensity. This kind of trend in the doubly charged fragments yield is never reported before and suggests that the revisiting electrons play a paramount role in the dissociation dynamic of CO<sub>2</sub><sup>2+</sup>.

The higher O<sup>2+</sup> yield from C<sup>2+</sup> at low laser intensity is possible to explain from channel [5.12], which can be accessed by the low energy revisiting electrons 8 - 30 eV (without considering the I.P. of CO<sub>2</sub><sup>+</sup>). The O<sub>2</sub><sup>2+</sup> bound states (formed from a channel [5.12]) are virtually non-existent and majorly (70%) dissociate into O<sup>2+</sup> [167]. On the other hand, the channel [5.13] is less likely to

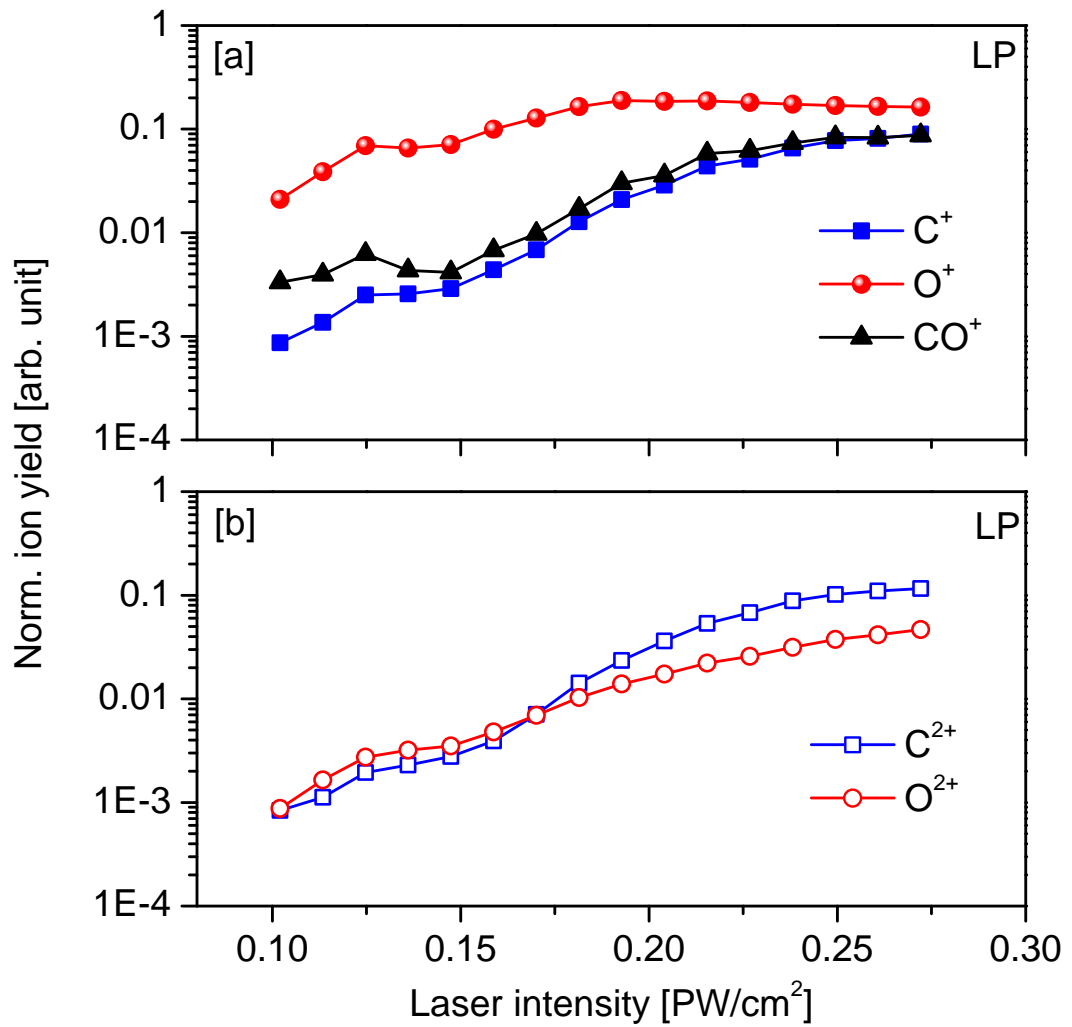


Figure 5.3: Intensity dependence of ion yield for linearly polarized light pulses having 29 fs pulse duration. LP: Linear Polarization and CP: Circular Polarization

be populated by low-energy electrons. This explains the observed higher O<sup>2+</sup> yield compared to C<sup>2+</sup> in the range 0.10 - 0.18 PW/cm<sup>2</sup> of laser intensity. It is possible that the formation of C<sup>2+</sup> (channel [5.13]) at high laser intensities is more efficient than the O<sup>2+</sup> from the combined yield from channels [5.12] & [5.14].

The O<sup>2+</sup> formation via the channel [5.14] requires about 54.213 eV, which is higher compared to the C<sup>2+</sup> formation via the channel [5.13], requiring about 51.198 eV [163]. Thus the revisiting electron (30 - 60 eV, without considering the I.P. of CO<sub>2</sub><sup>+</sup>), in the laser intensity range of 0.17 - 0.27 PW/cm<sup>2</sup> favors channel [5.13] over channel [5.14], which supports the observed ion yield trend.

### 5.3.2 Wavelength dependent photoionization of CO<sub>2</sub>

The wavelength-dependent strong-field ionization and fragmentation of CO<sub>2</sub> molecule are examined using 400 nm ( $\sim 3.1$  eV) and 800 nm ( $\sim 1.55$  eV) femtosecond pulses. The 800 nm laser intensity used in this study was 0.15 PW/cm<sup>-2</sup>, which is in the knee structure region. The intensity for 400 nm wavelength light was the same as 800 nm. The polarization (linear polarization) and the pulse duration (29 fs) of the FW and SH laser pulses were kept constant during the measurement.

The measured fragments yield is displayed in the figure [5.4]. The ionization by 400 nm photons is in the multi-photon ionization regime ( $\gamma \gg 1$ ), while ionization by 800 nm laser pulse is in the tunneling regime ( $\gamma \ll 1$ ), and thus the recollision-induced excitation/ionization of CO<sub>2</sub><sup>+</sup> is expected. Thus, at 800 nm wavelength, the fragments yield is expected to be more compared to 400 nm wavelength. The yield of CO<sub>2</sub><sup>+</sup> and CO<sub>2</sub><sup>2+</sup> is slightly higher at 800 nm compared to 400 nm, but fragmentation is high at 400 nm. This observation is advocating the non-adiabatic process of CO<sub>2</sub> ionization and fragmentation and rules out the adiabatic interaction, which was found to be wavelength independent[168].

It is interesting to note that the C<sup>+</sup>, O<sup>+</sup>, and CO<sup>+</sup> yields at 400 nm and 800 nm are almost the same (in the top panel of the figure). The singly charged

fragments are mostly formed from the repulsive states of  $\text{CO}_2^+$ , and some channels of doubly ionized  $\text{CO}_2$  may also contribute. The observed same yield of singly charged fragments indicates that both 400 nm and 800 nm populate the same dissociative states of singly and doubly ionized  $\text{CO}_2$  at the used intensity.

The doubly charged fragments ion yield at 400 nm and 800 nm are shown in the bottom panel of figure [5.4]. Interestingly, the yield of  $\text{C}^{2+}$  and  $\text{O}^{2+}$  at 400 nm is over 6 times more than the yield at 800 nm. This trend is not expected as revisiting electrons in the case of 800 nm may also contribute to the photoionization of  $\text{CO}_2^+$ . The observed result is possibly due to the higher yield of double ionization at 400 nm as compared to 800 nm at the same intensity. A similar observation has been reported previously, in which the fragmentation was more at lower wavelengths [94].

### 5.3.3 Pulse duration dependence photoionization of $\text{CO}_2$

This section discusses the pulse duration (chirp) dependent on the ionization and fragmentation of  $\text{CO}_2$ . The laser's pulse duration is varied from 29 fs to 374 fs, and the fragments yield is recorded with the same laser intensity for linearly and circularly polarized light.

The results of singly charged ion yields as a function of pulse duration are shown in Fig 5.5. The ion yields increase as the pulse duration gets longer for linearly and circularly polarized light. These findings are consistent with previous work on other molecules [169, 170, 171], which have shown us that fragmentation is more at a longer pulse duration. The peak intensity was kept constant at  $\sim 0.31 \text{ PW/cm}^2$  during the entire measurements. At this laser intensity level, the tunneling ionization process dominates. As pulse duration increases, the recollision probability of tunneled electrons goes up, and the double ionization cross-section is enhanced [172, 173]. To confirm the recollision process and its contribution to the yields, we switched the laser polarization to circular and performed the ion yield measurement at the same intensity range. The results are shown in the bottom panel of Fig 5.5. The yield of  $\text{C}^+$ ,  $\text{O}^+$ , and  $\text{CO}^+$  are lower with circularly polarized light in comparison to linearly polarized light.

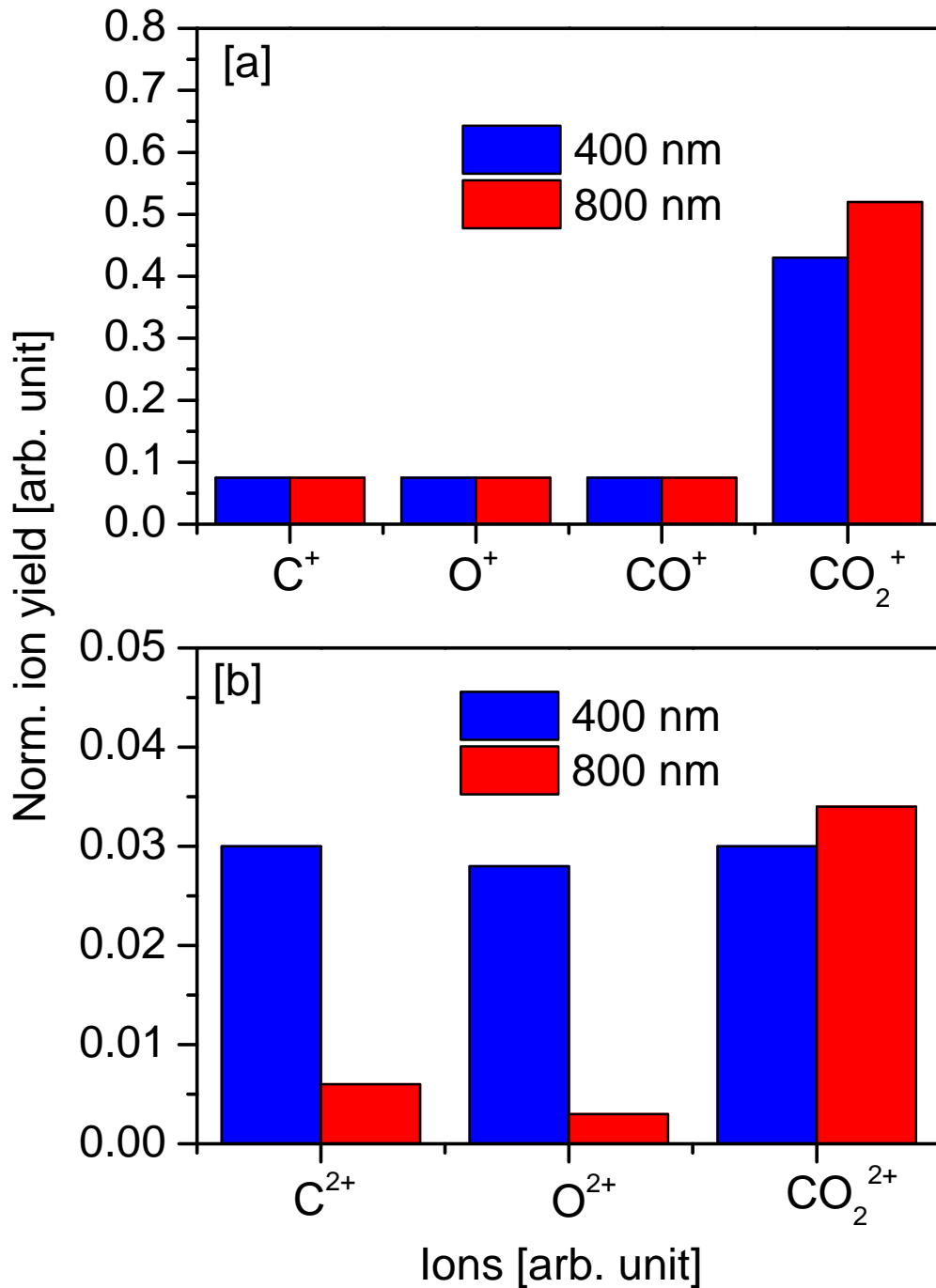


Figure 5.4: Normalized fragment ion yield with 400 nm and 800 nm wavelengths at the same laser intensity. [a] Yield of singly charged ions, [b] Yield of doubly charged fragments.

This result confirms that a significant portion of the fragmentation and ion yields is from the recollision of tunneled electrons.

The yield of doubly charged fragments (such as C<sup>2+</sup> and O<sup>2+</sup>) for linearly and circularly polarized light are shown in Fig 5.6. The yield of C<sup>2+</sup> and

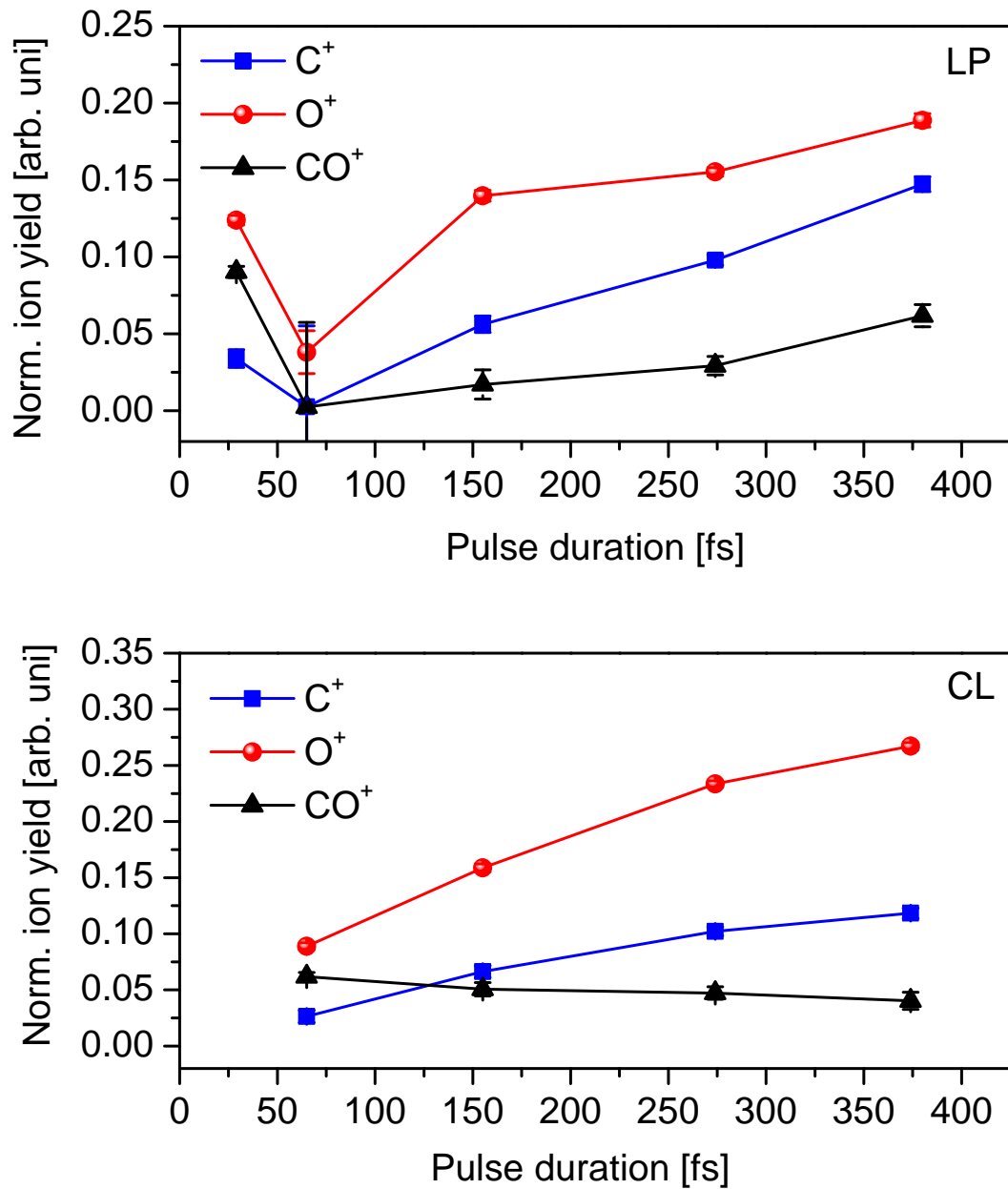


Figure 5.5: (top panel) Singly charged ion yield ratio as a function of femtosecond pulse durations. The peak intensity was maintained at  $0.309 \text{ PW/cm}^2$ . This is recorded using linearly polarized light pulses and 800 nm wavelength. (Bottom panel) The ion yield ratio for circularly polarized light pulses.

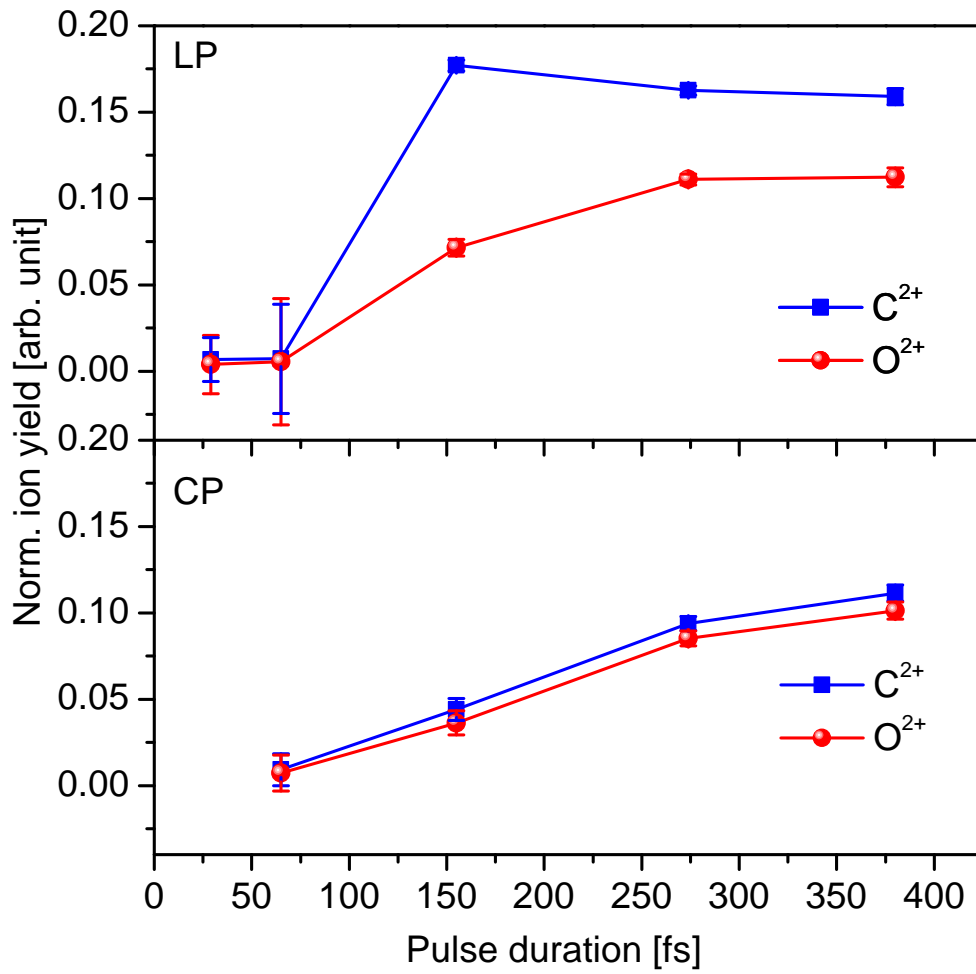


Figure 5.6: (top panel) The  $\text{CO}_2^{2+}/\text{CO}_2^+$  ion yield ratio for linearly and circularly polarized light pulses. (bottom panel) Doubly charged fragment ion ( $\text{C}^{2+}$  and  $\text{O}^{2+}$ ) yield ratio as a function of femtosecond pulse durations. The peak intensity was maintained at  $0.309 \text{ PW}/\text{cm}^2$ , wavelength of  $800 \text{ nm}$ .

$\text{O}^{2+}$  increases as a function of pulse duration. This ion yield trend is a signature of the dissociative  $\text{CO}_2^{2+}$  or multiply charged ion formation is more at longer pulse duration, which produces doubly charged fragments. In summary, the ionization and fragmentation are more at longer pulse durations.

## [B] Two-color photoionization of CO<sub>2</sub>

### 5.3.4 Intensity dependent two-color photoionization CO<sub>2</sub>: PTC

The ionization rate of a molecule in a two-color field depends on both field strengths, the relative phase between them, and its effect on the tunnel electrons. Here, the enhanced ionization is investigated by varying the intensity ratio. The SH intensity was 0.2 PW/cm<sup>2</sup> fixed during all measurements and FW intensities varied from 0.10 to 0.46 PW/cm<sup>2</sup>. The SH intensity is in the MPI regime ( $\gamma = 1.88$ ), and the FW intensity changes from the MPI to the TI regime ( $\gamma =$  from 1.618 to 0.809). Thus, there are two regimes of two-color ionization. When both SH and FW intensities are in MPI, the ionization and fragmentation in the two-color field are only due to the MPI processes. The other case is when SH intensity is in MPI, and FW intensity is in TI then the ionization process is complex as the MPI by SH, the TI by FW, and the revisiting electron-induced ionization are competing.

Figure [5.7] [top, left] shows the yield of CO<sub>2</sub><sup>+</sup> and CO<sub>2</sub><sup>2+</sup> as a function of the intensity ratio.

It is interesting to notice that the CO<sub>2</sub><sup>+</sup> and CO<sub>2</sub><sup>2+</sup> yield is constant over the intensity ratio ( $I_{2\omega}/I_{\omega}$ ) of 0.6 - 1.2. In this range, the multiple electronic states of CO<sub>2</sub><sup>+</sup>, CO<sub>2</sub><sup>2+</sup> and even higher charged CO<sub>2</sub> (3+, 4+) are populated by absorption of photons or tunnel electron recollision mechanism. The observed fragment yield trend can be understood from the possible excited dissociative states of ionized CO<sub>2</sub>. The  $X^2 \Pi_g$  is the ground state of CO<sub>2</sub><sup>+</sup>, and the  $A^2 \Pi_u$  and  $B^2 \Sigma_u$  are stable bound states. On the other hand, the  $C^2 \Sigma_g^+$  is highly unstable. The  $X^2 \Pi_g$ ,  $A^2 \Pi_u$ ,  $B^2 \Sigma_u$ ,  $C^2 \Sigma_g^+$  and other states of CO<sub>2</sub><sup>+</sup> are accessible by two-color field. Their population gets altered with some delay (sub fs, recollision time) by the revisiting electrons, which excites or ionizes the CO<sub>2</sub><sup>+</sup> to higher charged states. The electron recollision induces excitation/ionization, competing with the decay of the nuclear wavepacket in the repulsive states of CO<sub>2</sub><sup>+</sup> (e. g.  $C^2 \Sigma_g^+$ ). It is expected that the yield of CO<sub>2</sub><sup>+</sup> should deplete when the yield

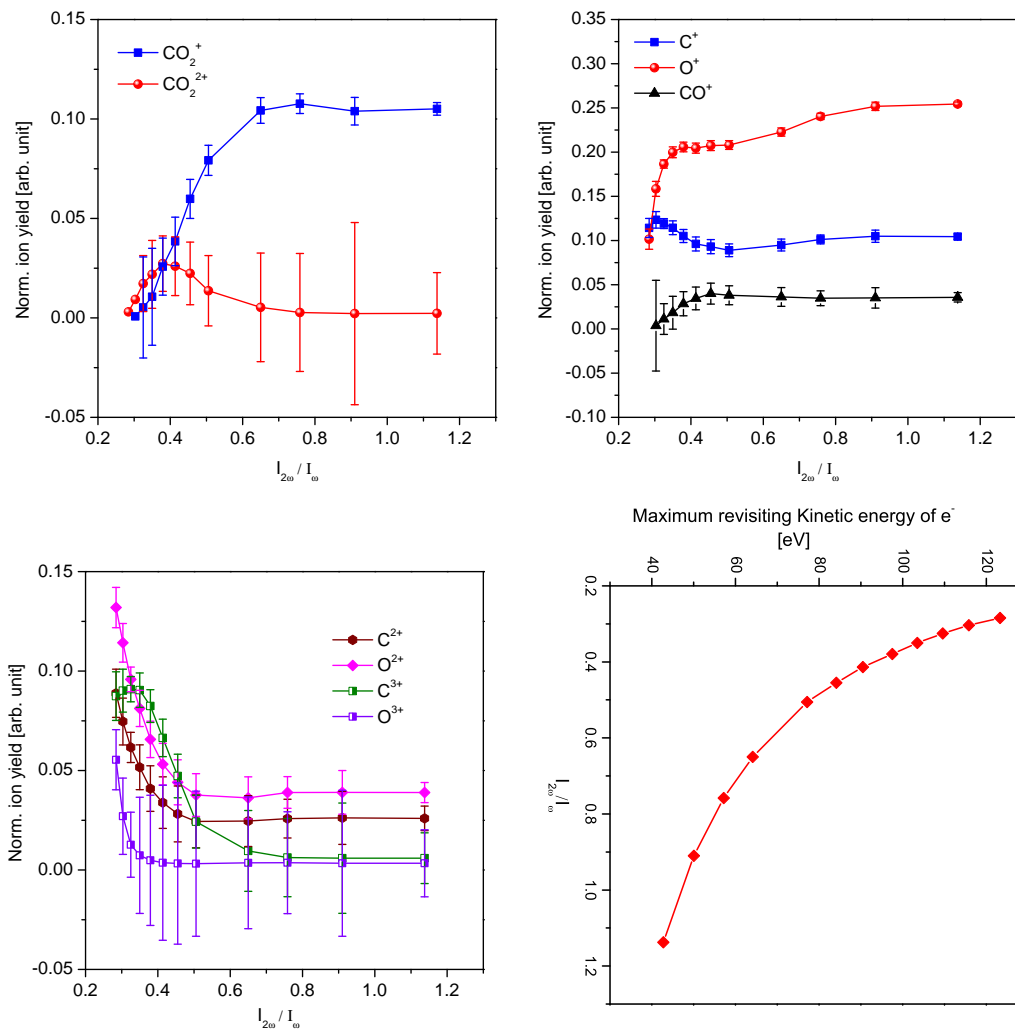


Figure 5.7: [top, left] The  $\text{CO}_2^+$  and  $\text{CO}_2^{2+}$  ion yield as a function of intensity ratio ( $I_{2\omega}/I_{\omega}$ ). [top, right] The charged fragments  $\text{C}^+$ ,  $\text{O}^+$ , and  $\text{CO}^+$  ion yield as a function of intensity ratio. [bottom] Doubly charged fragments trend as a function of intensity ratio. Error bars obtained from measured counts are shown in each plot.

of  $\text{CO}_2^{2+}$  increases which are not observed in this range of intensity ratio. This observation indicates that the rate of  $\text{CO}_2^+$  formation in the intensity described above range is not affected by either recollision or decay of the nuclear wavepacket in repulsive states leading to the dissociation.

The unique trend in ion yield of  $\text{CO}_2^+$  and  $\text{CO}_2^{2+}$  is observed in the range of the intensity ratio ( $I_{2\omega}/I_\omega$ ) of 0.24 - 0.60. In this regime, the ionization is not only from the MPI by SH and TI by FW, but also from the revisiting tunnel electrons. As a result, the enhancement in yield of  $\text{CO}_2^{2+}$  yield, and depletion of  $\text{CO}_2^+$  is expected and observed in the intensity ratio ( $I_{2\omega}/I_\omega$ ) of 0.24 - 0.60.

Figure [5.7][top, right] shows the fragments yield trend as a function of intensity ratio. In the 0.6 - 1.2 range of intensity ratio ( $I_{2\omega}/I_\omega$ ), the  $\text{C}^+$  and  $\text{CO}^+$  yield is constant but yield of  $\text{O}^+$  is gradually increasing. Interestingly the  $\text{O}^+$  yield is the highest, and the  $\text{CO}^+$  yield is the lowest. This yield trend is due to the population of multiple repulsive states of precursors and their fragmentation. It is intriguing to observe the decreasing trend in  $\text{O}^+$  and  $\text{CO}^+$  yield and the increasing trend in  $\text{C}^+$  in the intensity ratio of 0.6-0.3. The detailed mechanism involved in this trend is difficult to disentangle as many dissociative channels are involved in the formation of these singly charged fragments. The observed trend is possibly due to the revisiting electron-induced excitation/ionization of  $\text{CO}_2^+$ .

The higher charged fragments yield trend is shown in Figure [5.7][bottom]. The doubly and the triply charged fragments have an exponentially decreasing trend in the range of 0.24 - 0.50 of intensity ratio. The saturation of the different fragments starts at different ratios. For example, the  $\text{C}^{2+}$  and  $\text{O}^{2+}$  saturate at around 0.5, while  $\text{C}^{3+}$  at around 0.75 and  $\text{O}^{3+}$  is very close to 0.4. This trend can understand from the classical trajectories simulation results shown in Figure [5.7][bottom, right]. The simulation result reveals that the revisiting kinetic energy at 0.5 or less than this value of intensity ratio is 75eV. Thus, it is enough to ionize the  $\text{CO}_2$ . As the Ionization potential of  $\text{CO}_2^{2+}$  is about 37 eV and Ionization potential of  $\text{CO}_2^{3+}$  is 72 eV, the revisiting electron can multiply (2+, 3+) ionize the  $\text{CO}_2$  [174]. The simulation supports the formation of doubly and triply charged fragments in the intensity range of 0.24 - 0.60 in which the revisiting electron has more kinetic energy than the ionization potential of doubly

or triply ionized CO<sub>2</sub>. The process of ionization induced by revisiting electrons and the formation of charged fragments are schematically represented in Figure 5.8. This figure explains the possible pathways for the formation of singly, doubly, and triply ionized CO<sub>2</sub>. The pathways for singly charged C<sup>+</sup>, O<sup>+</sup>, CO<sup>+</sup> ions, doubly charged C<sup>2+</sup>, O<sup>2+</sup> and triply charged C<sup>3+</sup>, O<sup>3+</sup> ions observed and shown in figure 5.7 are described in equations [5.4 to 5.14]. The revisiting electrons easily access these dissociative states. In summary, the revisiting electrons in the PTC field affect the ionization and fragmentation in CO<sub>2</sub>.

### 5.3.5 Intensity dependent two-color photoionization CO<sub>2</sub>: OTC

Two-color (OTC) induced ionization of CO<sub>2</sub> is investigated to understand the ionization and fragmentation in the OTC field. The intensity dependence is discussed in this section. The CO<sub>2</sub><sup>+</sup> and CO<sub>2</sub><sup>2+</sup> ion yield as a function of the intensity ratio ( $I_{2\omega}/I_{\omega}$ ) for OTC field is shown in figure 5.9. The yield of CO<sub>2</sub><sup>2+</sup> beyond 0.6 of intensity ratio is about zero (a sub hundred counts, huge error bar, not shown in figure). In the range of 0.24 - 0.5, the yield of CO<sub>2</sub><sup>2+</sup> ions have a peak kind of profile. We can notice the enhancement in CO<sub>2</sub><sup>2+</sup> yield and the depletion of CO<sub>2</sub><sup>+</sup> yield in this range. This trend in CO<sub>2</sub><sup>2+</sup> formation is due to nonsequential double ionization (NSDI) in the OTC field. Interestingly, the yield of CO<sub>2</sub><sup>+</sup> is increasing as a function of the intensity ratio, peaking at around 0.6 and decreasing. This trend indicates a formation of metastable CO<sub>2</sub><sup>+</sup> ions in 0.4 - 0.8 of intensity ratio. Below 0.4 of intensity ratio, the NSDI process is dominant, and thus, depletion of CO<sub>2</sub><sup>+</sup> population is observed.

Singly charged fragments such as C<sup>+</sup>, O<sup>+</sup>, and CO<sup>+</sup> yield as a function of intensity ratio is shown in the middle panel of figure 5.9. The O<sup>+</sup> yield is the highest, and the CO<sup>+</sup> yield is the lowest. The yield trend is almost constant in the range of 0.6 - 1.2, which is possible when the ionization rate and fragmentation yield are not much affected by the intensity ratio in this range. A slightly increasing trend in O<sup>+</sup> and C<sup>+</sup> ions in this range is due to multiple dissociative channels contributing to the yield of these ions. In the range of 0.24

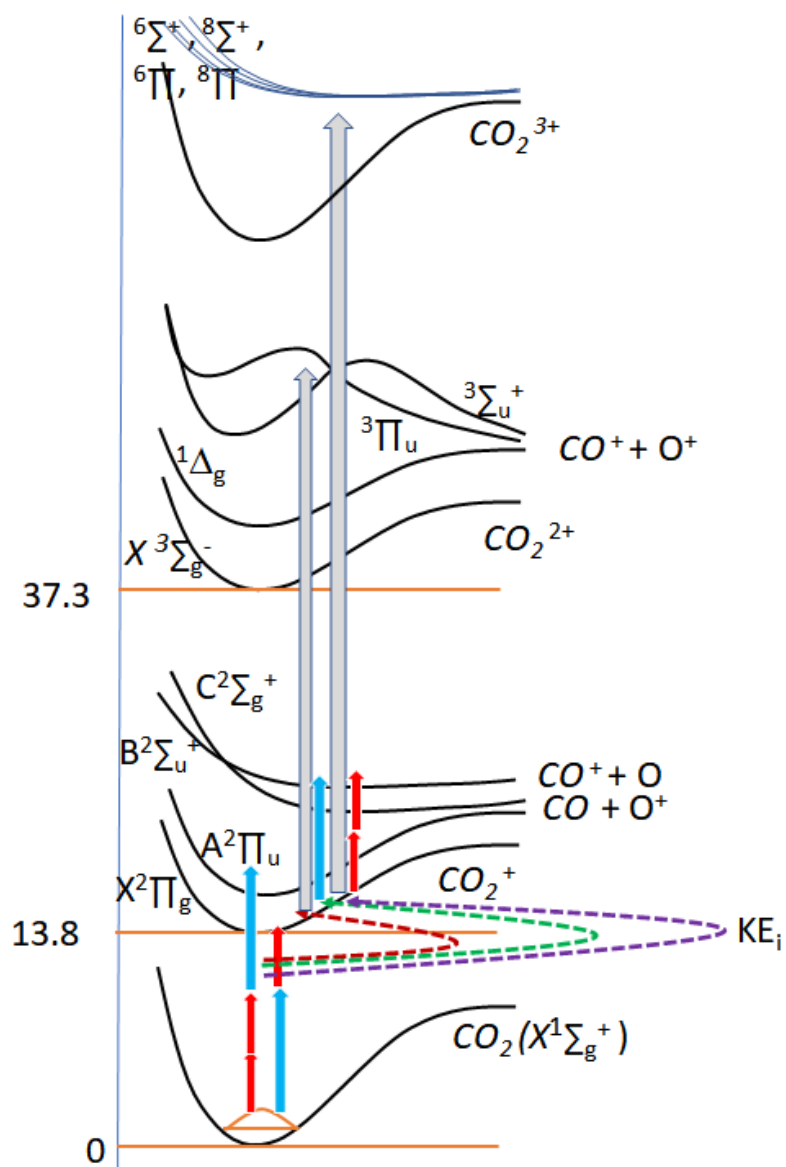


Figure 5.8: Schematic of potential energy curves for singly, doubly, and triply ionized CO<sub>2</sub>. The two colors-induced ionization and tunnel electron revisit are schematically presented.

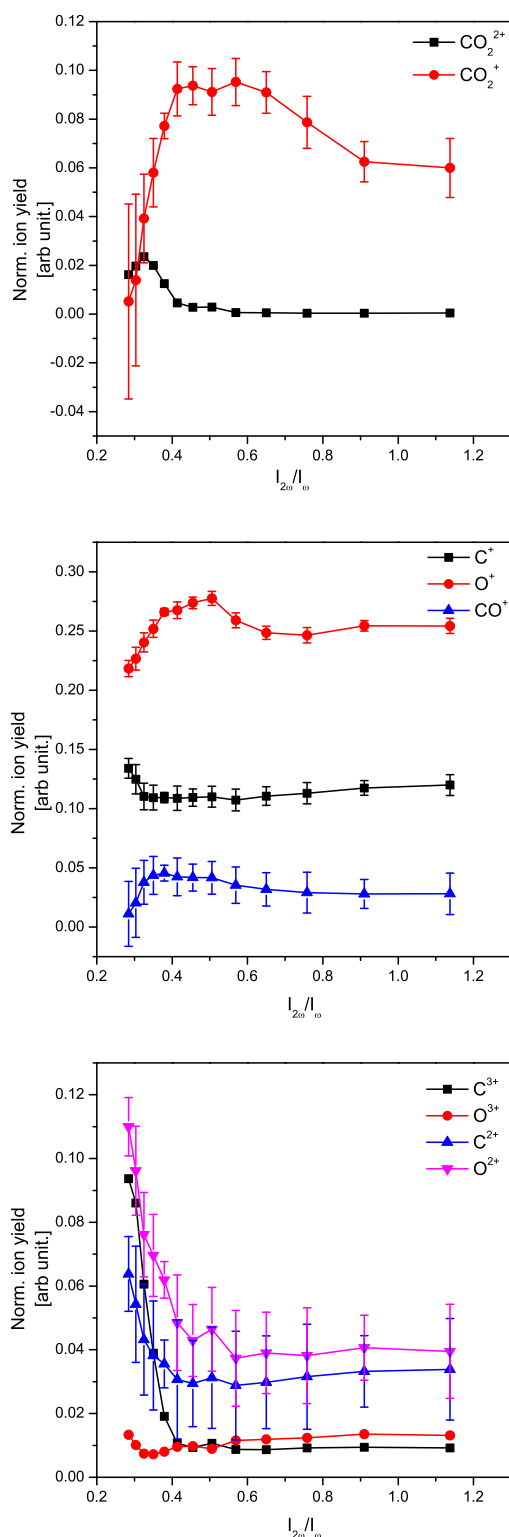


Figure 5.9: [top] The  $\text{CO}_2^+$  and  $\text{CO}_2^{2+}$  ion yield as a function of intensity ratio ( $I_{2\omega}/I_{\omega}$ ) induced by OTC field. [mid] The charged fragments  $\text{C}^+$ ,  $\text{O}^+$ , and  $\text{CO}^+$  ion yield as a function of intensity ratio. [bottom] Doubly and triply charged fragments trend as a function of intensity ratio. Error bars obtained from measured counts are shown in each plot.

- 0.6 of intensity ratio, single-charged fragments  $O^+$  and  $CO^+$  follow the  $CO_2^+$  trend. Further, the trend of these ions is similar to the trend induced by PTC.

The doubly and triply charged fragments yield trend as a function of intensity ratio is shown in the bottom panel of figure 5.9. It is observed that all the ions saturate (have constant yield) beyond the ratio of 0.4. The  $O^{2+}$  yield is highest compared to other doubly and triply charged species. The  $C^{2+}$  and  $O^{2+}$  yield trend is similar. In the range of 0.24 - 0.5 of intensity ratio, the  $O^{3+}$  has the lowest yield, and beyond the 0.5, its yield increases slightly and crosses the yield trend of  $C^{3+}$ . It is interesting to see a high yield of  $C^{3+}$  in the range of 0.24 - 0.5 of intensity ratio. The observed trend in yield of  $C^{2+}$ ,  $O^{2+}$ ,  $C^{3+}$ , and  $O^{3+}$  is due to the processes induced by two-color field and contribution of multiple dissociative channels of doubly or multiply ionized  $CO_2$ . The observed trend is similar to the PTC case. In summary, we learned that the intensity of two-color play a role in ionization and fragmentation. We now extend our study to the relative phase dependence ionization and fragmentation of  $CO_2$ , which is discussed in the next section.

### 5.3.6 Phase dependent two-color photoionization $CO_2$ : PTC

Single and doubly charged  $CO_2$  ions yield as a function of the relative phase between fundamental wave (FW) and second harmonic (SH) is shown in the top panel of Figure [5.10]. The FW intensity ( $I_\omega = 0.24 \text{ PW/cm}^2$ ) and SH intensity ( $I_{2\omega} = 0.48 \text{ PW/cm}^2$ ) were fixed during the measurement. Interestingly, the yield of  $CO_2^{2+}$  is more than the yield of  $CO_2^+$ . The  $CO_2^+$  and  $CO_2^{2+}$  yields trend are oscillatory, and it oscillates with a period of  $\pi$ . Further, these ion yield trends are correlated, which means that the formation and fragmentation rates of these ions are similar as a function of relative phase at the used intensities.

The singly charged fragments yield trend as a function of relative phase is shown in the mid panel of Figure [5.10]. The oscillatory trend in single-charged fragments is also observed. Further, the yield of  $O^+$  and  $CO^+$  are correlated, but the yield of  $C^+$  is anti-correlated with  $O^+$  and  $CO^+$  ions yield. In the yield

of these ions, the dissociative states of CO<sub>2</sub><sup>+</sup> and CO<sub>2</sub><sup>2+</sup> are contributed through various dissociative channels [5.6 - 5.10]. The O<sup>+</sup> and CO<sup>+</sup> yield trend follows the yield trend of CO<sub>2</sub><sup>+</sup> and CO<sub>2</sub><sup>2+</sup> which is expected and found here. On the other hand, the C<sup>+</sup> yield is maximum when the parent ion or O<sup>+</sup> and CO<sup>+</sup> yields are lowest. This observation suggests the dissociation process which is producing C<sup>+</sup> has more probability at  $-0.5\pi$  or  $-1.5\pi$  of the relative phase.

The doubly and triply charged fragments yield trend as a function of relative phase is shown in the bottom panel of Figure [5.10]. The doubly charged fragments, C<sup>2+</sup> and O<sup>2+</sup>, are correlated with each other, while both are anti-correlated with the parent ions. The yield of triply charged C<sup>3+</sup> and O<sup>3+</sup> are both correlated with the parent ions. This anti-correlation between the doubly and triply-charged fragments can be attributed to multiple dissociative channels, which are enhanced or depleted at a fixed relative phase. Thus the unique trend in doubly or triply-charged fragments yield is observed.

For the observed oscillation in the yield of singly and doubly charged ions we have estimated the modulation depth of about 6 times for C<sup>+</sup>, 10 times for O<sup>+</sup> and 1.15 times for CO<sup>+</sup> compared to the modulation depth of CO<sub>2</sub><sup>+</sup>. The doubly ionized fragments O<sup>2+</sup> and C<sup>2+</sup> are 5.4% and 9.42% respectively. While the triply charged fragments O<sup>3+</sup> and C<sup>3+</sup> are at 41% and 3.65% respectively. To understand these ions yield trends induced by the tunnel electrons, we have performed the classical electron trajectories simulation. For the revisiting trajectories, the birth time as a function of the relative phase is shown in the top panel of Figure [5.11]. This result tells us that the tunnel electrons are revisiting to parent ion and have a high probable at 0.2 of the relative phase and a low probable at 0.9 of the relative phase. Similar to this simulation result, we have experimentally observed the yield trend of singly, doubly ionized CO<sub>2</sub> and its fragments. Thus the simulation confirmed that revisiting electrons further ionizes the parent, contributing to the various charged fragments. The maximum return electron kinetic energy as a function of the relative phase is shown in the bottom panel of Figure [5.11]. The maximum kinetic energy varies from 130 eV to 110 eV, which is enough to multiply ionized CO<sub>2</sub>. The observed doubly, and triply charged fragments are possibly due to revisiting electron-induced

processes. The results are consistent with the observed ion yield results.

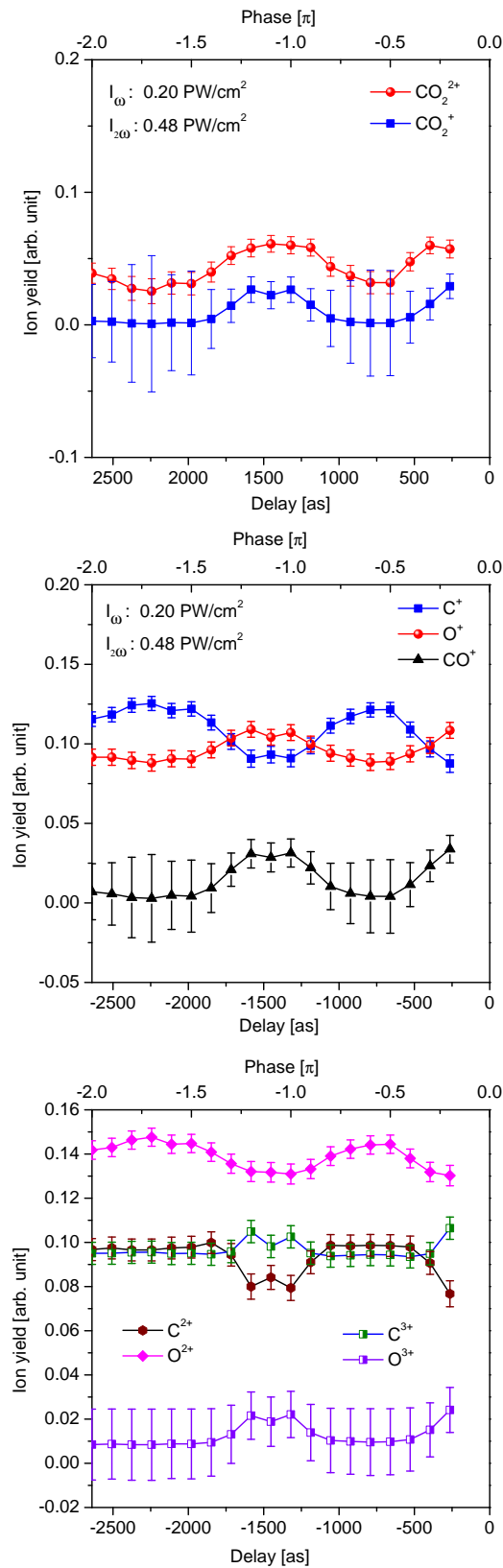


Figure 5.10: [top]  $\text{CO}_2^+$  and  $\text{CO}_2^{2+}$  ion yield as a function of relative phase ( $\Delta\phi$ ) induced by PTC field. [mid] The charged fragments  $\text{C}^+$ ,  $\text{O}^+$  and  $\text{CO}^+$  ion yield as a function of relative phase ( $\Delta\phi$ ). [bottom] Doubly and triply charged fragments  $\text{C}^{2+}$ ,  $\text{O}^{2+}$ ,  $\text{C}^{3+}$  and  $\text{O}^{3+}$  ion yields are represented as a function of relative phase ( $\Delta\phi$ ). The ion yields are observed at intensities  $0.20 \text{ PW/cm}^2$  of FW and  $0.48 \text{ PW/cm}^2$  of SH.

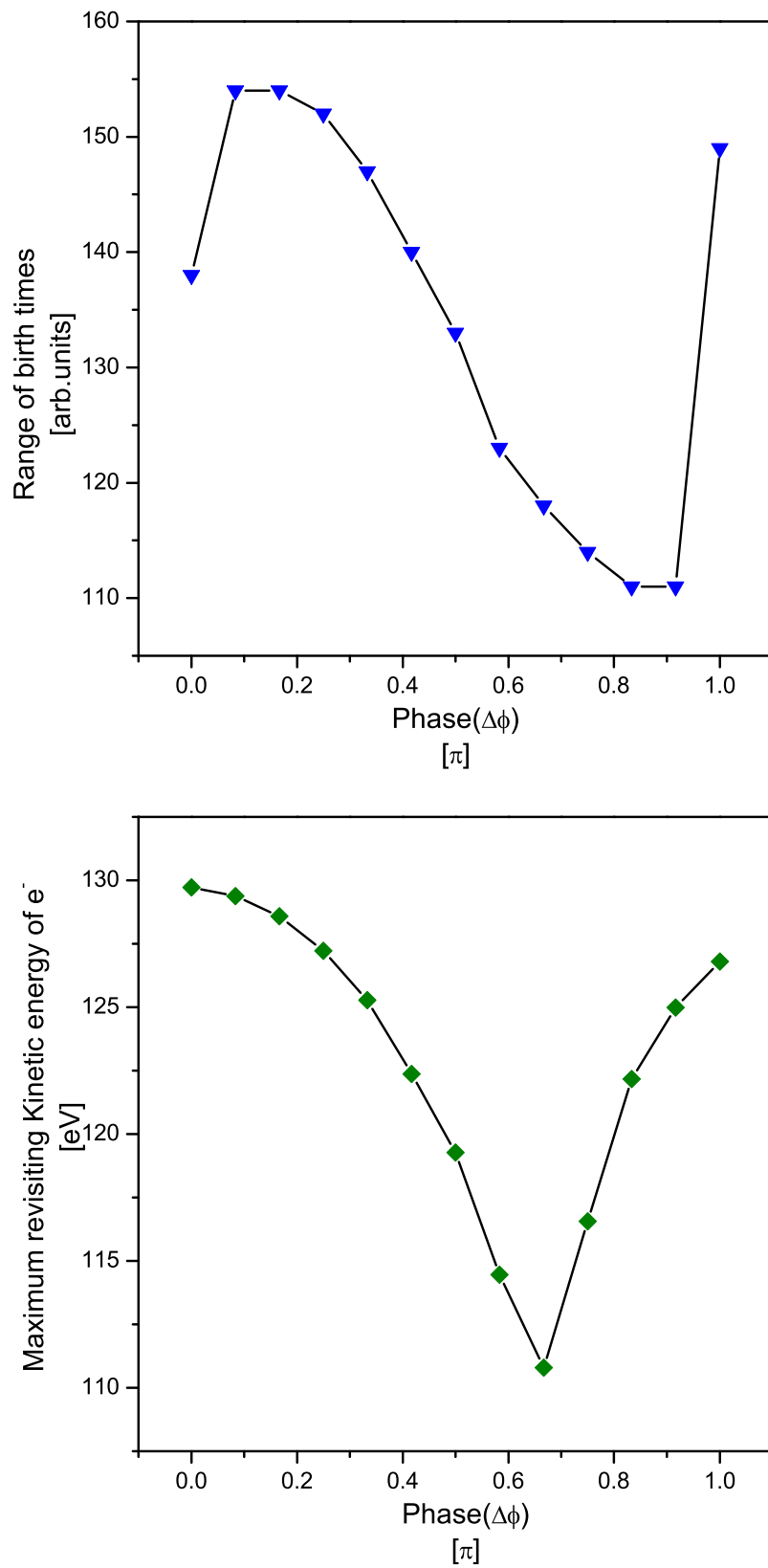


Figure 5.11: The revisiting kinetic energy of the electrons as a function of relative phase ( $\Delta\Phi$ ) at intensities  $0.20\text{PW}/\text{cm}^2$  of FW and  $0.48\text{PW}/\text{cm}^2$  of SH.

### 5.3.7 Phase dependent two-color photoionization CO<sub>2</sub>: OTC

Our investigation on the OTC-induced photoionization and fragmentation of CO<sub>2</sub> is discussed here. Similar to PTC, we have observed the singly and doubly charged CO<sub>2</sub> and their yields are oscillating as a function of the relative phase of the two-color OTC field. The yield trend of CO<sub>2</sub><sup>+</sup> and CO<sub>2</sub><sup>2+</sup> as a function of relative phase is shown in the top panel of Figure [5.12]. Interestingly, the yield of CO<sub>2</sub><sup>2+</sup> is lower compared to CO<sub>2</sub><sup>+</sup>. Further, the yield trend of CO<sub>2</sub><sup>2+</sup> is anti-correlated with the yield trend of CO<sub>2</sub><sup>+</sup>. These observations in the OTC case are opposite that the PTC case (Figure [5.10]). The observed trend in the case of OTC is due to the modulation of tunnel electron trajectories. The revisiting electron kinetic energy is also low compared to PTC (this is based on simulation), which explains the low yield of CO<sub>2</sub><sup>2+</sup>. Further, the opposite trend in yield of CO<sub>2</sub><sup>2+</sup> with CO<sub>2</sub><sup>+</sup> indicates that the formation of CO<sub>2</sub><sup>2+</sup> is due to the NSDI in this process, the double ionization enhanced and singly ionization population depleted.

The singly charged fragments (like C<sup>+</sup>, O<sup>+</sup>, and CO<sup>+</sup>) yield as a function of phase is shown in the bottom panel of Figure [5.12]. The yield of C<sup>+</sup> is the highest, and the yield of CO<sup>+</sup> is the lowest. This trend is similar to PTC. The yield of O<sup>+</sup> and CO<sup>+</sup> oscillates with a period of  $\pi$ . The trend is also correlated similarly to PTC. The yield C<sup>+</sup> fluctuates as a function of the relative phase, and thus difficult to confirm the oscillatory trend. The observed trend of these singly charged fragments is due to OTC-induced ionization and fragmentation of ionized CO<sub>2</sub>.

The doubly and triply charged fragments yield as a function of the relative phase is shown in Figure 5.13. The O<sup>2+</sup> yield is more than the C<sup>2+</sup> and oscillates in phase (correlated) similar to PTC. In the case of triply charged fragments, C<sup>3+</sup> yield is more than the O<sup>3+</sup> yield which is similar to PTC, but it differs from PTC in the case of an oscillatory trend. Here the oscillatory trend is anti-correlated between the yield of O<sup>3+</sup> and C<sup>3+</sup>. This trend is due to the population of multiple dissociative states (contributing to the yield of

these ions) induced by revisiting electrons. Here, the OTC induced-modulation of electron trajectories selectively ionizes the CO<sub>2</sub><sup>+</sup> ion to multiply ionized CO<sub>2</sub><sup>+</sup> which produces more C<sup>3+</sup> and less O<sup>3+</sup> at 0.5  $\pi$  phase and trend follow the relative phase.

For the observed oscillation in the yield of singly and doubly charged ions we have estimated the modulation depth of about 12 times for C<sup>+</sup>, about 25 times for O<sup>+</sup> and about 5 times for CO<sup>+</sup> compared to the modulation depth of CO<sub>2</sub><sup>+</sup>.

The modulation depth of doubly ionized fragments O<sup>2+</sup> and C<sup>2+</sup> are 12% and 5% respectively. While the triply charged fragments O<sup>3+</sup> and C<sup>3+</sup> are at 16.7% and 10.48% respectively.

In ion yield as a function of relative phase, we learned that the yields are oscillatory and sensitive to the relative phase. Based on classical trajectories simulation, we attempted to explain the observed oscillation. The two-color may also influence the photoelectron yield, and the modulation of tunnel electron trajectories may induce the asymmetry in photoelectron momentum distribution. In the next section, we have discussed the two-color-induced effect on the photoelectron momentum distribution.

## 5.4 Photoelectron momentum distribution of CO<sub>2</sub> induced by two-color (PTC) field

Photoelectron momentum distribution (PEMD)s of CO<sub>2</sub> induced by the two-color (PTC) fields at relative phase 0 is displayed in Figure 5.14, recorded at 0.2 PW/cm<sup>2</sup> and 0.46 PW/cm<sup>2</sup> for FW and SH respectively. The polarization of both colors was horizontal at a relative phase of 0. ATI rings are clearly visible from the figure. Similarly, at different relative phases, photoelectron momentum distribution (PEMD) induced by 400 nm is represented in the bottom panel of Figure 5.14. The photon energy of 400 nm (3.3eV) is double that of 800 nm, and thus the ATI rings are much farther spaced. At the used intensity, the counts of the low-energy electrons induced by 400 nm pulse are clearly visible in the bottom

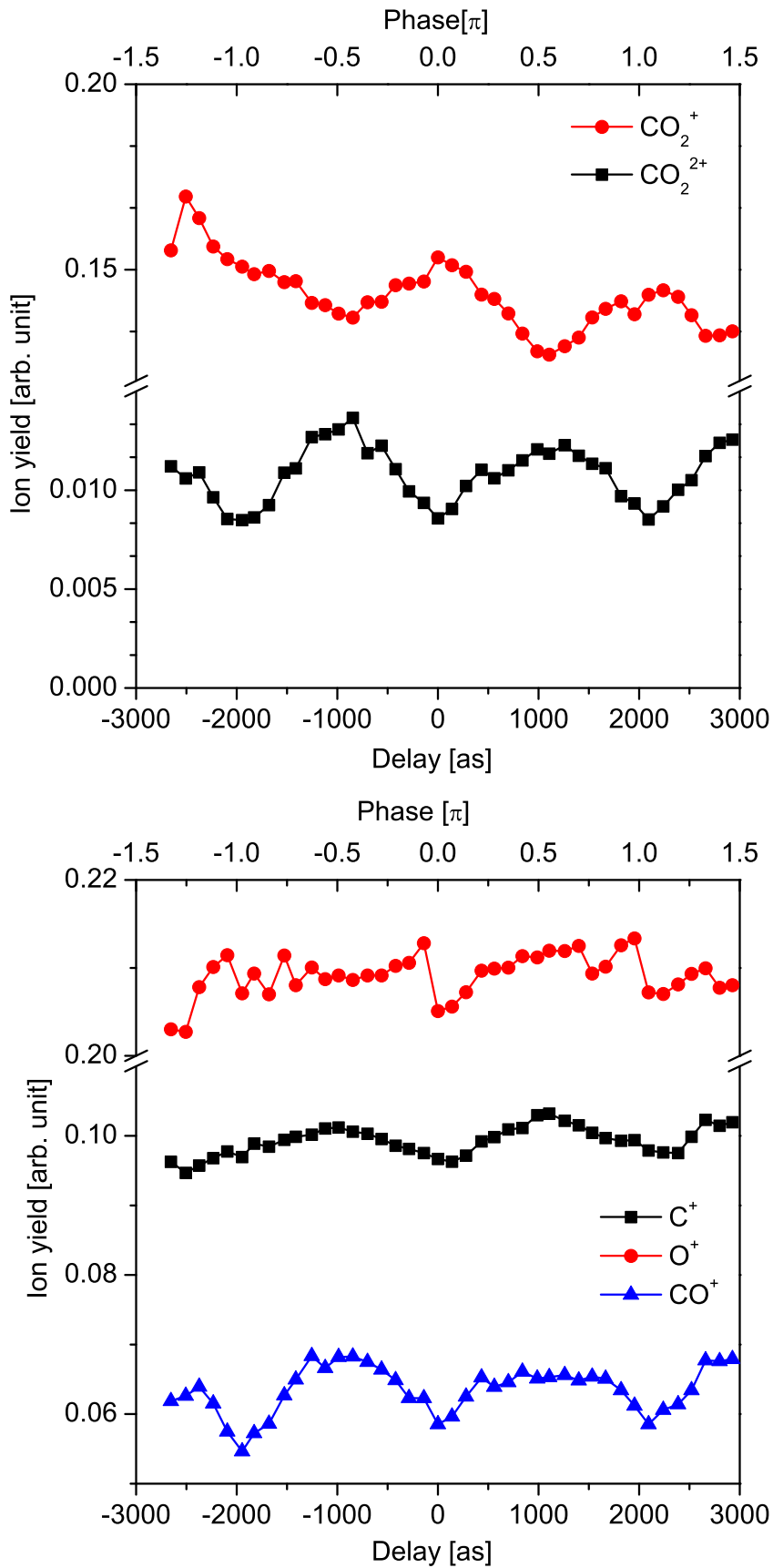


Figure 5.12: [top]  $\text{CO}_2^+$  and  $\text{CO}_2^{2+}$  ion yield as a function of relative phase ( $\Delta\phi$ ) induced by OTC field. [bottom] The charged fragments  $\text{C}^+$ ,  $\text{O}^+$  and  $\text{CO}^+$  ion yield as a function of relative phase ( $\Delta\phi$ ). The ion yields are observed at intensities 0.20 PW/cm<sup>2</sup> of FW and 0.168 PW/cm<sup>2</sup> of SH. The counts of  $\text{CO}^+$ ,  $\text{C}^+$ , and  $\text{O}^+$  are about 12000 to 4000, and the error bar is not plotted for clarity.

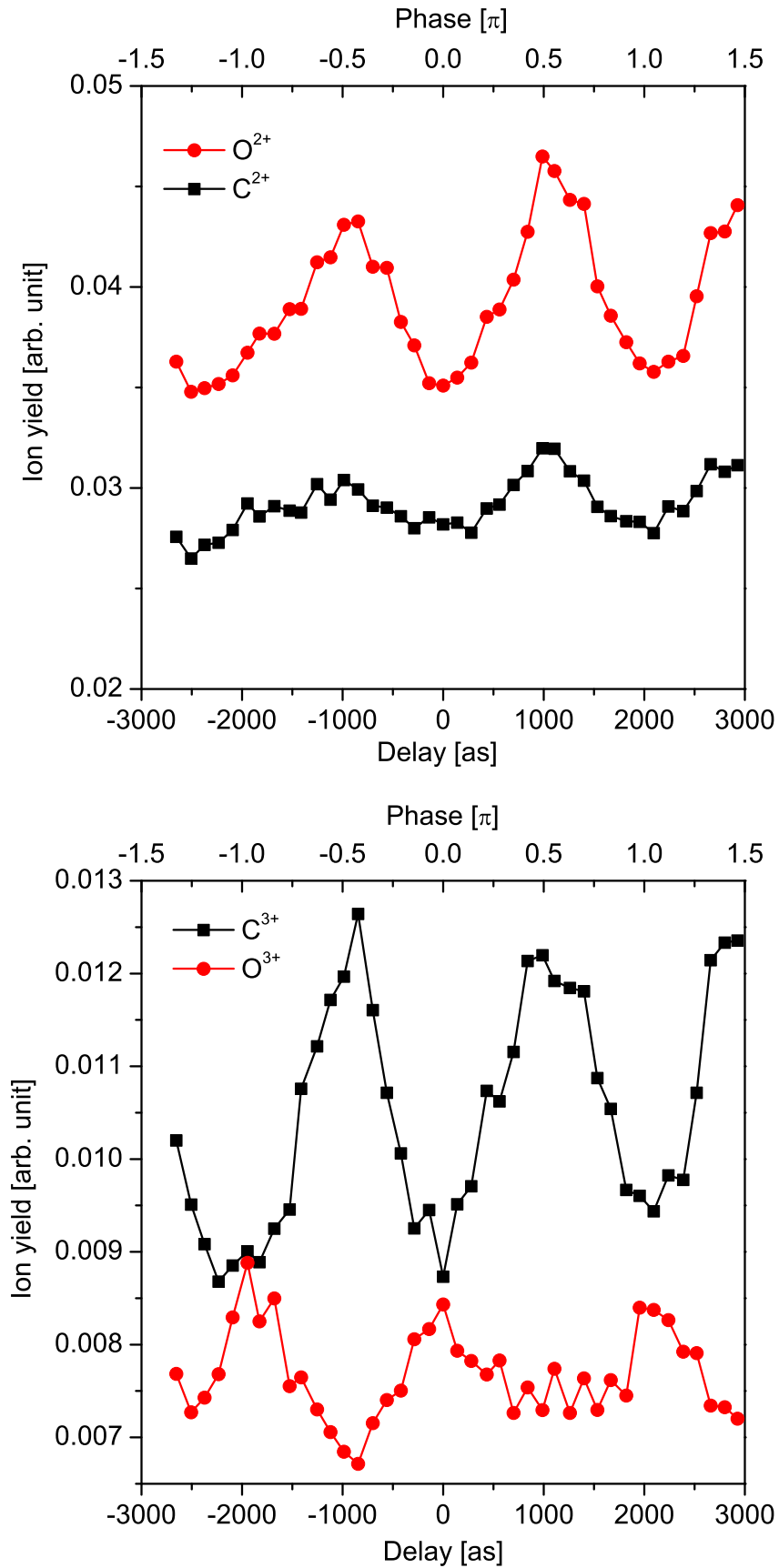


Figure 5.13: [top] Doubly charged fragments C<sup>2+</sup>, O<sup>2+</sup> ion yields as a function of relative phase ( $\Delta\phi$ ). The counts of C<sup>2+</sup> and O<sup>2+</sup> are about 5000 to 7000, and the error bar is not plotted for clarity. [Bottom] Triply charged fragments C<sup>3+</sup> and O<sup>3+</sup> ion yields as a function of relative phase ( $\Delta\phi$ ). The ion yields are observed at intensities 0.20 PW/cm<sup>2</sup> of FW and 0.168 PW/cm<sup>2</sup> of SH. The counts of C<sup>3+</sup> and O<sup>3+</sup> are about 1200 to 2500, and the error bar is not plotted for clarity.

panel of the figure. Due to contrast, the low-energy electrons in the top panel of the figure are not as clear as in the bottom figure. By comparing both PEMDs, we can see a slight variation, which is due to the two-color effect. For clear relative phase dependence on photoelectron yield, we have recorded the PEMD as a function of relative phase. The integrated PEMD yield as a function of relative phase is shown in Figure 5.15. The photoelectron yield is oscillatory as a function of the relative phase and has a period of  $\pi$ . This observation is attributed to the ionization rate by the two-color field and also due to the tunnel electron trajectories modulation in the two-color (PTC) field. As discussed, the two-color may also induce the asymmetry in photoelectron momentum distribution. The asymmetry parameter defined in equation [5.15] can tell us about the induced asymmetry by a two-color field. Detail about asymmetry parameter is discussed in the previous chapter.

Asymmetry along  $p_x$  has been evaluated at  $p_y = 0$ . Similarly, asymmetry along  $p_y$  can be obtained at  $p_x = 0$ . The asymmetry between two pixels is determined by selecting one pixel (intensity at this pixel) along the x-axis to the right of the center with intensity  $I_X$  and a matching equidistant pixel (intensity at this pixel) to the left of the center with intensity  $I_{X'}$ .

$$Asymmetry(p_x) = \frac{I_X - I_{X'}}{I_X + I_{X'}} \quad (5.15)$$

The asymmetry in PEMD induced by a two-color(400 nm + 800 nm) field is compared with a single color(400 nm) to see the variation due to the two-color field. The asymmetry parameter along  $p_x$  and also along  $p_y$  is shown in Figure 5.14 [bottom]. It is clear that the asymmetry of the photoelectron distribution is more in the presence of two-color.

## 5.5 Photoelectron momentum distribution of CO<sub>2</sub> induced by two-color (OTC) field

PEMD of CO<sub>2</sub> in the presence of two-color orthogonal fields (OTC) at a relative phase of 0 is shown in Figure 5.16. This PEMD is obtained at FW intensity of

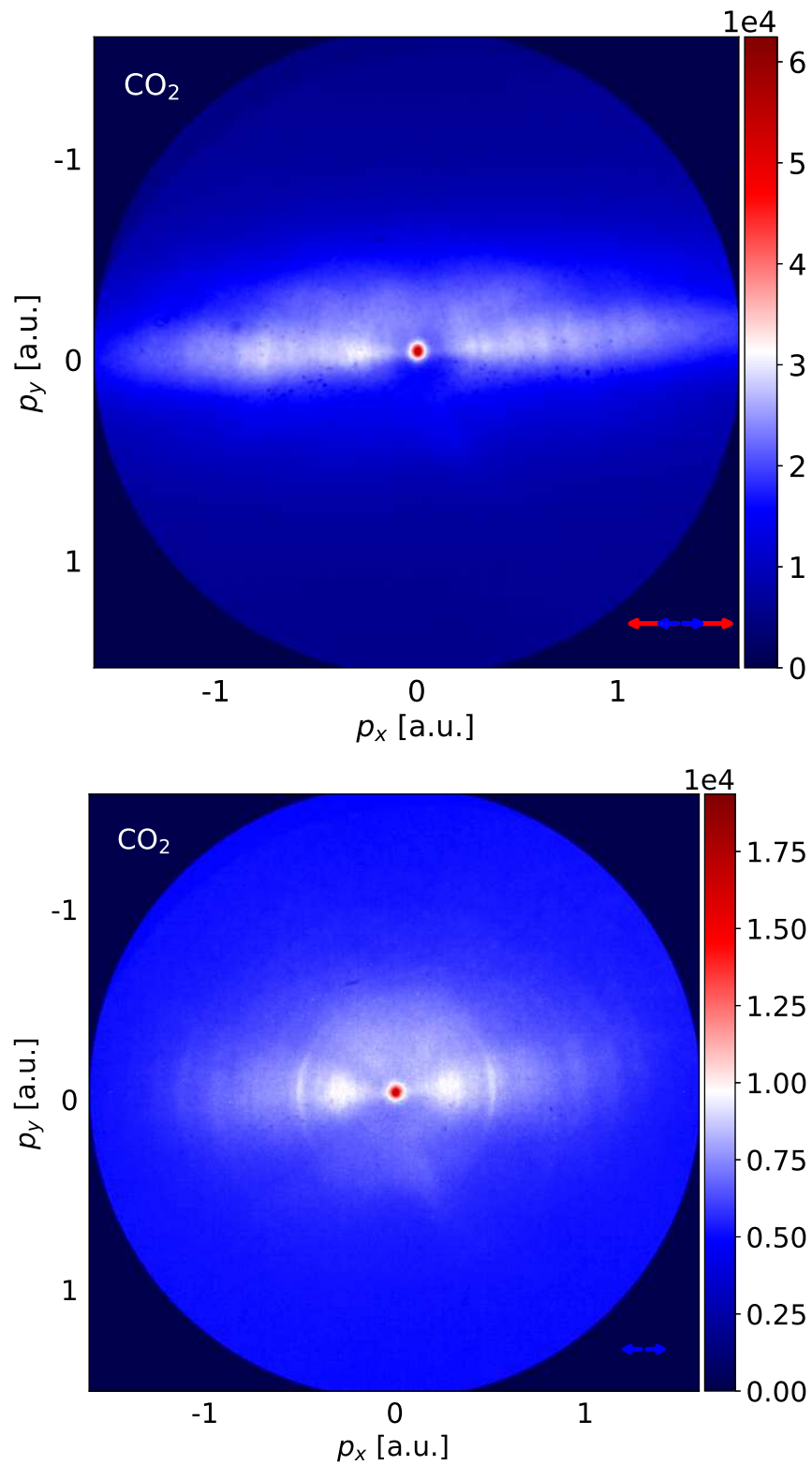


Figure 5.14: [top]Photoelectron momentum distribution induced by two-color (PTC, 800 nm + 400 nm) field. [bottom]Photoelectron momentum distribution induced by single-color (400 nm) field. The polarization direction is shown in the figure.

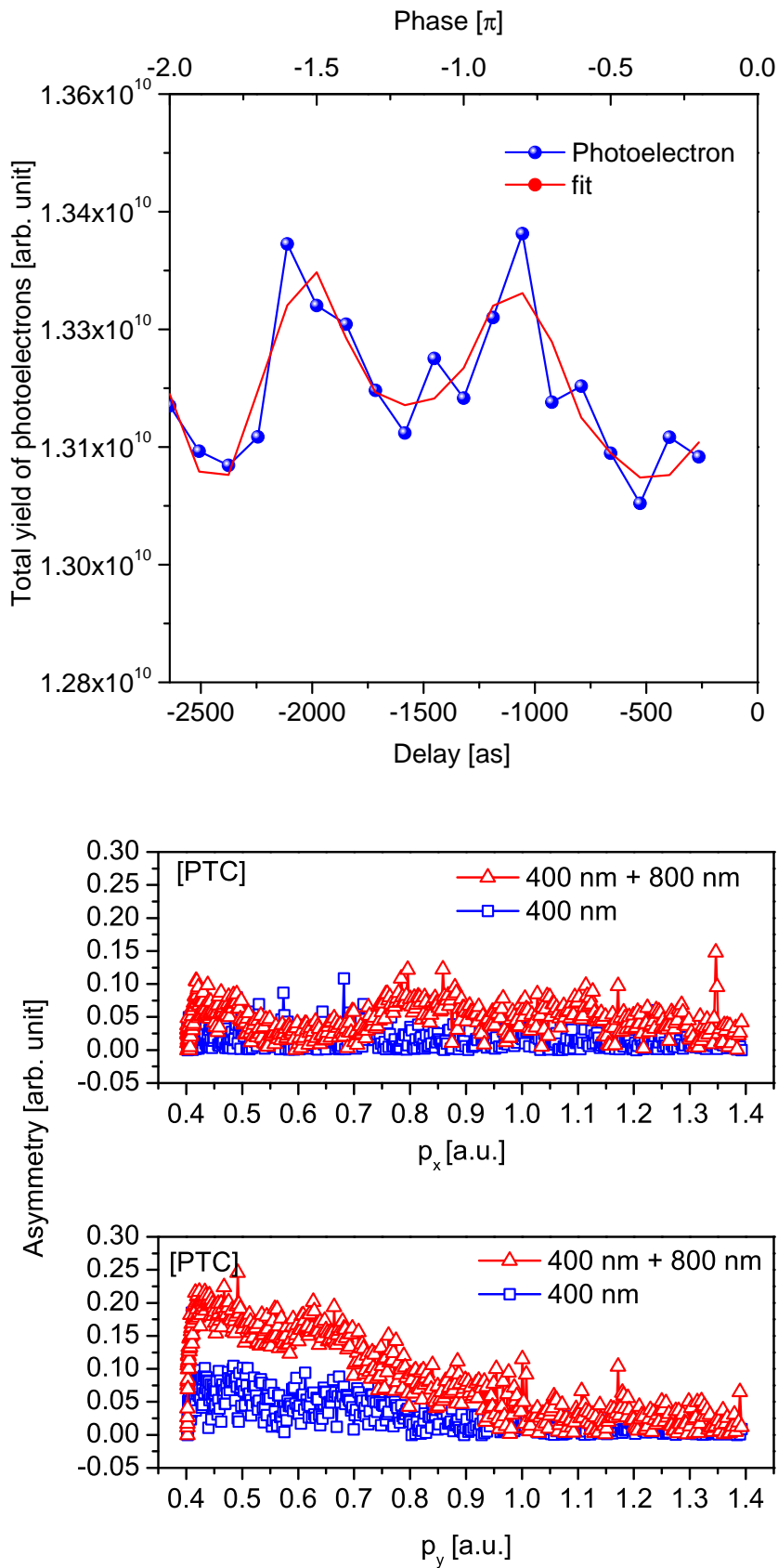


Figure 5.15: [top] Photoelectron yield as a function of relative phase. [bottom] Asymmetry along  $p_x$  and  $p_y$  induced by two-color (PTC) field at 0 relative phase.

0.2 PW/cm<sup>2</sup> and SH intensity of 0.46 PW/cm<sup>2</sup>. The observed PEMD induced by OTC is different than the PEMD of PTC (top panel of Figure 5.14). The ATI rings are not as clearly visible in OTC-induced PEMD but visible in PTC-induced PEMD. This effect is due to the polarization effect of both fields.

The PEMD induced by a single-color (400 nm, polarization was perpendicular to the detector) field is represented in the bottom panel of Figure 5.16. The distribution of electrons is concentrated at the center (zero energy) due to the polarization of the incident pulses. By comparing the single-color-induced and OTC-induced PEMDs, we can see a significant electron streaking due to the 800 nm field in the case of the OTC field.

The relative phase of the OTC field may affect the yield of photoelectrons. The integrated PEMD yield as a function of relative phase is shown in the top panel of Figure 5.16. An oscillatory trend of photoelectron yield with a period  $\pi$  is observed. This observation is similar to PTC. In summary, the relative phase between two colors plays a role in the generation of photoelectrons.

The OTC fields may also induce asymmetry in the photoelectron momentum distribution. The asymmetry parameter discussed in the previous section is computed in the presence of OTC fields. The asymmetry parameter along  $p_x$  and along  $p_y$  is shown in the bottom panel of Figure 5.16. The red data points are asymmetry values for OTC (400 nm + 800 nm), and the blue data points are asymmetry values for 400 nm. The asymmetry of OTC along  $p_x$  is comparable to that of 400 nm in the low energy regime but shows a higher degree of asymmetry beyond 0.8 a.u.

The asymmetry along  $p_y$  of the single color SH is more dominant in the lower regime ( $<0.8$  a. u. of  $p_y$ ), while in the presence of the two-color fields, the asymmetry is distributed for the low-energy electrons while for high energies (beyond 0.8), a similar trend as  $p_x$  is observed. The observed asymmetry is due to the Coulomb effect and two-color induced modulation of electron trajectories.

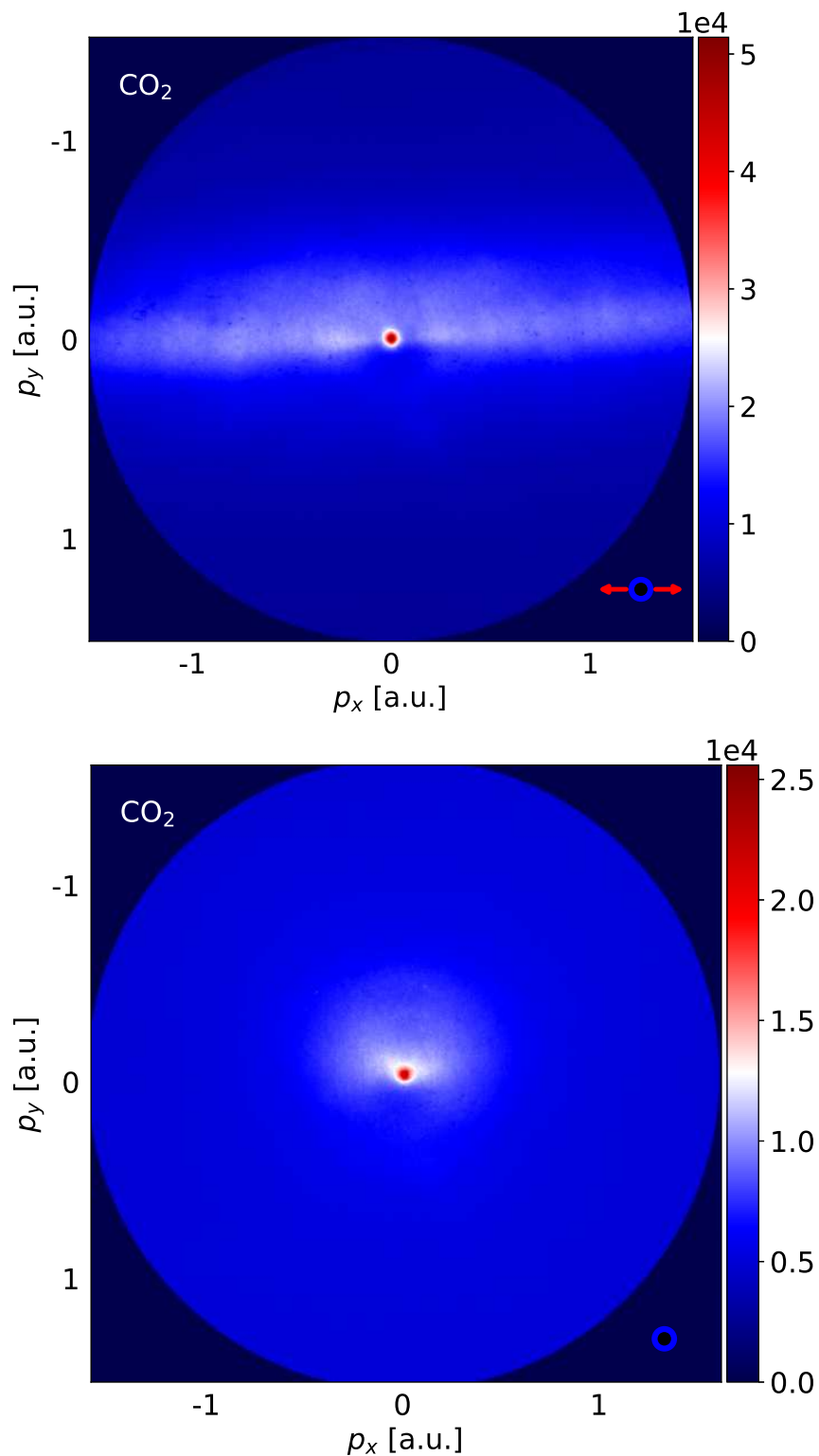


Figure 5.16: [top]Photoelectron momentum distribution induced by two-color (OTC, 800 nm + 400 nm) field. [bottom]Photoelectron momentum distribution induced by single-color (400 nm) field. The polarization direction is shown in the figure.

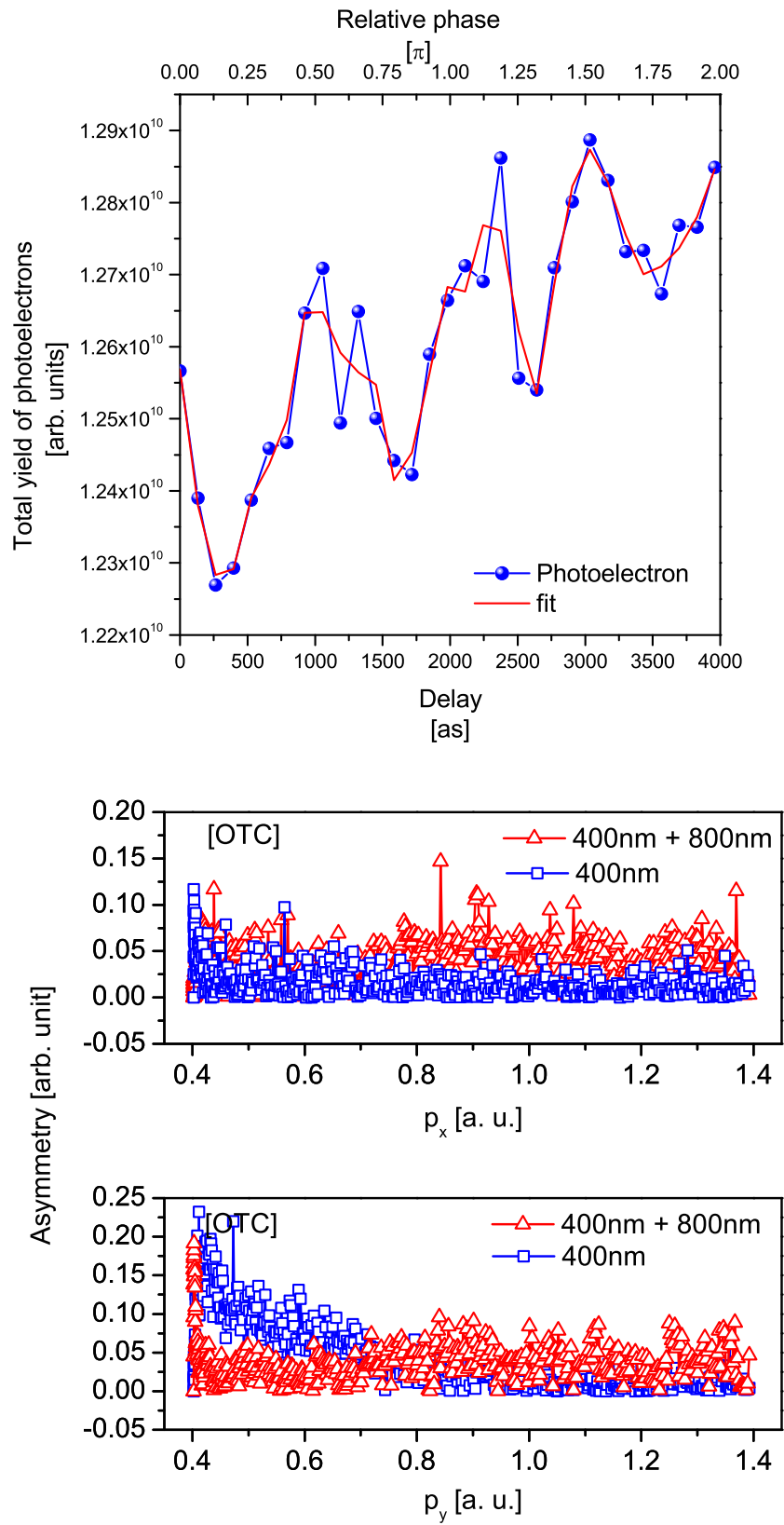


Figure 5.17: [top] Photoelectron yield as a function of relative phase. [bottom] Asymmetry along  $p_x$  and  $p_y$  induced by two-color (OTC) field at 0 relative phase.

## 5.6 Summary and Conclusions

This chapter discussed our findings on the strong-field ionization of CO<sub>2</sub> induced by single-color and two-color fields. In the single-color case, we investigated the intensity, wavelength, and pulse duration dependence on ionization and fragmentations. The findings on single-color ionization of CO<sub>2</sub> are listed below:

- **Intensity dependence:** We observed the knee structure in CO<sub>2</sub><sup>2+</sup>/CO<sub>2</sub><sup>+</sup> ion yield ratio. This knee structure is due to non-sequential double ionization (NSDI). Interestingly, the knee structure was also found in fragment ions, and results are interpreted based on classical electron trajectory simulation.
- **Wavelength dependence:** We studied the 400 nm induced ionization (MPI) and 800 nm induced ionization (TI) of CO<sub>2</sub>. We observed that the yield of CO<sub>2</sub><sup>+</sup> and CO<sub>2</sub><sup>2+</sup> is slightly higher at 800 nm compared to 400 nm, but fragmentation is high at 400 nm.
- **Pulse duration dependence:** We studied the pulse duration dependence ionization of CO<sub>2</sub>. The peak intensity was kept constant at 0.31 PW/cm<sup>2</sup> during the entire measurement in the pulse duration-dependent study. We observed that the yield of singly and doubly charged fragment yields increases as a function of increasing pulse duration.

In the two-color study, we investigated the OTC and PTC fields-induced photoionization of CO<sub>2</sub> and its fragmentation as a function of relative phase and intensity. The findings on two-color ionization of CO<sub>2</sub> are summarized below:

- **Two-color intensity dependence (PTC & OTC):** We observed that the two-color fields enhance the ionization of CO<sub>2</sub>. The doubly and triply charged fragments were observed in the mass spectrum induced by OTC and PTC fields. The intensity dependence ionization of CO<sub>2</sub> and findings are listed below:

- In PTC and OTC, the  $\text{CO}_2^+$ ,  $\text{CO}_2^{2+}$  and fragments (singly, doubly, and triply charged) yield trend is constant over the intensity ratio ( $I_{2\omega}/I_\omega$ ) of 0.6 - 1.2.
  - In the range of 0.3 - 0.6 of intensity ratio ( $I_{2\omega}/I_\omega$ ), the enhanced doubly ionization and depletion of single ionization rate is observed. This is due to NSDI in the two-color field. This trend is observed in both OTC and PTC fields.
  - Unique fragments yield trend as a function of the intensity ratio ( $I_{2\omega}/I_\omega$ ) is observed and interpreted based on the population of multiple dissociative states of doubly or triply charged  $\text{CO}_2$  by revisiting electrons.
- **Two-color phase dependence (PTC & OTC):** We studied the two-color relative phase dependence on the ion and photoelectron yields at 0.2 and 0.48 PW/cm<sup>2</sup> of FW and SH, respectively. At used intensity and given relative phase, singly, doubly, and triply charged fragments are observed, and each ion follows a unique trend as a function of relative phase, suggesting the influence of relative phase on ionization and fragmentation of ionized  $\text{CO}_2$ . The relative phase dependence ionization of  $\text{CO}_2$  and findings are listed below:
    - In PTC, the  $\text{CO}_2^+$  and  $\text{CO}_2^{2+}$  yields are correlated and oscillating as a function of relative phase. In contrast to PTC, the  $\text{CO}_2^+$  and  $\text{CO}_2^{2+}$  yields are anti-correlated in OTC. This is due to the modulation of revisiting electrons in the OTC field, which affects the double ionization rate by revisiting electrons.
    - In PTC and OTC, the  $\text{O}^+$  and  $\text{CO}^+$  yields are correlated but anti-correlated with the yield of  $\text{C}^+$ .
    - In PTC, the doubly charged fragments ( $\text{C}^{2+}$ ,  $\text{O}^{2+}$ ) yields are correlated but anti-correlated with the triply charged fragments ( $\text{C}^{3+}$ ,  $\text{O}^{3+}$ ). These findings suggest that the revisiting electrons are affecting the fragmentation dynamics of ionized  $\text{CO}_2$ .

- The photoelectron yield (induced by PTC or OTC) as a function of relative phase is oscillatory and has a period of  $\pi$ . This observation is attributed to the relative phase effect on the photoionization of CO<sub>2</sub>.
  
- **Photoelectron momentum distribution and asymmetry (PTC & OTC):** We studied the photoelectron momentum distribution (PEMD) induced by the two-color fields using Velocity Map Imaging Spectrometer. We compared the PMED of two-color with the single-color SH-induced PEMD. We observed the signature of two-color influences on the PEMD. Further, we investigated the asymmetry in momentum distribution induced by a two-color field. The results suggest that the two-color modulates the revisiting electron trajectories and thus induces the asymmetry in photoelectrons.

In conclusion, a two-color scheme is a powerful technique to investigate the sub-cycle(attosecond) resolved processes in molecules. Further, we find that the revisiting electrons play a crucial role in enhanced ionization and fragmentation.

# Chapter 6

## Summary and Future Scope

In conclusion, strong-field ionization of atoms (Ar, Xe) and molecules ( $\text{N}_2$ , CO and  $\text{CO}_2$ ) were investigated using single-color and two-color laser fields in this thesis work. The thesis focuses on tunneling electron revisit-induced processes in atoms and molecules. We use a two-color scheme to modulate the revisiting electron trajectories, and their influence on the excitation, ionization, and fragmentation of molecules is investigated in detail. The findings have strengthened our understanding of tunnel electron revisit-induced process and control of molecular reactions.

### [A] Summary of scientific instruments developed for thesis work

For my thesis, I have developed the following scientific instruments

- Multi-plate Velocity Map Imaging Spectrometer
  - I have performed charged particle simulation for the development of VMI setup. From the fabrication of electrodes to their assembly, detector mounting, etc., were done by me. I have also performed the calibration of VMI and utilized this setup for thesis work.
- Two-color setup: I have developed three types of two-color setups to confirm that my oscillatory nature of ion yield is reproducible. Below is the

list of setups that I developed for thesis work. After calibration and reproducibility check, I utilized only the pump-probe type setup in most of the experiments for the thesis.

- Two-color pump-probe type setup
- Calcite plate-based two-color setup
- Wedge mirror-based two-color setup

## [B] Summary of scientific studies for thesis work

### Strong-field ionization of Atoms:

First, we studied the strong-field ionization of atoms (Argon and Xenon) using the single-color (800nm) and two-color (800 nm + 400 nm) laser field. We measured the ions yield by utilizing the time-of-flight mode of VMI spectrometer. The ion yield as a function of laser intensity is obtained, and this experimental result is fitted with the ADK ionization rate. The experimental and theoretical (ADK) ionization rate matches well beyond the  $0.5 \times 10^{-14}$  W/cm<sup>2</sup> of laser intensity. Below this value, we noticed a deviation of ADK ionization rate with experimental results. As the ADK theory gives us the tunneling ionization rate, its prediction breaks down in the low-intensity multiphoton absorption regime, which explains the deviation. This observation is consistent with previously reported works.

To understand the ionization rate with a two-color laser field, we obtained the ions yield ratio ( $\text{Ar}^{2+}/\text{Ar}^+$ ) as a function of two-color laser intensity. These results were compared with the single-color case. Interestingly, we observed a significant deviation in ion yield ratio in the two-color field compared to the single-color field in the same intensity range ( $0.3 \times 10^{-14}$  W/cm<sup>2</sup> -  $0.7 \times 10^{-14}$  W/cm<sup>2</sup>). This unique trend in two-color is due to electron revisit induced enhanced double ionization and depletion of single ionization rate. Our simulation also supports the experimental findings.

Further, in Ar, we investigated the ion yield as a function of the relative phase. We observed that the ion yield is very much sensitive to the two-color

phase and also the polarization of both colors. The oscillation with a period of  $\pi$  in ion yield as a function of relative phase is observed in OTC and PTC. Similar to Argon, we have also performed a study on Xenon and found that the ion yield trend as a function of intensity and relative phase has a similar trend as we observed in Argon.

## **Strong-field ionization of diatomic molecules: N<sub>2</sub> and CO**

Next, we studied the strong-field ionization of diatomic molecules (N<sub>2</sub> and CO) using a two-color laser field and a Velocity Map Imaging spectrometer. Both OTC and PTC polarization combinations were used in this study.

First, we investigated the strong-field ionization of N<sub>2</sub> and CO using two-color laser fields with orthogonal (OTC) and parallel (PTC) polarizations. The intensity dependence on fragmentation yield is studied in detail. We observed that the fragments yield is sensitive to the intensity of the two-color field. The observed results are explained based on simulations. The phase-dependent ion yield and fragmentation of these molecules were evaluated under both OTC and PTC conditions. It was found that the ion yield oscillates with a period of  $\pi$  for both CO and N<sub>2</sub>. The fragment ion yield was found to have an anti-correlated trend with the parent ions in the case of OTC in N<sub>2</sub>, but not in CO. In contrast, the CO<sup>+</sup> ion yield was found to be anti-correlated with its charged fragments in the case of PTC and was found to be three times higher than the OTC case. On the other hand, the anti-correlated oscillatory trend in the N<sub>2</sub><sup>+</sup> yield with fragment N<sup>+</sup> was found to be similar in both OTC and PTC. The results of this study suggest that the ion yield is highly sensitive to the relative phase of the two-color field, and that the two-color field can be used to modulate electron trajectories and control the fragment ion yield of ionized molecules.

Additionally, the photoelectron momentum distributions of CO and N<sub>2</sub> induced by OTC and PTC at relative phases of 0 and  $\pi/2$  were studied. It was found that the PEMD of N<sub>2</sub> is different from the PEMD of CO induced by the two-color fields and that this difference is likely due to molecular orbital contributions and the modulation of electron trajectories in the two-color field.

The asymmetry parameter was also computed and analyzed for  $p_x$  and  $p_y$  at the relative phases of 0 and  $\pi/2$ . Variation in the asymmetry parameter was observed for both molecules under both OTC and PTC conditions, and classical electron trajectory simulations suggest that electron revisiting-induced processes in the two-color fields may influence the ion yield trend and the asymmetry in the photoelectrons.

### **Strong-field ionization of triatomic molecule: CO<sub>2</sub>**

This study has two parts. In part I, we focused on the laser (single-color) induced ionization of CO<sub>2</sub>. In part II, we studied the two-color laser field-induced ionization and fragmentation of CO<sub>2</sub>.

The findings of single-color induced ionization and fragmentation of ionized CO<sub>2</sub> are summarized below:

1. We observed that the doubly ionization of CO<sub>2</sub> at 0.15 PW/cm<sup>-2</sup> is due to the nonsequential double ionization. This finding is based on the observed knee structure in yield ratio (CO<sub>2</sub><sup>2+</sup>/CO<sub>2</sub><sup>+</sup>) as a function of laser intensity.
2. The knee structure is even observed in the fragment yield as a function of laser intensity. The yield of singly and doubly charged fragments above 0.25 PW/cm<sup>-2</sup> are the same and have saturating trend, representing the fragmentation processes at such high intensity is reached to a saturation level.
3. In wavelength-dependent ionization and fragmentation of ionized CO<sub>2</sub> is studied using 400 nm and 800 nm wavelengths, 29fs, and linearly polarized laser pulses. We observed the significant yield of doubly charged ions such as CO<sub>2</sub><sup>2+</sup>, C<sup>2+</sup>, and O<sup>2+</sup> at 400nm. These ions are not observed at 800nm with the same intensity.
4. The pulse duration-dependent ionization of CO<sub>2</sub> and its fragmentation and ions yield analysis is performed. We have found that the singly and doubly charged ions yield is more at longer pulse durations.

5. We observed that linearly polarized light dominates over circularly polarized in the ions yield at the same intensity.

In conclusion, we have investigated the strong field ionization of CO<sub>2</sub> and observed that fragment ion yields are influenced by laser parameters.

In the two-color induced study, we investigated the ion yield as a function of two-color intensity and also its relative phase. The findings of two-color induced ionization and fragmentation of ionized CO<sub>2</sub> are summarized below:

1. We observed that the CO<sub>2</sub><sup>+</sup> and CO<sub>2</sub><sup>2+</sup> yield is constant over the intensity ratio ( $I_{2\omega}/I_{\omega}$ ) of 0.6 - 1.2. In this range, the multiple electronic states of CO<sub>2</sub><sup>+</sup>, CO<sub>2</sub><sup>2+</sup> and even higher charged CO<sub>2</sub> (3+, 4+) are populated by absorption of photons or tunnel electron recollision mechanism.
2. The oscillation in fragment ion yield as a function of relative phase is observed both in OTC and PTC.
3. We observed the asymmetry in photoelectron momentum distribution.

## Future plans

In the near future, I would like to study the followings.

- Two-color induced photoionization of Chiral molecules:
  - to understand the asymmetry induced by a two-color field in photoelectron momentum distribution (PEMD) and also the chiral potential effect on PEMD will strengthen our understanding of the chirality of molecules.
  - I would like to perform two-color photoionization of Fenchone and Camphor molecules.
- Bicircular two-color induced photoionization of PAH type molecules:
  - Iodo-Benzene

- Nitro-Benzene
- Two-color laser field-induced High Harmonic generation from molecules:
  - OCS
  - SO<sub>2</sub>

# Bibliography

- [1] Yu Hang Lai, Junliang Xu, Urszula B. Szafruga, Bradford K. Talbert, Xiaowei Gong, Kaikai Zhang, Harald Fuest, Matthias F. Kling, Cosmin I. Bologa, Pierre Agostini, and Louis F. DiMauro. Experimental investigation of strong-field-ionization theories for laser fields from visible to midinfrared frequencies. *Phys. Rev. A*, 96:063417, Dec 2017.
- [2] C Marletto, DM Coles, T Farrow, and V Vedral. Entanglement between living bacteria and quantized light witnessed by rabi splitting. *Journal of Physics Communications*, 2(10):101001, 2018.
- [3] Tanjung Krisnanda, Chiara Marletto, Vlatko Vedral, Mauro Paternostro, and Tomasz Paterek. Probing quantum features of photosynthetic organisms. *npj Quantum Information*, 4(1):1–7, 2018.
- [4] Denis G Baranov, Martin Wersall, Jorge Cuadra, Tomasz J Antosiewicz, and Timur Shegai. Novel nanostructures and materials for strong light–matter interactions. *Acs Photonics*, 5(1):24–42, 2018.
- [5] Lei Xu, Mohsen Rahmani, Yixuan Ma, Daria A Smirnova, Khosro Zangeneh Kamali, Fu Deng, Yan Kei Chiang, Lujun Huang, Haoyang Zhang, Stephen Gould, et al. Enhanced light–matter interactions in dielectric nanostructures via machine-learning approach. *Advanced Photonics*, 2(2):026003, 2020.
- [6] Cheng-Wei Qiu, Darwin Palima, Andrey Novitsky, Dongliang Gao, Weiqiang Ding, Sergei V Zhukovsky, and Jesper Gluckstad. Engineering light-matter interaction for emerging optical manipulation applications. *Nanophotonics*, 3(3):181–201, 2014.

- [7] Jinxiu Wen, Hao Wang, Weiliang Wang, Zexiang Deng, Chao Zhuang, Yu Zhang, Fei Liu, Juncong She, Jun Chen, Huanjun Chen, et al. Room-temperature strong light–matter interaction with active control in single plasmonic nanorod coupled with two-dimensional atomic crystals. *Nano letters*, 17(8):4689–4697, 2017.
- [8] Peter Salén, Martina Basini, Stefano Bonetti, János Hebling, Mikhail Krasilnikov, Alexey Y Nikitin, Georgii Shamuilov, Zoltán Tibai, Vitali Zhaunerchyk, and Vitaliy Goryashko. Matter manipulation with extreme terahertz light: Progress in the enabling thz technology. *Physics reports*, 836:1–74, 2019.
- [9] S Roy. All-optical switching in rhodopsin proteins. *Nano Biophotonics: Science and Technology*, page 333, 2007.
- [10] Eva Darko, Parisa Heydarizadeh, Benoît Schoefs, and Mohammad R Sabzalian. Photosynthesis under artificial light: the shift in primary and secondary metabolism. *Philosophical Transactions of the Royal Society B: Biological Sciences*, 369(1640):20130243, 2014.
- [11] Atanu Bhattacharya. *Ultrafast Optics and Spectroscopy in Physical Chemistry*. World Scientific, 2018.
- [12] Robert Dods, Petra Båth, Dmitry Morozov, Viktor Ahlberg Gagnér, David Arnlund, Hoi Ling Luk, Joachim Kübel, Michał Maj, Adams Vallejos, Cecilia Wickstrand, et al. Ultrafast structural changes within a photosynthetic reaction centre. *Nature*, 589(7841):310–314, 2021.
- [13] Andrey V Sharkov, Andrey V Pakulev, Sergey V Chekalin, and Yuri A Matveetz. Primary events in bacteriorhodopsin probed by subpicosecond spectroscopy. *Biochimica et Biophysica Acta (BBA)-Bioenergetics*, 808(1):94–102, 1985.
- [14] Yonghao Mi. *Strong-field ionization of atoms and molecules with two-color laser pulses*. PhD thesis, 2017.

- [15] LV Keldysh et al. Ionization in the field of a strong electromagnetic wave. *Sov. Phys. JETP*, 20(5):1307–1314, 1965.
- [16] Yu Hang Lai, Junliang Xu, Urszula B Szafruga, Bradford K Talbert, Xiaowei Gong, Kaikai Zhang, Harald Fuest, Matthias F Kling, Cosmin I Bologa, Pierre Agostini, et al. Experimental investigation of strong-field-ionization theories for laser fields from visible to midinfrared frequencies. *Physical Review A*, 96(6):063417, 2017.
- [17] GA DELONE, NB DELONE, OV KUDREVATOVA, and GS VORONOV. Multiphoton ionization of a hydrogen molecule in a strong electric field of ruby-laser emission (hydrogen molecule multiphoton ionization, determining probability of absorption, effected by ruby laser emission). *ZHETF PIS'MA V REDAKTSIIU*, 2:377–380, 1965.
- [18] P Agostini, G Barjot, J Bonnal, G Mainfray, C Manus, and J Morellec. Multiphoton ionization of hydrogen and rare gases. *IEEE Journal of Quantum Electronics*, 4(10):667–669, 1968.
- [19] G Mainfray and G Manus. Multiphoton ionization of atoms. *Reports on progress in physics*, 54(10):1333, 1991.
- [20] Paul B Corkum. Plasma perspective on strong field multiphoton ionization. *Physical review letters*, 71(13):1994, 1993.
- [21] Giuseppe Sansone, Enrico Benedetti, Francesca Calegari, Caterina Vozzi, Lorenzo Avaldi, Roberto Flammini, Luca Poletto, P Villoresi, C Altucci, R Velotta, et al. Isolated single-cycle attosecond pulses. *Science*, 314(5798):443–446, 2006.
- [22] Juergen Grotemeyer and Edward W Schlag. Biomolecules in the gas phase: multiphoton ionization mass spectrometry. *Accounts of Chemical Research*, 22(11):399–406, 1989.
- [23] Olof Echt, P Di Dao, S Morgan, and AW Castleman Jr. Multiphoton ionization of ammonia clusters and the dissociation dynamics of protonated cluster ions. *The Journal of chemical physics*, 82(9):4076–4085, 1985.

- [24] S Henz and J Herrmann. Self-channeling and pulse shortening of femtosecond pulses in multiphoton-ionized dispersive dielectric solids. *Physical Review A*, 59(3):2528, 1999.
- [25] Ralph Howard Fowler and Lothar Nordheim. Electron emission in intense electric fields. *Proceedings of the Royal Society of London. Series A, Containing Papers of a Mathematical and Physical Character*, 119(781):173–181, 1928.
- [26] JR Oppenheimer. On the quantum theory of the autoelectric field currents. *Proceedings of the National Academy of Sciences*, 14(5):363–365, 1928.
- [27] J Robert Oppenheimer. Three notes on the quantum theory of aperiodic effects. *Physical review*, 31(1):66, 1928.
- [28] Maxim V Ammosov, Nikolai B Delone, and Vladimir P Krainov. Tunnel ionization of complex atoms and of atomic ions in an alternating electromagnetic field. *Soviet Journal of Experimental and Theoretical Physics*, 64(6):1191, 1986.
- [29] Farhad HM Faisal. Multiple absorption of laser photons by atoms. *Journal of Physics B: Atomic and Molecular Physics (1968-1987)*, 6(4):L89, 1973.
- [30] Howard R Reiss. Effect of an intense electromagnetic field on a weakly bound system. *Physical Review A*, 22(5):1786, 1980.
- [31] IA Ivanov, AS Kheifets, JE Calvert, S Goodall, X Wang, Han Xu, AJ Palmer, D Kielpinski, IV Litvinyuk, and Robert T Sang. Transverse electron momentum distribution in tunneling and over the barrier ionization by laser pulses with varying ellipticity. *Scientific reports*, 6(1):1–8, 2016.
- [32] James S Cohen. Reexamination of over-the-barrier and tunneling ionization of the hydrogen atom in an intense field. *Physical Review A*, 64(4):043412, 2001.

- [33] A Emmanouilidou and DS Tchitchekova. Strongly driven molecules: probing the tunneling phase in the over-the-barrier regime and prevalence of different double ionization pathways. *arXiv preprint arXiv:1101.4960*, 2011.
- [34] WC Wiley and Ii H McLaren. Time-of-flight mass spectrometer with improved resolution. *Review of scientific instruments*, 26(12):1150–1157, 1955.
- [35] André TJB Eppink and David H Parker. Velocity map imaging of ions and electrons using electrostatic lenses: Application in photoelectron and photofragment ion imaging of molecular oxygen. *Review of Scientific Instruments*, 68(9):3477–3484, 1997.
- [36] Simon Brennecke, Martin Ranke, Anastasios Dimitriou, Sophie Walther, Mark J Prandolini, Manfred Lein, and Ulrike Frühling. Control of electron wave packets close to the continuum threshold using near-single-cycle thz waveforms. *Physical Review Letters*, 129(21):213202, 2022.
- [37] Sergey Zhrebtsov, Adrian Wirth, Thorsten Uphues, Irina Znakovskaya, Oliver Herrwerth, Justin Gagnon, Michael Korbman, Vladislav S Yakovlev, MJJ Vrakking, M Drescher, et al. Attosecond imaging of xuv-induced atomic photoemission and auger decay in strong laser fields. *Journal of Physics B: Atomic, Molecular and Optical Physics*, 44(10):105601, 2011.
- [38] Yih Chung Chang, Kai Liu, Konstantinos S Kalogerakis, Cheuk-Yiu Ng, and William M Jackson. Branching ratios of the  $n(2d_{03/2})$  and  $n(2d_{05/2})$  spin-orbit states produced in the state-selected photodissociation of  $n_2$  determined using time-sliced velocity-mapped-imaging photoionization mass spectrometry (ts-vmi-pi-ms). *The Journal of Physical Chemistry A*, 123(12):2289–2300, 2019.
- [39] Pan Jiang, Liya Lu, and Hong Gao. Observation of rotationally dependent fine-structure branching ratios near the predissociation threshold  $n(2d_{5/2}, 3/2) + n(2d_{5/2}, 3/2)$  of  $14n_2$ . *The Journal of Chemical Physics*, 156(19):191101, 2022.

- [40] Michael NR Ashfold, Matthew Bain, Christopher S Hansen, Rebecca A Ingle, Tolga NV Karsili, Barbara Marchetti, and Daniel Murdock. Exploring the dynamics of the photoinduced ring-opening of heterocyclic molecules. *The journal of physical chemistry letters*, 8(14):3440–3451, 2017.
- [41] S Pandit, TJ Preston, SJ King, C Vallance, and AJ Orr-Ewing. (2016). evidence for concerted ring opening and c-br bond breaking in uv-excited bromocyclopropane. *journal of chemical physics*, 144 (24),[244312]. doi: 10.1063/1.4954373.
- [42] NG Kling, D Paul, A Gura, G Laurent, S De, H Li, Z Wang, B Ahn, CH Kim, TK Kim, et al. Thick-lens velocity-map imaging spectrometer with high resolution for high-energy charged particles. *Journal of Instrumentation*, 9(05):P05005, 2014.
- [43] D Schomas, N Rendler, J Krull, R Richter, and M Mudrich. A compact design for velocity-map imaging of energetic electrons and ions. *The Journal of chemical physics*, 147(1):013942, 2017.
- [44] Martin Richter, Maksim Kunitski, Markus Schöffler, Till Jahnke, Lothar P. H. Schmidt, Min Li, Yunquan Liu, and Reinhard Dörner. Streaking temporal double-slit interference by an orthogonal two-color laser field. *Phys. Rev. Lett.*, 114:143001, Apr 2015.
- [45] Serguei Patchkovskii, Marc JJ Vrakking, DM Villeneuve, and Hiromichi Niikura. Selection of the magnetic quantum number in resonant ionization of neon using an xuv-ir two-color laser field. *Journal of Physics B: Atomic, Molecular and Optical Physics*, 53(13):134002, 2020.
- [46] Warren S Warren, Herschel Rabitz, and Mohammed Dahleh. Coherent control of quantum dynamics: the dream is alive. *Science*, 259(5101):1581–1589, 1993.
- [47] Tobias Brixner and Gustav Gerber. Quantum control of gas-phase and liquid-phase femtochemistry. *ChemPhysChem*, 4(5):418–438, 2003.

- [48] Simon Petretti, Alvaro Magana, Alejandro Saenz, and Piero Decleva. Wavelength- and alignment-dependent photoionization of n 2 and o 2. *Physical Review A*, 94(5):053411, 2016.
- [49] Rituparna Das, Deepak K Pandey, Vinita Nimma, P Madhusudhan, Pranav Bhardwaj, Pooja Chandravanshi, Muhammed Shameem KM, Dheeraj K Singh, and Rajesh K Kushawaha. Strong-field ionization of polyatomic molecules: ultrafast h atom migration and bond formation in the photodissociation of ch 3 oh. *Faraday Discussions*, 228:432–450, 2021.
- [50] T Brixner, G Krampert, T Pfeifer, R Selle, G Gerber, M Wollenhaupt, O Graefe, C Horn, D Liese, and T Baumert. Quantum control by ultrafast polarization shaping. *Physical review letters*, 92(20):208301, 2004.
- [51] Stuart A Rice. New ideas for guiding the evolution of a quantum system. *Science*, 258(5081):412–413, 1992.
- [52] Eric Charron, Annick Giusti-Suzor, and Frederick H Meis. Coherent control of photodissociation in intense laser fields. *The Journal of chemical physics*, 103(17):7359–7373, 1995.
- [53] Ali Mehdinejad. Quantum control of atom-photon entanglement via structure light in a three-level medium. *International Journal of Theoretical Physics*, 61(6):1–9, 2022.
- [54] Yue Zeng, Dongkai Zhang, Fangqing Tang, Shaochen Fang, Wuhong Zhang, and Lixiang Chen. Controlling quantum correlations in optical-angle-orbital-angular-momentum variables. *Physical Review A*, 104(5):053719, 2021.
- [55] KC Prince, E Allaria, C Callegari, R Cucini, G De Ninno, S Di Mitri, B Diviacco, E Ferrari, P Finetti, D Gauthier, et al. Coherent control with a short-wavelength free-electron laser. *Nature Photonics*, 10(3):176–179, 2016.

- [56] Moshe Shapiro and Paul Brumer. Quantum control of chemical reactions. *Journal of the Chemical Society, Faraday Transactions*, 93(7):1263–1277, 1997.
- [57] Johan Mauritsson, Per Johnsson, E Gustafsson, Anne L’Huillier, KJ Schafer, and MB Gaarde. Attosecond pulse trains generated using two color laser fields. *Physical review letters*, 97(1):013001, 2006.
- [58] Eiji J Takahashi, Pengfei Lan, Oliver D Mücke, Yasuo Nabekawa, and Katsumi Midorikawa. Infrared two-color multicycle laser field synthesis for generating an intense attosecond pulse. *Physical review letters*, 104(23):233901, 2010.
- [59] Jérémie Caillat, Alfred Maquet, Stefan Haessler, Baptiste Fabre, Thierry Ruchon, Pascal Salières, Yann Mairesse, and Richard Taïeb. Attosecond resolved electron release in two-color near-threshold photoionization of n 2. *Physical review letters*, 106(9):093002, 2011.
- [60] D Habibović, A Gazibegović-Busuladžić, M Busuladžić, A Čerkić, and DB Milošević. Strong-field ionization of homonuclear diatomic molecules using orthogonally polarized two-color laser fields. *Physical Review A*, 102(2):023111, 2020.
- [61] M Meyer, D Cubaynes, P O’keeffe, H Luna, Patrick Yeates, Eugene T Kennedy, John T Costello, P Orr, R Taïeb, A Maquet, et al. Two-color photoionization in xuv free-electron and visible laser fields. *Physical Review A*, 74(1):011401, 2006.
- [62] Candong Liu, Maurizio Reduzzi, Andrea Trabattoni, Anumula Sunilkumar, Antoine Dubrouil, Francesca Calegari, Mauro Nisoli, and Giuseppe Sansone. Carrier-envelope phase effects of a single attosecond pulse in two-color photoionization. *Physical Review Letters*, 111(12):123901, 2013.
- [63] Siqiang Luo, Min Li, Hui Xie, Peng Zhang, Shengliang Xu, Yang Li, Yueming Zhou, Pengfei Lan, and Peixiang Lu. Angular-dependent asymmetries

- of above-threshold ionization in a two-color laser field. *Physical Review A*, 96(2):023417, 2017.
- [64] Huai-Hang Song, Wei-Min Wang, Jian-Xing Li, Yan-Fei Li, and Yu-Tong Li. Spin-polarization effects of an ultrarelativistic electron beam in an ultraintense two-color laser pulse. *Physical Review A*, 100(3):033407, 2019.
- [65] Meng Han, Peipei Ge, Ming-Ming Liu, Qihuang Gong, and Yunquan Liu. Spatially and temporally controlling electron spin polarization in strong-field ionization using orthogonal two-color laser fields. *Physical Review A*, 99(2):023404, 2019.
- [66] Michael Spanner, Serguei Patchkovskii, Eugene Frumker, and Paul Corkum. Mechanisms of two-color laser-induced field-free molecular orientation. *Phys. Rev. Lett.*, 109:113001, Sep 2012.
- [67] Je Hoi Mun, Hirofumi Sakai, and Rosario González-Férez. Orientation of linear molecules in two-color laser fields with perpendicularly crossed polarizations. *Physical Review A*, 99(5):053424, 2019.
- [68] Donna Strickland and Gerard Mourou. Compression of amplified chirped optical pulses. *Optics communications*, 55(6):447–449, 1985.
- [69] Malini Ramaswamy-Paye and JG Fujimoto. Compact dispersion-compensating geometry for kerr-lens mode-locked femtosecond lasers. *Optics letters*, 19(21):1756–1758, 1994.
- [70] Zhenlin Liu, Shinji Izumida, Shingo Ono, Hideyuki Ohtake, and Nobuhiko Sarukura. High-repetition-rate, high-average-power, mode-locked ti: sapphire laser with an intracavity continuous-wave amplification scheme. *Applied physics letters*, 74(24):3622–3623, 1999.
- [71] James D Kafka, Michael L Watts, and J-WJ Pieterse. Picosecond and femtosecond pulse generation in a regeneratively mode-locked ti: sapphire laser. *IEEE journal of quantum electronics*, 28(10):2151–2162, 1992.

- [72] T Südmeyer, SV Marchese, S Hashimoto, CRE Baer, G Gingras, B Witzel, and U Keller. Femtosecond laser oscillators for high-field science. *Nature photonics*, 2(10):599–604, 2008.
- [73] P Madhusudhan, Rituparna Das, Pranav Bharadwaj, Pooja Chandravanshi, Swetapuspa Soumyashree, Vinitha Nimma, and Rajesh K Kushawaha. Modern experimental techniques in ultrafast atomic and molecular physics. In *Modern Techniques of Spectroscopy*, pages 257–285. Springer, 2021.
- [74] Rick Trebino, Kenneth W DeLong, David N Fittinghoff, John N Sweetser, Marco A Krumbügel, Bruce A Richman, and Daniel J Kane. Measuring ultrashort laser pulses in the time-frequency domain using frequency-resolved optical gating. *Review of Scientific Instruments*, 68(9):3277–3295, 1997.
- [75] Chris Iaconis and Ian A Walmsley. Self-referencing spectral interferometry for measuring ultrashort optical pulses. *IEEE Journal of quantum electronics*, 35(4):501–509, 1999.
- [76] Chris Iaconis and Ian A. Walmsley. Self-referencing spectral interferometry for measuring ultrashort optical pulses. *IEEE Journal of Quantum Electronics*, 35:501–509, 1999.
- [77] W. C. Wiley and I. H. McLaren. Time-of-flight mass spectrometer with improved resolution. *Review of Scientific Instruments*, 26(12):1150–1157, 1955.
- [78] André T. J. B. Eppink and David H. Parker. Velocity map imaging of ions and electrons using electrostatic lenses: Application in photoelectron and photofragment ion imaging of molecular oxygen. *Review of Scientific Instruments*, 68(9):3477–3484, 1997.
- [79] David W. Chandler and Paul L. Houston. Two-dimensional imaging of state-selected photodissociation products detected by multiphoton ionization. *The Journal of Chemical Physics*, 87(2):1445–1447, 1987.
- [80] P. B. Corkum. Plasma perspective on strong field multiphoton ionization. *Phys. Rev. Lett.*, 71:1994–1997, Sep 1993.

- [81] O Herrwerth, A Rudenko, M Kremer, VLB de Jesus, B Fischer, G Gademann, K Simeonidis, A Achtelik, Th Ergler, B Feuerstein, et al. Wavelength dependence of sub-laser-cycle few-electron dynamics in strong-field multiple ionization. *New Journal of Physics*, 10(2):025007, 2008.
- [82] Xiao-Min Tong, ZX Zhao, and Chii-Dong Lin. Theory of molecular tunneling ionization. *Physical Review A*, 66(3):033402, 2002.
- [83] A. McPherson, G. Gibson, H. Jara, U. Johann, T. S. Luk, I. A. McIntyre, K. Boyer, and C. K. Rhodes. Studies of multiphoton production of vacuum-ultraviolet radiation in the rare gases. *J. Opt. Soc. Am. B*, 4(4):595–601, Apr 1987.
- [84] M Ferray, A L'Huillier, X F Li, L A Lompre, G Mainfray, and C Manus. Multiple-harmonic conversion of 1064 nm radiation in rare gases. *Journal of Physics B: Atomic, Molecular and Optical Physics*, 21(3):L31–L35, feb 1988.
- [85] Y. Huismans, A. Rouzée, A. Gijsbertsen, J. H. Jungmann, A. S. Smolkowska, P. S. W. M. Logman, F. Lépine, C. Cauchy, S. Zamith, T. Marchenko, J. M. Bakker, G. Berden, B. Redlich, A. F. G. van der Meer, H. G. Muller, W. Vermin, K. J. Schafer, M. Spanner, M. Yu. Ivanov, O. Smirnova, D. Bauer, S. V. Popruzhenko, and M. J. J. Vrakking. Time-resolved holography with photoelectrons. *Science*, 331(6013):61–64, 2011.
- [86] J. M. Glowia, A. Natan, J. P. Cryan, R. Hartsock, M. Kozina, M. P. Minitti, S. Nelson, J. Robinson, T. Sato, T. van Driel, G. Welch, C. Weninger, D. Zhu, and P. H. Bucksbaum. Self-referenced coherent diffraction x-ray movie of ångstrom- and femtosecond-scale atomic motion. *Phys. Rev. Lett.*, 117:153003, Oct 2016.
- [87] Jiro Itatani, Jérôme Levesque, Dirk Zeidler, Hiromichi Niikura, Henri Pépin, Jean-Claude Kieffer, Paul B Corkum, and David M Villeneuve. Tomographic imaging of molecular orbitals. *Nature*, 432(7019):867–871, 2004.

- [88] Martin Richter, Maksim Kunitski, Markus Schöffler, Till Jahnke, Lothar PH Schmidt, Min Li, Yunquan Liu, and Reinhard Dörner. Streaking temporal double-slit interference by an orthogonal two-color laser field. *Physical Review Letters*, 114(14):143001, 2015.
- [89] Martin Richter, Maksim Kunitski, Markus Schöffler, Till Jahnke, Lothar Ph H Schmidt, and Reinhard Dörner. Ionization in orthogonal two-color laser fields: Origin and phase dependences of trajectory-resolved coulomb effects. *Physical Review A*, 94(3):033416, 2016.
- [90] Xinhua Xie, Tian Wang, ShaoGang Yu, XuanYang Lai, Stefan Roither, Daniil Kartashov, Andrius Baltuška, XiaoJun Liu, André Staudte, Markus Kitzler, et al. Disentangling intracycle interferences in photoelectron momentum distributions using orthogonal two-color laser fields. *Physical Review Letters*, 119(24):243201, 2017.
- [91] Li Zhang, Xinhua Xie, Stefan Roither, Yueming Zhou, Peixiang Lu, Daniil Kartashov, Markus Schöffler, Dror Shafir, Paul B Corkum, Andrius Baltuška, et al. Subcycle control of electron-electron correlation in double ionization. *Physical Review Letters*, 112(19):193002, 2014.
- [92] Yueming Zhou, Cheng Huang, Aihong Tong, Qing Liao, and Peixiang Lu. Correlated electron dynamics in nonsequential double ionization by orthogonal two-color laser pulses. *Optics express*, 19(3):2301–2308, 2011.
- [93] P Madhusudhan, Rituparna Das, Pranav Bharadwaj, Pooja Chandravanshi, Swetapuspa Soumyashree, Vinitha Nimma, and Rajesh K Kushawaha. Modern experimental techniques in ultrafast atomic and molecular physics. *Modern Techniques of Spectroscopy: Basics, Instrumentation, and Applications*, 13:257, 2021.
- [94] Rituparna Das, Deepak K Pandey, Vinitha Nimma, P Madhusudhan, Pranav Bhardwaj, Pooja Chandravanshi, Muhammed Shameem KM, Dheeraj K Singh, and Rajesh K Kushawaha. Strong-field ionization of

- polyatomic molecules: ultrafast h atom migration and bond formation in the photodissociation of  $\text{CH}_3\text{OH}$ . *Faraday Discussions*, 228:432–450, 2021.
- [95] X. M. Tong, Z. X. Zhao, and C. D. Lin. Theory of molecular tunneling ionization. *Phys. Rev. A*, 66:033402, Sep 2002.
- [96] Yu Hang Lai, Junliang Xu, Urszula B. Szafruga, Bradford K. Talbert, Xiaowei Gong, Kaikai Zhang, Harald Fuest, Matthias F. Kling, Cosmin I. Blaga, Pierre Agostini, and Louis F. DiMauro. Experimental investigation of strong-field-ionization theories for laser fields from visible to midinfrared frequencies. *Phys. Rev. A*, 96:063417, Dec 2017.
- [97] Th Weber, M Weckenbrock, A Staudte, L Spielberger, O Jagutzki, V Mergel, F Afaneh, G Urbasch, M Vollmer, H Giessen, and R Dörner. Sequential and nonsequential contributions to double ionization in strong laser fields. *Journal of Physics B: Atomic, Molecular and Optical Physics*, 33(4):L127, feb 2000.
- [98] A. l’Huillier, L. A. Lompre, G. Mainfray, and C. Manus. Multiply charged ions induced by multiphoton absorption in rare gases at  $0.53 \mu\text{m}$ . *Phys. Rev. A*, 27:2503–2512, May 1983.
- [99] K. J. Schafer, Baorui Yang, L. F. DiMauro, and K. C. Kulander. Above threshold ionization beyond the high harmonic cutoff. *Phys. Rev. Lett.*, 70:1599–1602, Mar 1993.
- [100] T Marchenko, H G Muller, K J Schafer, and M J J Vrakking. Electron angular distributions in near-threshold atomic ionization. *Journal of Physics B: Atomic, Molecular and Optical Physics*, 43(9):095601, apr 2010.
- [101] T Marchenko, H G Muller, K J Schafer, and M J J Vrakking. Wavelength dependence of photoelectron spectra in above-threshold ionization. *Journal of Physics B: Atomic, Molecular and Optical Physics*, 43(18):185001, sep 2010.
- [102] D. G. Arbó, C. Lemell, S. Nagele, N. Camus, L. Fechner, A. Krupp, T. Pfeifer, S. D. López, R. Moshhammer, and J. Burgdörfer. Ionization

- of argon by two-color laser pulses with coherent phase control. *Phys. Rev. A*, 92:023402, Aug 2015.
- [103] Zhangjin Chen, Toru Morishita, Anh-Thu Le, M. Wickenhauser, X. M. Tong, and C. D. Lin. Analysis of two-dimensional photoelectron momentum spectra and the effect of the long-range coulomb potential in single ionization of atoms by intense lasers. *Phys. Rev. A*, 74:053405, Nov 2006.
- [104] V Schyja, T Lang, and H Helm. Channel switching in above-threshold ionization of xenon. *Physical Review A*, 57(5):3692, 1998.
- [105] Jia Tan, Yueming Zhou, Mingrui He, Yinbo Chen, Qinghua Ke, Jintai Liang, Xiaosong Zhu, Min Li, and Peixiang Lu. Determination of the ionization time using attosecond photoelectron interferometry. *Physical review letters*, 121(25):253203, 2018.
- [106] Daniel D Hickstein, Predrag Ranitovic, Stefan Witte, Xiao-Min Tong, Ymkje Huisman, Paul Arpin, Xibin Zhou, K Ellen Keister, Craig W Hogle, Bosheng Zhang, et al. Direct visualization of laser-driven electron multiple scattering and tunneling distance in strong-field ionization. *Physical Review Letters*, 109(7):073004, 2012.
- [107] N Dudovich, Olga Smirnova, J Levesque, Yu Mairesse, M Yu Ivanov, DM Villeneuve, and Paul B Corkum. Measuring and controlling the birth of attosecond xuv pulses. *Nature physics*, 2(11):781–786, 2006.
- [108] Leonardo Brugnera, David J. Hoffmann, Thomas Siegel, Felix Frank, Amelle Zair, John W. G. Tisch, and Jonathan P. Marangos. Trajectory selection in high harmonic generation by controlling the phase between orthogonal two-color fields. *Phys. Rev. Lett.*, 107:153902, Oct 2011.
- [109] Ji-Wei Geng, Wei-Hao Xiong, Xiang-Ru Xiao, Liang-You Peng, and Qi-huang Gong. Nonadiabatic electron dynamics in orthogonal two-color laser fields with comparable intensities. *Phys. Rev. Lett.*, 115:193001, Nov 2015.

- [110] Ming-Ming Liu, Meng Han, Peipei Ge, Chaoxiong He, Qihuang Gong, and Yunquan Liu. Strong-field ionization of diatomic molecules in orthogonally polarized two-color fields. *Phys. Rev. A*, 97:063416, Jun 2018.
- [111] Oren Pedatzur, Gal Orenstein, V Serbinenko, Hadas Soifer, BD Bruner, AJ Uzan, DS Brambila, AG Harvey, L Torlina, F Morales, et al. Attosecond tunnelling interferometry. *Nature Physics*, 11(10):815–819, 2015.
- [112] Jia Tan, Yueming Zhou, Qinghua Ke, Mingrui He, Jintai Liang, Yang Li, Min Li, and Peixiang Lu. Resolving strong-field tunneling ionization with a temporal double-slit interferometer. *Physical Review A*, 101(1):013407, 2020.
- [113] Rolf Wiehle, Bernd Witzel, Hanspeter Helm, and Eric Cormier. Dynamics of strong-field above-threshold ionization of argon: Comparison between experiment and theory. *Physical Review A*, 67(6):063405, 2003.
- [114] Katarzyna Krajewska, Ilya I Fabrikant, and Anthony F Starace. Threshold effects in strong-field ionization: Energy shifts and rydberg structures. *Physical Review A*, 86(5):053410, 2012.
- [115] Yingbin Li, Jingkun Xu, Hongmei Chen, Yihan Li, Jinjin He, Lingling Qin, Luke Shi, Yiguang Zhao, Qingbin Tang, Chunyang Zhai, et al. Manipulating frustrated double ionization by orthogonal two-color laser pulses. *Optics Communications*, 493:127019, 2021.
- [116] Guoqiang Shi, Yulin Xiang, Jianting Lei, Shaohua Sun, Zuoye Liu, and Bitao Hu. Dissociation pathways established in strong-field single ionization of molecular co. *Applied Physics B*, 128(11):1–8, 2022.
- [117] Guoqiang Shi, Yulin Xiang, Pingquan Wang, Zexuan Wang, Shaohua Sun, Zuoye Liu, and Bitao Hu. Coulomb explosion and angular distributions of the fragment ions of highly charged co in the strong laser field. *Journal of Modern Optics*, 68(1):10–18, 2021.
- [118] Qiyong Song, Hui Li, Junping Wang, Peifen Lu, Xiaochun Gong, Qinying Ji, Kang Lin, Wenbin Zhang, Junyang Ma, Hanxiao Li, Heping Zeng, Feng

- He, and Jian Wu. Double ionization of nitrogen molecules in orthogonal two-color femtosecond laser fields. *Journal of Physics B: Atomic, Molecular and Optical Physics*, 51(7):074002, mar 2018.
- [119] Xiaonan Tang, Yu Hou, CY Ng, and Branko Ruscic. Pulsed field-ionization photoelectron-photoion coincidence study of the process  $n 2+ h \nu \rightarrow n++ n+ e-$ : Bond dissociation energies of  $n 2$  and  $n 2+$ . *The Journal of chemical physics*, 123(7):074330, 2005.
- [120] Robert Locht. The dissociative ionization of carbon monoxide. *Chemical Physics*, 22(1):13–27, 1977.
- [121] P Madhusudhan, Rituparna Das, Pranav Bhardwaj, Muhammed Shameem KM, Vinitha Nimma, Swetapuspa Soumyashree, and Rajesh K Kushawaha. Strong-field ionization of  $n2$  and  $co$  molecules using two-color laser field. *Journal of Physics B: Atomic, Molecular and Optical Physics*, 55(23):234001, 2022.
- [122] Marius Cristian Stroe and Magda Fifirig. Ionization of the  $co$  molecule in intense short two-color laser pulses. *Optik*, 247:167883, 2021.
- [123] Pradeep Kumar and N Sathyamurthy. Potential energy curves for neutral and multiply charged carbon monoxide. *Pramana*, 74(1):49–55, 2010.
- [124] Hui Li, Dipanwita Ray, Sankar De, Irina Znakovskaya, W Cao, G Laurent, Z Wang, Matthias F Kling, Anh-Thu Le, and CL Cocke. Orientation dependence of the ionization of  $co$  and  $no$  in an intense femtosecond two-color laser field. *Physical Review A*, 84(4):043429, 2011.
- [125] D. Habibović, A. Gazibegović-Busuladžić, M. Busuladžić, and D. B. Milošević. Strong-field ionization of heteronuclear diatomic molecules using an orthogonally polarized two-color laser field. *Phys. Rev. A*, 103:053101, May 2021.
- [126] D. Milošević, Dino Habibovic, M. Busuladžić, Azra Gazibegović-Busuladžić, and Aner Čerkić. Strong-field ionization of homonuclear di-

- atomic molecules using orthogonally polarized two-color laser fields. *Physical review A: General physics*, 102:023111, 08 2020.
- [127] S Skruszewicz, J Tiggesbäumker, K-H Meiwes-Broer, M Arbeiter, Th Fennel, and D Bauer. Two-color strong-field photoelectron spectroscopy and the phase of the phase. *Physical Review Letters*, 115(4):043001, 2015.
- [128] DG Arbó, C Lemell, S Nagele, Nicolas Camus, Lutz Fechner, A Krupp, Thomas Pfeifer, Sebastián David López, Robert Moshhammer, and J Burgdörfer. Ionization of argon by two-color laser pulses with coherent phase control. *Physical Review A*, 92(2):023402, 2015.
- [129] Ya-Nan Qin, Min Li, Yang Li, Mingrui He, Siqiang Luo, Yali Liu, Yueming Zhou, and Peixiang Lu. Asymmetry of the photoelectron momentum distribution from molecular ionization in elliptically polarized laser pulses. *Phys. Rev. A*, 99:013431, Jan 2019.
- [130] Siqiang Luo, Min Li, Hui Xie, Peng Zhang, Shengliang Xu, Yang Li, Yueming Zhou, Pengfei Lan, and Peixiang Lu. Angular-dependent asymmetries of above-threshold ionization in a two-color laser field. *Phys. Rev. A*, 96:023417, Aug 2017.
- [131] Xu Zheng, Ming-Ming Liu, Hui Xie, Peipei Ge, Min Li, and Yunquan Liu. Control of photoelectron interference in asymmetric momentum distributions using two-color laser fields. *Physical Review A*, 92(5):053422, 2015.
- [132] K Burnett, VC Reed, and PL Knight. Atoms in ultra-intense laser fields. *Journal of Physics B: Atomic, Molecular and Optical Physics*, 26(4):561, 1993.
- [133] Misha Yu Ivanov, Michael Spanner, and Olga Smirnova. Anatomy of strong field ionization. *Journal of Modern Optics*, 52(2-3):165–184, 2005.
- [134] SV Popruzhenko. Keldysh theory of strong field ionization: history, applications, difficulties and perspectives. *Journal of Physics B: Atomic, Molecular and Optical Physics*, 47(20):204001, 2014.

- [135] M Bashkansky, PH Bucksbaum, and DW Schumacher. Asymmetries in above-threshold ionization. *Physical review letters*, 60(24):2458, 1988.
- [136] David N Fittinghoff, Paul R Bolton, Britton Chang, and Kenneth C Kulander. Observation of nonsequential double ionization of helium with optical tunneling. *Physical review letters*, 69(18):2642, 1992.
- [137] Barry Walker, Brian Sheehy, Louis F DiMauro, Pierre Agostini, Kenneth J Schafer, and Kenneth C Kulander. Precision measurement of strong field double ionization of helium. *Physical review letters*, 73(9):1227, 1994.
- [138] Peter Lambropoulos, Paul Maragakis, and Jian Zhang. Two-electron atoms in strong fields. *Physics Reports*, 305(5):203–293, 1998.
- [139] Wilhelm Becker, XiaoJun Liu, Phay Jo Ho, and Joseph H. Eberly. Theories of photoelectron correlation in laser-driven multiple atomic ionization. *Rev. Mod. Phys.*, 84:1011–1043, Jul 2012.
- [140] A McPherson, G Gibson, H Jara, U Johann, Ting S Luk, IA McIntyre, Keith Boyer, and Charles K Rhodes. Studies of multiphoton production of vacuum-ultraviolet radiation in the rare gases. *JOSA B*, 4(4):595–601, 1987.
- [141] M Ferray, Anne L’Huillier, XF Li, LA Lompre, G Mainfray, and C Manus. Multiple-harmonic conversion of 1064 nm radiation in rare gases. *Journal of Physics B: Atomic, Molecular and Optical Physics*, 21(3):L31, 1988.
- [142] Paul B Corkum. Plasma perspective on strong field multiphoton ionization. *Physical review letters*, 71(13):1994, 1993.
- [143] C. Guo, M. Li, J. P. Nibarger, and G. N. Gibson. Single and double ionization of diatomic molecules in strong laser fields. *Phys. Rev. A*, 58:R4271–R4274, Dec 1998.
- [144] Chunlei Guo, Ming Li, John P. Nibarger, and George N. Gibson. Nonsequential double ionization of molecular fragments. *Phys. Rev. A*, 61:033413, Feb 2000.

- [145] Chunlei Guo. Holding molecular dications together in strong laser fields. *Phys. Rev. A*, 73:041401, Apr 2006.
- [146] David N Fittinghoff, Paul R Bolton, Britton Chang, and Kenneth C Kulander. Observation of nonsequential double ionization of helium with optical tunneling. *Physical review letters*, 69(18):2642, 1992.
- [147] K. Kondo, A. Sagisaka, T. Tamida, Y. Nabekawa, and S. Watanabe. Wavelength dependence of nonsequential double ionization in he. *Phys. Rev. A*, 48:R2531–R2533, Oct 1993.
- [148] B. Walker, B. Sheehy, L. F. DiMauro, P. Agostini, K. J. Schafer, and K. C. Kulander. Precision measurement of strong field double ionization of helium. *Phys. Rev. Lett.*, 73:1227–1230, Aug 1994.
- [149] C. Cornaggia and Ph. Hering. Nonsequential double ionization of small molecules induced by a femtosecond laser field. *Phys. Rev. A*, 62:023403, Jul 2000.
- [150] J. Liu, D. F. Ye, J. Chen, and X. Liu. Complex dynamics of correlated electrons in molecular double ionization by an ultrashort intense laser pulse. *Phys. Rev. Lett.*, 99:013003, Jul 2007.
- [151] X. Y. Jia, W. D. Li, J. Fan, J. Liu, and J. Chen. Suppression effect in the nonsequential double ionization of molecules by an intense laser field. *Phys. Rev. A*, 77:063407, Jun 2008.
- [152] E. Eremina, X. Liu, H. Rottke, W. Sandner, M. G. Schätzel, A. Dreischuh, G. G. Paulus, H. Walther, R. Moshhammer, and J. Ullrich. Influence of molecular structure on double ionization of  $n_2$  and  $o_2$  by high intensity ultrashort laser pulses. *Phys. Rev. Lett.*, 92:173001, Apr 2004.
- [153] Qing yun Xu, Shuai Ben, Yue Sun, Hai feng Xu, Xue shen Liu, Hang Lv, and Jing Guo. Non-sequential double ionization of triatomic molecules ocs in intense laser fields. *Chemical Physics Letters*, 747:137326, 2020.

- [154] M. Oppermann, S. J. Weber, L. J. Frasinski, M. Yu. Ivanov, and J. P. Marangos. Multichannel contributions in the nonsequential double ionization of  $\text{CO}_2$ . *Phys. Rev. A*, 88:043432, Oct 2013.
- [155] Hongtao Hu, Sarayoo Kangaparambi, Martin Dörner-Kirchner, Václav Hanus, Andrius Baltuška, Markus Kitzler-Zeiler, and Xinhua Xie. Quantitative retrieval of the angular dependence of laser-induced electron rescattering in molecules. *Phys. Rev. A*, 103:013114, Jan 2021.
- [156] Linsen Pei and Chunlei Guo. Nonsequential double ionization of triatomic molecules in strong laser fields. *Phys. Rev. A*, 82:021401, Aug 2010.
- [157] Jun-Feng Zhang, Ri Ma, Wan-Long Zuo, Hang Lv, Hong-Wei Huang, Hai-Feng Xu, Ming-Xing Jin, and Da-Jun Ding. Ellipticity-dependent ionization/dissociation of carbon dioxide in strong laser fields\*. *Chinese Physics B*, 24(3):033302, mar 2015.
- [158] Qingyong Meng, Ming-Bao Huang, and Hai-Bo Chang. Theoretical study on the predissociation mechanism of  $\text{CO}_2^+$  ( $c\ 2g^+$ ). *The Journal of Physical Chemistry A*, 113(46):12825–12830, 2009. PMID: 19795827.
- [159] Zhengfang Zhou, Shaowen Feng, Zefeng Hua, Zhen Li, Yang Chen, and Dongfeng Zhao. Dissociation dynamics of carbon dioxide cation ( $\text{CO}_2^+$ ) in the  $c2g^+$  state via  $[1+1]$  two-photon excitation. *The Journal of Chemical Physics*, 152(13):134304, 2020.
- [160] H Hogreve. Stability properties of  $\text{CO}_2^{2+}$ . *Journal of Physics B: Atomic, Molecular and Optical Physics*, 28(8):L263, apr 1995.
- [161] M Hochlaf, F R Bennett, G Chambaud, and P Rosmus. Theoretical study of the electronic states of. *Journal of Physics B: Atomic, Molecular and Optical Physics*, 31(10):2163, may 1998.
- [162] Dongwen Zhang, Bo-Zhen Chen, Ming-Bao Huang, Qingyong Meng, and Zhiyuan Tian. Photodissociation mechanisms of the  $\text{CO}_2^{2+}$  dication studied using multi-state multiconfiguration second-order perturbation theory. *The Journal of Chemical Physics*, 139(17):174305, 2013.

- [163] Cechan Tian and CR Vidal. Single to quadruple ionization of  $\text{CO}_2$  due to electron impact. *Physical Review A*, 58(5):3783, 1998.
- [164] Nora G. Kling, J. McKenna, A. M. Sayler, B. Gaire, M. Zohrabi, U. Ablikim, K. D. Carnes, and I. Ben-Itzhak. Charge asymmetric dissociation of a  $\text{CO}^+$  molecular-ion beam induced by strong laser fields. *Phys. Rev. A*, 87:013418, Jan 2013.
- [165] IA Bocharova, AS Alnaser, U Thumm, Th Niederhausen, D Ray, Charles L Cocke, and IV Litvinyuk. Time-resolved coulomb-explosion imaging of nuclear wave-packet dynamics induced in diatomic molecules by intense few-cycle laser pulses. *Physical Review A*, 83(1):013417, 2011.
- [166] Hang Yuan, Shenyue Xu, Enliang Wang, Jiawei Xu, Yue Gao, Xiaolong Zhu, Dalong Guo, Binghui Ma, Dongmei Zhao, Shaofeng Zhang, Shuncheng Yan, Ruitian Zhang, Yong Gao, Zhongfeng Xu, and Xinwen Ma. Fragmentation dynamics of a carbon dioxide dication produced by ion impact. *The Journal of Physical Chemistry Letters*, 13(32):7594–7599, 2022. PMID: 35950906.
- [167] Cechan Tian and CR Vidal. Electron impact ionization of and: contributions from different dissociation channels of multiply ionized molecules. *Journal of Physics B: Atomic, Molecular and Optical Physics*, 31(24):5369, 1998.
- [168] M. Lezius, V. Blanchet, D. M. Rayner, D. M. Villeneuve, Albert Stolow, and Misha Yu. Ivanov. Nonadiabatic multielectron dynamics in strong field molecular ionization. *Phys. Rev. Lett.*, 86:51–54, Jan 2001.
- [169] Vadim V Lozovoy, Xin Zhu, Tissa C Gunaratne, D Ahmasi Harris, Janelle C Shane, and Marcos Dantus. Control of molecular fragmentation using shaped femtosecond pulses. *The Journal of Physical Chemistry A*, 112(17):3789–3812, 2008.
- [170] André D Bandrauk, S Chelkowski, and Isao Kawata. Molecular above-

- threshold-ionization spectra: The effect of moving nuclei. *Physical Review A*, 67(1):013407, 2003.
- [171] Xinhua Xie, Erik Lötstedt, Stefan Roither, Markus Schöffler, Daniil Kartashov, Katsumi Midorikawa, Andrius Baltuška, Kaoru Yamanouchi, and Markus Kitzler. Duration of an intense laser pulse can determine the breakage of multiple chemical bonds. *Scientific reports*, 5(1):1–11, 2015.
- [172] Zhangjin Chen, Lina Zhang, Yali Wang, Oleg Zatsarinny, Klaus Bartschat, Toru Morishita, and C. D. Lin. Pulse-duration dependence of the double-to-single ionization ratio of ne by intense 780-nm and 800-nm laser fields: Comparison of simulations with experiments. *Phys. Rev. A*, 99:043408, Apr 2019.
- [173] Fang Liu, Zhangjin Chen, Toru Morishita, Klaus Bartschat, Birger Böning, and Stephan Fritzsche. Single-cycle versus multicycle nonsequential double ionization of argon. *Phys. Rev. A*, 104:013105, Jul 2021.
- [174] Cong Wu, Chengyin Wu, Di Song, Hongmei Su, Yudong Yang, Zhifeng Wu, Xianrong Liu, Hong Liu, Min Li, Yongkai Deng, Yunquan Liu, Liang-You Peng, Hongbing Jiang, and Qihuang Gong. Nonsequential and sequential fragmentation of  $\text{CO}_2^{3+}$  in intense laser fields. *Phys. Rev. Lett.*, 110:103601, Mar 2013.